Forced Water Entry and Exit of Two-dimensional Bodies Through a Free Surface

by

Rasadurai Rajavaheinthan

A thesis submitted in partial fulfillment for the
degree of Doctor of Philosophy

in the
School of Information Systems, Computing
and Mathematics, Brunel University

April 2014

Declaration

I, Rasadurai Rajavaheinthan, hereby declare that the work reported in this thesis has wholly been carried out by me for a degree of PhD mathematics at Brunel University under the supervision and advice of Dr M. Greenhow. This thesis or any part of it has not previously been submitted for a degree or any other qualification.

Signed: _____

Date: _____

Acknowledgements

I would like to express my gratitude and thanks to Dr M. Greenhow for his support, continuous guidance and encouragement provided throughout the years of study to complete my studies successfully.

I also would like to give my thanks to Dr Michael K. Warby for provided help and support during the review of my research progress to move onto the next level and to Dr Matthias Maischak for his introduction to the Fortran compiler and plotting techniques.

My thanks also go to the academic and support staff from the Department of Mathematical Sciences at Brunel University.

I also thank my friends, especially M. Kayanan who helped and supported me during this research.

My special thanks go to my beloved parents, relatives and friends.

BRUNEL UNIVERSITY

School of Information Systems, Computing
and Mathematics, Brunel University

Doctor of Philosophy

by Rasadurai Rajavaheinthan

Abstract

The forced water entry and exit of two-dimensional bodies through a free surface is computed for various 2D bodies (symmetric wedges, asymmetric wedges, truncated wedges and boxes). These bodies enter or exit water with constant velocity or constant acceleration. The calculations are based on the fully non-linear time-stepping complex-variable method of Vinje and Brevig.

The model was formulated as an initial boundary-value problem with boundary conditions specified on the boundaries (dynamic and kinematic free-surface boundary conditions) and initial conditions at time zero (initial velocity and position of the body and free-surface particles). The formulated problem was solved by means of a boundary-element method using collocation points on the boundary of the domain and solutions at each time were calculated using time stepping (Runge-Kutta and Hamming predictor corrector) methods.

Numerical results for the deformed free-surface profile, the speed of the point at the intersection of the body and free surface, the pressure along the wetted region of the bodies and force experienced by the bodies, are given for the entry and exit.

To verify the results, various tests such as convergence checks, self-similarity for entry (gravity-free solutions) and Froude number effect for constant velocity entry and exit (half-wedge angles 5 up to 55 degrees) are investigated. The numerical results are compared with Mackie's analytical theory for water entry and exit with constant velocities, and the analytical added mass force computed for water entry and exit of symmetric wedges and boxes with constant acceleration and velocity using conformal mapping. Finally, numerical results showing the effect of finite depth are investigated for entry and exit.

Contents

List of Figures

List of Tables

Nomenclature

Symbols

(x,y)	Cartesian coordinate system of horizontal x and vertical y axis
z(x,y)	Complex variable in x and y
$\eta(x, y)$	Free-surface elevation
ρ_w	Water density
g	Gravity acceleration
t	Time
τ	Non-dimensional time
$D\tau$	Non-dimensional time step size
F_r	Froude number
F_b	Total body force
F_a	Added mass force
$\phi(x, y)$	Velocity potential
$\psi(x, y)$	Stream function
$\beta(x, y)$	Complex potential
P	Pressure
P_a	Atmospheric pressure
u	Horizontal velocity
v	Vertical velocity
v_b	Velocity of the body
D_i	Initial submergence
C_t	Characteristic time
$\forall(t)$	Submerged volume at a time t

R_a^t	**Aspect ratio of the truncated wedge**
α_h	**Right vertical half-angle of the wedge**
β_h	**Left vertical half-angle of the wedge**
R_a^b	**Aspect ratio of the box**

Abbreviations

2D	**Two dimensional**
ZG	**Centre of rotation**
ZCG	**Centre of gravity**
IBVP	**Initial-boundary-value problem**
BVP	**Boundary-value problem**
BEM	**Boundary-element method**

This thesis is dedicated to Rasavarothayam and Poomany who provided financial and moral support to complete my studies. It is also dedicated to my family and relatives.

Chapter 1

Introduction

1.1 Research motivation

The study of hydrodynamic effects due to the interaction between fluid (water) and offshore structures (ships, very large floating structures (VLFS), etc.) has attracted many researchers in recent years. It is a well-studied problem and has various applications in the field of coastal and marine engineering, where most of the studies are concerned with two-dimensional bodies.

The interaction may be in the form of wave loading upon a fixed structure (seawall, bulkheads, breakwaters, etc.) or floating offshore structures (VLFS, wind farms, oil platforms, etc.). The direct impact of bodies (with sharp corners or curved shapes) in forced motion of constant velocity or constant acceleration has applications for e.g. free-fall lifeboats. Bodies moving from the free surface or below it (partially or totally submerged) have applications for various marine operations.

The deadrise angle between the free surface and the body surface (ship hull) is also a crucial parameter in the forward motion of ship in rough sea conditions. The impact pressure load increases as the deadrise angle decreases.

Normal ship motions can be predicted by the linear theory of seakeeping. This splits the problem into two categories: wave loading on a fixed body (diffraction) and the body executing motion, giving radiation. Motions may happen in three modes (sway, heave and roll) for 2D analysis or in additional three modes to the 2D case (surge, yaw and pitch) for 3D analysis. Given the usual assumptions of linearity, the underlying velocity potential for the problems can be computed

by summing the six modes, or three modes depending on the dimension of the problem, and the diffraction problem. Then the flow around the body moving in waves can be studied using potential flow theory, see Newman (1977). For the extreme situations described in this thesis, linear theory does not apply, so, no such simplifications are possible.

After the impact of the body, the fluid particles near to the impact region are accelerated and consequently there is some amount of fluid mass moving with the body as an additional mass (added mass) to the system which opposes the motion of the body. The added mass theory is available at time t=0 to compute the forces analytically which can be used to compare with the numerical force computed using the non-linear theory of Vinje and Brevig (1981a; 1981b).

Important applications of the extreme fluid-body interaction problems considered here are the impact force upon a moving ship by waves (slamming), sloshing causing impacts upon LNG- carrier walls, roof baffles and cooling pipes, planing of V-form fast hulls, free-fall life boat designing, crane operations at sea (there one needs to avoid snatching in the cables) and landing and taking off of sea planes.

Slamming impact on offshore structures

One of the major goals in ship design is to increase the forward speed of a ship and maintain the speed while moving in extreme weather conditions (rough seas). In this situation, the ship experiences a great deal of force at the impact part of the hull (bow-flare) due to the wave loading upon it. The impact load excited by the water wave on the ship hull is called slamming. Green-water on deck can also happen as a consequence of large relative vertical motion (heave) between the ship and water wave.

It may also happen that while trying to reduce speed in extreme sea conditions (large waves) the encounter frequency becomes small, and water can then enter as plunging breaker causing slamming load on the deck (wheelhouse). This may lead to structural damage to the ship (see for more details, Faltinsen (2004)).

Bottom slamming may occur when the amplitude of the attacking wave on the bow of a ship is significantly larger than the draft of the ship or very large floating structures (VLFS). The free surface moves along the bow to the bottom of the hull and then turns rapidly back to the bow point where local impact is created.

This sort of local impact force may badly damage the impact region of the hull structure and the impact loads may propagate throughout entire hull of the ship causing it to vibrate (whipping, springing) for a certain time period. This event may lead to severe structural damage by fatigue, see Faltinsen (2004).

During bottom slamming, it can be noticed that the bow of the ship emerges out of the water (water EXIT phenomena) and then the bow falls down through the water (water ENTRY phenomena). As a result of the water entry and exit, it is possible that air may be entrapped between the bottom part of the hull and the free surface. This could lead to another direction of study with an air cavity (air-cushion model) causing effects upon the pressure distribution along the wetted part of the hull (for more details, see Faltinsen (2004)).

(a) Bottom slamming

(b) Slamming loads upon VLFS

(c) Waves loading upon a structure

(d) Green-water on deck slamming

FIGURE 1.1: Water waves loading upon ships and coastal structures: (`http://www.scribd.com/doc/24727159/Storm-Op-Zee?autodown=pdf`)

Floating structures in finite water depth

Numerical calculations of hydrodynamic coefficients and wave exciting forces on a VLFS for transporting crude oil show very significant shallow water effects (finite water depth), especially upon added mass forces, see Oliver (2002) and Korobkin (1999). The bottom of the body in the finite-depth case becomes more significant than for ordinary floating structures since the structural length to vertical scale (depth) is less than that for the infinite depth. Thus the proximity change of the bottom should be considered in estimating hydrodynamic loads, including those of slamming.

By considering all the above physical phenomena, it is therefore necessary to investigate the effects of finite depth on the hydrodynamic loads during the entry and exit phases analytically, numerically and experimentally to understand and develop a well-formulated mathematical model.

1.2 Literature review

Various theoretical, numerical and experimental approaches have been used to study interactions of fluid and structure (and air) by means of suitable assumptions about the fluid and the structure. Water entry and exit problems have been studied by mathematical modelling since the research on water entry of 2D bodies was begun by von Karman (1929), Wagner (1932) and many other researchers (for a complete review, see Korobkin and Pukhnachov (1988)). Initially, the research started with the intention of investigating the effects caused by landing seaplanes in sea water based on simplified analytical theories of expanding thin-plate approximations. Apart from seaplane landing, one of the most important and well-studied problems is slamming, causing local and global damage on ships, which was studied by many researchers, especially Greenhow and Li (1987), Faltinsen (2004) and Greco et al. (2009).

Earlier researchers mostly focused on the impact of the early stage of water entry which causes high impact load pressure distribution on the body. Following the initial impact, it is possible that air may be entrapped between the free-surface piercing bodies and the fluid. This affects the pressure distribution due to the interaction between air, fluid and structure, which depends on the shape of the

body (sharp corners and edges: symmetric wedges, asymmetric wedges or boxes; flat-bottom bodies (small dead-rise angles): elliptic or parabolic bodies) and the speed of entry and exit (for the air-cushioning effect, see Verhagen (1967); Lewison and Maclean (1968)). The another possibility is that high-speed entry causes the fluid particles in motion around the body to be accelerated by the entry and consequently splash-up the fluid which leads to a very thin fast-moving jets. These may break up into spray under the action of surface tension (Greenhow and Lin (1983)). The splash jet break-up into spray causes complicated physical problems in the mathematical and numerical solutions because of the spray moving as a free projectiles and falling into the underlying free surface (see also, Greenhow (1987)).

The solutions to the formulated problems are based on potential flow theory and a complex variable method (Greenhow (1993; 1983); Hughes (1973); John (1953)) with the usual modelling assumptions (inviscid, incompressible and irrotational flow). In practice, it may be possible to extend the modelling to include that each structure is an elastic body with complex shape (see Korobkin and Malenica (2005); Xu et al. (1998); Zhao et al. (1997)), the fluid is compressible (see Korobkin (1992)), the flow is rotational, the effect of gravity is considerable, and the entrapped air cavity. In such cases, despite the present high level of development of Computational Fluid Dynamics (CFD) methods, solutions based on analytical theories or numerical methods are very difficult or impossible because of the complex phenomena (see, Tassin et al. (2013)). Therefore, the study of the problem should use experimental techniques, but there may then be additional difficulties (for more details, see Tassin et al. (2013; 2010)).

In the water entry case, a considerable amount of progress has been made using self-similarity solutions (for more details, see Dobrovol'skaya (1966); Garabedian (1953)) which requires zero gravity of entry of an infinite body. This implies high speed in experimental results (see Greenhow (1987; 1983); Yettou et al. (2006)). Based on the Wagner theory and utilised the self-similarity solutions, many theories exist such as non-linear slamming theory (Dobrovolskaya (1969)), slamming theory with air trapped (see for more information Lewison and Maclean (1968), Bagnold (1939) and Verhagen (1967)), hydroelastic effect in slamming by (Kavaalsvold (1994); Kavaalsvold and Faltinsen (1995)) and statistical approach to slamming by Tick (1958) and Ochi (1964). These have been developed to improve the existing theories and present modified theories to study water entry problems.

An explicit analytical solution to water entry and exit of slender bodies based on linearised boundary conditions was given by Mackie (1962, 1965 and 1969). For wedges, numerical solutions of Dobrovol'skya (1969) and Hughes (1972; 1973) utilised self-similarity based on fully nonlinear and exact boundary conditions. Dobrovol'skya (1966) presented a numerical method based on nonlinear singular integral equations and used the theory to compute results for deadrise angles larger than 30^o. Thereafter, Zhao and Faltinsen (1993) presented results for dead-rise angles between 4^o and 81^o utilising the method of Dobrovol'skya (1969).

The very thin splash jet flow causes numerical issues for the computation of pressure which may lead to the free-surface instability (Greenhow et al. (1983)). To avoid the numerical issues and compute the pressure, Zhao and Faltinsen (1993) used nonlinear boundary element method (NBEM) and truncated the jet (cut-off) when a certain critical angle was reached, introducing a new panel at the spray root that was perpendicular to the body surface (for similar approaches, see Kihara (2004); Battistin and Iafran (2004); Sun and Faltinsen (2007); Tsai and Yue (1993) and for a horizontally moving surface-piercing plate; Needham, Billingham, and King (2007)). The pressure distribution was computed by Zhao et al. (1997) using the nonlinear Bernoulli equation and the exact kinematic boundary condition was satisfied in the computation of the velocity potential based on a generalised Wagner model.

Korobkin (2004) developed the Modified Logvinovich Model (MLM) to compute the pressure on the body using the nonlinear Bernoulli equation and the velocity potential on the body by means of a Taylor expansion of the velocity potential of the original Wagner model. The computational cost of the MLM model is lower than that of the generalised Wagner model (more details, see Tassin et al. (2010)). The MLM was also used to study asymmetric body shapes by Korobkin and Malenica (2005), a 3D analytical model of water impact by Korobkin (2005) and further development by Tassin et al. (2012).

In the recent paper by Tassin et al. (2013), a 2D analytical method and numerical modelling of the partial water entry and subsequent partial exit of a body was considered, with the limitation of relatively small penetration depths compared with the wetted width. They assumed that there is no air cavity behind the body and the upper part of the body remains dry.

Compared to the study of water entry related problems, very little work has been published for water exit problems (see Greenhow (1990); Tassin et al. (2013)).

Greenhow (1990) pointed out some difficulties; for high enough constant speed of wedge entry (see Greenhow (1987)), the gravity-free solution agreed well with numerical calculations, but for exit Greenhow conjectured that gravity is essential for the fluid particles to be in contact with the body at all points and to avoid the formation of triangular deformation in the free-surface (see Greenhow (1990). It is certainly far from clear that the infinite Froude number (g=0) solution is unique or that this solution is approached as the Froude number increases from a finite value. In any case, self-similarity solution is not possible for exit because of the characteristic length scale introduced by the initial submerged depth. Other difficulties to do with stability of the solution were pointed out by Howison et al. (1991). Greenhow (1990) also presented some water exit calculations based on the fully non-linear time-stepping method of Vinje and Brevig (1981b) and compared his slender body calculations with Mackie's (1965) analytical time-dependent wave maker theory by linearising the free-surface elevation and including gravity.

This thesis presents some 2D calculations for water entry with constant speed or constant acceleration based on the formulation of the theory of Vinje and Brevig (1981a; 1981b) and computations for 2D water exit with constant speed or constant acceleration by modifying the model used by Greenhow to study water exit of symmetric (wedges, truncated wedges and boxes) and asymmetric bodies (asymmetric wedges). More details on the derivation of the equations and model can be found in Barringer (1996) and Moyo (1996).

1.3 Thesis structure

A very useful and relatively simple non-linear time stepping theory was developed by Vinje and Brevig (1981a; 1981b) to study non-linear ship motion and the effect of breaking waves. Then the theory was modified by Greenhow and other researchers (see Barringer (1996); Moyo (1996)) to study water entry problems, where they made some progress which agreed with the experimental results of Greenhow and Lin (1983). The aim of this study is to extend the existing theory of Vinje and Brevig to study water exit problems and carry out extensive numerical computations on forced water entry and exit with constant velocities and constant accelerations. However, in this thesis, more attention is given to the computation of water exit problems which is not yet well-studied numerically or experimentally (see Greenhow (1990); Tassin et al. (2013)).

In chapter 2, the detailed explanation is given of the formulation of the two-dimensional initial boundary-value problem (IBVP) using a mixed Eulerian and Lagrangian formulation (see Vinje and Brevig (1981a; 1981b), Barringer (1996) and Greenhow (1193)) . The model assumptions, boundary conditions and initial conditions are clearly explained. The solution method for the IBVP using a boundary-element method (BEM) to give integral equation is precisely specified.

In chapter 3, the numerical formulation of the IBVP which is used to implement the equations in Matlab is explained. The time-stepping algorithms (Runge-Kutta and Hamming predictor-corrector methods) commonly used in the numerical methods of ordinary differential equations (ODE) are also given for the Matlab implementation.

In chapter 4, non-dimensional parameters and computed dimensionless numerical results using the numerical formulation of the IBVP are presented for water entry of symmetric wedges, asymmetric wedges, truncated wedges and boxes with constant velocities and constants accelerations. In particular, the added mass effects, finite depth effect and velocity of the intersection points are investigated numerically. Moreover, the numerical results computed using the IBVP is compared with the analytical theory developed by Mackie (1965).

The chapter 5 for water exit is very similar to the previous chapter on water entry with some additional calculations on the combined body of both wedge and box-shaped bodies but with the exception of some test cases such as self-similarity solutions (this does not apply for exit, see Greenhow (1990)).

The conclusions based on the numerical results computed for the forced water entry and exit of the 2D bodies and the future directions on the study are outlined in chapter 6.

In Appendix A, a useful graphical user interface (GUI), which was developed in Matlab to study water entry or exit, is presented. Implementation of the GUI showing one example for entry of a symmetric wedge is presented.

Chapter 2

Mathematical Theory

In general, most of the real world problems are formulated as mathematical equations by means of physical theories. To simplify the formulated equations, appropriate assumptions are made on the real problems. Then the modelled problems are solved by suitable mathematical methods. In this chapter, we explain a complete formulation of mathematical equations to study water entry and exit problems based on T. Vinje and P. Brevig's research on numerical study of breaking waves on finite water depths. Section (2.1) gives the basic concepts of mixed Euler and Lagrangian representation of fluid particles in the two-dimensional plane. The formulation of initial boundary value problem, model assumptions, and boundary and initial conditions are described in section (2.2). The solution method for the problem based on complex potential theory is explained in section (2.3).

2.1 Fluid particle motion

We can describe the motion of the system of fluid particles and the moving body in a two-dimensional complex Cartesian coordinate system. The particles on the body surface and the free surface can be considered by a mixed Eulerian and Lagrangian description. The Euler description is given in section (2.1.2), whereas the Lagrangian description is explained in section (2.1.1).

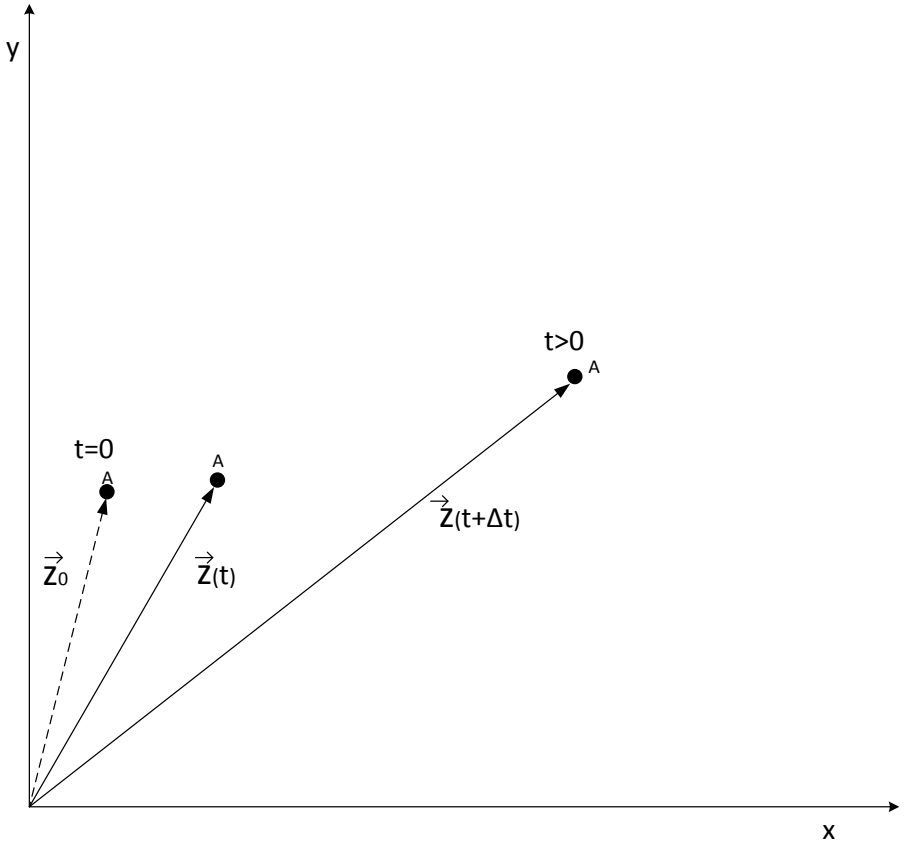

FIGURE 2.1: Definition sketch for motion of a particle A in complex plane

2.1.1 Lagrangian description

We now consider a particle with complex material position vector $\overrightarrow{z}_0$ in the complex plane at a time $t = 0$ as shown in Fig. (2.1). The material position is used to identify the particular particle A in the domain $\Omega(t)$ in which we are interested in solving the problem. The particle has moved to a spatial position vector $\overrightarrow{z}(t)$ at time t. Velocity of the particle $\overrightarrow{V}_z$ is equal to time rate of change of the spatial position vector $\overrightarrow{z}(t)$ which is a function of time t and material position z_0. It can be expressed as $\overrightarrow{z}(t) = \overrightarrow{z}(\overrightarrow{z}_0, t)$. We can now define the velocity by holding the material coordinate z_0 fixed as

$$\overrightarrow{V}_z = \left(\frac{d\overrightarrow{z}}{dt}\right)_{z_0} \equiv \frac{D\overrightarrow{z}}{Dt}, \tag{2.1}$$

where $\frac{D\overrightarrow{z}}{Dt}$ is called as material derivative of the particle A. This approach describes the particle motion as if one is moving with the fluid particle. It is called the Lagrangian description of the particle.

2.1.2 Eulerian description

In general, a fluid property (temperature, density, pressure, etc.) $Q(z_0, t)$ for the material particle can be described as discussed in the previous section. However, it can also be measured by holding by the spatial coordinate fixed as $Q(z, t)$. The rate of change at fixed z is given by $\left(\frac{dQ(\overrightarrow{z}(t),t)}{dt}\right)_z$. This representation is called the Euler description of the fluid. The relationship between two descriptions can be given by $Q = Q(\overrightarrow{z}(t), t) = Q(\overrightarrow{z}(\overrightarrow{z}_0, t), t)$ where the vector $\overrightarrow{z} = x(\overrightarrow{z}_0, t)\widehat{i} + y(\overrightarrow{z}_0, t)\widehat{j}$ and complex position $z = x(\overrightarrow{z}_0, t) + iy(\overrightarrow{z}_0, t)$. The time rate of change of the fluid property for the material can be defined as

$$\left(\frac{dQ}{dt}\right)_{z_0} = \left(\frac{\partial Q}{\partial x}\right)\left(\frac{dx}{dt}\right)_{z_0} + \left(\frac{\partial Q}{\partial y}\right)\left(\frac{dy}{dt}\right)_{z_0} + \frac{\partial Q}{\partial t}, \tag{2.2}$$

$$\left(\frac{dQ}{dt}\right)_{z_0} = \left(\frac{dQ}{dt}\right)_z + \overrightarrow{V}_z.\nabla Q, \tag{2.3}$$

which we can write in the form

$$\frac{DQ}{Dt} = \frac{\partial Q}{\partial t} + \overrightarrow{V}_z.\nabla Q. \tag{2.4}$$

The Lagrangian derivative of any property of a fluid can be related to its Eulerian derivative by the material derivative

$$\frac{D()}{Dt} = \frac{\partial()}{\partial t} + \overrightarrow{V}_z.\nabla(). \tag{2.5}$$

2.2 Initial-boundary-value problem

The initial boundary value problem (IBVP) is formulated to study the motion executed by an object moving into and out of a fluid. We can derive the mathematical governing equation for the problem based on a system of fluid and the object in a time-dependent domain $\Omega(t)$ as shown in Fig. (2.2). The kinematic and dynamic boundary conditions for the flow are specified. Moreover, the initial conditions are given to solve the IBVP.

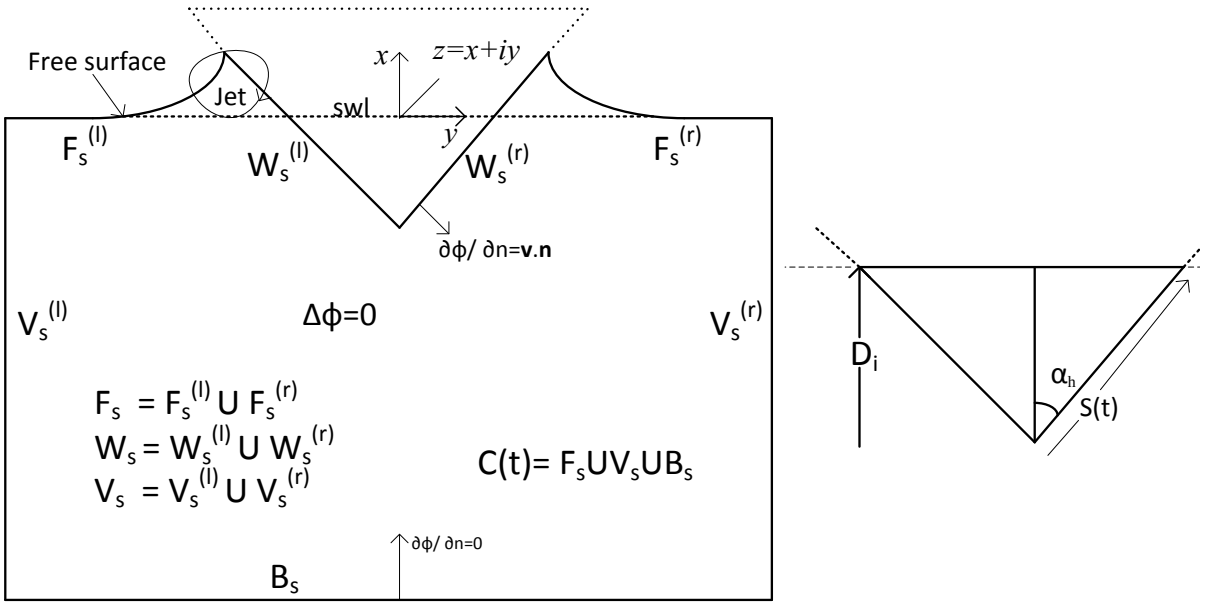

FIGURE 2.2: Definition sketch for the domain representation of the fluid and its boundary

2.2.1 Governing equation

Motion of the particles on the boundary of the domain as shown in Fig. (2.1) is described by a mixed Lagrangian and Eulerian description as discussed in the previous sections (2.1.1) and (2.1.2). The domain of the problem is varying as the body and free surface moves. It consists of fluid and interacting fluid and body boundaries. The particle position is represented with respect to its origin in the still water level (SWL). The Euler's field representation of velocity of the particles is given by the velocity field $\overrightarrow{V}_z = u(r_z, t)\widehat{i} + v(r_z, t)\widehat{j}$ where u is the velocity component in x direction and v is the velocity component in y direction and $\widehat{i}$ and $\widehat{j}$ are unit vectors along the directions x and y respectively.

The fluid is assumed to be homogeneous, incompressible and irrotational. The density ρ_w of the fluid is constant since we are considering the fluid to be incompressible. This incompressible condition states that the mass for the fluid within any volume will remain constant. This principle of conservation of mass is then expressed for incompressible fluid flow by the following equation

$$\nabla . \overrightarrow{V}_z = 0. \tag{2.6}$$

This states that the divergence of the velocity field $\overrightarrow{V}_z = 0$ for the incompressible fluid flow at every point must be zero.

We further assume that the fluid flowing around the body is irrotational. The flow is then a flow in which the vorticity is equal to zero at every point of the fluid domain. This can be written as

$$\nabla \times \overrightarrow{V}_z = 0. \tag{2.7}$$

This assumption requires that the fluid is inviscid so there are no shear forces on the body. It follows that the flow velocity field for the potential flow can be expressed in terms of a scalar velocity potential function $\phi(z,t)$. It is the gradient of the scalar potential function ϕ such that $\mathbf{V} = \nabla\phi(z,t)$. We can now obtain the relation as

$$\nabla \times \nabla\phi = 0. \tag{2.8}$$

The governing equation for the flow around the object can be described by the Laplace equation in two independent variables in the simply connected domain $\Omega(t)$ at a instant time t

$$\nabla^2\phi(z,t) = 0, \quad z = x + iy. \tag{2.9}$$

This equation is extensively applied to solve many potential flow problems. The solutions to the equation are harmonic functions. The sum of the particular solutions to the linear second-order partial differential equation is also a solution (superposition). However, as we shall see, the boundary conditions are non-linear so we can not superpose solutions for our problems. We can compute the 2D stream function ψ, from the scalar velocity potential ϕ, and vice versa using the Cauchy-Riemann equations

$$\begin{aligned} u &= \frac{\partial\phi}{\partial x} = \frac{\partial\psi}{\partial y}, \\ v &= \frac{\partial\phi}{\partial y} = -\frac{\partial\psi}{\partial x}. \end{aligned} \tag{2.10}$$

These equations show that equipotential lines represented by the velocity potential and the stream lines given by the stream function are perpendicular at each point.

2.2.2 Boundary conditions

The boundary of the domain $\Omega(t)$ is represented by a simply-connected closed contour $C(t)$ as shown in Fig. (2.3). The boundary $C(t)$ and domain $\Omega(t)$ are assumed to be dependent on time representing the deformation of the free surface and displacement of the body. The $C(t)$ consists of three kinds of boundaries. The first part represents the boundary $C_d(t)$ where the mixed boundary conditions (dynamic and kinematic boundary conditions) are specified, while the other parts $C_n(t)$ and $C_p(t)$ describe the boundaries where Neuman boundary conditions (body and seabed boundary conditions) and periodic boundary conditions (see, Chapter 3 for the mathematical formulation to the periodic boundary conditions) are given respectively.

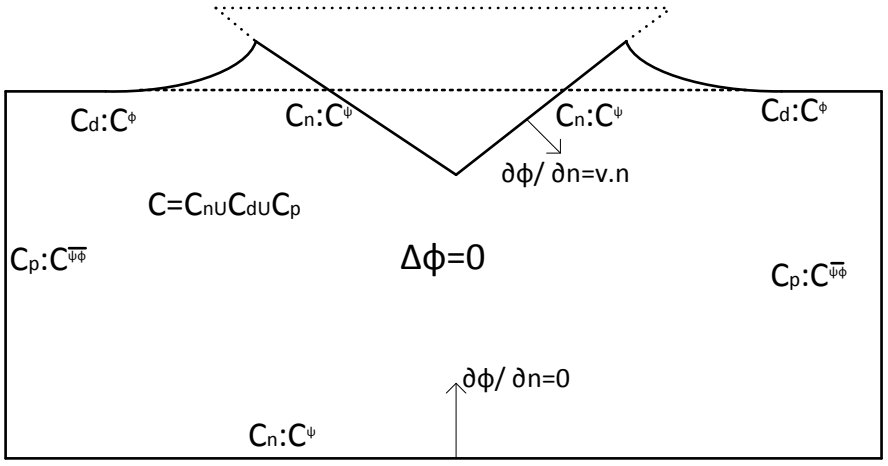

FIGURE 2.3: Geometrical representation of the contour

2.2.2.1 Free-surface boundary conditions

We can impose the kinematics and dynamic boundary conditions on the free surface $F_s(t)$ which is a part of $C_d(t)$, see Newman (1977). The kinematic free-surface boundary condition states that the fluid particles on the free surface will remain on the free surface. The free-surface elevation can be denoted by $y = \eta(x, t)$ at a instant time t. It can be written in terms of material derivative as

$$\frac{D(y - \eta(x,t))}{Dt} = 0. \tag{2.11}$$

The dynamic boundary condition on the free surface $F_s(t)$ can be now obtained from the Bernoulli's equation by assuming that the pressure varies continuously across the free surface, ie. there is no surface tension:

$$\frac{\partial\phi(z,t)}{\partial t} + \frac{1}{2}\omega\overline{\omega} + gy + \frac{P_a}{\rho_w} = 0, \quad \forall z \in F_s(t), \tag{2.12}$$

where P_a is the atmospheric pressure, ρ_w is the density of the fluid, $\omega = u - iv$ is the complex velocity and g is the gravitational acceleration. We can further assume that the pressure along the free surface is atmospheric which can be taken to be zero. We can rewrite the boundary condition for the representation in the Eulerian description as

$$\frac{\partial\phi(z,t)}{\partial t} + \frac{1}{2}\omega\overline{\omega} + gy = 0, \quad z \in F_s(t). \tag{2.13}$$

2.2.2.2 Neumann boundary conditions

We assume that the fluid particles along the wetted part $W_s(t)$ of the boundary can not cross into the body or move away from it, leaving a void. Thus the normal velocity of the flow around the submerged body is equal to the normal velocity of the body in contact with the fluid, mathematically described as

$$\frac{\partial\phi(z,t)}{\partial n} = \phi_n = V_z.n, \qquad \forall z \in W_s(t). \tag{2.14}$$

2.2.2.3 Initial conditions

The free surface $F_s(t)$ is a part of the contour $C_d(t)$, whereas the wetted surface $W_s(t)$, and the bottom surface $B_s(t)$ are a part of the $C_n(t)$. The position vector, velocity and stream function are given along $W_s(t)$, while the initial position and velocity potential of the free surface particles are assumed to be known along $F_s(t)$ at a time t=0. The vertical surface $V_s(t)$ is a part of the C_p where the stream function and the velocity potential are unknown, but these are computed using the periodic-boundary condition (see Vinje and Brevig (1981a; 1981b)).

2.3 Solution to the IBVP

The formulated initial boundary-value problem (IBVP) is a Laplace equation in two variables. The velocity potential $\phi(z,t)$ and the stream function $\psi(z,t)$ are solutions to the governing equation. The complex coordinate point z is defined as $z = x+iy$ and the region R(t) is defined as a region comprising of both points on the boundary $C(t)$ and the domain $\Omega(t)$ at an instant time t. The complex potential theory is applicable to solve the problem. The analytical complex potential $\beta(z,t)$ can be defined as

$$\beta(z,t) = \phi(z,t) + i\psi(z,t), \quad \forall z \in R(t). \tag{2.15}$$

We can compute the solutions for the problem by time-stepping forward the kinematic and dynamic boundary condition. From the kinematic free surface boundary condition, we have

$$\frac{Dz}{Dt} = u + iv \equiv \overline{\omega}. \tag{2.16}$$

From the dynamic free surface boundary condition, we have

$$\frac{D\phi}{Dt} - \frac{1}{2}\omega\overline{\omega} + gy + \frac{P_a}{\rho_w} = 0. \tag{2.17}$$

The velocity can be computed by differentiating the complex potential with respect to z. It gives,

$$\omega(z,t) = \frac{d\beta(z,t)}{dz} = u(z,t) - iv(z,t). \tag{2.18}$$

Cauchy's integral theorem is valid for the analytic function $\beta(z,t)$, so that for any z_0 outside of any closed contour C(t) lying within the fluid region R(t) we have

$$\oint_{C(t)} \frac{\beta(z,t)}{z - z_0} dz = 0. \tag{2.19}$$

Here the closed contour $C(t)$ consists of the free surface in which the velocity potential ϕ is assumed to be zero initially which is denoted as the C^{ϕ} where ϕ is known, the wetted part of the body in which the stream function ψ can be computed using Eq. (2.12) which is denoted as C^{ψ} where ψ is known and the

vertical boundaries in which velocity potential ϕ and stream function ψ are not known which is denoted as $C^{\overline{\psi\phi}}$ where both ψ and ϕ are unknown, see Fig. (2.3).

2.3.1 Solution technique

We can now explain the techniques to compute the complex potential and its time derivative by formulating Eq. (2.19) as Fredholm's integral equation of second kind which, in general, has a solution.

Fig. (2.4) shows a part of the contour C consisting of two elements between z_k and z_{k-1}, where α_k is an angle between the lines connecting the point z_k from both sides of the points z_{k+1} and z_{k-1}. Mathematically, but not numerically, this is π for a smooth part of the surface.

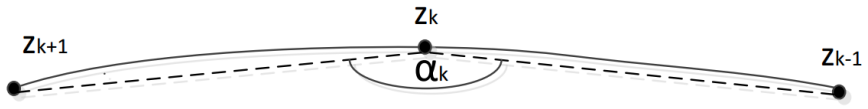

FIGURE 2.4: Geometrical representation of the angle α_k for the numerical computation

The closed contour C includes the free surface (F_s), the wetted surface of the body (W_s), the bottom surface (B_s) and the vertical surfaces (V_s) of the domain. We assume that the point z_0 is initially outside the contour approaching the point z_k on the contour.

We can now divide the contour integral of Eq. (2.19) into two parts. The first part integrates over the indented contour C_k of the contour C_ϵ with radius ϵ centered on the z_k from contour C. The second part integrates along the contour C_ϵ. By letting z_0 to approach from the outside of the contour to the point z_k, the Eq. (2.19) can be written as

$$\oint_C \frac{\beta}{z-z_0}dz = \oint_{C_k+C_\epsilon} \frac{\beta}{z-z_k}dz = \int_{C_k} \frac{\beta}{z-z_k}dz + \int_{C_\epsilon} \frac{\beta}{z-z_k}dz = 0. \tag{2.20}$$

The complex representation of points on the semicircle can be given by

$$z = z_k + \epsilon e^{i\alpha} \text{ and } dz = \epsilon i e^{i\alpha} d\alpha = (z - z_k) i d\alpha, \tag{2.21}$$

where we denote the angle α_k as α. Using Laurent expansion of the complex potential about z_k and the residue theorem, we get

$$\beta(z) = \beta(z_k) + \frac{d\beta(z_k)}{dz} e^{i\alpha}\epsilon + O(\epsilon^2) + ...$$

$$\begin{aligned}\int_{C_\epsilon} \frac{\beta}{z - z_k} dz &= \oint_0^{\alpha_k} \frac{\beta(z_k) + \frac{d\beta(z_k)}{dz} e^{i\alpha}\epsilon + O(\epsilon^2) + ...}{z - z_k} (z - z_k) i d\alpha \\ &= i\beta(z_k)\alpha_k + \frac{d\beta(z_k)}{dz} i\epsilon(e^{i\alpha_k} - 1) + O(\epsilon^2) + ...\end{aligned}$$

Finally, we take the limit of the integral as ϵ tends to zero

$$\lim_{\epsilon \to 0} \int_{C_\epsilon} \frac{\beta}{z - z_k} dz = i\alpha_k \beta(z_k). \tag{2.22}$$

Using Eq. (2.20) and (2.22), we get

$$-i \oint_C \frac{\beta(z)}{z - z_k} dz = \alpha_k \beta(z_k) - i \int_{C_k} \frac{\beta(z)}{z - z_k} e^{i\theta} ds, \tag{2.23}$$

where ds is a line element of the contour and θ is denoted as α. Using Eq. (2.19) and (2.21), we can write the line element as

$$ds = \epsilon i d\alpha. \tag{2.24}$$

We note that real or imaginary part of Eq. (2.23) can be equated to zero. However, this is chosen according to the point lying on the contour where the C^ϕ or C^ψ is known and the existence of the solution to the integral equation formed by equating the real or imaginary part of Eq. (2.23) to zero, see Vinje and Brevig (1981a; 1981b).

To compute the complex potential, we need to know ϕ and ψ which are known along C^ϕ and C^ψ respectively. By considering that z_k is on C^ψ where ϕ is unknown

and equating the real part of Eq. (2.23) to be zero, we get

$$\begin{aligned}
Re\Big\{ -i \oint_C \frac{\beta(z)}{z-z_k}dz \Big\} &= \alpha_k\phi(z_k) - Re\Big\{ i\int_{C_k} (\phi(s)+i\psi(s))\frac{e^{i\theta}}{z-z_k}ds \Big\} \\
&= \alpha_k\phi(z_k) - Re\Big\{ \int_{C_k} (\phi(s)+i\psi(s))\frac{ie^{i\theta}}{z-z_k}ds \Big\} \\
&= \alpha_k\phi(z_k) - \int_{C_k} Re\Big\{ \phi(s)\frac{ie^{i\theta}}{z-z_k} - i\psi(s)\frac{ie^{i\theta}}{z-z_k} \Big\}ds \\
&= \alpha_k\phi(z_k) + \int_{C_k} \phi(s) Im\Big\{ \frac{e^{i\theta}}{z-z_k} \Big\}ds + \int_{C_k} \psi(s) Re\Big\{ \frac{e^{i\theta}}{z-z_k} \Big\}ds \\
&= 0,
\end{aligned}$$

which we can write in the form

$$-Re\Big\{ i \oint_C \frac{\beta(z)}{z-z_k}dz \Big\} = \alpha_k\phi(z_k) + h(z_k) + \int_{C_k} \phi(s)g(z_k,s)ds = 0. \tag{2.25}$$

Similarly, by assuming that z_k is on C^{ϕ} where ψ is unknown and equating the imaginary part of Eq. (2.23) to be zero, we get

$$\begin{aligned}
Im\Big\{ -i \oint_C \frac{\beta(z)}{z-z_k}dz \Big\} &= \alpha_k\psi(z_k) + Im\Big\{ -i\int_{C_k} \frac{\beta(z_k)}{z-z_k}e^{i\theta}ds \Big\} \\
&= \alpha_k\psi(z_k) + Im\Big\{ \int_{C_k} \frac{(\phi(s)+i\psi(s))}{z-z_k} - ie^{i\theta}ds \Big\} \\
&= \alpha_k\psi(z_k) + Im\Big\{ \int_{C_k} \frac{\phi(s)}{z-z_k} - ie^{i\theta}ds + \int_{C_k} \frac{\psi(s)}{z-z_k}e^{i\theta}ds \Big\} \\
&= \alpha_k\psi(z_k) - \int_{C_k} \phi(s) Re\Big\{ \frac{e^{i\theta}}{z-z_k} \Big\}ds + \int_{C_k} \psi(s) Im\Big\{ \frac{e^{i\theta}}{z-z_k} \Big\}ds \\
&= 0,
\end{aligned}$$

which can be written as

$$Re\Big\{ \oint_C \frac{\beta(z)}{z-z_k}dz \Big\} = -\alpha_k\psi(z_k) + j(z_k) - \int_{C_k} \psi(s)l(z_k,s)ds = 0, \tag{2.26}$$

where the functions g h, j and l are known. The Eq. (2.25) and (2.26) are inhomogeneous Fredholm integral equations of the second kind, see Polyanin and Manzhirov (1998). We can also take the imaginary parts of Eq. (2.23) for the points on C^{ψ} and real part of the Eq. (2.23) for the points on C^{ϕ}, but it gives inhomogeneous Fredholm integral equations of first kind which do not have unique solutions (see Vinje and Brevig (1981; 1981)). With z_k on a smooth part of the

contour C and C_0 is the deleted contour of C avoiding the singular point z_0, we have

$$\pi\psi(z_0) + Re\left\{ \int_{C_0} \frac{\phi + i\psi}{z - z_0} dz \right\} = 0, \quad \forall\ z_k \in C^{\phi}, \tag{2.27}$$

$$\pi\phi(z_0) + Re\left\{ i\int_{C_0} \frac{\phi + i\psi}{z - z_0} dz \right\} = 0, \quad \forall\ z_k \in C^{\psi}. \tag{2.28}$$

Eq. (2.27) and (2.28) are simply Eq. (2.25) and Eq. (2.26), which are used to compute the complex potential. Similarly, we can state, as we did for the computation of the complex potential, that the time derivative of the complex potential is also an analytical function of z in the domain. We can derive the following equations

$$\oint_C \frac{\frac{\partial\phi}{\partial t} + i\frac{\partial\psi}{\partial t}}{z - z_0} dz = 0, \quad \forall\ z \in \Omega, \tag{2.29}$$

$$\pi\frac{\partial\psi(z_0)}{\partial t} + Re\left\{ \int_{C_0} \frac{\frac{\partial\phi}{\partial t} + i\frac{\partial\psi}{\partial t}}{z - z_0} dz \right\} = 0, \quad \forall\ z_k \in C^{\phi}, \tag{2.30}$$

$$\pi\frac{\partial\phi(z_0)}{\partial t} + Re\left\{ i\int_{C_0} \frac{\frac{\partial\phi}{\partial t} + i\frac{\partial\psi}{\partial t}}{z - z_0} dz \right\} = 0, \quad \forall\ z_k \in C^{\psi}. \tag{2.31}$$

These equations are of the same form as Eq. (2.27) and (2.28) and hence lead to identical equations to Eq. (2.27) and (2.28) in the time derivative.

We now know the complex potential and its time derivative on the closed contour C. However, it can also be noted that we can compute the values for $\beta(z)$ and $\frac{\partial\beta(z)}{\partial t}$ inside the domain using the Cauchy's integral formula. The derivation can be given by

$$\beta(z_0, t) = \frac{1}{2\pi i}\oint_C \frac{\beta(z,t)}{z - z_0} dz, \tag{2.32}$$

and differentiating with respect to t, we get

$$\frac{\partial\beta(z_0,t)}{\partial t} = \frac{1}{2\pi i}\oint_C \frac{\frac{\partial\beta(z,t)}{\partial t}}{z - z_0} dz. \tag{2.33}$$

Higher-order derivatives can also be computed by extending the Cauchy's integral formula as

$$f^{(n)}(z_0) = \frac{n!}{2\pi i} \oint_C \frac{f(z)}{(z - z_0)^{(n+1)}}. \tag{2.34}$$

This approach was taken by Cooker (1990) and allows larger time steps to be taken. However, this would be very complicated to implement in the present case when the number of body, and sometimes free-surface, points changes throughout time.

The complex velocity ω can be computed by differentiating the complex potential with respect to z as

$$\omega(z_0, t) = \frac{1}{2\pi i} \oint_C \frac{\beta(z, t)}{(z - z_0)^2} dz, \tag{2.35}$$

$$\frac{\partial \omega(z_0, t)}{\partial t} = \frac{1}{2\pi i} \oint_C \frac{\frac{\partial \beta(z,t)}{\partial t}}{(z - z_0)^2} dz, \tag{2.36}$$

$$\frac{d\omega(z_0, t)}{dz} = \frac{1}{\pi i} \oint_C \frac{\beta(z, t)}{(z - z_0)^3} dz. \tag{2.37}$$

The pressure at the free surface is assumed to be zero and the pressure inside the contour can be found by a rearrangement of Bernoulli's equation as

$$\frac{-P(x, y, t)}{\rho} = \frac{\partial \phi}{\partial t} + \frac{1}{2}\omega\overline{\omega} + gy.$$

We can define the acceleration from the kinematic boundary condition as

$$\frac{D\omega(z, t)}{Dt} = a_x(r_z, t) + ia_x(z, t), \ \forall z \in C(t). \tag{2.38}$$

The acceleration inside the contour can be calculated using

$$a_x(x, y, t) + ia_y(x, y, t) = \frac{\partial \omega}{\partial t} + \omega . \frac{d\overline{\omega}}{dt}. \tag{2.39}$$

Chapter 3

Numerical Formulation

In the previous chapter, we defined the equations to compute values of the complex potential, velocity, pressure and acceleration mathematically. In this chapter, we explain a numerical formulation to compute the values based on the derivations given by Vinje and Brevig (1981a; 1982b), and Barringer (1996). Section (3.1) describes the collocation method using points on the boundary of the domain. The numerical formulation to the compute complex potential, stream function, pressure, force and complex velocity are given in sections (3.2), (3.3), (3.4), (3.5) and (3.6), respectively. Finally, a mathematical formulation of the periodic boundary condition, numerical algorithms for time-stepping and implementation of the equations are explained in sections (3.7), (3.8) and (3.9) respectively.

3.1 Collocation method

The collocation method is used to solve Eq. (2.27), (2.28), (2.29) and (2.30). The nodal points are generated by dividing the contour C into finite number of elements as shown in Fig. (3.1). To generate points on the free surface and the body surface, we choose appropriate point-spacing ratios by considering the fact that the points close to the body in motion are affected much more than points far from the body. We can also note that the point-spacing ratios and the time-step size play a very important role in the computation of the solution and need to be chosen carefully to compute the numerical results without breaking the computation and to achieve long runs of the codes.

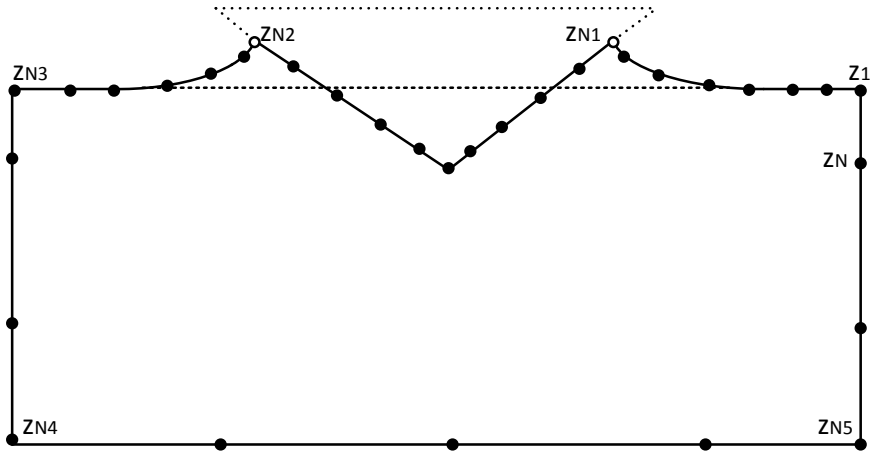

FIGURE 3.1: Geometrical representation of the collocation points along the contour C

3.2 Computation of complex potential

We know either the real or imaginary part of the complex potential $\beta(z)$ and its time derivative $\frac{\partial \beta}{\partial t}$ on every nodal point of the contour C. By assuming that the complex potential and its time derivative vary linearly in the complex variable z, we can write the complex potential for all z on the contour C as follows

$$\beta(z) = \begin{cases} \dfrac{z - z_j}{z_{j-1} - z_j}\beta_{j-1} + \dfrac{z - z_{j-1}}{z_j - z_{j-1}}\beta_j & \forall z \in [z_{j-1}, z_j], \\ \dfrac{z - z_j}{z_{j+1} - z_j}\beta_{j+1} + \dfrac{z - z_{j+1}}{z_j - z_{j+1}}\beta_j & \forall z \in [z_j, z_{j+1}], \end{cases} \tag{3.1}$$

where z_{j-1}, z_j and z_{j+1} are three consecutive nodes on the contour, and the complex potential β_{j-1}, β_j and β_{j+1} are known values on the points z_{j-1}, z_j and z_{j+1} respectively. Hence, the complex potential and its time derivative can be expressed as a linear combination of the complex potential at all nodes along the contour as follows

$$\beta(z) = \sum_j \wedge_j \beta_j, \tag{3.2}$$

$$\frac{\partial \beta(z)}{\partial t} = \sum_j \wedge_j \frac{\partial \beta_j}{\partial t}, \tag{3.3}$$

where $\wedge_j(z)$ is the influence function at node z_j which can be computed by using

$$\wedge_j(z) = \begin{cases} \dfrac{z - z_{j+1}}{z_j - z_{j+1}} & \forall z \in [z_j, z_{j+1}], \\ \dfrac{z - z_{j-1}}{z_j - z_{j-1}} & \forall z \in [z_{j-1}, z_j], \\ 0 & \text{otherwise.} \end{cases} \tag{3.4}$$

Now, the contour integral can be numerically approximated by

$$\oint_C \frac{\beta(z)}{z - z_k} dz = \oint_C \frac{\sum_j \wedge_j \beta_j}{z - z_k} dz = \sum_j (I^1_{k,j} + I^2_{k,j})\beta_j, \tag{3.5}$$

where

$$\begin{aligned} I^1_{k,j} = \int_{z_{j-1}}^{z_j} \frac{z - z_{j-1}}{z_j - z_{j-1}} . \frac{1}{z - z_k} dz &= \frac{1}{z_j - z_{j-1}} \Big[z + z_k \ln(z - z_k) - z_{j-1} \ln(z - z_k) \Big]_{z_{j-1}}^{z_j} \\ &= \frac{z_k - z_{j-1}}{z_j - z_{j-1}} \ln \left[\frac{z_{j-1} - z_k}{z_{j-1} - z_k} \right] + 1, \end{aligned} \tag{3.6}$$

$$\begin{aligned} I^2_{k,j} = \int_{z_j}^{z_{j+1}} \frac{z - z_{j+1}}{z_j - z_{j+1}} . \frac{1}{z - z_k} dz &= \frac{1}{z_j - z_{j+1}} \Big[z + z_k \ln(z - z_k) - z_{j+1} \ln(z - z_k) \Big]_{z_j}^{z_{j+1}} \\ &= \frac{z_k - z_{j+1}}{z_j - z_{j+1}} \ln \left[\frac{z_{j+1} - z_k}{z_j - z_k} \right] - 1. \end{aligned} \tag{3.7}$$

The function $\Gamma_{k,j}$ denotes the sum of the terms $I^1_{k,j}$ and $I^2_{k,j}$ as

$$\Gamma_{k,j} = I^1_{k,j} + I^2_{k,j} = \frac{z_k - z_{j-1}}{z_j - z_{j-1}} \ln \left[\frac{z_j - z_k}{z_{j-1} - z_k} \right] + \frac{z_k - z_{j+1}}{z_j - z_{j+1}} \ln \left[\frac{z_{j+1} - z_k}{z_j - z_k} \right]. \tag{3.8}$$

However, we note that the $\lim_{z\to 0}\left(z \ln \frac{1}{z}\right)$ goes to zero. To avoid the singularity, the function can be explicitly expressed as

$$\Gamma_{k,j} = \begin{cases} \dfrac{z_{j-1} - z_{j+1}}{z_j - z_{j+1}} \ln \dfrac{z_{j+1} - z_{j-1}}{z_j - z_{j-1}} & \text{for } \; k = j-1, \\ \dfrac{z_{j+1} - z_{j-1}}{z_j - z_{j-1}} \ln \dfrac{z_j - z_{j+1}}{z_{j-1} - z_{j+1}} & \text{for } \; k = j+1, \\ \ln \dfrac{z_{j+1} - z_j}{z_{j-1} - z_j} & \text{for } \; k = j. \end{cases} \tag{3.9}$$

Finally, we note that the closed contour begins with the node z_1 and ends with the node z_N. We need to choose the values of $z_{j-1} = z_0$ at j=1 and $z_{j+1} = z_{N+1}$ at j=N+1 when we evaluate the function $\Gamma_{k,j}$ which depends on the values of z_{j-1}, z_j and z_{j+1}. The values are given by assuming a periodic domain and setting the index j when $j = 1 \Rightarrow j-1 = N$ and when $j = N \Rightarrow j+1 = 1$. N is the maximum number of collocation points on the contour.
Therefore, we can numerically compute the contour integral by expressing the Eq. (2.19) as

$$\oint_C \frac{\beta(z)}{z - z_k} dz \approx \sum_j \Gamma_j(z_{j-1}, z_j, z_{j+1}, z_k)\beta_j, \tag{3.10}$$

and similarly, the derivative of the contour integral can be written as

$$\oint_C \frac{\frac{\partial \beta(z)}{\partial t}}{z - z_k} dz \approx \sum_j \Gamma_j(z_{j-1}, z_j, z_{j+1}, z_k)\frac{\partial \beta_j}{\partial t}. \tag{3.11}$$

We know ϕ on the free surface which is the part of C^ϕ and take the real and imaginary parts according to the existence of solution using the Eq. (2.27), (2.28), (2.29) and (2.30) while solving Eq. (3.10) and Eq. (3.11).

3.3 Computation of stream function

In this section, we explain the numerical computation of the stream function, the derivative of the stream function and computation of the material derivative. Fig. (3.2) shows the definition sketch of the wetted surface of the body which is a part of the C^ψ where ϕ is unknown. By applying the kinematic boundary

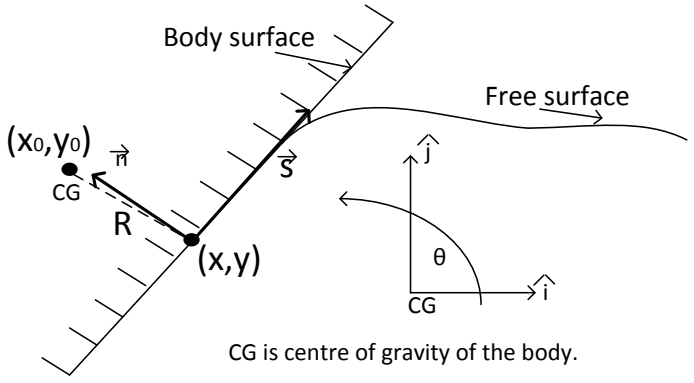

FIGURE 3.2: Definition sketch of the wetted part of the body and the vectors acting along the body surface

condition along the surface, we can get

$$\frac{\partial \psi}{\partial s} = \vec{V_b}.\vec{n}, \tag{3.12}$$

where $\vec{V_b}$ is the body velocity at the point in question which can be expressed in terms of the velocity V_c of the center of gravity (CG) and the rotational velocity of the body $\dot{\theta}$ as

$$\vec{V_b} = \vec{V_c} + \dot{\theta}\hat{k} \times \vec{p}, \tag{3.13}$$

where $\vec{p} = (x - x_0)\hat{i} + (y - y_0)\hat{j}$ is the radius from the center of gravity CG (ie., $z_c = x_0 + iy_0$) to the point $z = x + iy$ and $\hat{k}$ is a vector perpendicular to the unit vectors $\hat{i}$ and $\hat{j}$.

By defining the normal vector $\vec{n} = \hat{k} \times \vec{s}$, we can obtain

$$d\psi = (\vec{V_b} \cdot \vec{n})d\vec{s} = \vec{V_b} \cdot (\hat{k} \times d\vec{s}) = -(\vec{V_b} \times \hat{k}) \cdot d\vec{s} = -(\vec{V_b} \times \hat{k} + \dot{\theta}\vec{\rho}) \cdot d\vec{s}. \tag{3.14}$$

By transforming the line segment coordinate s to Cartesian co-ordinates system, we get

$$d\psi = -\dot{y_0}dx + \dot{x_0}dy - \dot{\theta}[(x - x_0)dx + (y - y_0)dy], \tag{3.15}$$

where the velocity of CG is $\vec{V_c} = \dot{x_0}\hat{i} + \dot{y_0}\hat{j}$.

By integrating Eq. (3.15), the stream function can be computed by

$$\psi = \dot{x_0}(y - y_0) - \dot{y_0}(x - x_0) - \frac{1}{2}\dot{\theta}d^2 + \psi_0(t), \tag{3.16}$$

where d is the distance between the points z_c and z (ie., $d^2 = |z - z_c|^2 = (x - x_0)^2 - (y - y_0)^2$) and $\psi_0(t)$ is an arbitrary time dependent constant which may be set equal to zero.

The derivative of the stream function can be computed by differentiating the Eq. (3.16) with respect to t as

$$\begin{aligned}\frac{\partial\psi}{\partial t} &= -\frac{\partial\dot{y_0}}{\partial t}(x - x_0) - \dot{y_0}\frac{\partial(x - x_0)}{\partial t} + \frac{\partial\dot{x_0}}{\partial t}(y - y_0) + \dot{x_0}\frac{\partial(y - y_0)}{\partial t} - \frac{1}{2}d^2\frac{\partial\dot{\theta}}{\partial t} - \frac{1}{2}\dot{\theta}\frac{\partial d^2}{\partial t} \\ &= -\ddot{y_0}(x - x_0) - \dot{y_0}(\dot{x} - \dot{x_0}) + \ddot{x_0}(y - y_0) + \dot{x_0}(\dot{y} - \dot{y_0}) - \frac{1}{2}d^2\ddot{\theta} - \dot{\theta}[(x - x_0)(\dot{x} - \dot{x_0}) \\ &+ (y - y_0)(\dot{y} - \dot{y_0})]\end{aligned}$$

$$\begin{aligned}\frac{\partial\psi}{\partial t} &= -\ddot{y_0}(x - x_0) - \dot{y_0}\dot{x} + \ddot{x}(y - y_0) + \dot{x_0}\dot{y} - \frac{1}{2}d^2\ddot{\theta} - \dot{\theta}[(x - x_0)(\dot{x} - \dot{x_0}) \\ &+ (y - y_0)(\dot{y} - \dot{y_0})],\end{aligned} \tag{3.17}$$

and the gradient of the stream function is

$$\begin{aligned}\nabla\psi &= \frac{\partial\psi}{\partial x}\hat{i} + \frac{\partial\psi}{\partial y}\hat{j} \\ &= (-\dot{y_0} - \dot{\theta}(x - x_0))\hat{i} + (\dot{x_0} - \dot{\theta}(y - y_0))\hat{j}.\end{aligned} \tag{3.18}$$

The velocity of the point along the body is

$$\begin{aligned}\vec{V_b} &= \dot{x}\hat{i} + \dot{y}\hat{j} \\ &= (\dot{x_0} - \dot{\theta}(y - y_0))\hat{i} + (\dot{y_0} + \dot{\theta}(x - x_0))\hat{j}.\end{aligned} \tag{3.19}$$

We can obtain the following equations

$$\nabla\psi = -y\hat{i} + x\hat{j}, \tag{3.20}$$

$$\vec{V_b}\cdot\nabla\psi = -\dot{x_0}\dot{y} + \dot{y_0}\dot{x} + ((x-x_0)\dot{x} + (y-y_0)\dot{y})\dot{\theta}. \tag{3.21}$$

Finally, the material derivative can be obtained explicitly from the definition as

$$\frac{D\psi}{Dt} = \frac{\partial\psi}{\partial t} + \vec{V_b}\cdot\nabla\psi, \tag{3.22}$$

$$\frac{D\psi(x,y,t)}{Dt} = \ddot{x_0}(y-y_0) - \ddot{y_0}(x-x_0) - \frac{1}{2}d^2\ddot{\theta} + \dot{\theta}[(x-x_0)\dot{x_0} + (y-y_0)\dot{y_0}]. \tag{3.23}$$

Along the bottom surface B_s, we assume that the particles in motion form a streamline where ψ and $\frac{\partial\psi}{\partial t}$ are constant. The B_s can be denoted as the part of C^{ψ} where ϕ is unknown.

The vertical surface V_s is the part of $C^{\overline{\phi\psi}}$ where ϕ and ψ are unknown. However, by assuming that the problem is periodic in space, i.e. the vertical boundaries are chosen far from the body without affecting the calculations, we can compute ϕ and $\frac{\partial\phi}{\partial t}$ or ψ and $\frac{\partial\psi}{\partial t}$ by adding and subtracting pairs of equations, see Vinje and Brevig (1981a; 1981b).

For every node along the contour, we can rearrange the equations Eq. (2.27), (2.28), (2.29) and (2.30) to compute the unknown parts of the contour integral and solve the system of linear equations to obtain β and $\dfrac{\partial\beta}{\partial t}$ at all nodes on the contour C.

3.4 Computation of pressure

The pressure at each point along the wetted surface is computed using Bernoulli's equation as

$$\frac{P_j}{\rho_w} = -\frac{\omega_j\overline{\omega}_j}{2} - gy_j - \frac{\partial\phi_j}{\partial t}. \tag{3.24}$$

Along the wetted surface, we know the complex velocity ω, complex conjugate $\overline{\omega}$, the ψ and $\frac{\partial\psi}{\partial t}$, but the $\frac{\partial\phi}{\partial t}$ is unknown. It can be computed using the contour

integral of the derivative of the complex potential as

$$\oint_C \frac{\frac{\partial\phi}{\partial t} + i\frac{\partial\psi}{\partial t}}{z - _k} dz \cong \sum_{j=1}^{N} \Gamma_{k,j}(z_{j-1}, z_j, z_{j+1}, z_k)\frac{\partial\beta_j}{\partial t} = 0. \tag{3.25}$$

We note that we know ϕ along the free surface and $\omega = \dfrac{d\phi}{dz}$. To compute $\frac{\partial\phi}{\partial t}$ along the free surface, we can use

$$\frac{\partial\phi_j}{\partial t} = -\frac{w_j\overline{w}_j}{2} - gy_j - \frac{P_a}{\rho_w}. \tag{3.26}$$

The vertical ends of the contour we again assume periodicity: in practice for the transient motion considered here, no fluid motion occurs at these distant boundaries anyway.

We assume that along the bottom ψ is unknown but it is constant. The derivative of the ψ (ie., $\dfrac{\partial\psi}{\partial t} = 0.$) can be set to be zero.

By splitting Eq. (3.17), we can compute the unknown acceleration terms ($\ddot{x}$,$\ddot{y}$ and $\ddot{\theta}$) as follows

$$\frac{\partial\psi_j}{\partial t} = \frac{\partial\psi_{j1}}{\partial t} + \ddot{x}\frac{\partial\psi_{j2}}{\partial t} + \ddot{y}\frac{\partial\psi_{j3}}{\partial t} + \ddot{\theta}\frac{\partial\psi_{j4}}{\partial t}, \tag{3.27}$$

where

$$\frac{\partial\psi_{j1}}{\partial t} = -\dot{y}_0\dot{x}_j + \dot{x}_0\dot{y}_j - \dot{\theta}[(x_j - x_0)(\dot{x}_j - \dot{x}_0) + (y_j - y_0)(\dot{y}_j - \dot{y}_0)], \tag{3.28}$$

$$\frac{\partial\psi_{j2}}{\partial t} = (y_j - y_0), \tag{3.29}$$

$$\frac{\partial\psi_{j3}}{\partial t} = -(x_j - x_0), \tag{3.30}$$

$$\frac{\partial\psi_{j4}}{\partial t} = -\frac{1}{2}d_j^2. \tag{3.31}$$

The linear system of four equations can be formulated as

$$\sum_{j=1}^{N} \Gamma_{k,j}\left(\frac{\partial\phi_{jn}}{\partial t} + i\frac{\partial\psi_{jn}}{\partial t}\right) = 0 \quad \text{for } n = 1, ..., 4; \tag{3.32}$$

i.e. $Ax_n = b_n$ for $n = 1, ..., 4$. We can note that the coefficient matrix A is same as the matrix used in Eq. (3.11). Therefore, the pressure can be computed using the following equations by assuming that we only consider the vertical motion of

the body (the rotational velocity $\dot{\theta} = 0$) while solving the sub-equations:

$$P_{j1} = -x_{j1} - \frac{1}{2} w_j \overline{w}_j - g y_j \quad \text{for } j = N_1, ..., N_2; \tag{3.33}$$

$$P_{jn} = -x_{jn} \qquad \text{for } n = 2, ..., 4. \tag{3.34}$$

3.5 Computation of force

The total numerical force experienced by the body is computed by integrating the pressures along the wetted surface of the body. The hydrodynamic forces and moments related to the pressures (F_{xn}, F_{yn}, M_n) can be defined by

$$m\ddot{x}_0 = F_{x1} + F_{x2}\ddot{x}_0 + F_{x3}\ddot{y}_0 + F_{x4}\ddot{\theta}, \tag{3.35}$$

$$m\ddot{y}_0 = F_{y1} + F_{y2}\ddot{x}_0 + F_{y3}\ddot{y}_0 + F_{y4}\ddot{\theta} - mg, \tag{3.36}$$

$$I\ddot{\theta} = M_1 + M_2\ddot{x}_0 + M_3\ddot{y}_0 + M_4\ddot{\theta}. \tag{3.37}$$

Using the system of equation for the force and moment, we can compute the translational and rotational accelerations of the body. Finally, the total solution x_j (i.e., the complex potential β_j at each point) to Eq. (3.32) can be given by

$$x_j = x_{j1} + \ddot{x}_0 x_{j2} + \ddot{y}_0 x_{j3} + \ddot{\theta} x_{j4} \text{ for } j = 1, ..., N. \tag{3.38}$$

The pressure can be computed by

$$P_j = P_{j1} + \ddot{x}_0 P_{j2} + \ddot{y}_0 P_{j3} + \ddot{\theta} P_{j4} \text{ for } j = N_1, ..., N_2. \tag{3.39}$$

3.6 Computation of complex velocity

We assume that the complex potential (and its derivative) vary linearly in complex variable z between the nodal points. It can be computed using $\dfrac{d\omega}{dz}$. However, the solution using Eq. (2.18) is singular at the nodes. To avoid the difficulty, we use a central differentiation method to compute the derivative of the complex potential along the contour. At a point z_j, we can define the derivative of the complex

potential as

$$\left(\frac{\partial\beta}{\partial z}\right)_j = a_{j-1}\beta_{j-1} + a_j\beta_j + a_{j+1}\beta_{j+1} - E. \tag{3.40}$$

where E is an error term. Using Taylor's theorem to expand the complex potential about z_j, we get

$$\beta_{j-1} = \sum_{n=0}^{\infty} \frac{\beta_j^{(n)}}{n!}(z_{j-1} - z_j)^n, \tag{3.41}$$

$$\beta_{j+1} = \sum_{n=0}^{\infty} \frac{\beta_j^{(n)}}{n!}(z_{j+1} - z_j)^n. \tag{3.42}$$

Using Eq. (3.40), (3.41) and (3.42), we get

$$\begin{aligned}\left(\frac{\partial\beta}{\partial z}\right)_j =& (a_{j-1} + a_j + a_{j+1})\beta_j + \{a_{j-1}(z_{j-1} - z_j) + a_{j+1}(z_{j+1} - z_j)\}\left(\frac{\partial\beta}{\partial z}\right)_j \\ &+ \frac{1}{2}\{a_{j-1}(z_{j-1} - z_j)^2 + a_{j+1}(z_{j+1} - z_j)^2\}\left(\frac{\partial^2\beta}{\partial z^2}\right)_j \\ &+ \sum_{n=3}^{\infty} \frac{\beta_j^{(n)}}{n!}\{a_{j-1}(z_{j-1} - z_j)^n + a_{j+1}(z_{j+1} - z_j)^n\}.\end{aligned} \tag{3.43}$$

We can formulate the following system of equations

$$a_{j-1} + a_j + a_{j+1} = 0, \tag{3.44}$$

$$a_{j-1}(z_{j-1} - z_j) + a_{j+1}(z_{j+1} - z_j) = 1, \tag{3.45}$$

$$a_{j-1}(z_{j-1} - z_j)^2 + a_{j+1}(z_{j+1} - z_j)^2 = 0, \tag{3.46}$$

$$-\sum_{n=3}^{\infty} \frac{\beta_j^{(n)}}{n!}\{a_{j-1}(z_{j-1} - z_j)^n + a_{j+1}(z_{j+1} - z_j)^n\} = E. \tag{3.47}$$

By solving the equations, we can calculate the coefficients as follows

$$a_{j-1} = \frac{z_{j+1} - z_j}{(z_{j+1} - z_j)(z_{j+1} - z_j) - (z_{j-1} - z_j)^2}, \tag{3.48}$$

$$a_{j+1} = \frac{z_{j-1} - z_j}{(z_{j-1} - z_j)(z_{j+1} - z_j) - (z_{j+1} - z_j)^2}, \tag{3.49}$$

$$a_j = -a_{j-1} - a_{j+1}. \tag{3.50}$$

By assuming the periodicity of the system, we can also use the central differentiation scheme at the endpoints of the free surface. We allow the points to join up

such that the last free surface point in one domain is the first free surface point in the next by setting the points z_p and z_m as

$$z_p = z_1 + (z_{N3-1} - z_{N3}), \tag{3.51}$$

$$z_m = z_{N3} + (z_1 - z_2). \tag{3.52}$$

We can conclude that the coefficients can be computed as

$$a_{1-1} = \frac{z_2 - z_1}{(z_2 - z_1)(z_p - z_1) - (z_p - z_1)^2}, \tag{3.53}$$

$$a_{1+1} = \frac{z_p - z_1}{(z_p - z_1)(z_2 - z_1) - (z_2 - z_1)^2}, \tag{3.54}$$

$$a_{N3-1} = \frac{z_m - z_{N3}}{(z_m - z_{N3})(z_{N3-1} - z_{N3}) - (z_{N3-1} - z_{N3})^2}, \tag{3.55}$$

$$a_{N3+1} = \frac{z_{N3-1} - z_{N3}}{(z_{N3-1} - z_{N3})(z_m - z_{N3}) - (z_m - z_{N3})^2}. \tag{3.56}$$

where N_3 is the point on the left-vertical side of the contour (see Fig. (3.1)).

3.7 Matrix formulation and the periodic boundary condition

To compute the complex potential along the contour, we need to calculate the following integral

$$\oint_C \frac{\beta(z,t)}{z - z_k} dz = 0, \quad 1 \leq k \leq N. \tag{3.57}$$

The numerical solution to the problem is computed using the solution technique (see section (2.3.1) for more details) as

$$Re\left\{ \oint_C \frac{\beta(z,t)}{z - z_k} dz \right\} \cong Re\left\{ \sum_{j=1}^{N} \Gamma_{k,j} \beta_j \right\} = 0, \tag{3.58}$$

when z_k is on along the boundary C^ϕ where the velocity potential ϕ is known from the free surface boundary condition at a time t=0 and

$$Re\left\{ i \oint_C \frac{\beta(z,t)}{z - z_k} dz \right\} \cong Re\left\{ i \sum_{j=1}^{N} \Gamma_{k,j} \beta_j \right\} = 0, \tag{3.59}$$

when z_k is on along the boundary C^ψ where the stream function ψ is known from the matching boundary condition of body and fluid. Along the vertical boundaries, we do not know the ϕ and ψ. However, we compute the unknown parts of the complex potential along the vertical boundaries using the periodic boundary condition by assuming ϕ is the unknown variable at the left-side vertical control surface while evaluating the sums of Eq. (3.60) for the index j running from N_3 to N_4 and N_5 to N, see Fig. (3.1).

For z_k on C^ϕ, we then get the sums as

$$\begin{aligned} Re\Bigg\{ & \sum_{j=1}^{N_1-1} \Gamma_{k,j}(\phi_j + iX_j) + \sum_{j=N_1}^{N_2} \Gamma_{k,j}(X_j + i\psi_j) + \sum_{j=N_2+1}^{N_3} \Gamma_{k,j}(\phi_j + iX_j) \\ & + \sum_{\substack{j_1=N_3+1 \\ j_2=N}}^{\substack{j_2=N_5 \\ j_1=N_4}} \Gamma_{k,j_1}(X_{j_1} + iX_{j_2}) + \sum_{j=N_4+1}^{N_5-1} \Gamma_{k,j}(X_j + iX_{N_5}) + \sum_{\substack{j_2=N_5 \\ j_1=N_4}}^{\substack{j_1=N_3+1 \\ j_2=N}} \Gamma_{k,j_2}(X_{j_1} + iX_{j_2}) \Bigg\} = 0, \end{aligned} \tag{3.60}$$

where X_1, X_2, X_{j_1} and X_{j_2} are the unknown parts of the complex potential $\beta_z = \phi + i\psi$ along the contour changing with the boundary conditions.

Consider the following terms in Eq. (3.60):

$$\sum_{\substack{j_1=N_3+1 \\ j_2=N}}^{\substack{j_2=N_5 \\ j_1=N_4}} \Gamma_{k,j_1}(X_{j_1} + iX_{j_2}), \tag{3.61}$$

and

$$\sum_{\substack{j_2=N_5 \\ j_1=N_4}}^{\substack{j_1=N_3+1 \\ j_2=N}} \Gamma_{k,j_2}(X_{j_1} + iX_{j_2}), \tag{3.62}$$

where X_{j1} is the unknown velocity potential along the left-vertical boundary and X_{j2} is the unknown stream function along the right-vertical boundary. To evaluate the sums along the vertical boundaries, we use the periodic condition (for the case of the ϕ is unknown) as given in Eq. (3.61) and Eq. (3.62) by taking the X_{j1} along the left side and corresponding X_{j2} along the right side while computing the sums.

By collecting the known to the left side of Eq. (3.60) and unknown to the right side of Eq. (3.60), we get

$$\begin{aligned}
&- \sum_{j=1}^{N_1-1} Im\Gamma_{k,j}X_j + \sum_{j=N_1}^{N_2} Re\Gamma_{k,j}X_j - \sum_{j=N_2+1}^{N_3} Im\Gamma_{k,j}X_j \\
&+ \sum_{\substack{j_1=N_3+1 \\ j_2=N}}^{\substack{j_2=N_5 \\ j_1=N_4}} Re\Big\{\Gamma_{k,j_1} + \Gamma_{k,j_2}\Big\}X_{j_1} + \sum_{j=N_4+1}^{N_5-1} Re\Gamma_{k,j}X_j - \sum_{j=N_4+1}^{N_5-1} Im\Gamma_{k,j}X_{N_5} \\
&- \sum_{\substack{j_2=N_5 \\ j_1=N_4}}^{\substack{j_1=N_3+1 \\ j_2=N}} Im\Big\{\Gamma_{k,j_1} + \Gamma_{k,j_2}\Big\}X_{j_2} = - \sum_{j=1}^{N_1-1} Re\Gamma_{k,j}\phi_j + \sum_{j=N_1}^{N_2} Im\Gamma_{k,j}\psi_j - \sum_{j=N_2+1}^{N_3} Re\Gamma_{k,j}\phi_j.
\end{aligned} \tag{3.63}$$

For z_k on C^{ψ}, we get

$$\begin{aligned}
&-Im\Bigg\{ \sum_{j=1}^{N_1-1} \Gamma_{k,j}(\phi_j + iX_j) + \sum_{j=N_1}^{N_2} \Gamma_{k,j}(X_j + i\psi_j) + \sum_{j=N_2+1}^{N_3} \Gamma_{k,j}(\phi_j + iX_j) \\
&+ \sum_{\substack{j_1=N_3+1 \\ j_2=N}}^{\substack{j_2=N_5 \\ j_1=N_4}} \Gamma_{k,j_1}(X_{j_1} + iX_{j_2}) + \sum_{j=N_4+1}^{N_5-1} \Gamma_{k,j}(X_j + iX_{N_5}) + \sum_{\substack{j_2=N_5 \\ j_1=N_4}}^{\substack{j_1=N_3+1 \\ j_2=N}} \Gamma_{k,j_2}(X_{j_1} + iX_{j_2}) \Bigg\} = 0.
\end{aligned} \tag{3.64}$$

By collecting the known to the left side of Eq. (3.64) and unknown to the right side of Eq. (3.64), we get

$$
\begin{aligned}
&- \sum_{j=1}^{N_1-1} Re\Gamma_{k,j}X_j - \sum_{j=N_1}^{N_2} Im\Gamma_{k,j}X_j - \sum_{j=N_2+1}^{N_3} Re\Gamma_{k,j}X_j \\
&- \sum_{\substack{j_1=N_3+1 \\ j_2=N}}^{\substack{j_2=N_5 \\ j_1=N_4}} Im\Big\{\Gamma_{k,j_1}+\Gamma_{k,j_2}\Big\}X_{j_1} - \sum_{j=N_4+1}^{N_5-1} Im\Gamma_{k,j}X_j - \sum_{j=N_4+1}^{N_5-1} Re\Gamma_{k,j}X_{N_5} \\
&- \sum_{\substack{j_2=N_5 \\ j_1=N_4}}^{\substack{j_1=N_3+1 \\ j_2=N}} Im\Big\{\Gamma_{k,j_1}+\Gamma_{k,j_2}\Big\}X_{j_2} = \sum_{j=1}^{N_1-1} Im\Gamma_{k,j}\phi_j + \sum_{j=N_1}^{N_2} Re\Gamma_{k,j}\psi_j + \sum_{j=N_2+1}^{N_3} Im\Gamma_{k,j}\phi_j.
\end{aligned}
\tag{3.65}
$$

Alternatively, we could assume ψ is the unknown variable at the left side vertical control surface. This gives a set of equations similar to Eq. (3.63) and (3.65). The numerical solution has shown to be improved when take the sum of these equations and Eq. (3.63) and (3.65) when z_k is on the vertical surfaces, see Vinje and Brevig (1981b).

3.8 Time-stepping schemes

Second-order Runge-Kutta and fourth-order Hamming predictor-corrector methods are used to solve the differential Eq. (3.66) and (3.67) by time-stepping forward with respect to time, see Ralston and Rabinowitz (2001). The initial conditions to the fourth-order Hamming predictor-corrector method are given by computing the four starting values for y and f(y) using the Runge-Kutta method where f(y)=$\frac{\mathrm{dy}}{\mathrm{dt}}$. The following equations are used to step forward in time.

$$\frac{Dz}{Dt} = u + iv, \tag{3.66}$$

$$\frac{D\phi}{Dt} = \frac{1}{2}w \cdot \overline{w} - gy - \frac{P_a}{\rho}. \tag{3.67}$$

3.8.1 Runge-Kutta method

The solution to the differential equation of the form

$$\dot{y}(t) = \frac{dy(t)}{dt} = f(y(t)) \tag{3.68}$$

can be computed as

$$y_{n+1} = y_n + \frac{1}{2}\triangle t(k_1 + k_2), \tag{3.69}$$

where

$$y_n = y(t_n), \tag{3.70}$$
$$\triangle t = t_{n+1} - t_n, \tag{3.71}$$
$$k_1 = f(y_n) = \dot{y}_n, \tag{3.72}$$
$$k_2 = f(y_n + \triangle t \cdot k_1) = f(\overline{y}_{n+1}) = \dot{\overline{y}}_{n+1}. \tag{3.73}$$

Here, the Euler's method is used to predict a value of y_{n+1}. The truncation error is given by $e_t = K\triangle t^3 + O(\triangle t^4)$, where K depends upon $f(y(t))$ and its higher-order derivatives.

3.8.2 Hamming predictor-corrector method

This multi-step method requires four starting values for y and $f(y)$. These values are calculated from the Runge-Kutta method explained above. The algorithm can be given as

Step 1 : calculate the starling values y_n and f_n for $n = 0, ..., 3$.

Step 2 : calculate the predictor

$$P_{n+1} = y_{n-3} + \frac{4}{3}\triangle t(2\dot{y}_n - \dot{y}_{n-1} + 2\dot{y}_{n-2}).$$

Step 3 : calculate the modifier

$$M_{n+1} = P_{n+1} - \frac{112}{121}(P_n - C_n) \quad \text{where } (P_4 - C_4) = 0.$$

Step 4 : calculate the time derivative of the modified predictor

$$\dot{\bar{y}}_{n+1} = f(M_{n+1}).$$

Step 5 : calculate the corrector

$$C_{n+1} = \frac{1}{8}\left[9y_n - y_{n-2} + 3\triangle t(\dot{\bar{y}}_{n+1} + 2\dot{\bar{y}}_n - \dot{\bar{y}}_{n-1})\right].$$

Step 6 : calculate the final value at $t_n + \triangle t$

$$y_{n+1} = C_{n+1} + \frac{9}{121}(P_{n+1} - C_{n+1}).$$

We can note that the method has a local truncation error $O(\triangle t^5)$. The numerical formulation of Eq. (2.29) and (2.33) to compute solution for the points inside the contour are obtained by

$$\beta(z_0,t) = \frac{1}{2\pi i}\oint_C \frac{\beta(z,t)}{z-z_0}dz \cong \sum_j \Gamma_j(z_{j-1},z_j,z_{j+1},z_0)\beta_j(z_j,t), \tag{3.74}$$

$$\frac{\partial\beta(z_0,t)}{\partial t} = \frac{1}{2\pi i}\oint_C \frac{\frac{\partial\beta(z,t)}{\partial t}}{z-z_0}dz \cong \sum_j \Gamma_j(z_{j-1},z_j,z_{j+1},z_0)\frac{\partial\beta_j}{\partial t}(z_j,t), \tag{3.75}$$

$$w(z_0,t) = \frac{1}{2\pi i}\oint_C \frac{\beta(z,t)}{(z-z_0)^2}dz \cong \sum_j \Gamma 2_j(z_{j-1},z_j,z_{j+1},z_0)\beta_j(z_j,t), \tag{3.76}$$

$$\frac{\partial w(z_0,t)}{\partial t} = \frac{1}{2\pi i}\oint_C \frac{\frac{\partial\beta(z,t)}{\partial t}}{(z-z_0)^2}dz \cong \sum_j \Gamma 2_j(z_{j-1},z_j,z_{j+1},z_0)\frac{\partial\beta_j}{\partial t}(z_j,t), \tag{3.77}$$

$$\frac{dw(z_0,t)}{dt} = \frac{1}{\pi i}\oint_C \frac{\beta(z,t)}{(z-z_0)^3}dz \cong \sum_j \Gamma 3_j(z_{j-1},z_j,z_{j+1},z_0)\beta_j(z_j,t). \tag{3.78}$$

3.9 Implementation

Vinje and Brevig (1981a; 1981b) developed a very useful program code in Fortran 77 to study non-linear ship motion (and impact of entry and exit of a wedge moving into and leaving out of water initially at rest) based on the fully non-linear time-stepping method. Then the code was developed by Greenhow to compute results for entry and exit of different shaped bodies. In addition to that, Barringer

(1996) and Moyo (1996) successfully studied various aspects of water entry and exit problems using the code.

The developed code consists of several variables involved in the computation process. Some of them are physically and numerically very significant. The variables are selected very carefully for the numerical accuracy of solution. The first part of the program is to generate the collocation points on the control volume on which the problem is formulated. The control volume consists of two vertical boundaries, body surface and the free surface. The point distribution depends on the ratio distance on the body and the surfaces. The ratios play very significant role in the solution of the problem.

The final part of the program is to step forward in time to predict the fluid (and body) motion. The time step size also plays a significant role in the solution. Suitable ratios and time stepping size can be selected to resolve the particle motion and compute the forces experienced by the body.

In Fortran 77, the code was much more complicated and not well suited to use for further development to study various applications of the problem due to the complex structure of the code. For example, the common block is not computationally efficient method. The main program is designed in a way of sharing several variables by other subroutines. In addition to that, other variables are passed between subroutines. Moreover, control structures such as one dimensional and two dimensional arrays were defined by assigning the size at beginning of the declaration of the program.

In general, the static memory allocation is not a good way of declaring arrays because the size is changing with time stepping forward. In that case, the size limit may increase beyond the initial declaration size. As a result, the program terminates without completing the full task of the run. Furthermore, it is very difficult to obtain and analyse graphical results in as simple a manner as the latest generation languages.

Considering all the facts, the code has been translated to Matlab with some modification to the original code. Matlab is a script language and very user friendly to implement mathematical equations, produce and analyse results in an efficient way. It is not necessary to define a common block. The array size dynamically changes during the run time. Also Matlab has very well defined graphic handling tools and built-in numerical methods to solve a system of equations in an efficient

way. It can also be noted that Matlab is more efficient in memory allocation size and is less complicated than the earlier version of Fortran 77.

Chapter 4

Water Entry of Different Shaped Bodies

We discussed the non-linear time-stepping method and the numerical formulation of study water entry and exit of a body in previous chapters. We now apply the formulated equations for a symmetric wedge-shaped body to compute results for the free surface profile, pressure distribution along the submerged part of the body and the vertical upward force exerted on the body due to the forced motion executed by the body in heave mode. However, it can be used to study any other shape (asymmetric wedges, truncated wedges or boxes) entering or leaving the fluid with further modifications to the original equations. The formulation can also be used for other modes of two-dimensional motion (sway and roll).

In this chapter, we present a set of selected results for water entry of symmetric wedges, asymmetric wedges, truncated wedges and boxes moving with constant velocity and constant acceleration into water initially at rest. To verify the computed results, we carry out a set of different tests such as convergence checks, Froude number effect for the constant velocity cases, time effect on the stages of the motion, an added mass model for the force for constant acceleration and velocity cases and a self-similarity check for a symmetric wedge (similarly the asymmetric wedge at high Froude number (F_r) (i.e. gravity g=0) will also be self-similar). The two-dimensional shapes used to compute results for water entry and exit and the non-dimensionalisation method are described in sections (4.1) and (4.2), respectively. Constant velocity entry and constant acceleration entry are considered in sections (4.3) and (4.4), respectively. We also give some results

showing the finite depth effect on entry problems for each shape and consider the speed of the intersection points varying with Froude numbers and finite depths for the symmetric wedges.

4.1 Shapes

We consider the following shapes with various angles to compute results for water entry cases with constant velocity or acceleration. The symmetric wedge is well studied, the other shapes less so, but they also have significant practical applications.

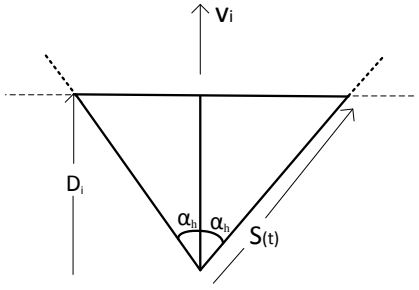

(a) Symmetric wedge

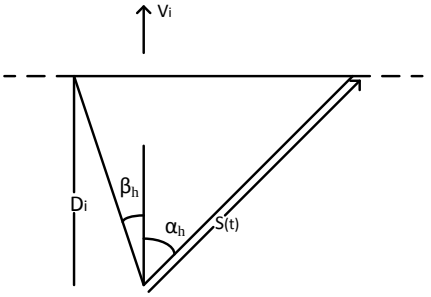

(b) Asymmetric wedge

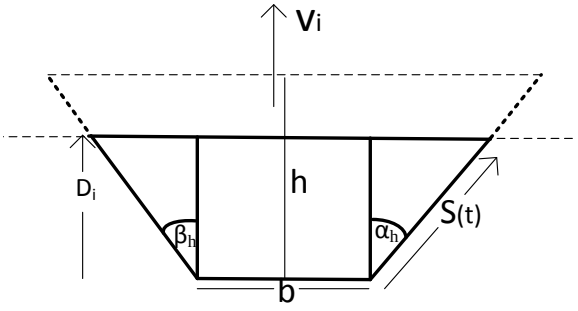

(c) Truncated wedge

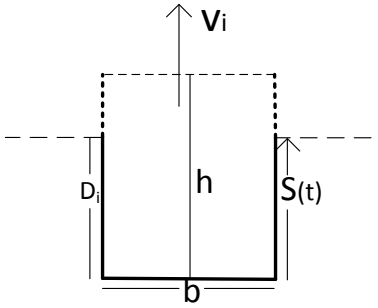

(d) Box

FIGURE 4.1: Geometrical representation of the different shaped bodies for water entry cases

For the symmetric wedge, vortex shedding from the vertex is not considered. However for the asymmetric wedge, if the left-half wedge angle $\beta_h < 0$ (see Fig. (4.1)) then vortex shedding from the sharp edge will certainly shed strong vortices. We do not consider this here. Neither do we consider the possibility of vortex shedding from the edges of the truncated wedge or the box (this will be discussed in

the Recommendation section). We note that Barringer (1996) also ignored vortex shedding from the knuckle-shaped body he considered. This is not to say that vortex shedding will be unimportant: shed vortices will certainly affect the fluid motion and hence forces and interact with the free surface. For wedges, these effects are likely to be much weaker and hence this thesis focuses mostly on them.

4.2 Non-dimensionalisation

We give computed results for the physical quantities (free-surface elevation, pressure distribution and force) in non-dimensional form. In this section, we outline a brief explanation of the process of non-dimensionalisation.

The dimensional characteristic time c_t is defined by

$$c_t = \sqrt{\frac{D_i}{g}},$$

where D_i is the initial submergence depth of the body below the free-surface at rest (see Fig. (4.1)) and gravitational field is denoted by g.
The dimension-less time τ is given by dividing time t by the characteristic time c_t as follows

$$\tau = \frac{t}{c_t}.$$

In the mathematical formulation of the problem, the spatial coordinate of the free-surface profile is formulated as complex variable z which consists of the x coordinate and y coordinate in the Cartesian coordinate system. We then do the non-dimensionalisation of z by dividing its real and imaginary parts by the initial submergence depth D_i as

$$\widehat{z} = \frac{z}{D_i} = \frac{x + iy}{D_i} = \widehat{x} + i\widehat{y},$$

where $\widehat{x} = \frac{x}{D_i}$ and $\widehat{y} = \frac{y}{D_i}$ are the non-dimensional forms of the coordinate of x and y respectively. The total pressure (static and dynamic) P computed by the Bernoulli's equation is divided by the initial hydrostatic pressure at $y = -D_i$ to get the non-dimensional pressure $\widehat{P}$ as below

$$\widehat{P} = \frac{P}{D_i \rho_w g},$$

where ρ_w is density of water. The vertical force f experienced by the body is computed using the fully non-linear numerical method which is non-dimensionalised by dividing the force by the initial buoyancy force and can be expressed as

$$\widehat{f} = \frac{f}{\rho_w g \forall},$$

where $\forall$ is the initial submerged volume (per unit length of the wedge prism). For the constant velocity case, we take account into the dimensionless Froude number F_r which is given by

$$F_r = \frac{v_b^2}{gD_i},$$

where v_b is the speed of the body executing motion in the fluid ($v_b = |V_b|$, where V_b is the velocity of the body). For the constant acceleration case, we are concerned with the dimensionless acceleration parameter which can be defined by dividing the original acceleration of the body by the gravity g as

$$G_\tau = \frac{a}{g}.$$

Finally, the dimensionless speed of the intersection point v_i is given by dividing the speed of the intersection point by the initial speed of the body as

$$\widehat{v_i} = \frac{v_i}{v_b}.$$

4.3 Constant velocity entry

This section, for constant velocity entry of symmetric wedges, asymmetric wedges, truncated wedges and box bodies, reviews the application of the non-linear theory and concerns numerical results computed using the implementation of the equations formulated to study water entry and exit problems in Matlab. For each shape shown in Fig. (4.1), we present the computed free-surface profile, pressure distribution along the wetted part of the body and total force experienced by the body as it moves through the free surface with constant velocity. To verify the results computed for the bodies, we carry out a set of test cases such as convergency check, Froude number effect, time effect on motion, self-similarity solution for symmetric wedges (it is also possible for asymmetric wedges), finite depth effect, comparison

of the free-surface profile with the Mackie's analytical theory for constant velocity entry of symmetric wedges and speed of intersection points between the symmetric wedges and the free surface changing with depths of fluid and Froude number of entry. The symmetric wedges, asymmetric wedges, truncated wedges and boxes entering with constant velocity are presented in sections (4.3.1), (4.3.2), (4.3.3) and (4.3.4) respectively.

4.3.1 Symmetric wedge entry

The main parameter of the problem of symmetric wedge entry is the vertical half wedge angle α_h and the initial submerged depth D_i, see Fig. (4.1(a)). We can compute numerical results for various symmetric wedges, which can be obtained by changing the main parameter of the problem, entering with different Froude numbers which can be chosen by changing values of the submerged depth and the speed of entry. However, the maximum of the half-wedge angle for larger entry speed is 55^o beyond which the calculations are unreliable due to the fast moving spray jets. In the symmetric-wedge entry case, we present results for various half-wedge angles, avoiding breaking the numerical computations by carefully selecting the number of points on the boundaries and the velocity of entry. Table (4.1) shows the symmetric wedges (for example, SW30 is a wedge of vertical half-wedge angle 30^0) selected to present results for constant velocity entry and constant acceleration entry. Many results are written on a CD as soft-copy for the future studies using this mathematical model, see Appendix (B). In section (4.3.1.1), we present results showing good agreement with the convergence check for the symmetric wedge SW30. The results for different Froude numbers are given in section (4.3.1.2). The computed numerical results showing the time effect and self-similarity solution are presented in sections (4.3.1.3) and (4.3.1.4) respectively. Finite depth effects and speed of the intersection points for constant velocity are presented in sections (4.3.1.5) and (4.3.1.6) respectively. Finally, a comparison of free-surface profile with Mackie's analytical results for constant velocity of entry is given in section (4.3.1.7).

Symmetric wedge (SW)	**Half wedge angle** (α_h)
SW5	5^o
SW20	20^o
SW30	30^o
SW45	45^o
SW55	55^o

TABLE 4.1: Symmetric wedges considered for water entry cases

4.3.1.1 Convergence check

To validate the computed numerical results of the free surface profile, pressure and force for symmetric wedges entering with constant velocity, we perform a set of tests that ensure other results can be relied upon. Having completed the tests, we can choose an appropriate set of input variables for long runs of the program. The following sections explain the test procedure carried out and give graphical results for wedge entry into initially calm water.

To check convergence of the numerical results, we consider the wedge SW30 entering with constant velocity. For the wedge, free-surface profile and pressure distribution are computed for different non-dimensional time step size $D\tau$ which is the only input variable changing for the run of the program and all other variables are the same. The results for entry of the wedge are plotted at a particular non-dimensional time τ for different non-dimensional time step size $D\tau$. For example, Fig. (4.2) shows the free-surface profile and pressure distribution computed for the wedge SW30 entering with Froude number $F_r = 0.5$ which is plotted for different non-dimensional time step size $D\tau$ of 0.1, 0.01 and 0.001 at a non-dimensional time τ of 1.3.

We see in Fig. (4.2) that the results show a good agreement in this convergence test. Results for the free surface and pressure at different time step sizes coincide for different time step sizes. From these convergence results, we use the non-dimensional time step size of 0.1 to do the most of the calculations of all other shapes for entry with constant velocity and constant acceleration. We also use different time step sizes for some cases. We notice that as we increase non-dimensional time step size from 0.001 to 0.1, we can see only a small deviation in the convergence of the results.

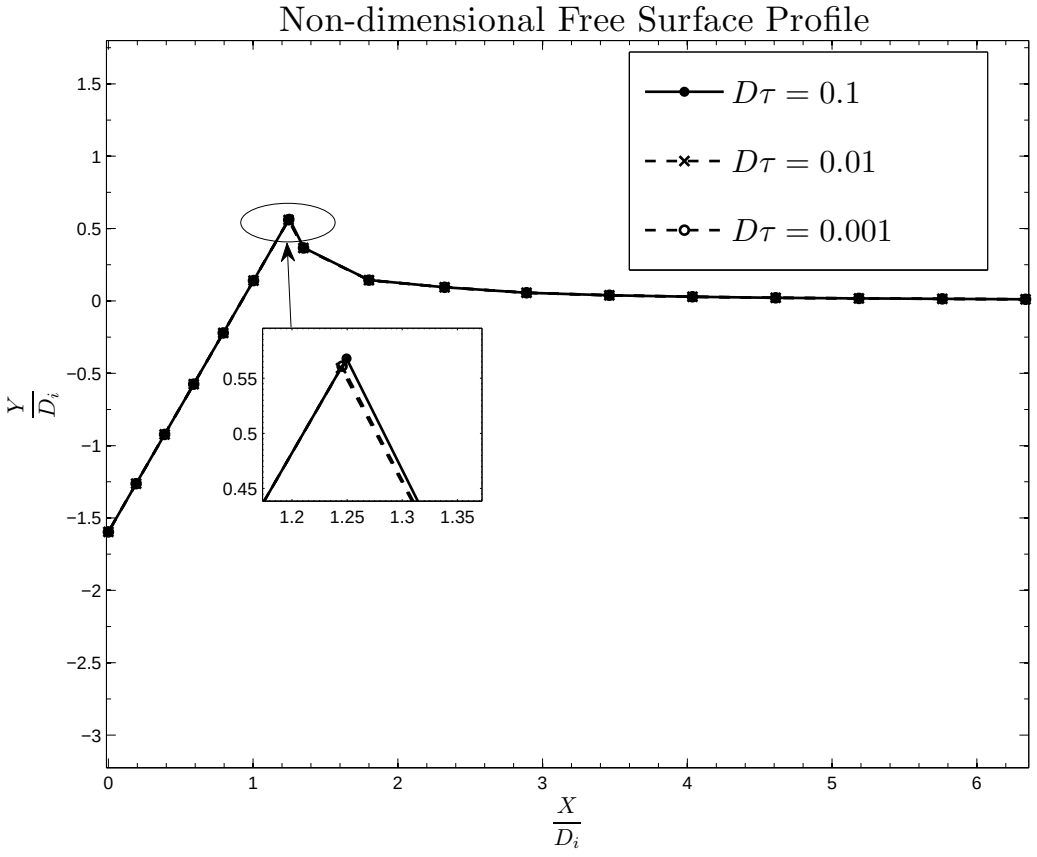

(a) Computed free surface profile

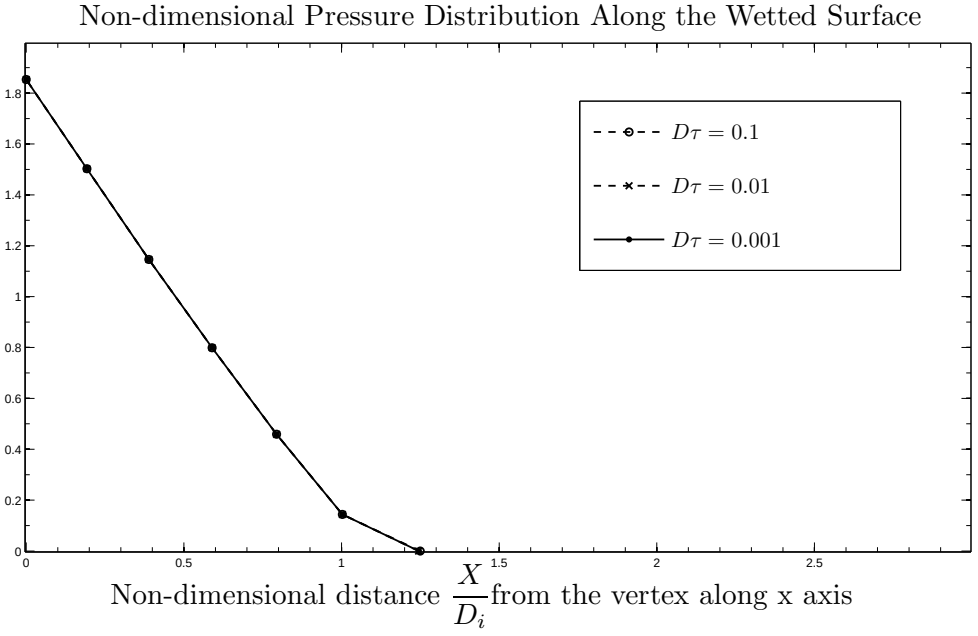

(b) Pressure distribution along the wetted part

FIGURE 4.2: Convergence of the symmetric wedge SW30 submerged at a non-dimensional initial depth $\widehat{d_i} = -1$ entering with constant velocity of Froude number $F_r = .5$: (a) and (b) are plotted for different non-dimensional time step size $D\tau$ at a non-dimensional time $\tau = 1.3$.

4.3.1.2 Froude number effect

In the study of water entry related problems, the Froude number defined in section (4.2) is a crucial dimensionless physical parameter. To study the effect of Froude number on the results, we carry out a set of test cases. For a particular wedge, the test process is to keep all the input variables of a specific run of the program constant, and obtain the Froude numbers by varying the velocity of the entry for the wedge. We plot the results for the free-surface profile, pressure and force at the same distance traveled by the wedge for different entry speeds as time progresses. The same process is repeated for the data sets and for the symmetric wedges considered. As we increase velocity of the entry, we notice much more deformation on the free surface and consequently in the pressure distribution and force as shown in Fig. (4.3) and (4.4) for the symmetric wedge SW30.

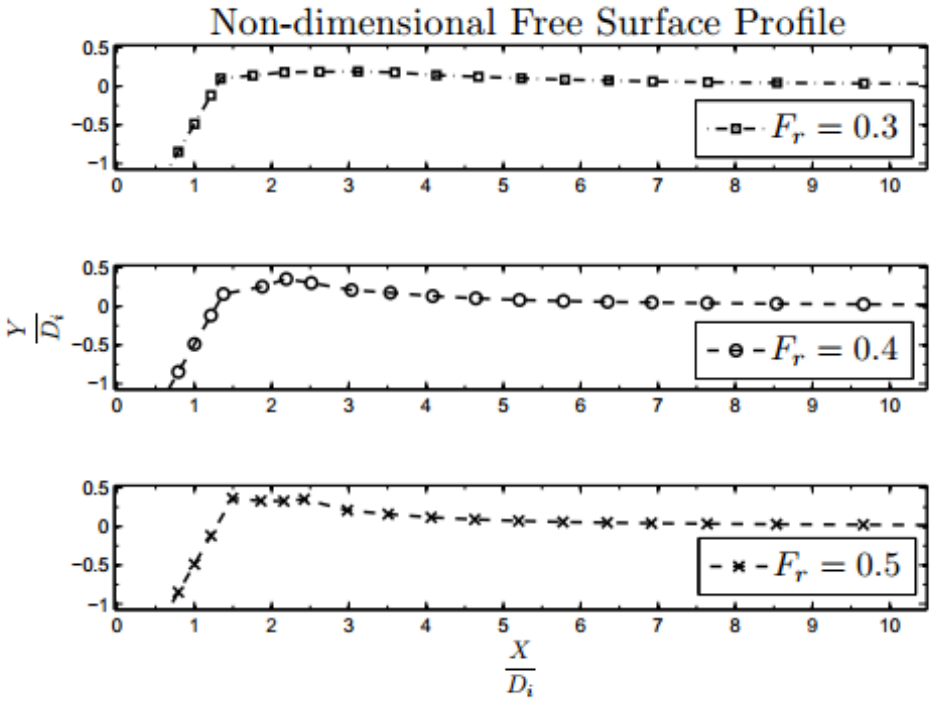

(a)

FIGURE 4.3: Froude number effect of the symmetric wedge SW30 submerged at a non-dimensional initial depth $\widehat{d}_i = -1$ entering with constant velocity of different Froude numbers F_r: plotted at different non-dimensional times $\tau = 4, 3, 2.4$ and distance $\widehat{d} = -2.22$.

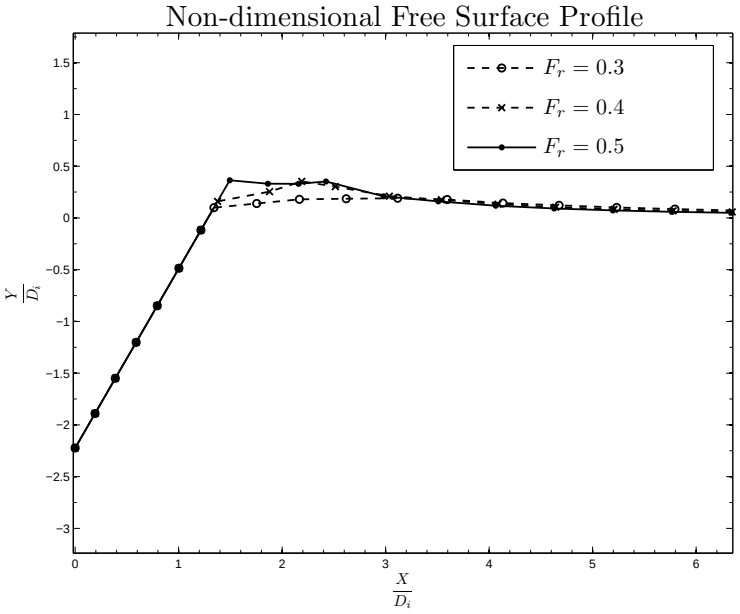

(a)

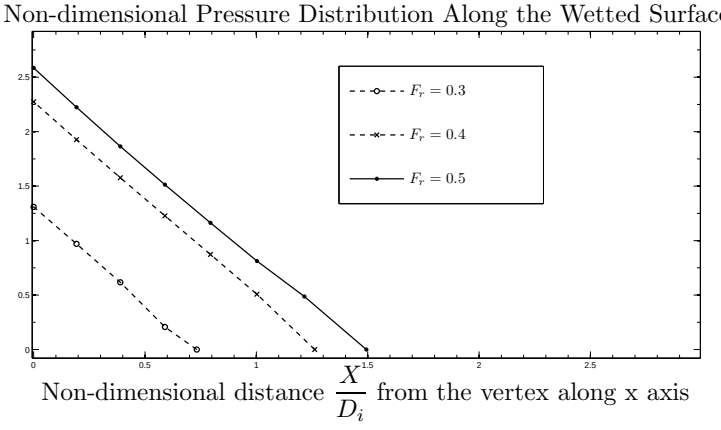

(b)

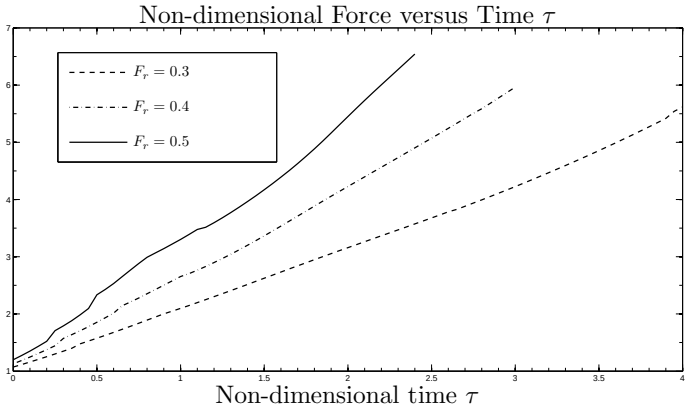

(c)

FIGURE 4.4: Froude number effect of the symmetric wedge SW30 submerged at a non-dimensional initial depth $\widehat{d_i} = -1$ entering with constant velocity of different Froude numbers F_r: (a), (b) and (c) are plotted at different non-dimensional times $\tau = 4, 3, 2.4$ and distance $\widehat{d} = -2.22$.

4.3.1.3 Time effect

The motion of the fluid changes as time progresses. We compute the deformed free-surface profile, pressure along the wetted part of the body and the upward force experienced by the body. The computed results showing the time effect on free surface, pressure and force at different stages of the entry with constant velocity are presented in this section. Fig. (4.5) and (4.6) show time effect of the symmetric wedge SW30 entering with Froude number of 0.5.

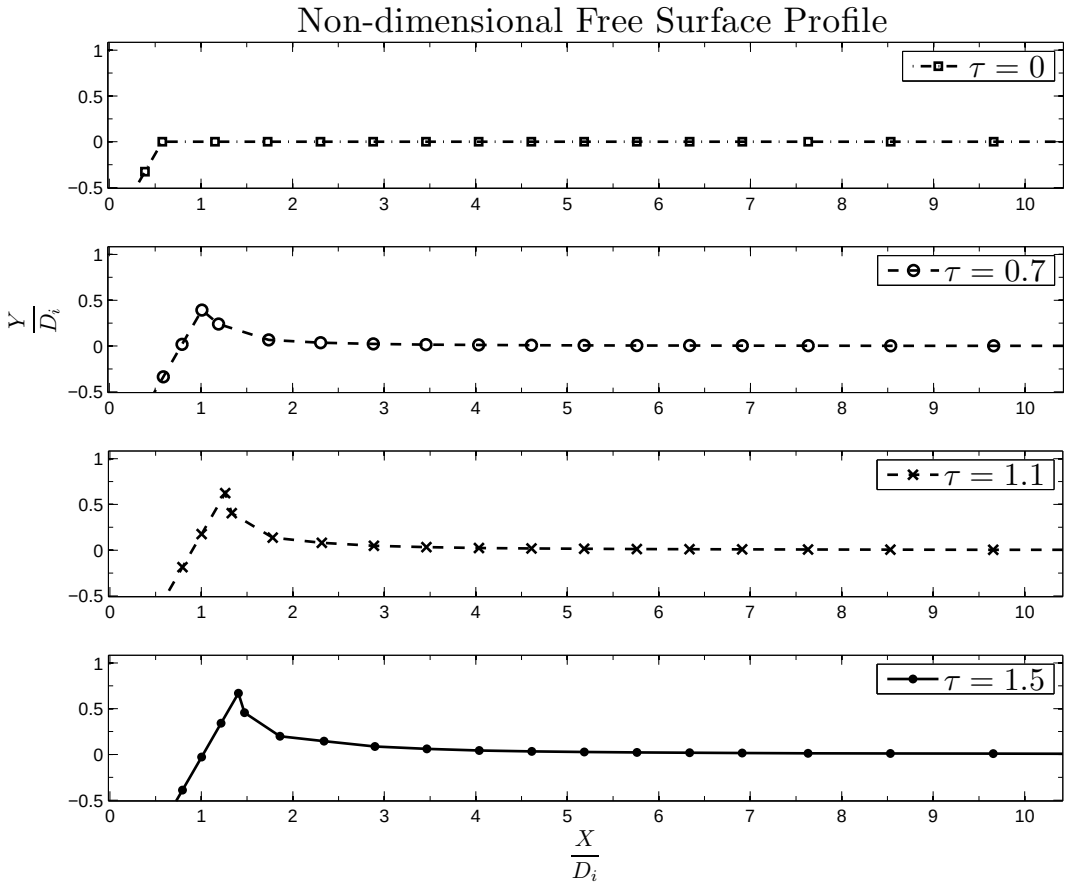

(a)

FIGURE 4.5: Time effect of the symmetric wedge SW30 submerged at a non-dimensional initial depth $\widehat{d}_i = -1$ entering with constant velocity of Froude number $F_r = 0.5$: plotted at different non-dimensional times τ.

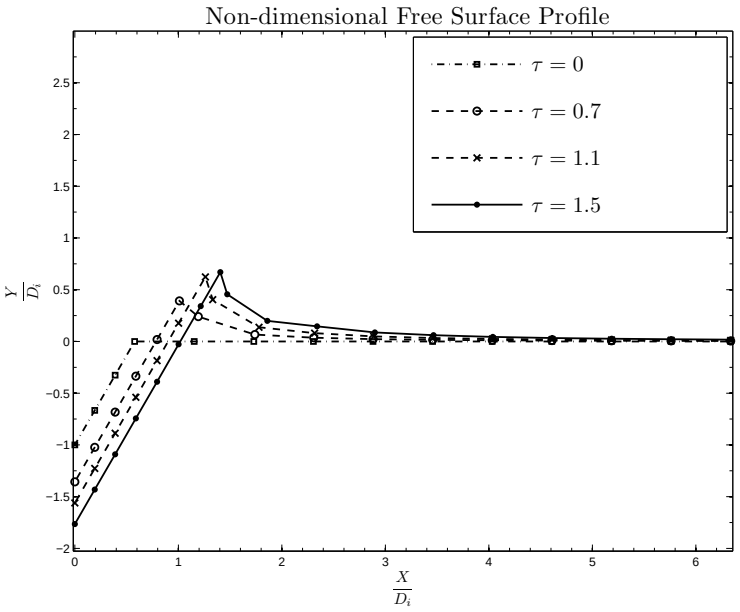

(a)

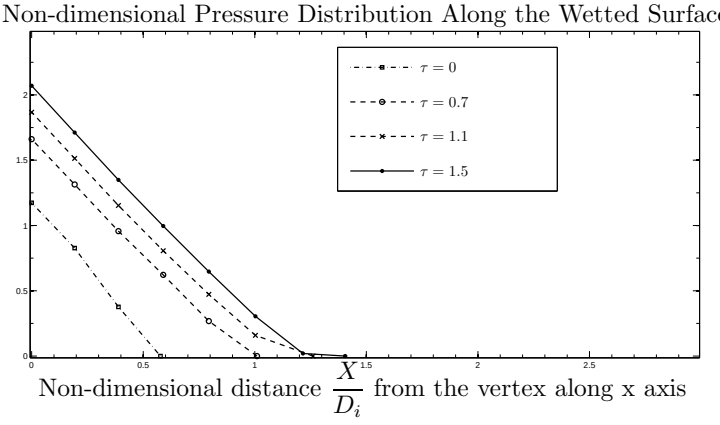

(b)

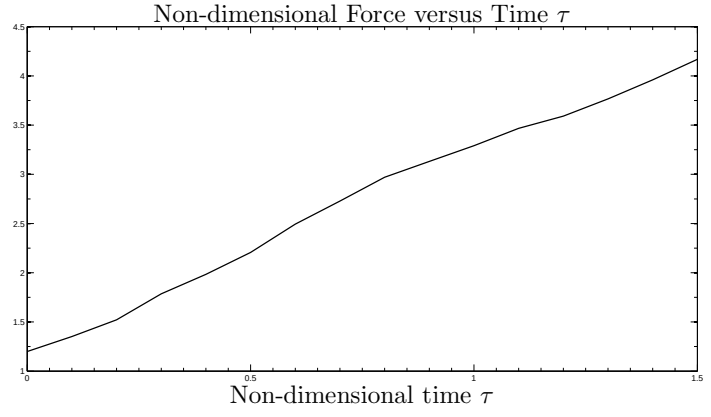

(c)

FIGURE 4.6: Time effect of the symmetric wedge SW30 submerged at a non-dimensional initial depth $\widehat{d_i} = -1$ entering with constant velocity of Froude number $F_r = 0.5$: (a), (b) and (c) are plotted at different non-dimensional times τ.

4.3.1.4 Self-similarity solution

A very important verification test in the study of water entry problem is self-similarity which requires a gravity-free condition in the numerical calculation of the results. Here we outline the main equations of the self-similar theory developed by Garabedian (1953) (also see Dobrovol'skaya (1969)).

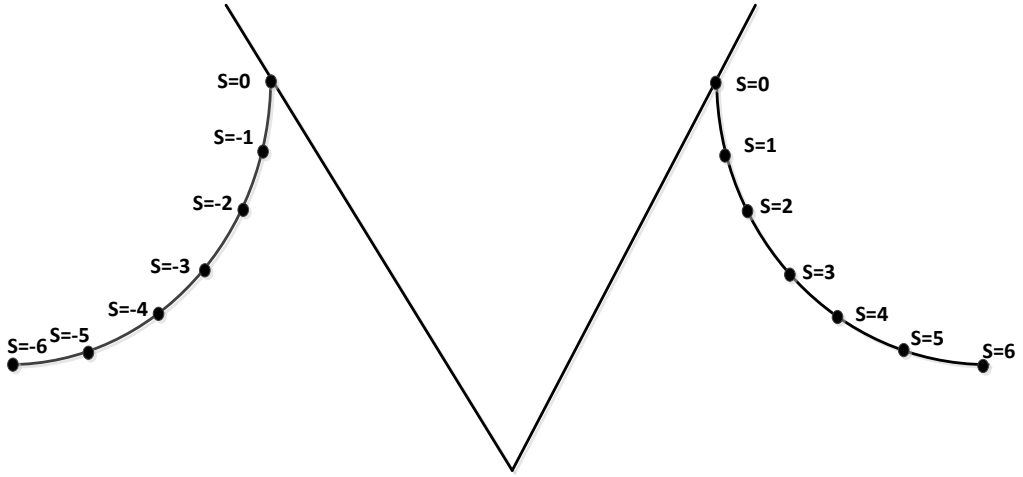

FIGURE 4.7: Definition sketch for the flow mapping in the plane

Using Garabedian's notation, we describe the free surface $z(s,t)$ as

$$\lambda z(s,t) = z(\lambda s, \lambda t) = z(\varsigma, \tau), \tag{4.1}$$

where s is a real parameter (Lagrangian marker) on the free surface (see Fig. (4.7)), t is time, $\varsigma = \lambda s$ and $\tau = \lambda t$ where λ is a constant. Differentiating with respect to λ, we get

$$z(s,t) = sz_{\varsigma} + tz_{\tau}. \tag{4.2}$$

If $\lambda = 1$, we have

$$z(s,t) = sz_s + tz_t. \tag{4.3}$$

Differentiating with respect to t, we have

$$z_t = sz_{st} + tz_{tt} + z_t. \tag{4.4}$$

Now when $g = 0$, we have John's (1953) equation (see Barringer (1996) for a more detail derivation):

$$z_{tt} = irz_s, \quad \text{where r is a real function.} \tag{4.5}$$

Then $z_{tt}\bar{z}_{tt} = irz_s\bar{z_{tt}}$ is a real:

$$\begin{aligned} \text{i.e., } & Re(z_s\bar{z}_{tt}) = 0. \\ \text{So, } & Re(z_s\bar{z}_{st}) = 0, \\ \text{i.e., } & \frac{\partial|z_s|^2}{\partial t} = 0. \end{aligned} \tag{4.6}$$

This means that the arc length $|z_s|$ between any two free-surface particles is constant with respect to time t.

We now give graphical results showing good agreement with the self-similarity test for the wedges entering with different deadrise angles (angle between the free surface and the body) by setting gravity to zero as required for the similarity. For a particular wedge entering with different velocity, the gravity-free numerical results for the free-surface profile are depicted at the same distance attained by the wedge. Fig. (4.9), (4.11) and (4.13) show a good agreement with the self-similarity check for the SW5, SW20 and SW30, respectively, except at the free surface/body intersection where the numerical resolution is not fully adequate.

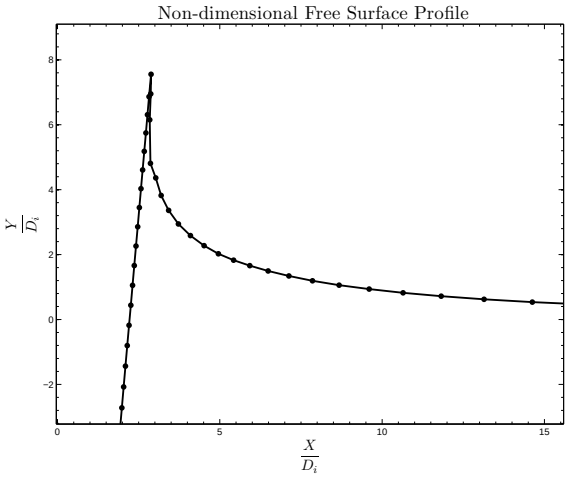

(a)

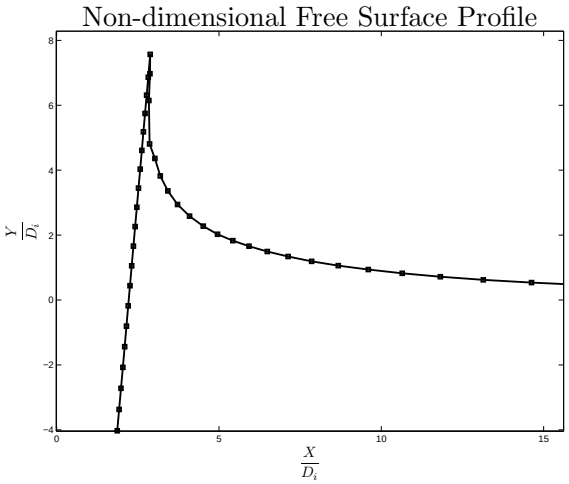

(b)

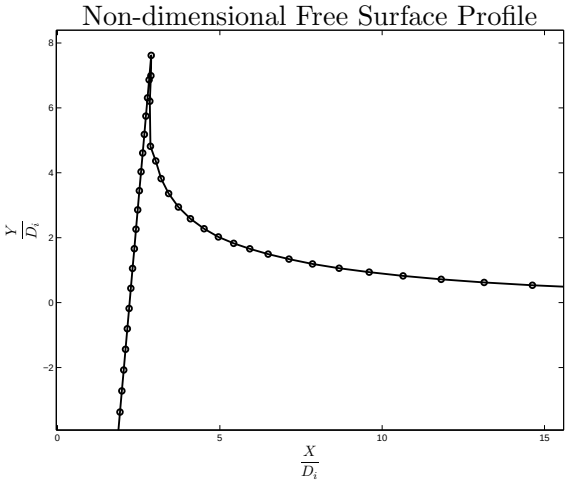

(c)

FIGURE 4.8: Computed free-surface profile showing self-similarity for the wedge SW5 submerged at a non-dimensional initial depth $\widehat{d_i} = -1$ entering with different velocities (v_1, v_2 and v_3) and zero gravity: a) $v_1 = 2.5$, (b) $v_2 = 5$ and (c) $v_3 = 7.5$ and plotted at a non-dimensional distance $\widehat{d} = -25.3$.

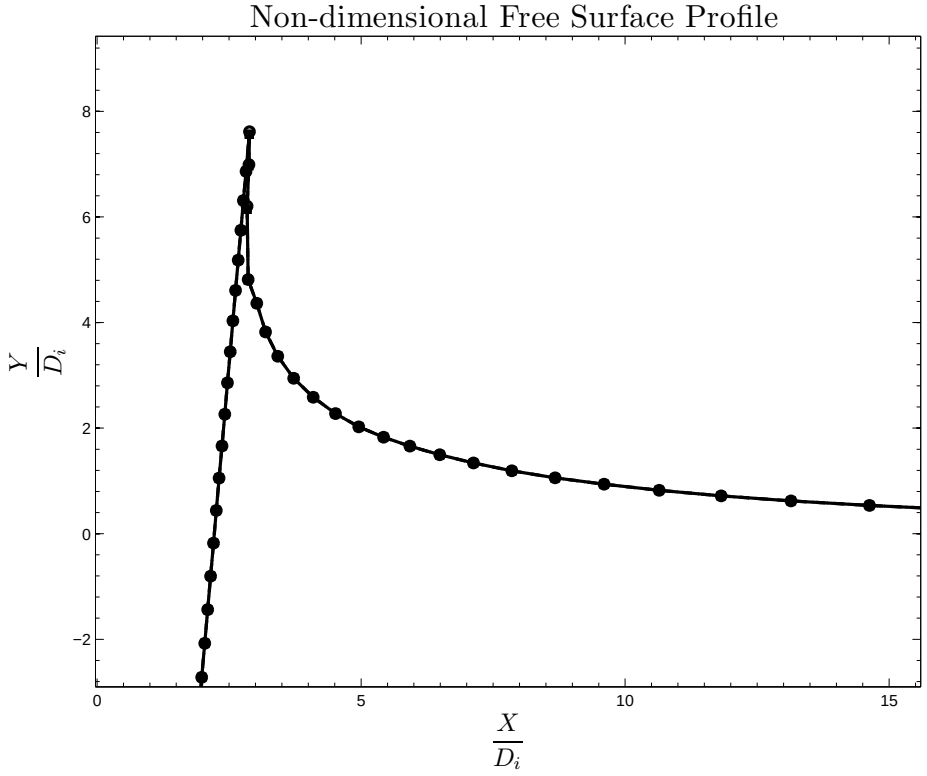

FIGURE 4.9: Computed free-surface profile showing self-similarity for the wedge SW5 submerged at a non-dimensional initial depth $\widehat{d}_i = -1$ entering with zero gravity: plotted at a non-dimensional distance $\widehat{d} = -25.3$.

To check self similarity of the results for the wedge SW5, we plot the three Fig. 4.8(a), 4.8(b) and 4.8(c) in Fig. (4.9).

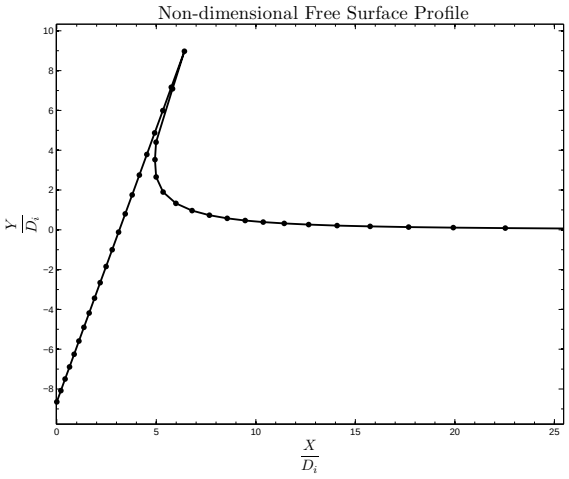

(a)

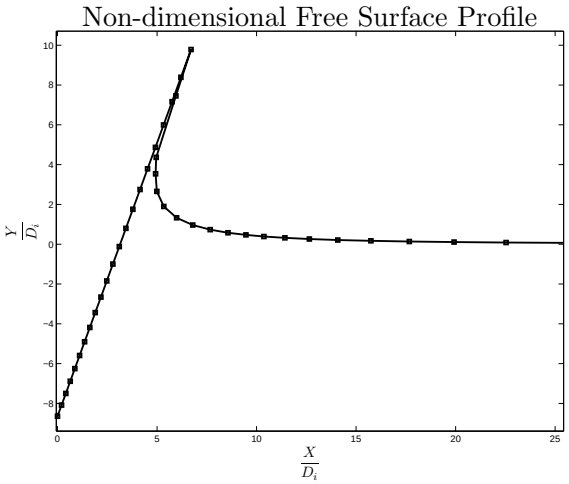

(b)

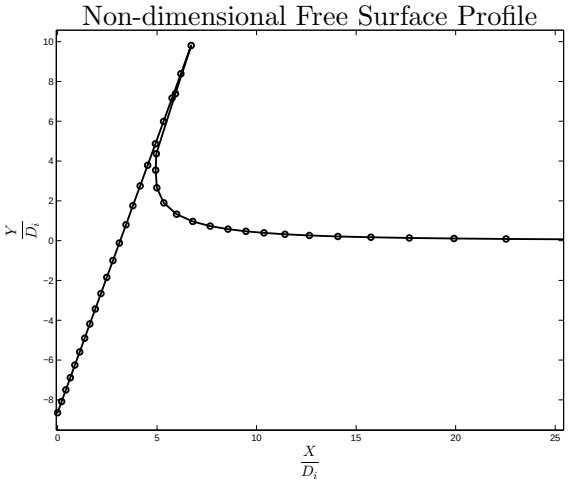

(c)

FIGURE 4.10: Computed free-surface profile showing self-similarity for the wedge SW5 submerged at a non-dimensional initial depth $\widehat{d_i} = -1$ entering with different velocities (v_1, v_2 and v_3) and zero gravity: a) $v_1 = 1$, (b) $v_2 = 2.5$ and (c) $v_3 = 5$ and plotted at a non-dimensional distance $\widehat{d} = -8.64$.

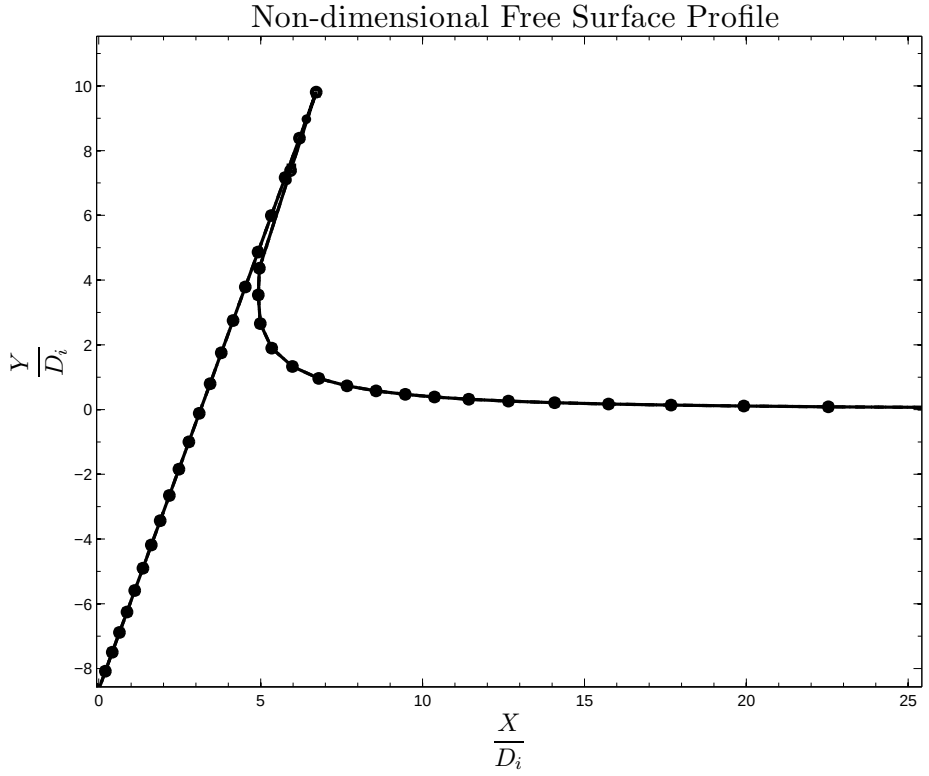

FIGURE 4.11: Computed free-surface profile showing self-similarity for the wedge SW20 submerged at a non-dimensional initial depth $\widehat{d}_i = -1$ entering with zero gravity: plotted at a non-dimensional distance $\widehat{d} = -8.64$.

To check self similarity of the results for the wedge SW20, we plot the three Fig. 4.10(a), 4.10(b) and 4.10(c) in Fig. (4.11).

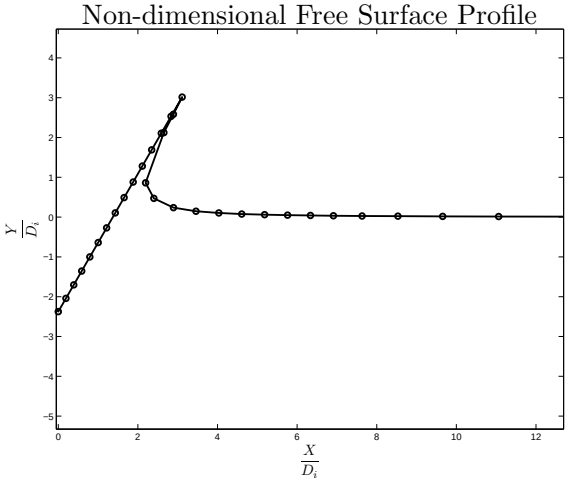

(a)

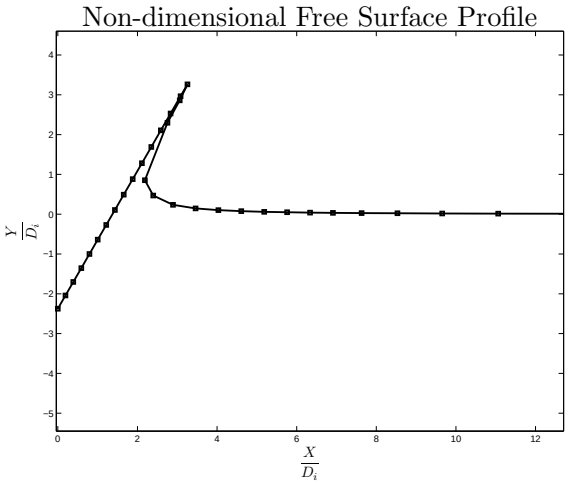

(b)

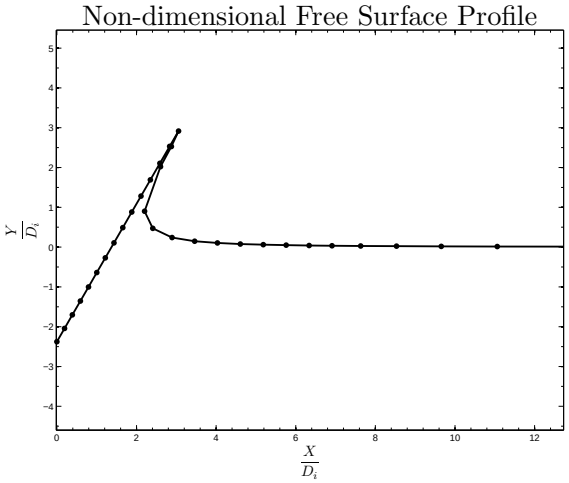

(c)

FIGURE 4.12: Computed free-surface profile showing self-similarity for the wedge SW30 submerged at a non-dimensional initial depth $\widehat{d}_i = -1$ entering with different velocities (v_1, v_2 and v_3) and zero gravity: a) $v_1 = 0.9$, (b) $v_2 = 1.8$ and (c) $v_3 = 2.7$ and plotted at a non-dimensional distance $\widehat{d} = -2.38$.

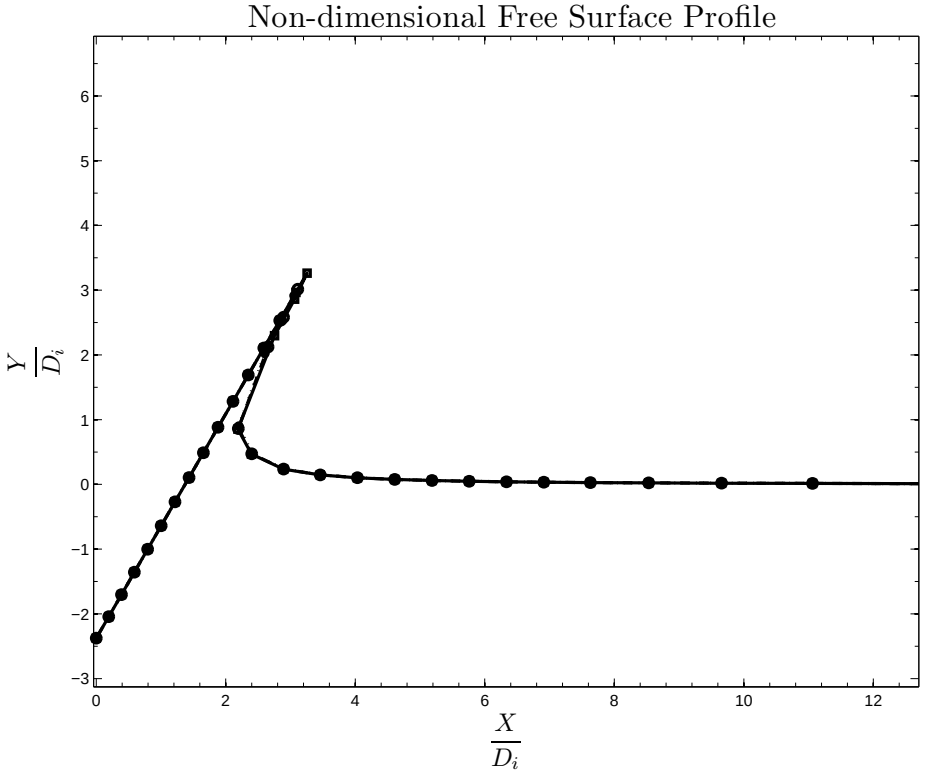

FIGURE 4.13: Computed free-surface profile showing self-similarity for the wedge SW30 submerged at a non-dimensional initial depth $\widehat{d}_i = -1$ entering with zero gravity: plotted at a non-dimensional distance $\widehat{d} = -2.38$.

To check self similarity of the results for the wedge SW30, we plot the three Fig. 4.12(a), 4.12(b) and 4.12(c) in Fig. (4.13).

We can see from the Fig. (4.9), (4.11) and (4.13) that the computed free-surface profiles for the wedges show a good agreement with the self-similarity check. We can also notice that the shape of jet formed by the deformation of the free surface after the transient motion decays remains unchanged as we required for the self similarity (constancy of the arc length of the free surface). We require the condition of zero gravity for the results to be self similar. We defined the Froude number which depends on gravity and tends to infinity as gravity goes to zero, but the results for free surface is valid numerically. However, the pressure at the vertex of the wedge and the force need to be resolved better for the higher Froude number cases.

4.3.1.5 Finite depth effect

It is very important to predict the motion due to marine vehicle operations near to the shore (shallow water) because it may be badly affected (hitting the seabed, snatching in the crane cables or instability due to broaching the free surface) by the unsteady forces, see Oliver (2002) for other effects. We present results showing the effect on the free-surface profile, pressure and force due to the change in depth of the entry with constant velocity using the non-linear time-stepping method. The results are plotted at the same distance close to the bottom surface (seabed) moved by the body for different depths of entry with the same velocity as it moves with time. Fig. (4.14) shows the computed free-surface profile, pressure distribution and force for the symmetric wedge SW30 entering with Froude number 0.5 showing finite depth effect on the motion. We notice that, as we expected for entering of the wedge SW30, the non-dimensional depth N_d below 1.53 experiences greater amount of free-surface deformation, pressure and force than that of other depths.

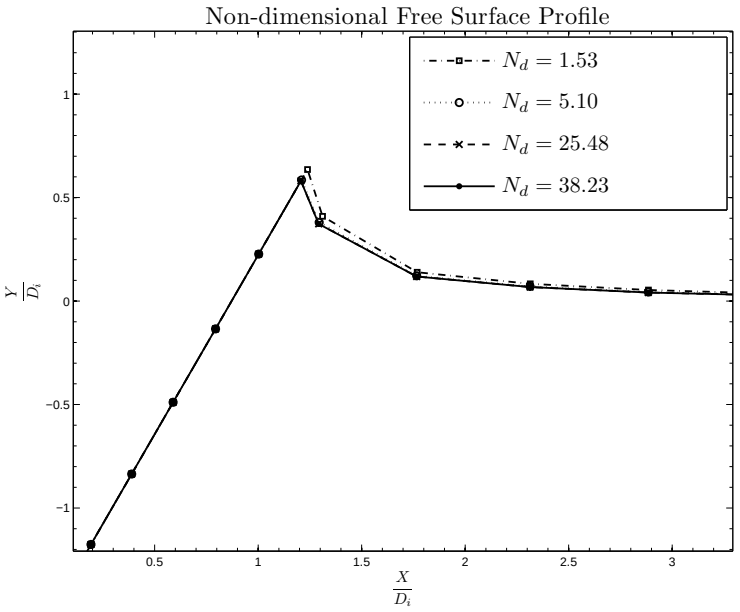

(a)

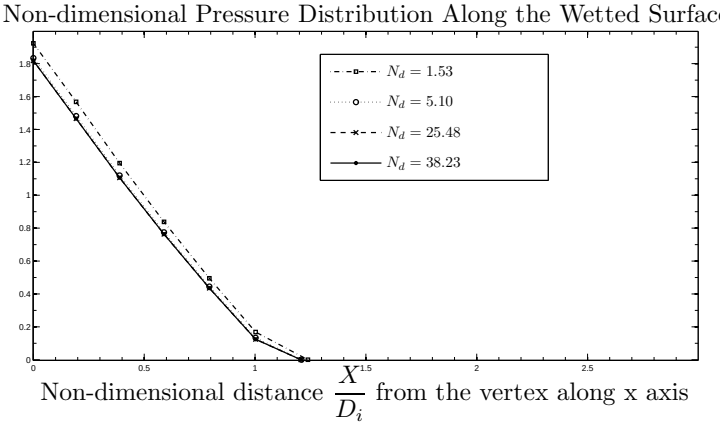

(b)

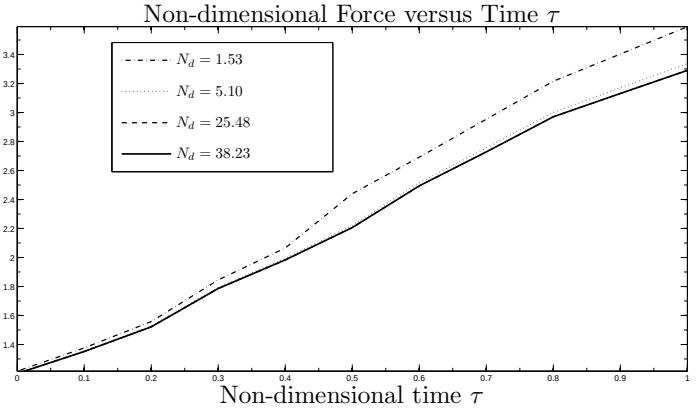

(c)

FIGURE 4.14: Finite depth effect of the symmetric wedge SW30 submerged at a non-dimensional initial depth $\widehat{d_i} = -1$ entering with constant velocity of Froude number $F_r = 0.5$: (a), (b) and (c) are plotted for different non-dimensional depths N_d at a non-dimensional time $\tau = 1$.

4.3.1.6 Speed of intersection point

A very thin jet is formed along each side of the body surface as it moves through a free surface between fluid and air. The formation of the jet depends on the dead-rise angle of the moving body and the velocity of the moving body. We initially define the points N_1 and N_2 (see Fig. (3.1)) to be the locations where the fluid particles on the both sides of the free surfaces first meet the body surfaces. Then the intersection points are computed by time stepping the kinematic boundary condition on the free surface at a later time. It is a very complicated to tackle the intersection points as time progresses. Numerical calculations will break down if the intersection points move to other side of the body surface (see, Sun and Faltinsen (2007)). So a special treatment can be used to control the errors caused by the movement of the intersection points (see, Iafrati and Korobkin (2001; 2000)). One way is to cut-off the jet flow near the intersection points, see Zhao and Faltinsen (1993). To study the local flow around the intersection points and avoid the numerical problem, it is very useful to compute the speed of the intersection points as the body moving with time. This section presents some results for the speed of intersection points of moving different symmetric wedges, but it can also be computed for all other shapes using this mathematical model. In this section, the computed speed of intersection points varying with Froude numbers and finite depths are considered for the symmetric wedges.

Speed effect with Froude number

Here we give the computed speed of the intersection points for the symmetric wedges considered showing the effect due to the change in Froude number of the entry. The plots are obtained for each shape entering with different Froude numbers at the same distance traveled by the symmetric wedge as it moves. Fig. (4.15) shows the Froude number effect on the speed of the intersection point of the symmetric wedge SW30. We can see that the initial speed at time zero is the same for any velocity of entry. This is not surprising because we are solving the same (non-dimensional) problem at t=0. However, for $t > 0$, wave effects are different at different Froude numbers and hence affect the motion of the intersection point. Results for higher Froude numbers are also possible for small time, but the calculations soon break down and hence are not shown here.

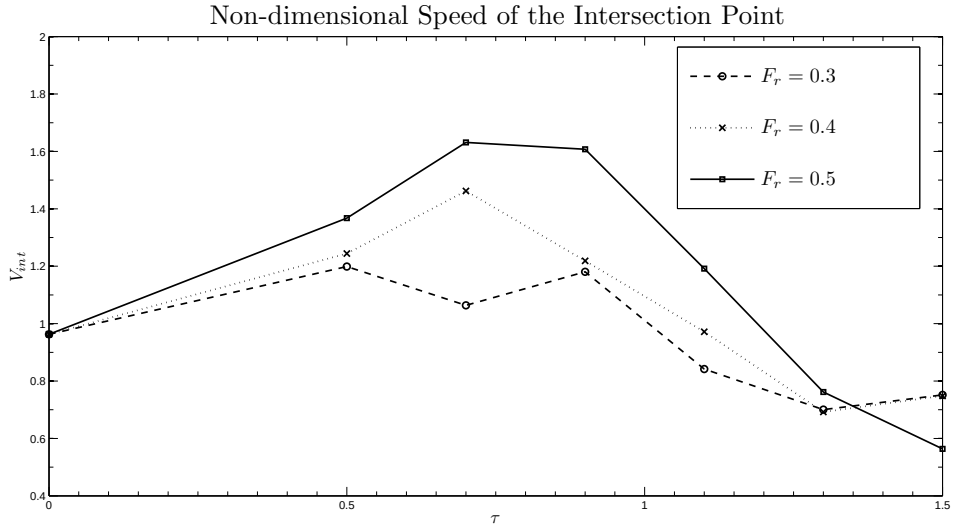

FIGURE 4.15: Effect of Froude number on the speed of intersection point for the wedge SW30 entering with constant velocity.

The speed of the intersection points depends on the free-surface point spacing and the time-step size. The intersection points move more rapidly as the point spacing and/or time step size decreases. Away from this point, we have established convergence of the free surface and hence use the same discretisation here for the intersection point speed. Thus Fig. (4.15) shows the computed speed of the intersection point for a particular free-surface point spacing and time-step size and may be used to inform future work, especially along the lines of Korobkin (2014) who has to assume this speed as an input to his analytical model of exit.

Speed effect with depth

Here we present the computed speed of the intersection points of the symmetric wedges as given in Table (4.1) showing effect due to the change in depth of the domain. The plots are obtained for each shape entering with constant velocity at a same distance, close to the bottom surface, traveled by the symmetric wedge as it moves. Fig. (4.16) shows the computed speeds for the symmetric wedge SW30 entering into the fluid of different depths. Here, we can note that starting values of the speed at time zero vary with depth of the fluid. We note that the plots for non-dimensional depths (N_d) 25.48 and 38.23 coincide.

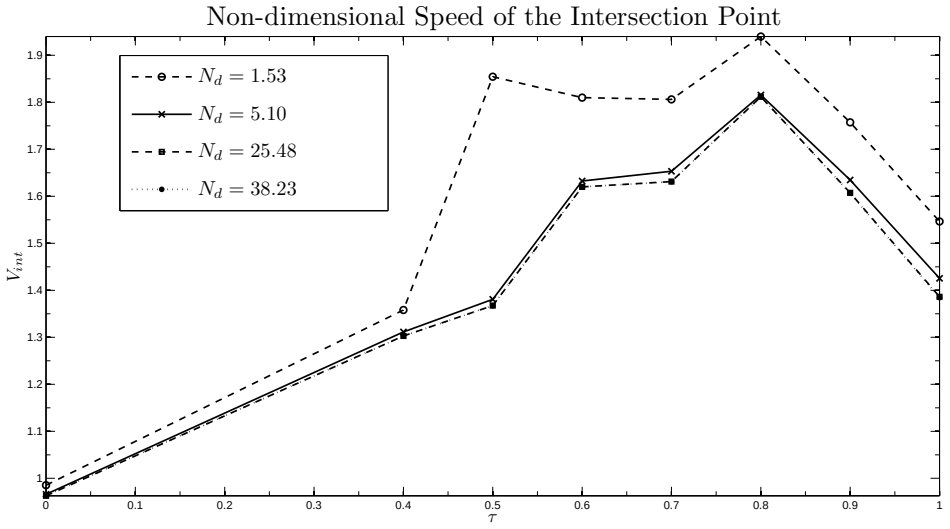

FIGURE 4.16: Effect of depth on the speed of intersection point for the wedge SW30 entering with constant velocity of Froude number $F_r = 0.5$.

4.3.1.7 Comparison with Mackie's theory

We compare the results for free surface elevation computed using the fully non-linear time-stepping method with the Mackie's (1969, 1965 and 1962) theory based on time-dependent wave-maker theory for a slender body using the method of Fourier series. The velocity along the vertical line (x=0) of the piston-type wave-maker is transferred to the body boundary condition for the slender body. Then the velocity is computed by using linearised Taylor series approximation with respect the vertical angle α_h. The linearised free surface profile can be expressed, see Greenhow (1990), as

$$\eta(x,t) = \frac{2}{\pi}\int_0^\infty \bar{\eta}(\lambda,t)\cos\lambda x d\lambda. \tag{4.7}$$

For entry, we have

$$\bar{\eta}(\lambda,t) = \frac{\alpha_h U^2}{\lambda(\lambda U^2+g)}\left[\cos(\sqrt{\lambda g}t) - U\sqrt{\frac{\lambda}{g}}\sin(\sqrt{\lambda g}t) - e^{-\lambda U t}\right], \tag{4.8}$$

where α_h is the wedge half-angle.

Based on the formulation, we present computed results showing rather poor agreement with the non-linear time-stepping theory of Vinje and Brevig (1981a; 1981b) for some symmetric wedges entering with constant velocities. Fig. (4.17) shows the comparison for the symmetric wedge SW5 entering with Froude number $F_r = 1$. Evidently the free-surface slope local to the wedge is not sufficiently small for linear theory to apply (later we will find better agreement with the wedge exit cases, where the free-surface slopes are smaller). At best we can say that Mackie's theory gives qualitatively correct behaviour, predicting an initial rise up wedge followed by wave propagation. Results for larger wedge angles (see Appendix B) show similar effects.

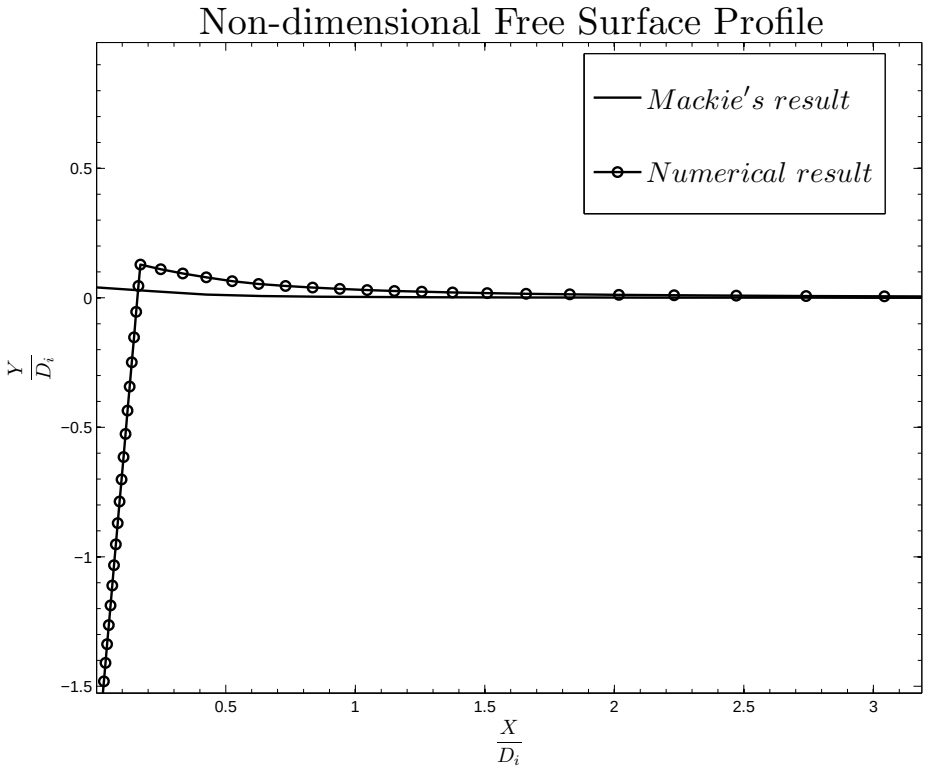

(a) at a non-dimensional time $\tau = 0.8$

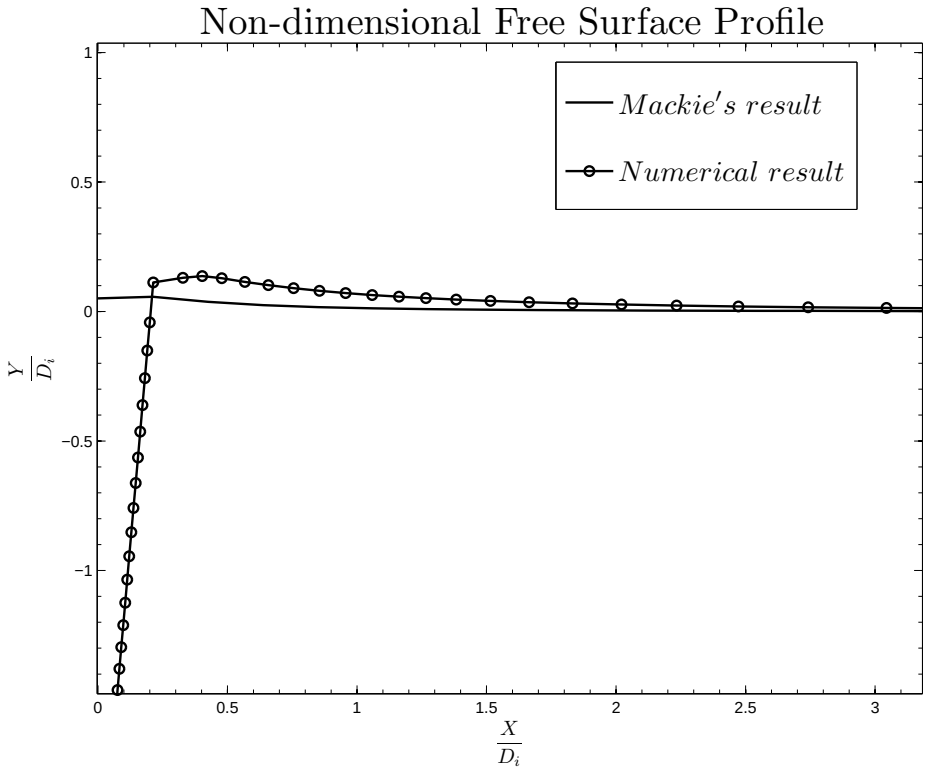

(b) at a non-dimensional time $\tau = 1.6$

FIGURE 4.17: Comparison of computed free-surface profile with Mackie's resuls for the wedge SW5 entering with constant velocity of $F_r = 1$.

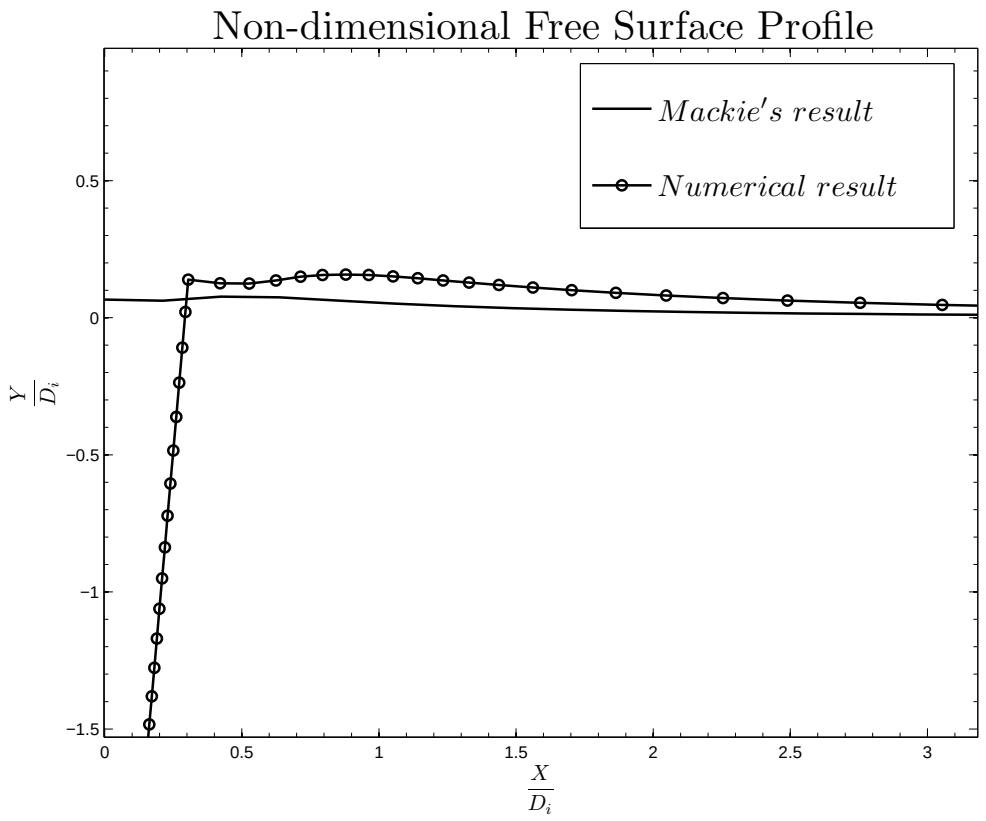

(c) at a non-dimensional time $\tau = 2.6$

FIGURE 4.17: Comparison of computed free-surface profile with Mackie's resuls for the wedge SW5 entering with constant velocity of $F_r = 1$.

4.3.2 Asymmetric wedge entry

It is important to study the motion of a ship in all modes of motions (translation and rotation) in order to predict the global response of the ship due to the slamming loads. In the case of rotation motions (e.g., roll motion), the entry and exit problems become asymmetric. In addition to that, to design propellers for ships in ballast, where the propeller blades exit and enter the water with each revolution, we need to consider the motion of the propeller which is asymmetric and has negative left-vertical angle (β_h). We consider the asymmetric wedges given in Table (4.2). The parameters for an asymmetric wedge are same as those for a symmetric wedge except for the left angle β_h as shown in Fig.(4.1(b)), see page 41. Table (4.2) gives the details for the test cases carried out for the wedge. The results for different Froude numbers of entry with constant velocity are given in section (4.3.2.1). The computed numerical results for the asymmetric wedges showing the time effect and finite depth effect are given in sections (4.3.2.3) and (4.3.2.4) respectively. The convergence of the asymmetric wedge was also checked and results are given in the CD as specified in Appendix (B).

Asymmetric wedge	**Half wedge angle**	
(AW)	(β_h)	(α_h)
AW1	5^o	10
AW2	0^o	15
AW3	-10^o	25
AW4	-10^o	30

TABLE 4.2: Asymmetric wedges considered for water entry cases

For asymmetric wedges we note that the fluid flow becomes singular at the vertex. In reality, vortices will shed from the vertex and this will affect the flow, especially on the left-hand side of the wedge (for negative angles). On the right-hand side, the flow may be much more realistic. However, further calculations with with vortex shedding and experiments would be highly desirable: comparison with the results below would then indicate how important vortex shedding is.

4.3.2.1 Froude number effect

To study the effect of Froude number on the results of the asymmetric wedges considered, we carry out a set of test cases. For a particular asymmetric wedge, the test process is to keep all the input variables of a specific run of the program constant, and obtain the Froude numbers by varying the velocity of the entry for the wedge. We plot the results for the free surface profile, pressure and force at the same distance traveled by the asymmetric wedge for different entry speeds as time progresses. The same process is repeated for the data sets and asymmetric wedges as shown in Table (4.2). As we increase velocity of the entry, we can notice much more deformation on the free surface and consequently in the pressure distribution and force as shown in Fig. (4.18) and (4.19) for the asymmetric wedge AW4.

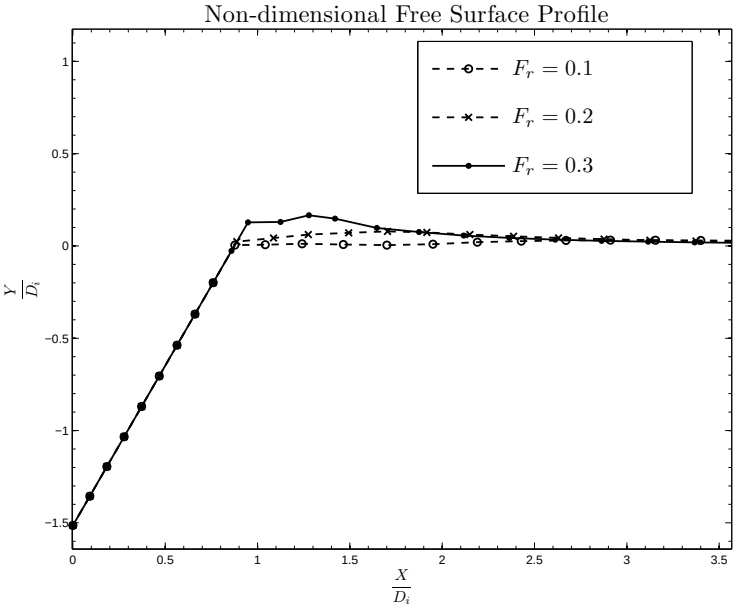

(a) right side of the wedge

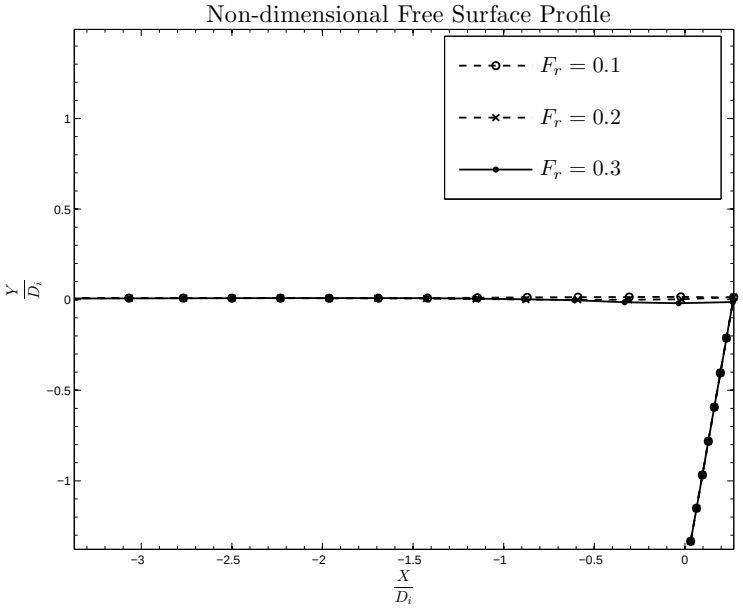

(b) left side of the wedge

FIGURE 4.18: Froude number effect of the asymmetric wedge AW4 submerged at a non-dimensional initial depth $\widehat{d_i} = -1$ entering with constant velocity of different Froude numbers: plotted at different non-dimensional times $\tau = 2.49, 2.7, 1.68$ and distance $\widehat{d} = -1.51$.

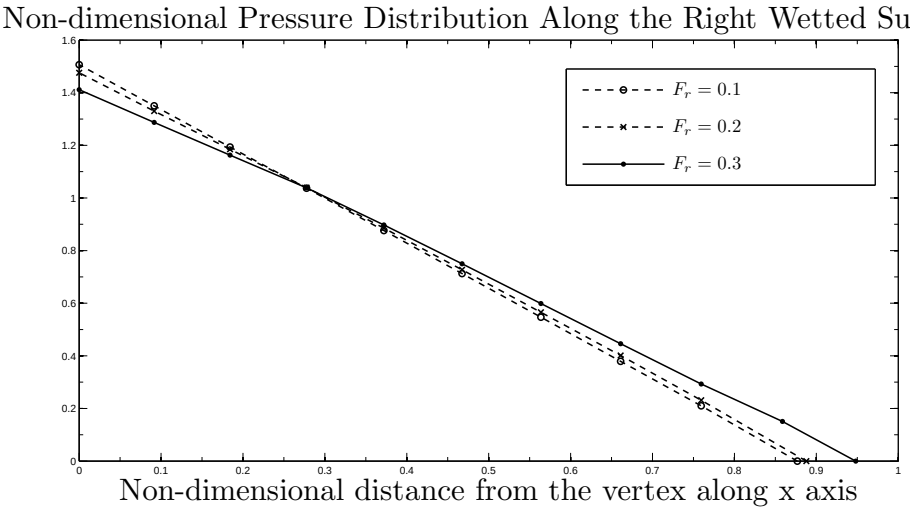

(a)

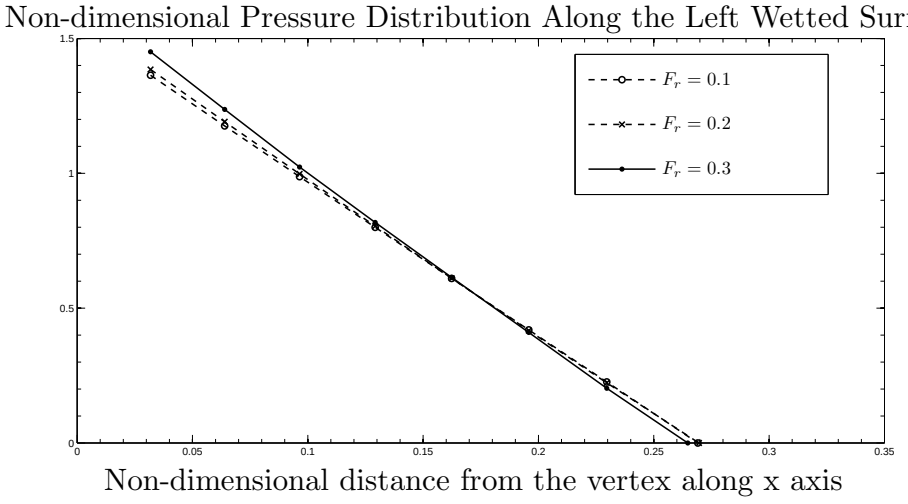

(b)

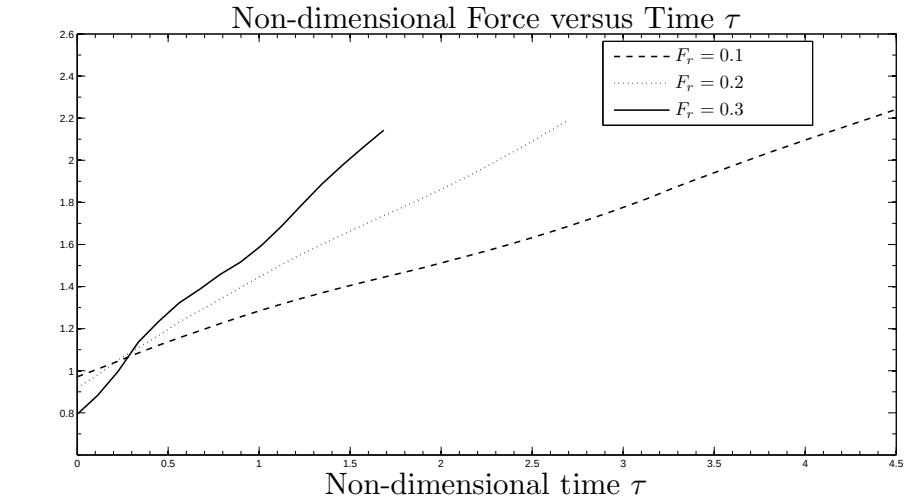

(c)

FIGURE 4.19: Froude number effect of the asymmetric wedge AW4 submerged at a non-dimensional initial depth $\widehat{d}_i = -1$ entering with constant velocity of different Froude numbers: plotted at different non-dimensional times $\tau = 2.49, 2.7, 1.68$ and distance $\widehat{d} = -1.51$.

4.3.2.2 Time effect

The motion of the asymmetric wedge and the free-surface profile change as time progresses. We can compute the deformed free-surface profile, pressure along the wetted part of the body and the upward force experienced by the body using the non-linear theory. The computed results showing the time effect on free surface, pressure and force at different stages of the entry with constant velocity are presented in this section. Figs. (4.20) to (4.23) show the time effect of the asymmetric wedge AW4 entering with a Froude number of 0.3 at each time interval.

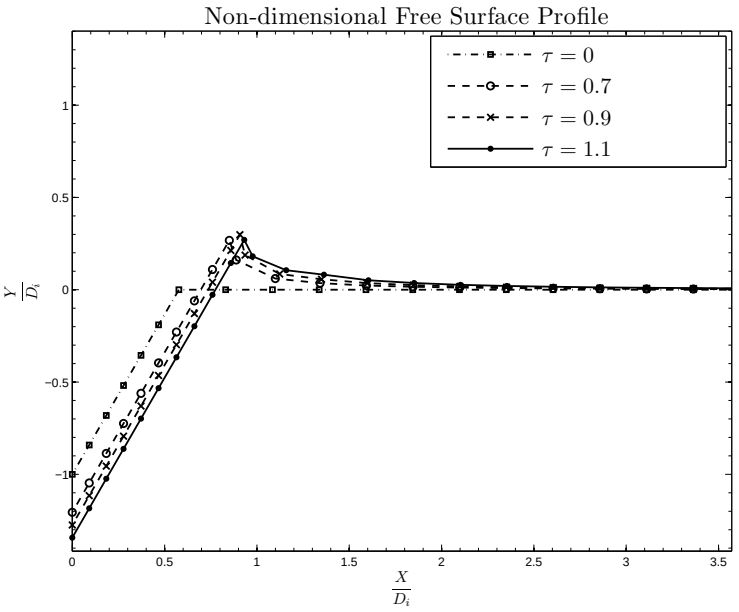

(a) right side of the wedge

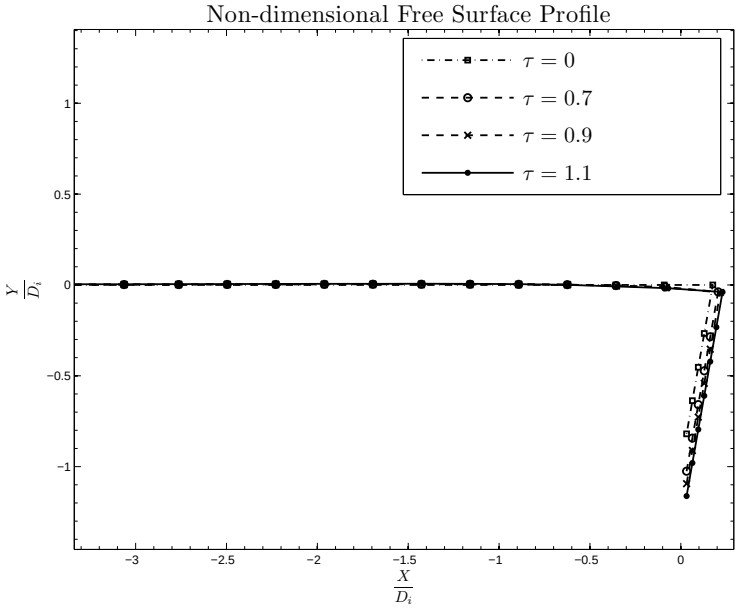

(b) left side of the wedge

FIGURE 4.20: Time effect of the asymmetric wedge AW4 submerged at a non-dimensional initial depth $\widehat{d}_i = -1$ entering with constant velocity of Froude number $F_r = 0.3$: plotted at different non-dimensional times τ.

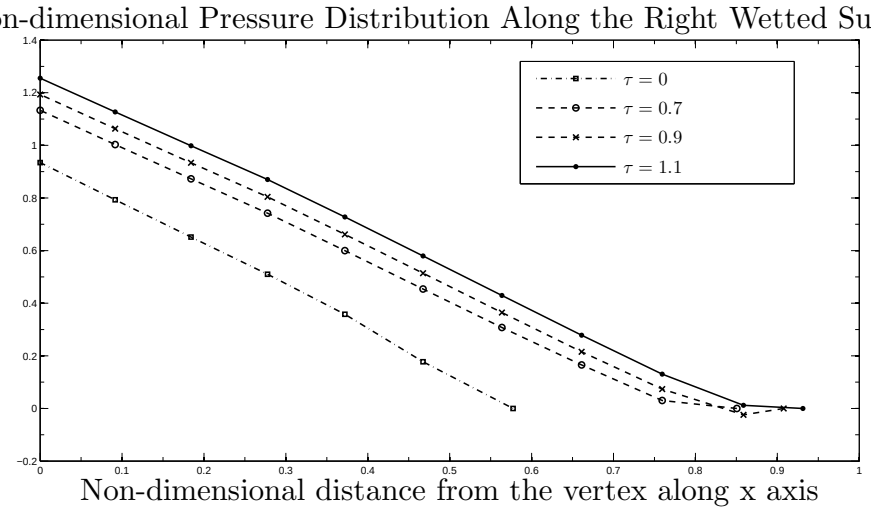

(a)

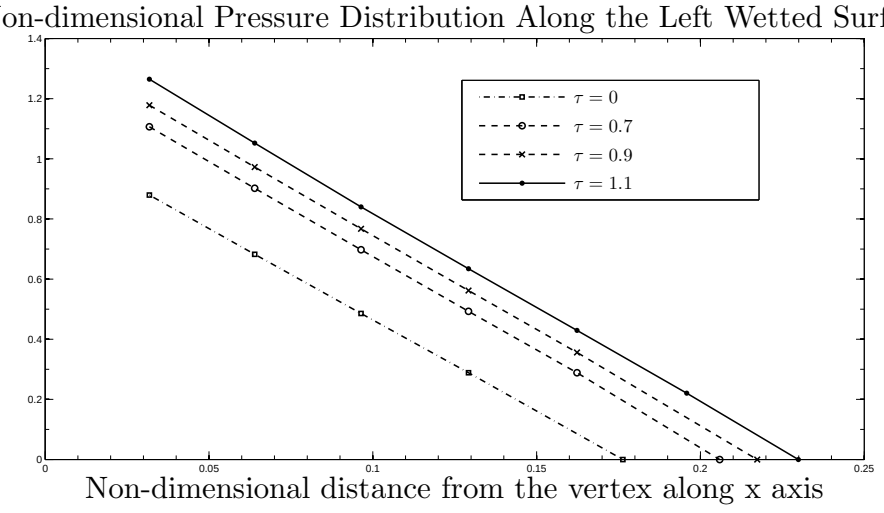

(b)

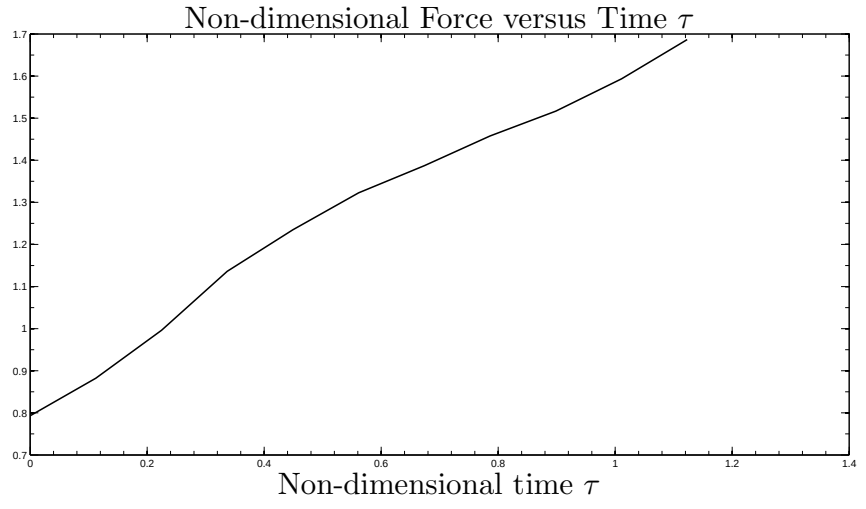

(c)

FIGURE 4.21: Time effect of the asymmetric wedge AW4 submerged at a non-dimensional initial depth $\widehat{d_i} = -1$ entering with constant velocity of Froude number $F_r = 0.3$: plotted at different non-dimensional times τ.

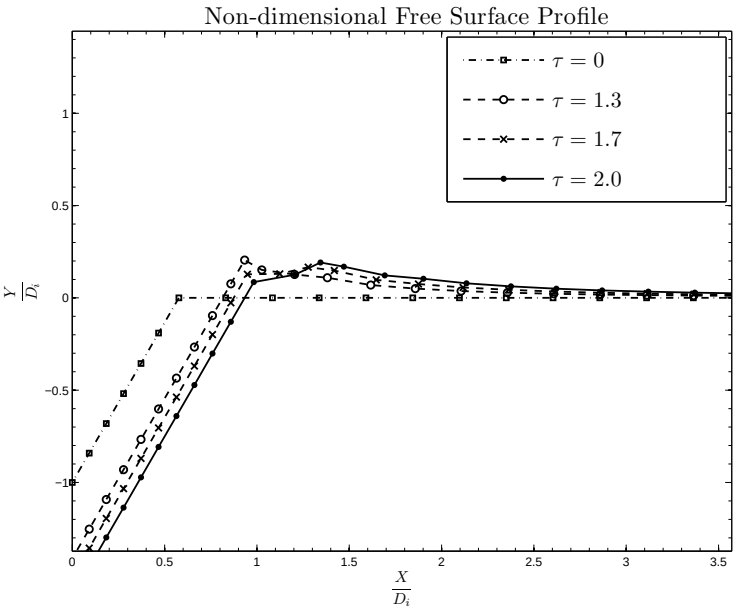

(a) right side of the wedge

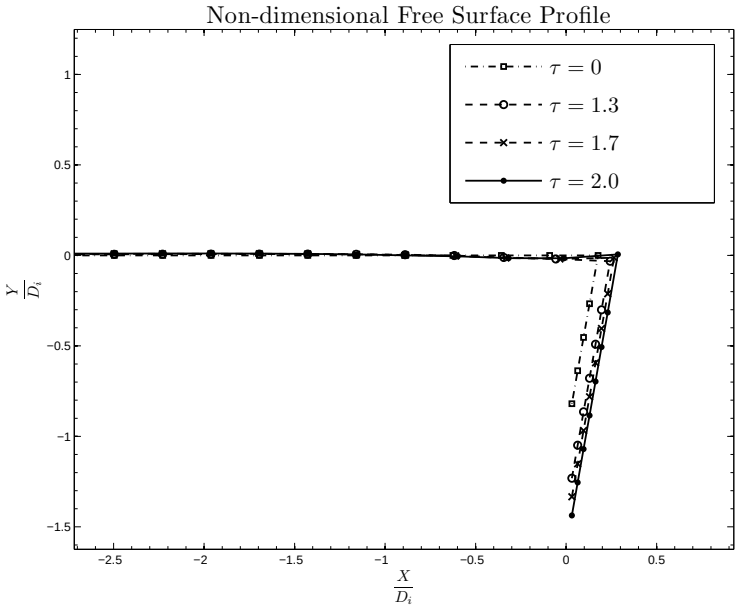

(b) left side of the wedge

FIGURE 4.22: Time effect of the asymmetric wedge AW4 submerged at a non-dimensional initial depth $\widehat{d}_i = -1$ entering with constant velocity of Froude number $F_r = 0.3$: plotted at different non-dimensional times τ.

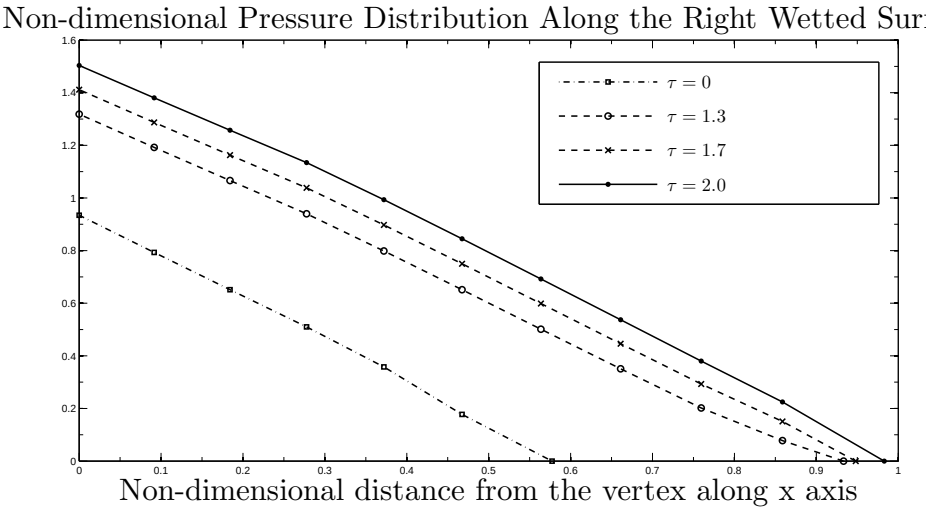

(a)

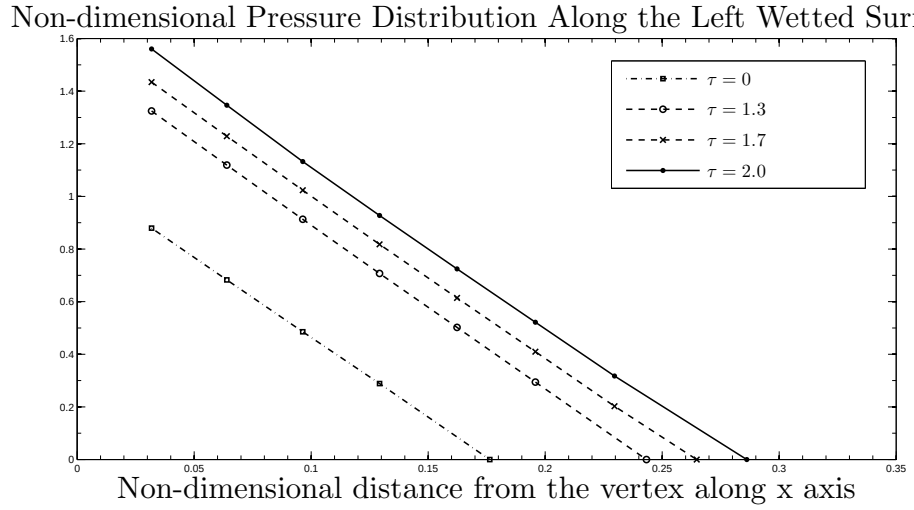

(b)

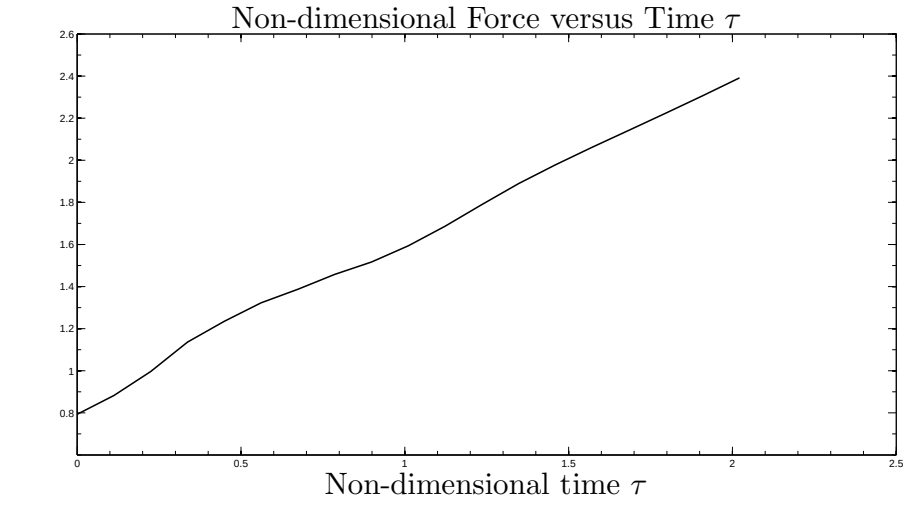

(c)

FIGURE 4.23: Time effect of the asymmetric wedge AW4 submerged at a non-dimensional initial depth $\widehat{d}_i = -1$ entering with constant velocity of Froude number $F_r = 0.3$: plotted at different non-dimensional times τ.

4.3.2.3 Finite depth effect

We present results showing the effect on the free-surface profile, pressure and force due to the change in depth for asymmetric wedges with constant velocity. The results are plotted at the same distance moved by the body for different depths of entry with the same velocity as it moves with time. Fig. (4.24) and (4.25) show the computed free-surface profile, pressure distribution and force for the asymmetric wedge AW4 entering with Froude number 0.3, showing the finite depth effect on the motion. We notice, as expected, that for entry of the asymmetric wedge AW4 a non-dimensional depth N_d below 1.4 experiences a greater difference in the free-surface deformation, pressure and force than that of other depths. Fig. 4.25(c) shows that the force is actually reduced in small depths. This is somewhat unexpected but we note an increased pressure on the left-hand side of the wedge, which would push the wedge down more.

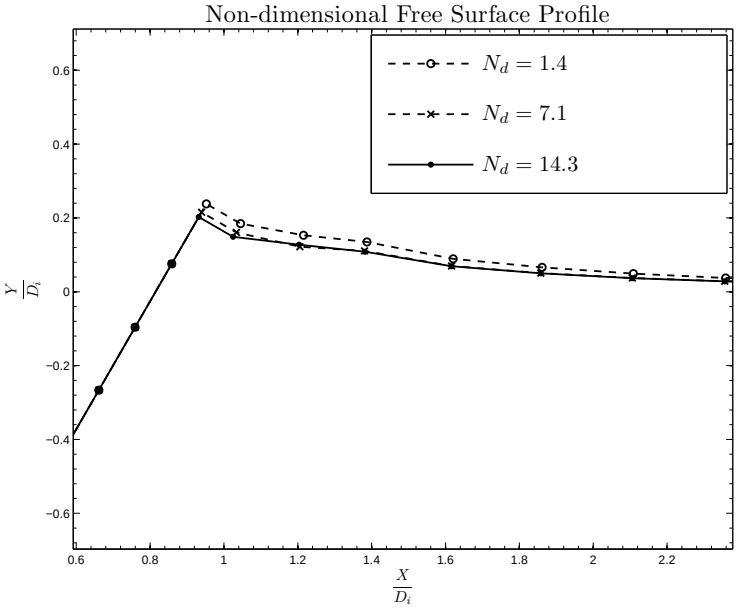

(a) right side of the wedge

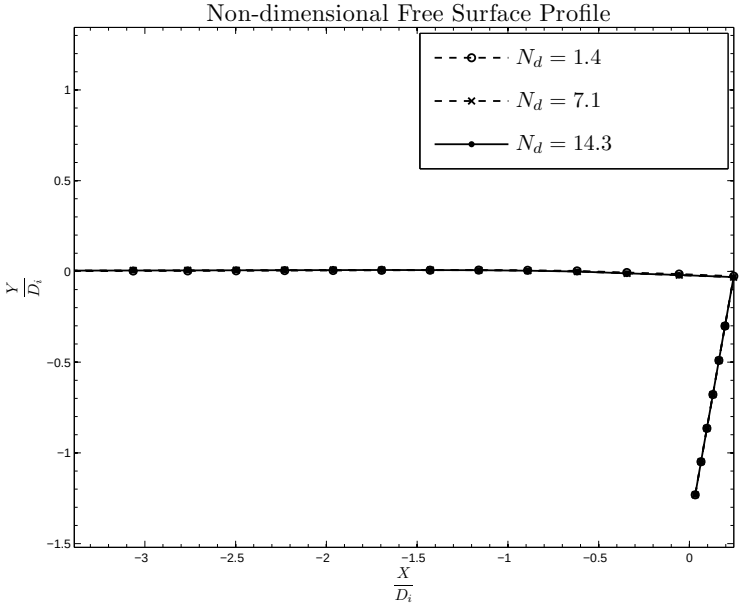

(b) left side of the wedge

FIGURE 4.24: Finite depth effect of the asymmetric wedge AW4 submerged at a non-dimensional initial depth $\widehat{d_i} = -1$ entering with constant velocity of Froude number $F_r = 0.3$: (a) and (b) are plotted for different non-dimensional depths N_d at a non-dimensional time $\tau = 1.35$.

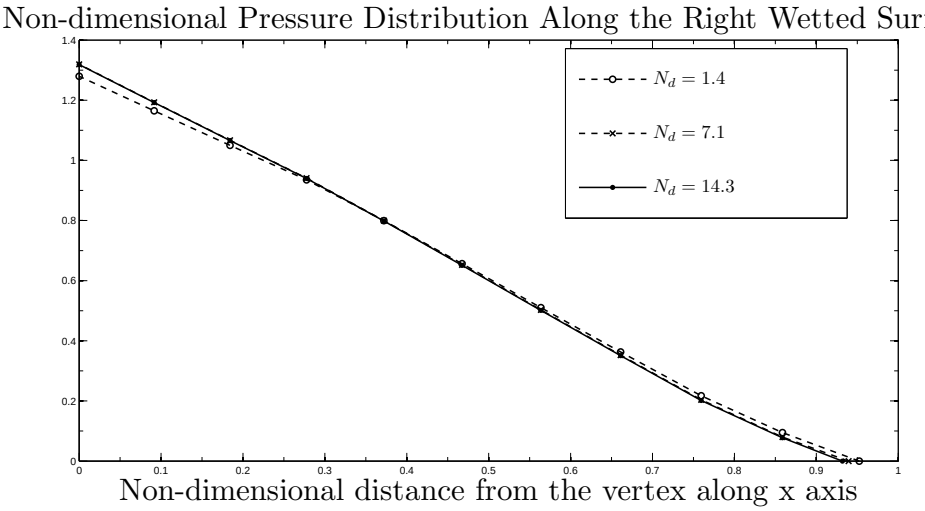

(a)

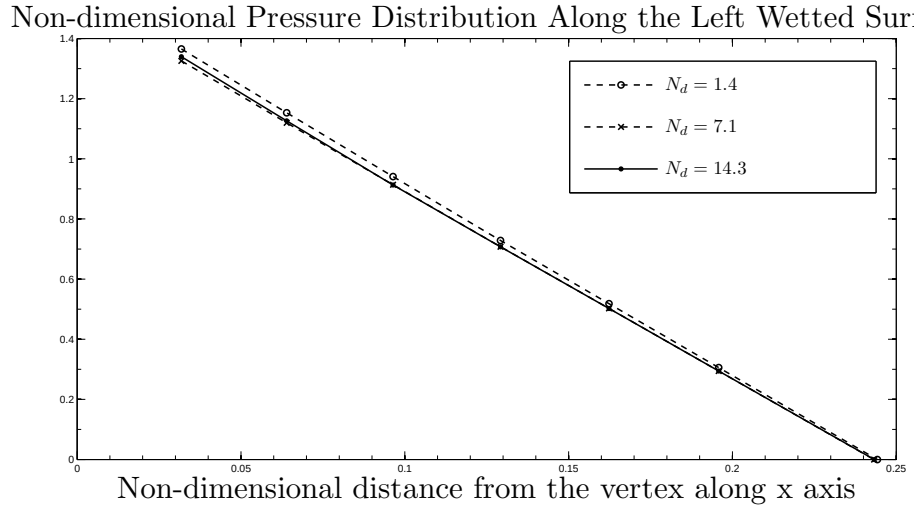

(b)

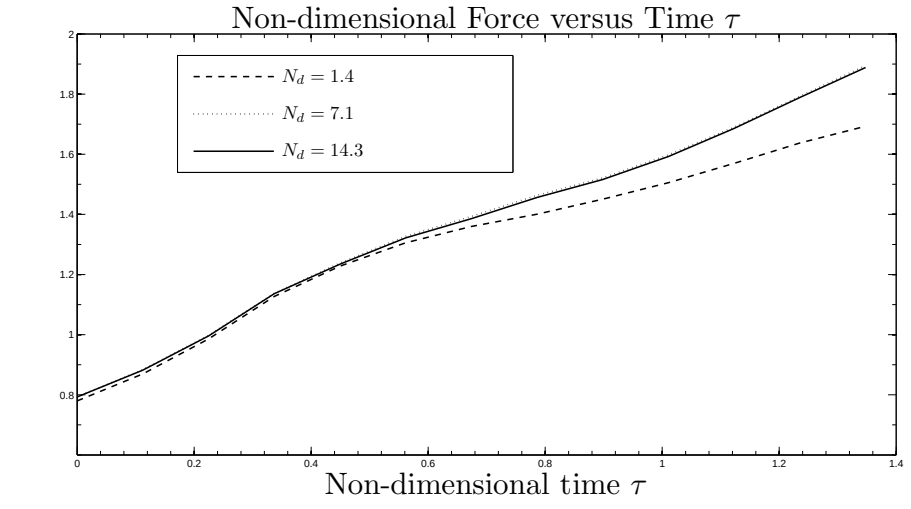

(c)

FIGURE 4.25: Finite depth effect of the asymmetric wedge AW4 submerged at a non-dimensional initial depth $\widehat{d_i} = -1$ entering with constant velocity of Froude number $F_r = 0.3$: (a) and (b) are plotted for different non-dimensional depths N_d at a non-dimensional time $\tau = 1.35$.

4.3.3 Truncated wedge entry

Control parameters for the truncated wedge shown on Fig.(4.1(c)) are the left half angle β_h, right half angle α_h, height of the wedge h, bottom width of the wedge b and the aspect ratio T_a. We produce results for the test cases given in the Table (4.3) by considering various aspect ratios T_a and wedge angles. The results for different Froude numbers of entry with constant velocity are given in section (4.3.3.1). The computed numerical results for the truncated wedges showing the time effect and finite depth effect are given in sections (4.3.3.2) and (4.3.3.3) respectively. Although vortex shedding from the corners of the body is a possibility, the results here indicate that it is less significant than for the asymmetric wedge or box (see later).

Truncated wedge (TW)	**Left angle** β_h	**Right angle** (α_h)
TW1	10^o	10^o
TW2	20^o	20^o
TW3	30^o	30^o

TABLE 4.3: Truncated wedges for entry cases

4.3.3.1 Froude number effect

To study the effect of Froude number on the results for entry of truncated wedges, we carry out a set of test cases. For a particular truncated wedge, the test process is to keep all the input variables of a specific run of the program constant, and obtain the Froude numbers by varying the velocity of the entry for the truncated wedge. We plot the results for the free-surface profile, pressure and force at the same distance traveled by the truncated wedge TW3 for different entry speeds as time progresses. The same process is repeated for the other truncated wedges considered. As we increase velocity of the entry, we can notice much more deformation on the free surface and consequently in the pressure distribution and force as shown in Fig. (4.26) for the truncated wedge TW3.

In reality for entry of bodies with a flat bottom (as in the truncated wedge and box shaped bodies - see later), compressibility effects are likely to be important in the marine context. Thus the peak pressure will be limited by the acoustic pressure $\rho_w c_w v$ where ρ_w is the density of the fluid, c_w is the speed of the sound in the fluid and v is the entry velocity of the body, see von Karman (1929). In unaviated water, the velocity of sound is approximately 800ms^{-1} but falls dramatically

in water with small bubble content which further reduces the maximum pressure that is possible for the flat bottom case, see Lundgern (1969).

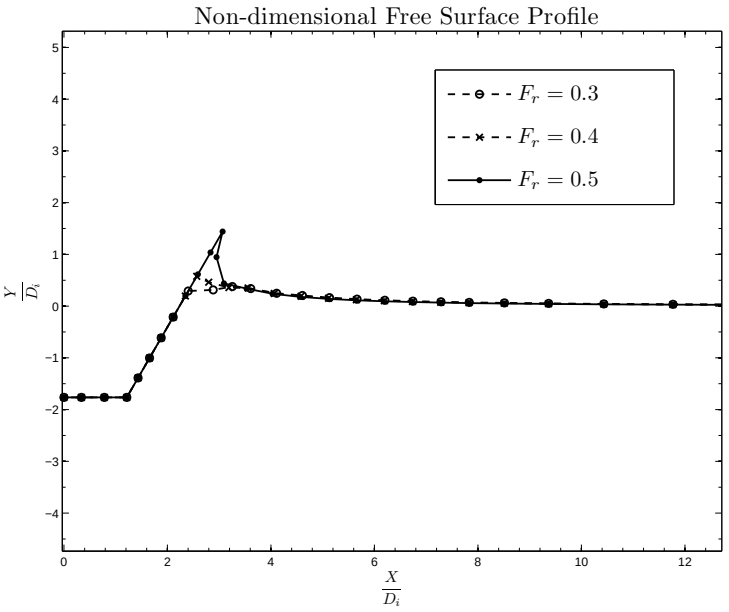

(a)

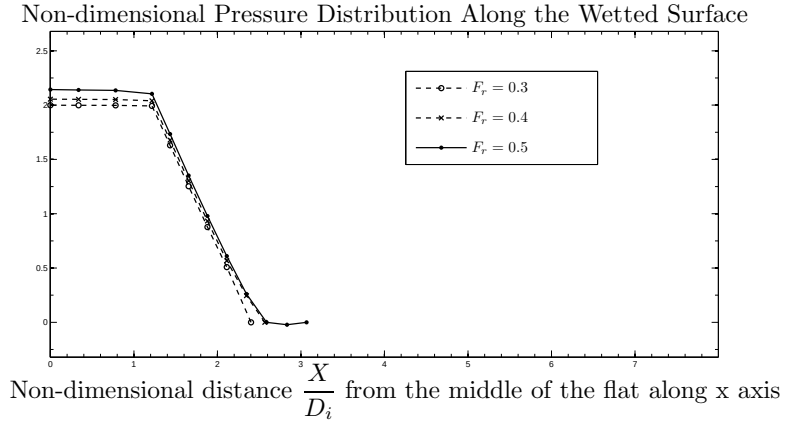

(b)

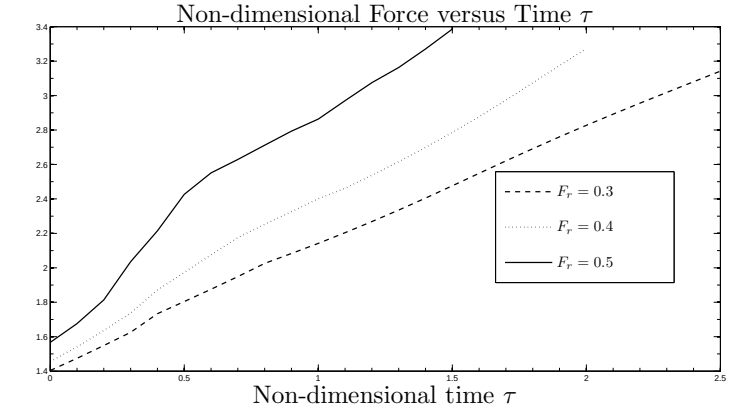

(c)

FIGURE 4.26: Froude number effect of the truncated wedge TW3 submerged at a non-dimensional initial depth $\widehat{d_i} = -1$ entering with constant velocity of different Froude numbers: (a) and (b) are plotted at a non-dimensional time $\tau = 2.5, 2, 1.5$ and distance $\widehat{d} = -1.76$.

4.3.3.2 Time effect

The motion of the truncated wedge changes as time progresses. We can compute the deformed free-surface profile, pressure along the wetted part of the body and the upward force experienced by the body using the non-linear theory. The computed results showing time effect on free surface, pressure and force at different stages of the entry of the truncated wedges with constant velocity are presented in this section. Figs. (4.27) to (4.28) show the time effect of the truncated wedge TW3 entering with Froude number of 0.5.

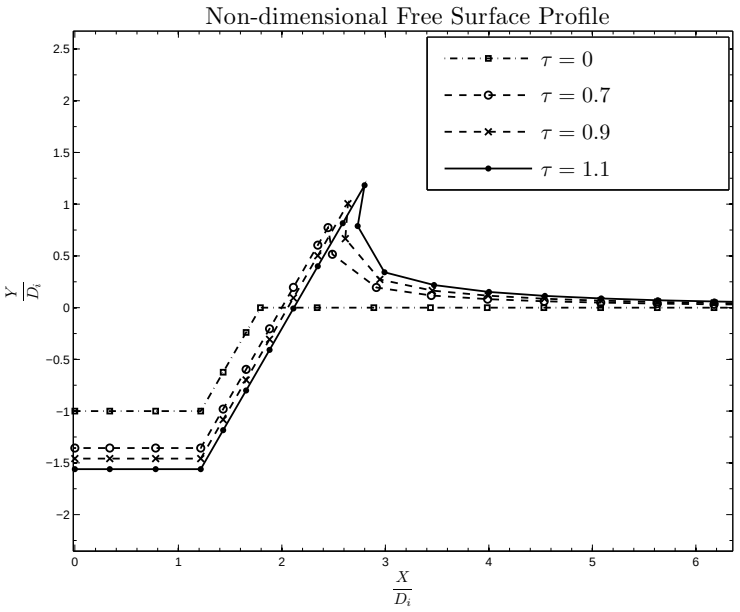

(a)

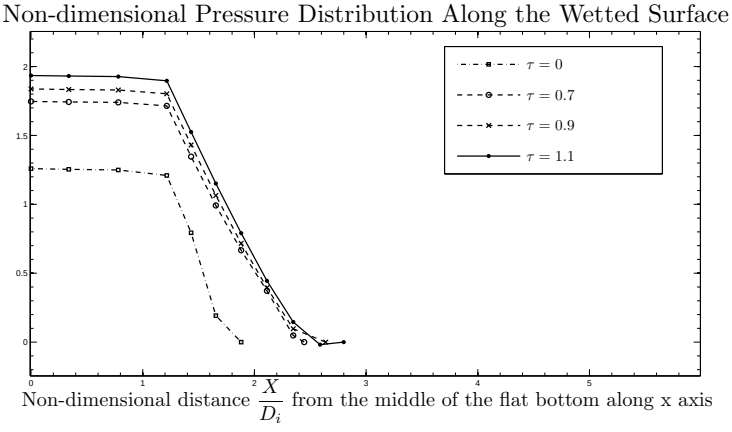

(b)

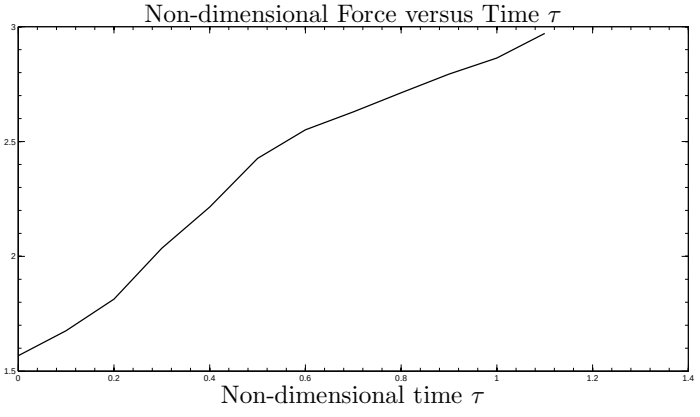

(c)

FIGURE 4.27: Time effect of the truncated wedge TW3 submerged at a non-dimensional initial depth $\widehat{d_i} = -1$ entering with constant velocity of Froude number $F_r = 0.5$: (a) and (b) are plotted at different non-dimensional times τ.

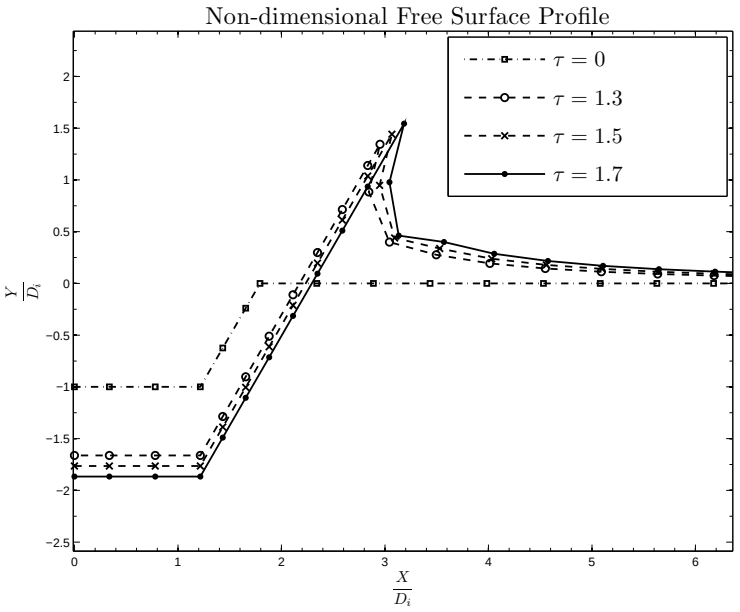

(a)

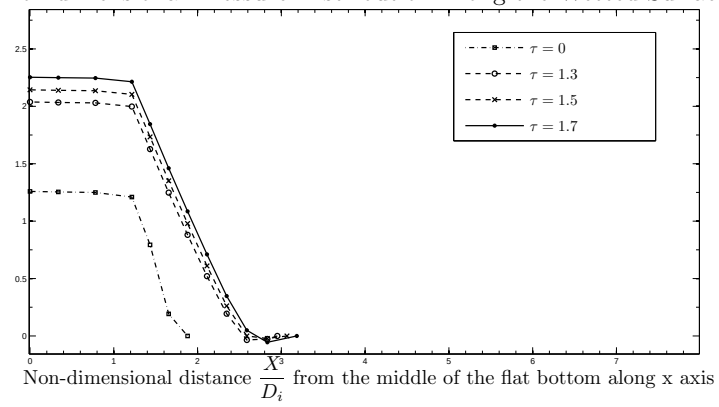

(b)

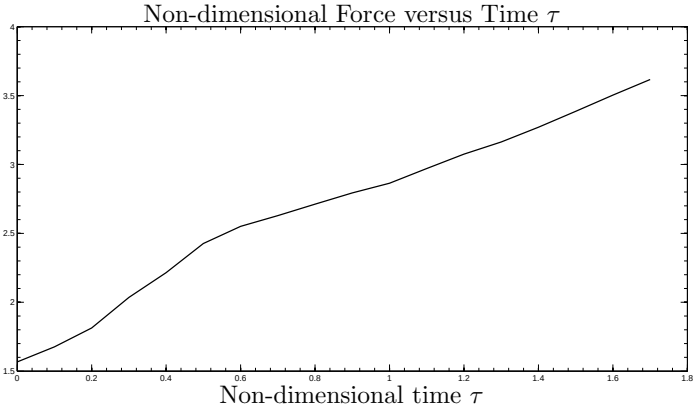

(c)

FIGURE 4.28: Time effect of the truncated wedge TW3 submerged at a non-dimensional initial depth $\widehat{d_i} = -1$ entering with constant velocity of Froude number $F_r = 0.5$: (a) and (b) are plotted at different non-dimensional times τ.

4.3.3.3 Finite depth effect

We present results showing finite depth effect on the free-surface profile, pressure and force due to the change in depth of the entry of truncated wedges with constant velocity using the non-linear time-stepping method. The results are plotted at the same distance close to the bottom surface (seabed) moved by the truncated wedge for different depths of entry with the same velocity as it moves with time. Fig. (4.29) represents the computed free-surface profile, pressure distribution and force for the truncated wedge TW3 entering with Froude number 0.5 showing the finite depth effect on the motion. We notice, as expected, that for entry of the truncated wedge TW3 a non-dimensional depth N_d below 2.55 experiences a greater difference in the free-surface deformation, pressure and force than that of other depths.

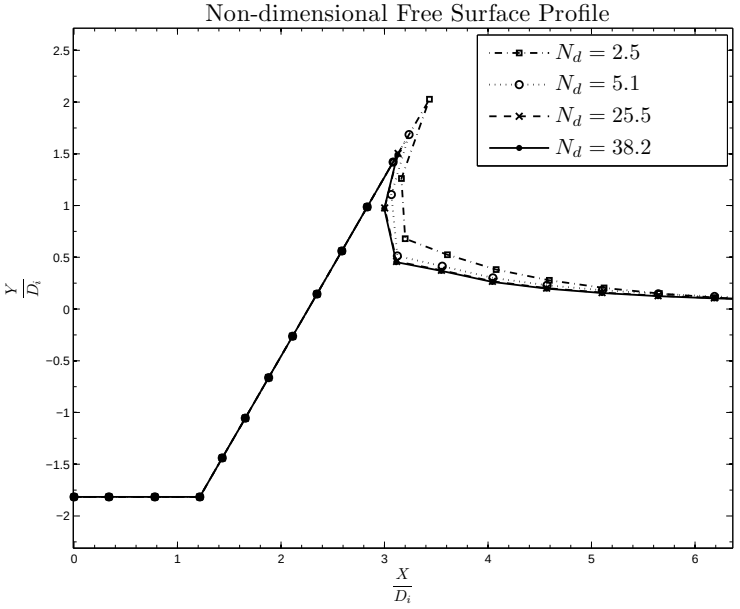

(a)

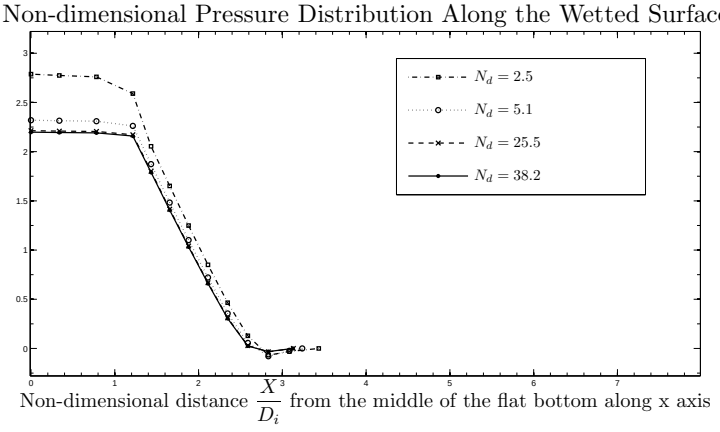

(b)

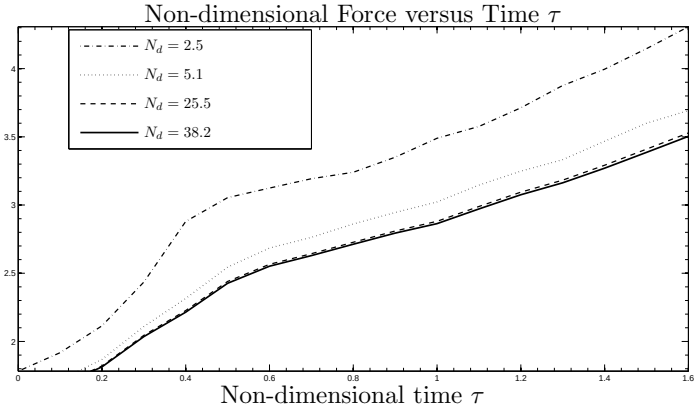

(c)

FIGURE 4.29: Finite depth effect of the truncated wedge TW3 submerged at a non-dimensional initial depth $\widehat{d_i} = -1$ entering with constant velocity of Froude number $F_r = 0.5$: (a) and (b) are plotted for different non-dimensional depths N_d at a non-dimensional time $\tau = 1.6$.

4.3.4 Box entry

As in the previous sections, the control parameter for a box body as geometrically sketched in Fig.(4.1(d)) is the aspect ratio R_a which is the ratio of the initial depth to the width of the box. We can produce more results, but, for simplicity, we present some results showing Froude number effect and time effect on the motion of the box BX1 with the aspect ratio 0.5 as explained in the previous sections for other shapes. The results for different Froude numbers of entry with constant velocity are given in section (4.3.4.1). The computed numerical results for the box body showing the time effect and finite depth effect in sections (4.3.4.2) and (4.3.4.3) respectively. As for the asymmetric wedge we can expect vortices to be shed from the sharp corners. Hence the pressures near those corners are not reliable in these calculations, but may form a basis for comparisons with future work.

4.3.4.1 Froude number effect

To study the effect of Froude number on the results for the entry of the box, we carry out a set of test cases. For a particular box, the test process is to keep all the input variables of a specific run of the program constant, and obtain the Froude numbers by varying the velocity of the entry for the box. We plot the results for the free-surface profile, pressure and force at the same distance traveled by the box for different entry speeds as time progresses. The same process is repeated for the data sets and for the box considered. As we increase velocity of the entry, we can notice much more deformation on the free surface and consequently in the pressure distribution and force as shown in Fig. (4.30) and (4.31) for the box BX1.

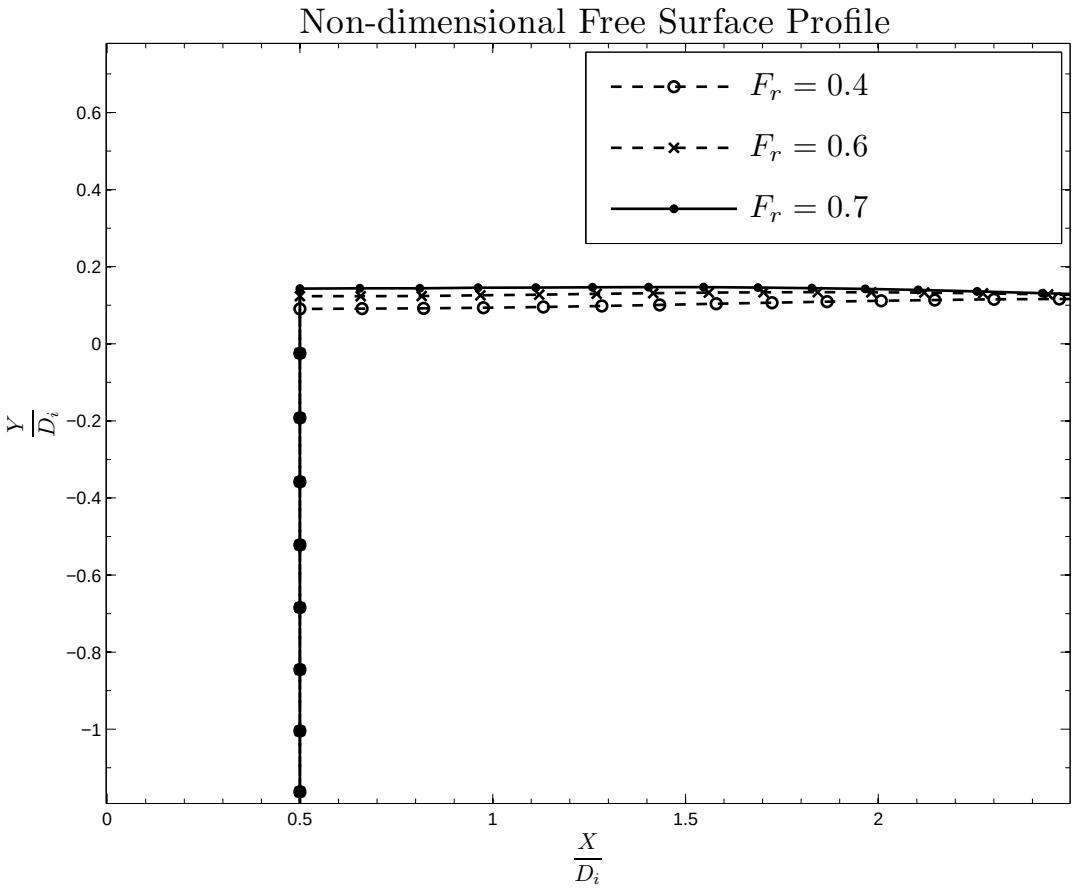

(a)

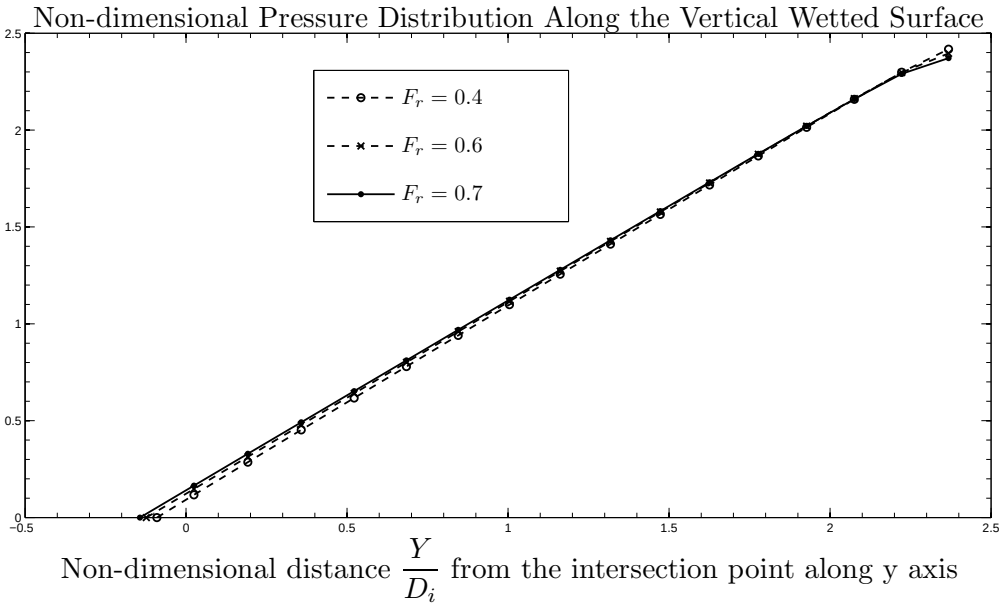

(b)

FIGURE 4.30: This figure shows the Froude number effect of the box BX1 submerged at a non-dimensional initial depth $\widehat{d_i} = -1$ entering with constant velocity of different Froude numbers: (a) and (b) are plotted at different non-dimensional times $\tau = 3.38, 263, 2.25$ and distance $\widehat{d} = -2.51$.

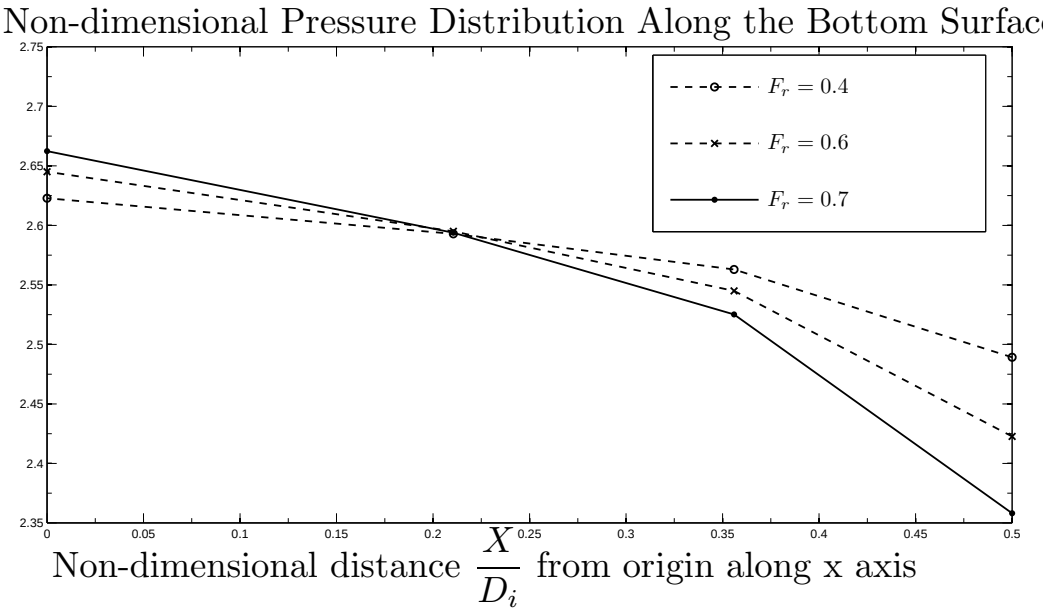

(a)

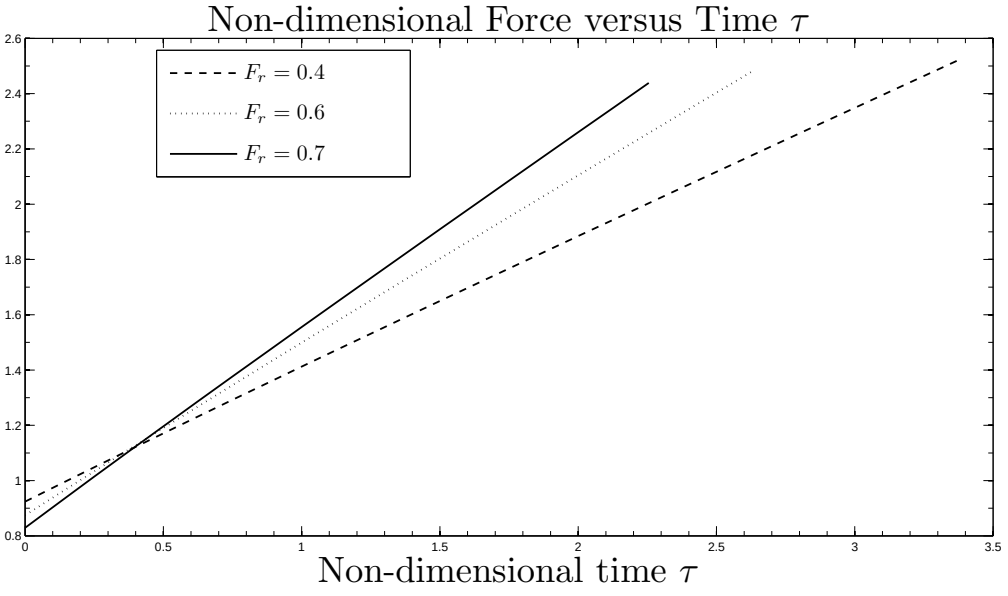

(b)

FIGURE 4.31: Froude number effect of the box BX1 submerged at a non-dimensional initial depth $\widehat{d_i} = -1$ entering with constant velocity of different Froude numbers: (a) is plotted at different non-dimensional time $\tau = 3.38, 263, 2.25$ and distance $\widehat{d} = -2.51$.

4.3.4.2 Time effect

The motion of the box changes as time progresses. We can compute the deformed free-surface profile, pressure along the wetted part of the box and the upward force experienced by the box using the non-linear theory. The computed results showing time effect on free surface, pressure and force at different stages of the entry of the box with constant velocity are presented in this section. Fig. (4.32) and (4.33) show time effect of the box BX1 entering with Froude number of 0.7.

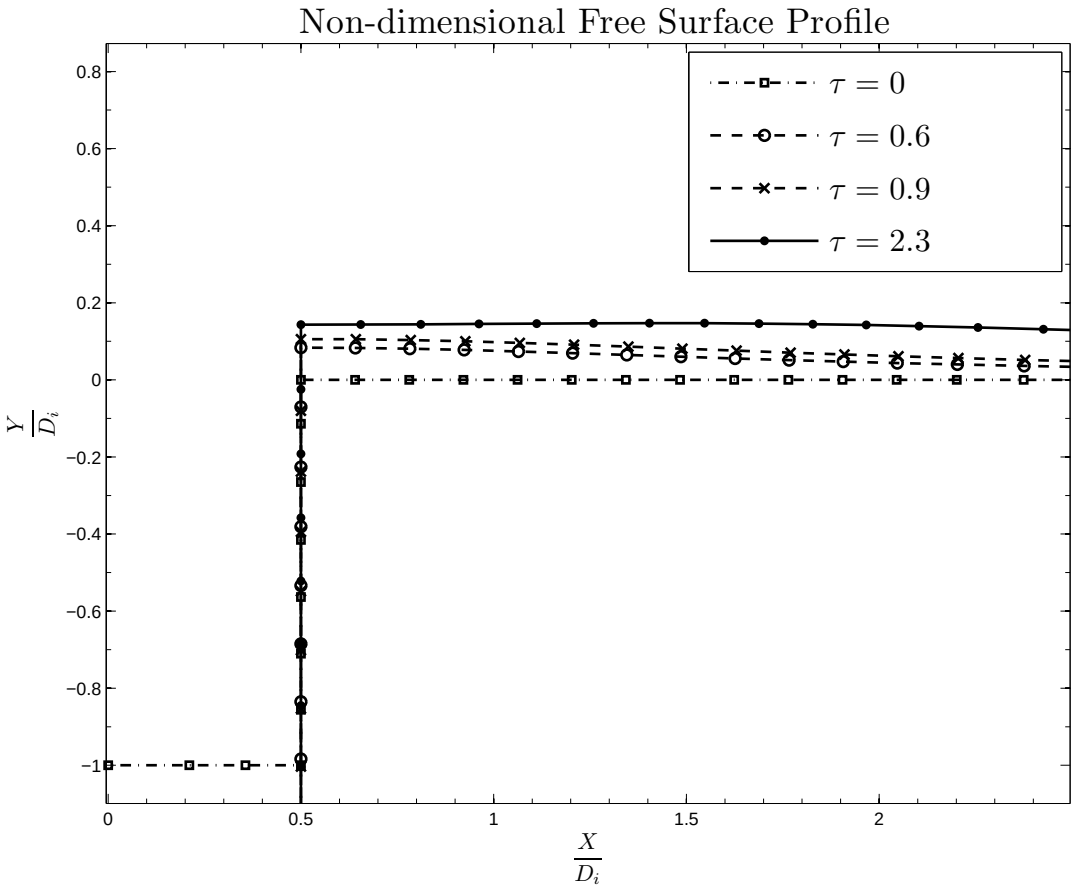

(a)

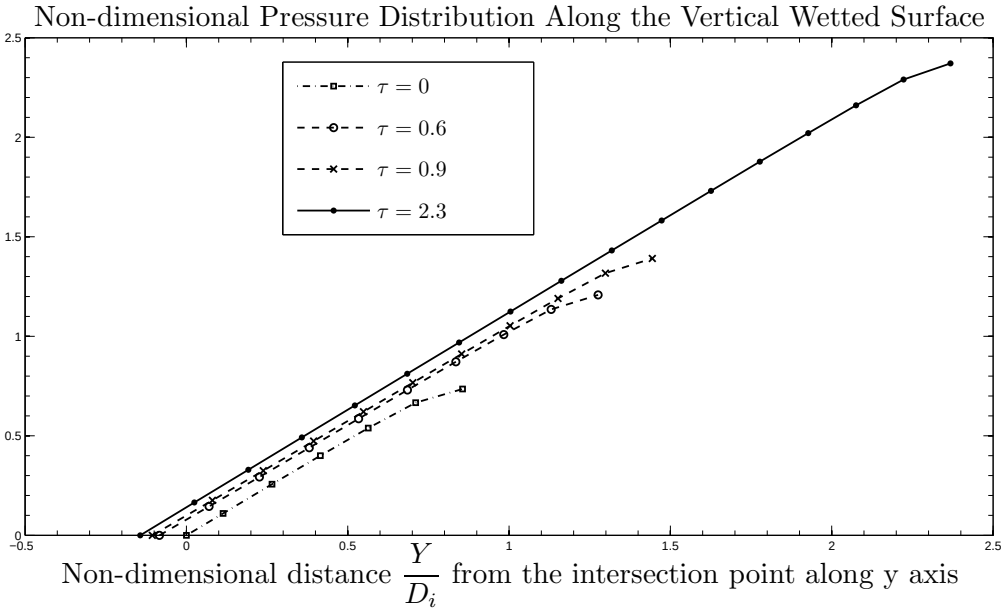

(b)

FIGURE 4.32: Time effect of the box BX1 submerged at a non-dimensional initial depth $\widehat{d_i} = -1$ entering with constant velocity of Froude number $F_r = 0.7$: (a) and (b) are plotted at different non-dimensional times τ.

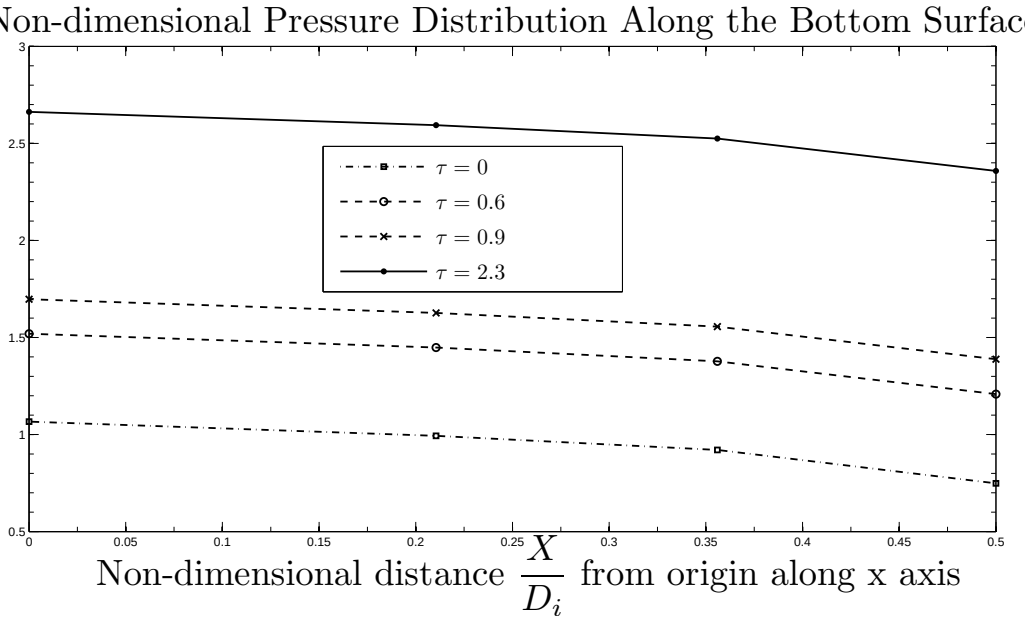

(a)

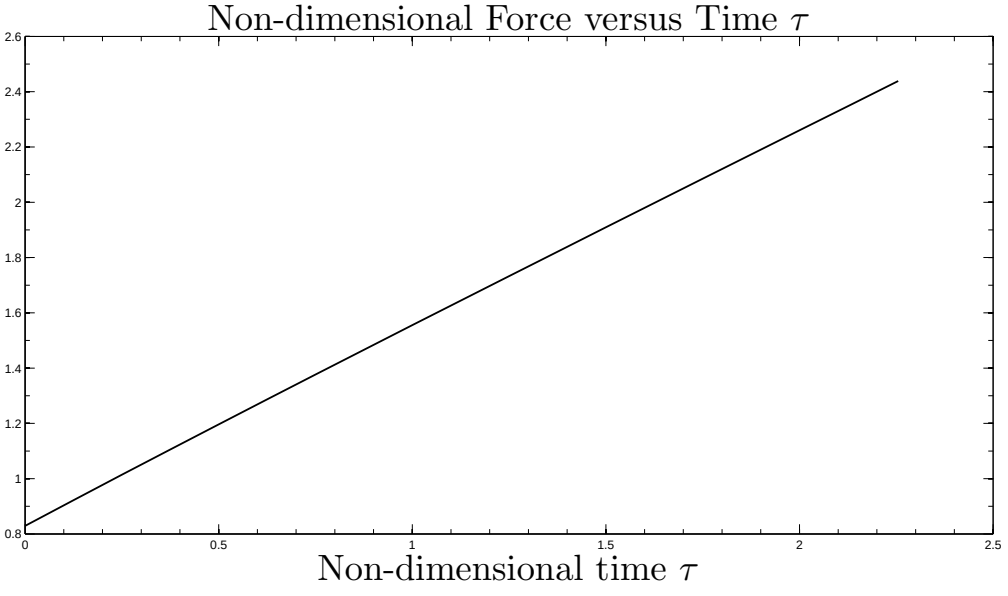

(b)

FIGURE 4.33: Time effect of the box BX1 submerged at a non-dimensional initial depth $\widehat{d}_i = -1$ entering with constant velocity of Froude number $F_r = 0.7$: (a) is plotted at different non-dimensional times τ.

4.3.4.3 Finite depth effect

We present results showing the effect on the free-surface profile, pressure and force due to the change in depth of the entry of the box with constant velocity. The results are plotted at the same distance close to the bottom surface (seabed) for different depths of entry with the same velocity as it moves with time. Fig. (4.34) and (4.35) present the computed free-surface profile, pressure distribution and force for the box BX1 entering with Froude number 0.7 showing finite depth effect on the motion. We notice, as expected, that for entry of the box BX1 a non-dimensional depth N_d below 1.5 experiences a greater difference in the free-surface deformation, and a very much greater difference in the pressure and force than that of other depths. Such effects are likely to be real but their accurate computation would need to include vortex shedding at the box corners, so we do not pursue this further here.

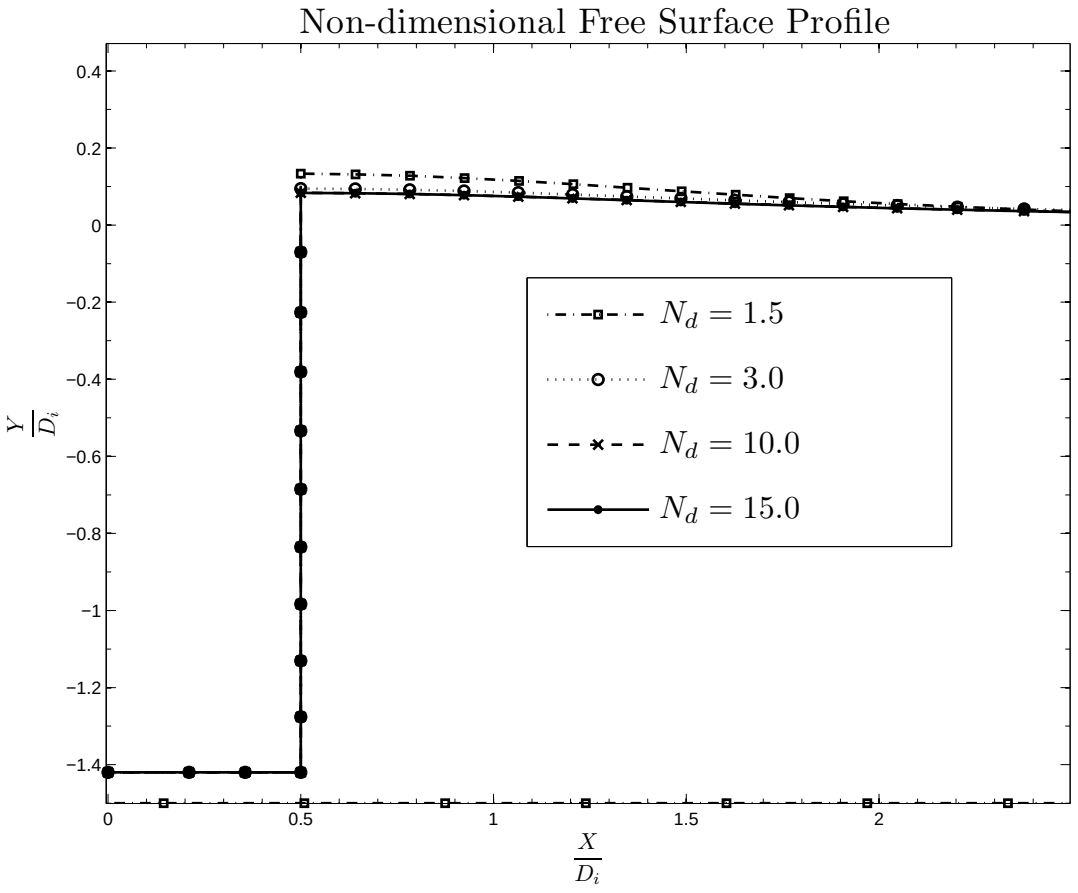

(a)

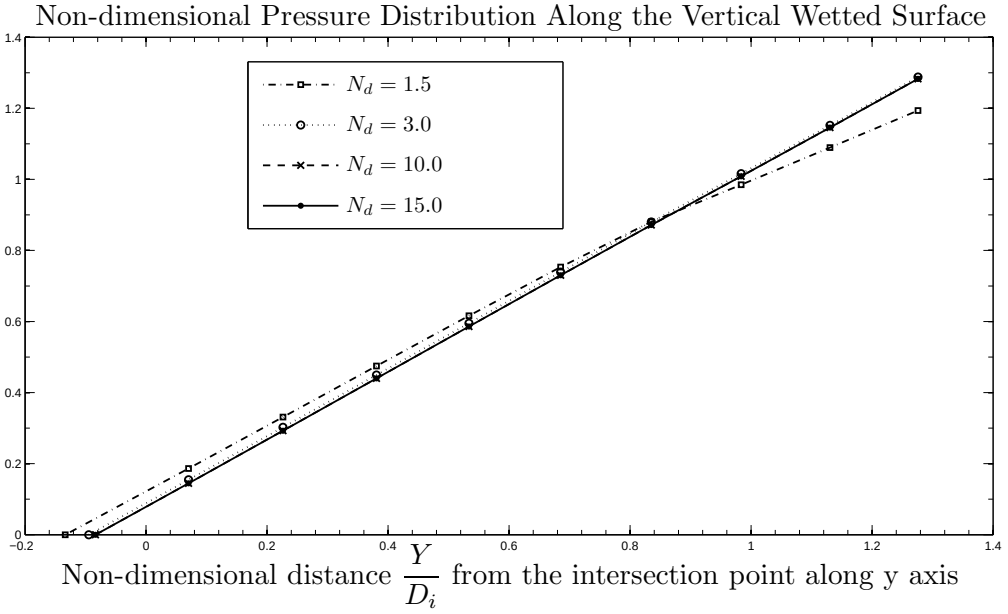

(b)

FIGURE 4.34: Finite depth effect of the box BX1 submerged at a non-dimensional initial depth $\widehat{d_i} = -1$ entering with constant velocity of Froude number $F_r = 0.7$: (a) and (b) are plotted for different non-dimensional depths N_d at a non-dimensional time $\tau = 0.63$.

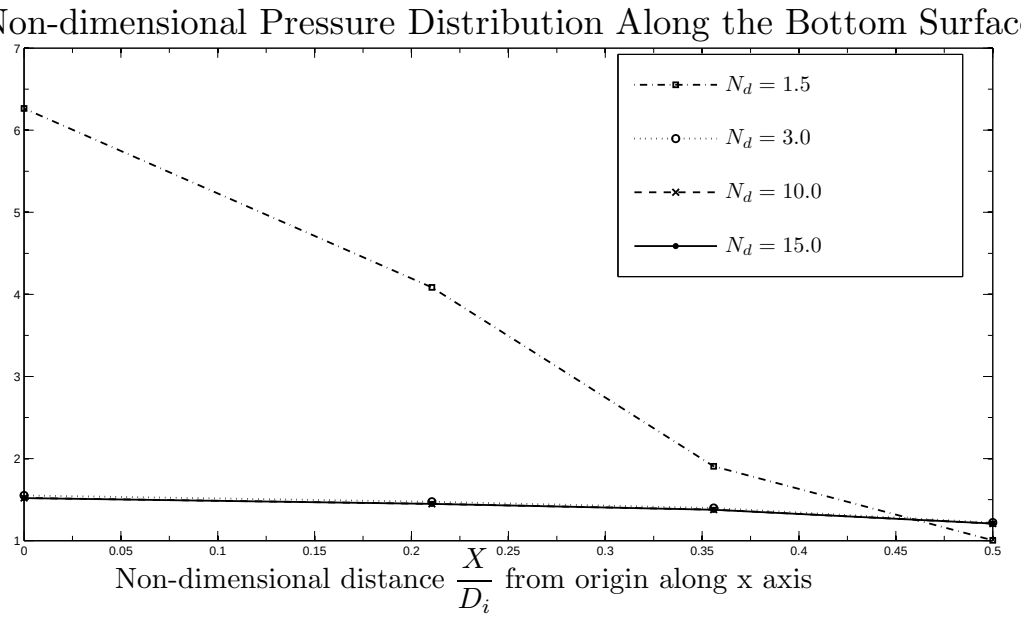

(a)

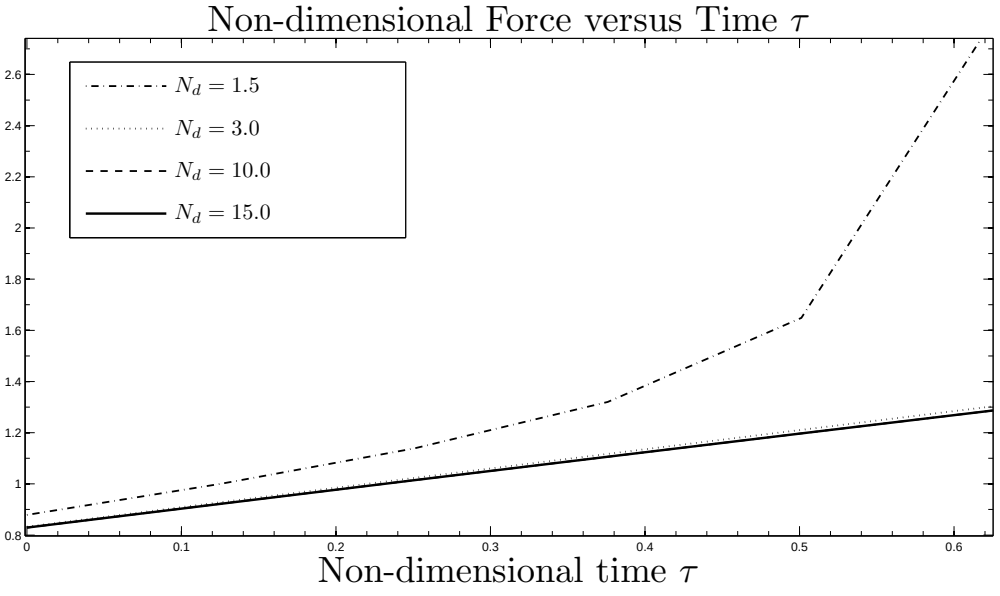

(b)

FIGURE 4.35: Finite depth effect of the box BX1 submerged at a non-dimensional initial depth $\widehat{d_i} = -1$ entering with constant velocity of Froude number $F_r = 0.7$: (a) is plotted for different non-dimensional depths N_d at a non-dimensional time $\tau = 0.63$.

4.4 Constant acceleration entry

This section, for constant acceleration entry of symmetric wedges, asymmetric wedges, truncated wedges and box bodies, reviews the application of the non-linear theory and shows numerical results. For each shape shown in Fig. (4.1), we present computed free-surface profile, pressure distribution along the wetted part of the body and total force experienced by the body as it enters through the free surface with constant acceleration. The symmetric wedges, asymmetric wedges, truncated wedges and boxes entering with constant acceleration are presented in section (4.3.1), (4.3.2), (4.3.2) and (4.3.4) respectively. We note that the comments about vortex shedding given in section (4.3) for constant velocity entry will still apply. However, for small time the velocity is small. So at least then, vortex shedding will be less significant.

4.4.1 Symmetric wedge entry

We present numerical results computed using the non-linear time-stepping method for the each symmetric wedge, as considered in the constant velocity entry. The test cases considered for the symmetric wedges entering with constant acceleration are explained in this section. For the symmetric wedges entering with constant acceleration, results showing time effect on the stages of the motion with constant acceleration are presented in section (4.4.1.1). The result of changing acceleration and the comparison of numerical force with the analytical added mass force is given in section (4.4.1.2) and (4.4.1.3) respectively.

4.4.1.1 Time effect

The time effects on free-surface profile, pressure distribution and total force are computed for the symmetric wedges considered, as for the constant velocity cases. The plots are obtained for different time intervals of entry with constant acceleration. The length of time interval for each symmetric wedge depends on the angle of the symmetric wedges and the acceleration of the entry. For each specific interval, the results are plotted at different times. Fig. (4.36) and (4.37) show the time effect of the symmetric wedge SW3 entering with the non-dimensional constant acceleration G_τ=1, whereas Fig. (4.38) and (4.39), and Fig. (4.40) and

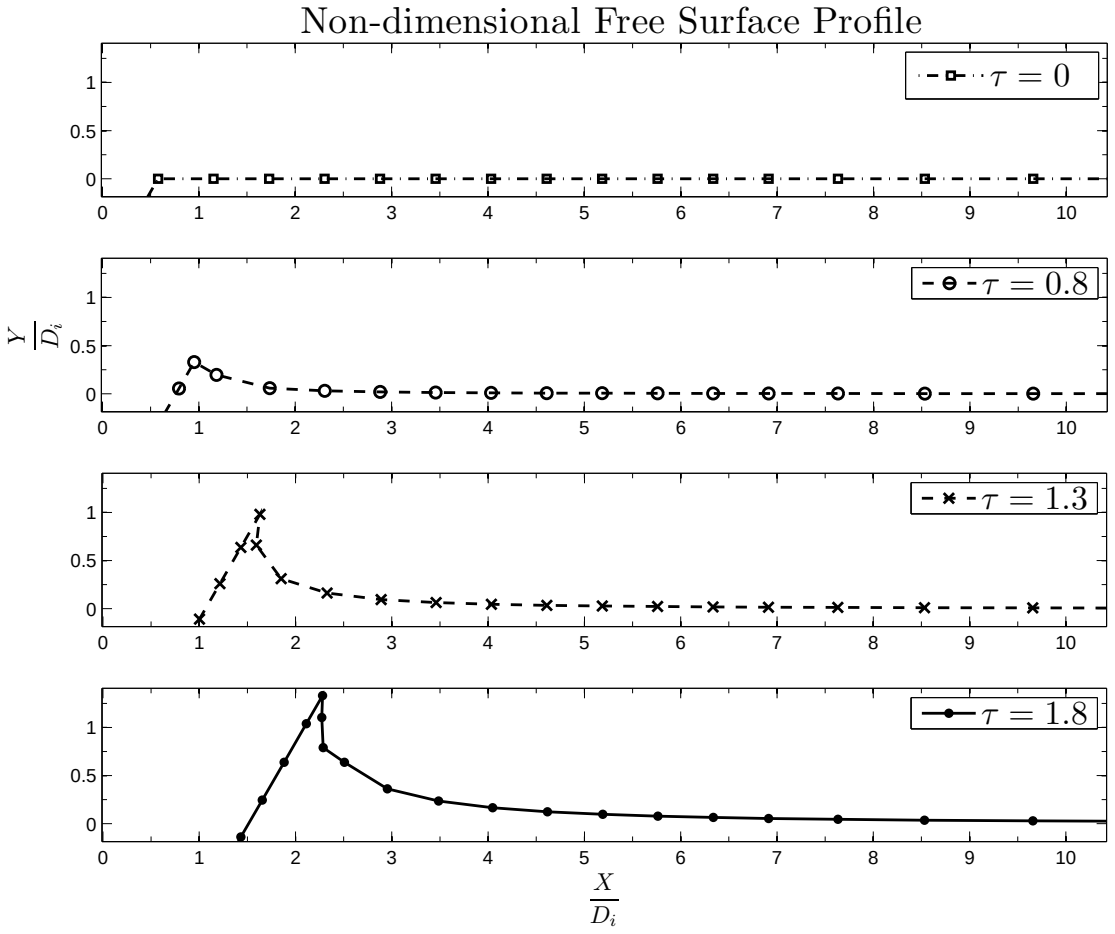

(a)

FIGURE 4.36: Time effect of the symmetric wedge SW30 submerged at a non-dimensional initial depth $\widehat{d}_i = -1$ entering with constant acceleration $G_\tau = 1$: plotted at different non-dimensional times τ.

(4.41) are for the wedge entering with the non-dimensional constant acceleration G_τ=0.5 and 0.2 respectively.

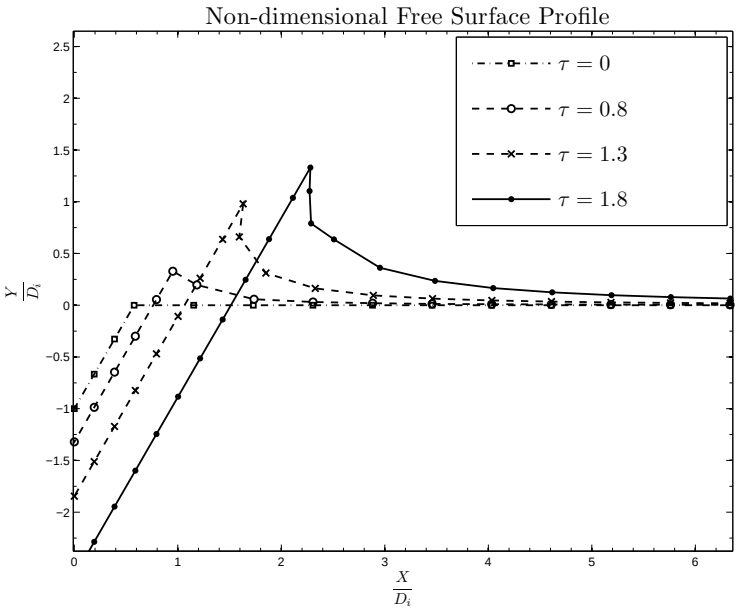

(a)

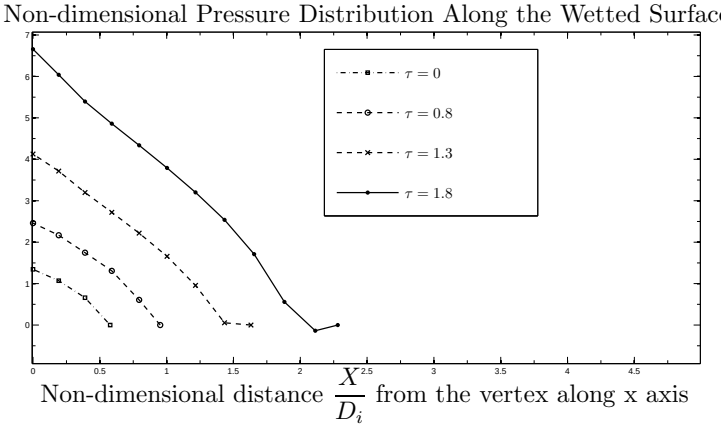

(b)

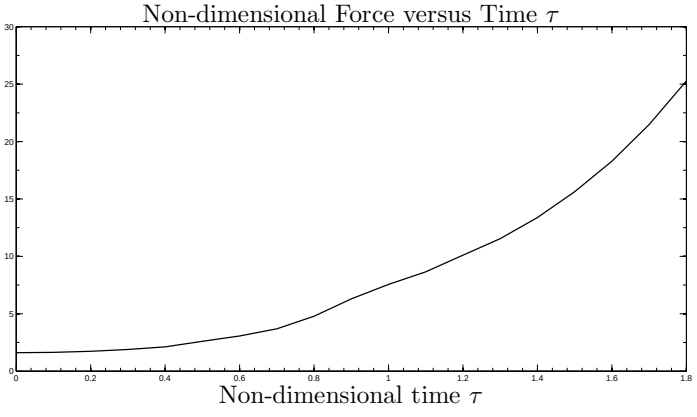

(c)

FIGURE 4.37: Time effect of the symmetric wedge SW30 submerged at a non-dimensional initial depth $\widehat{d}_i = -1$ entering with constant acceleration $G_\tau = 1$: (a) and (b) are plotted at different non-dimensional times τ.

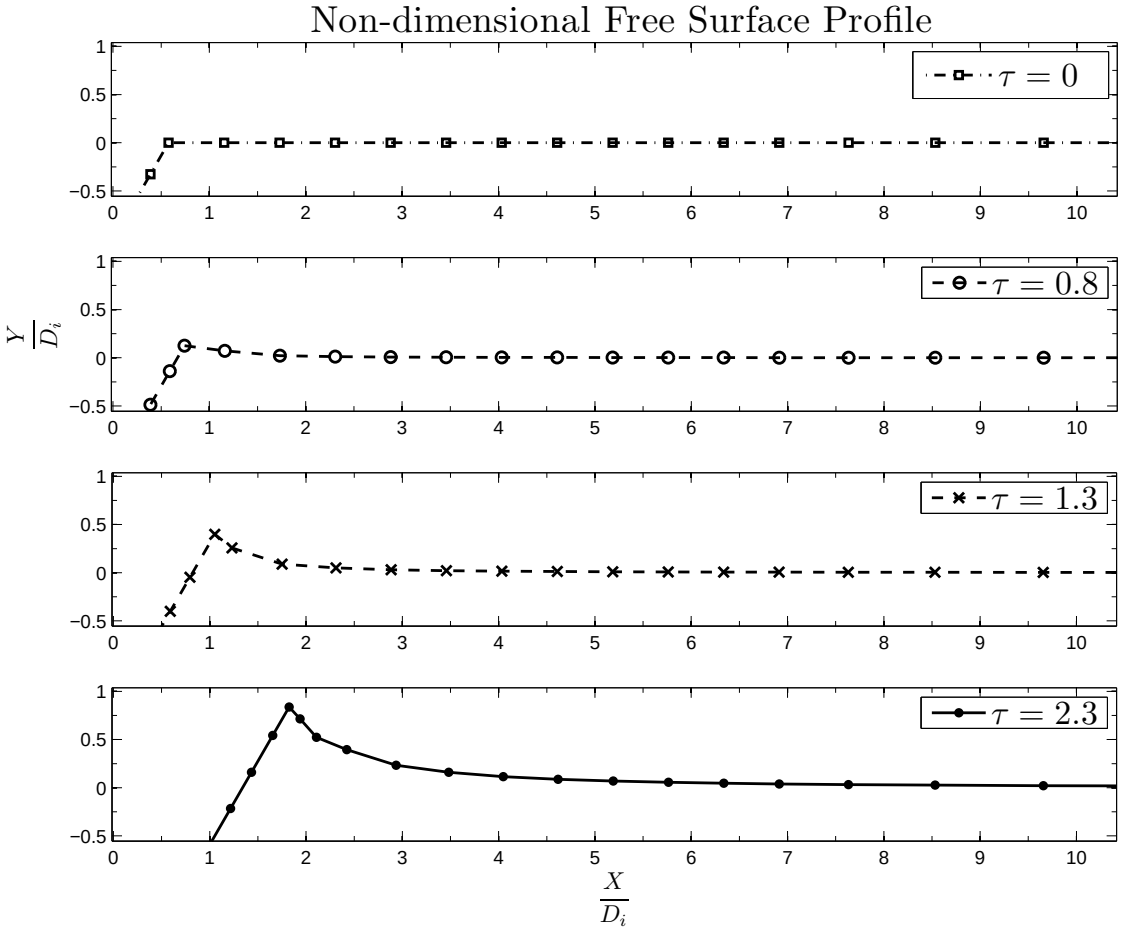

(a)

FIGURE 4.38: Time effect of the symmetric wedge SW30 submerged at a non-dimensional initial depth $\widehat{d_i} = -1$ entering with constant acceleration $G_\tau = 0.5$: plotted at different non-dimensional times τ.

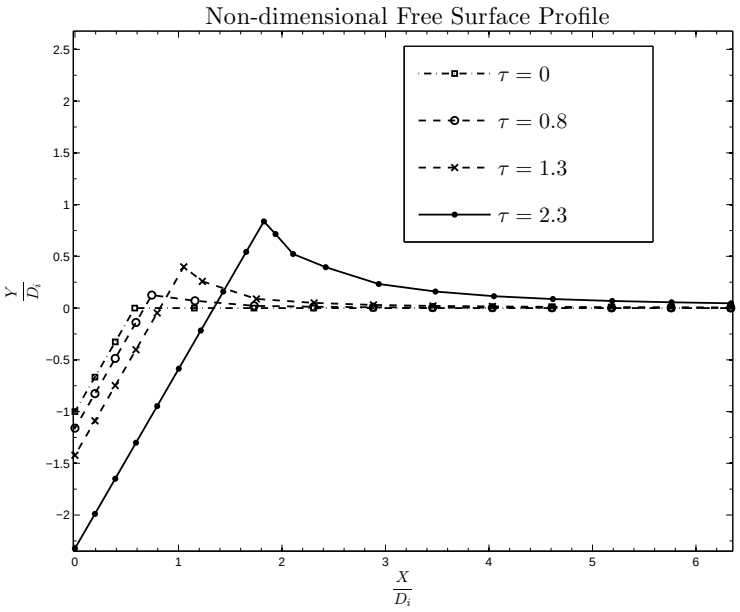

(a)

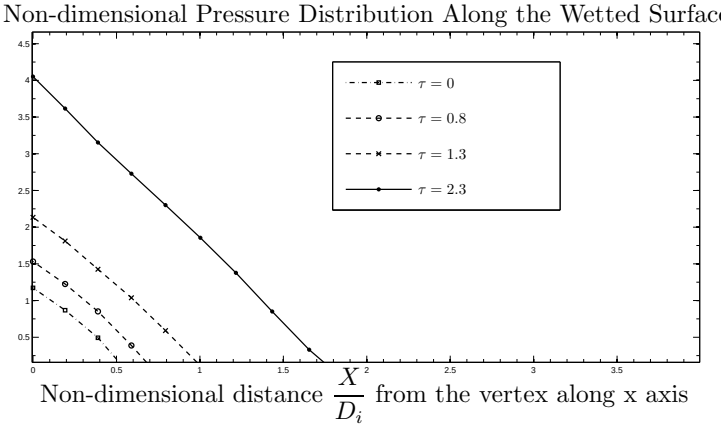

(b)

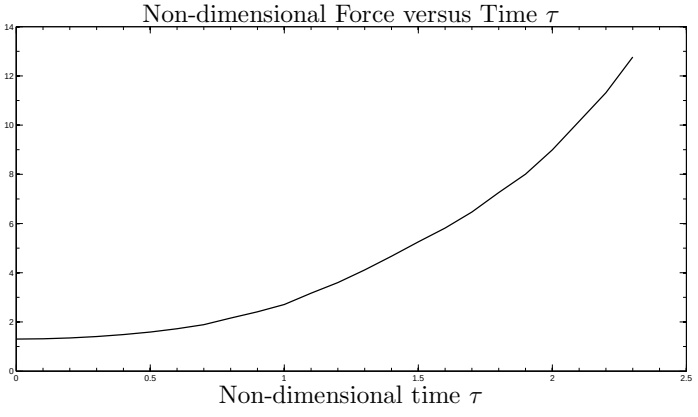

(c)

FIGURE 4.39: Time effect of the symmetric wedge SW30 submerged at a non-dimensional initial depth $\widehat{d_i} = -1$ entering with constant acceleration $G_\tau = 0.5$: (a) and (b) are plotted at different non-dimensional times τ.

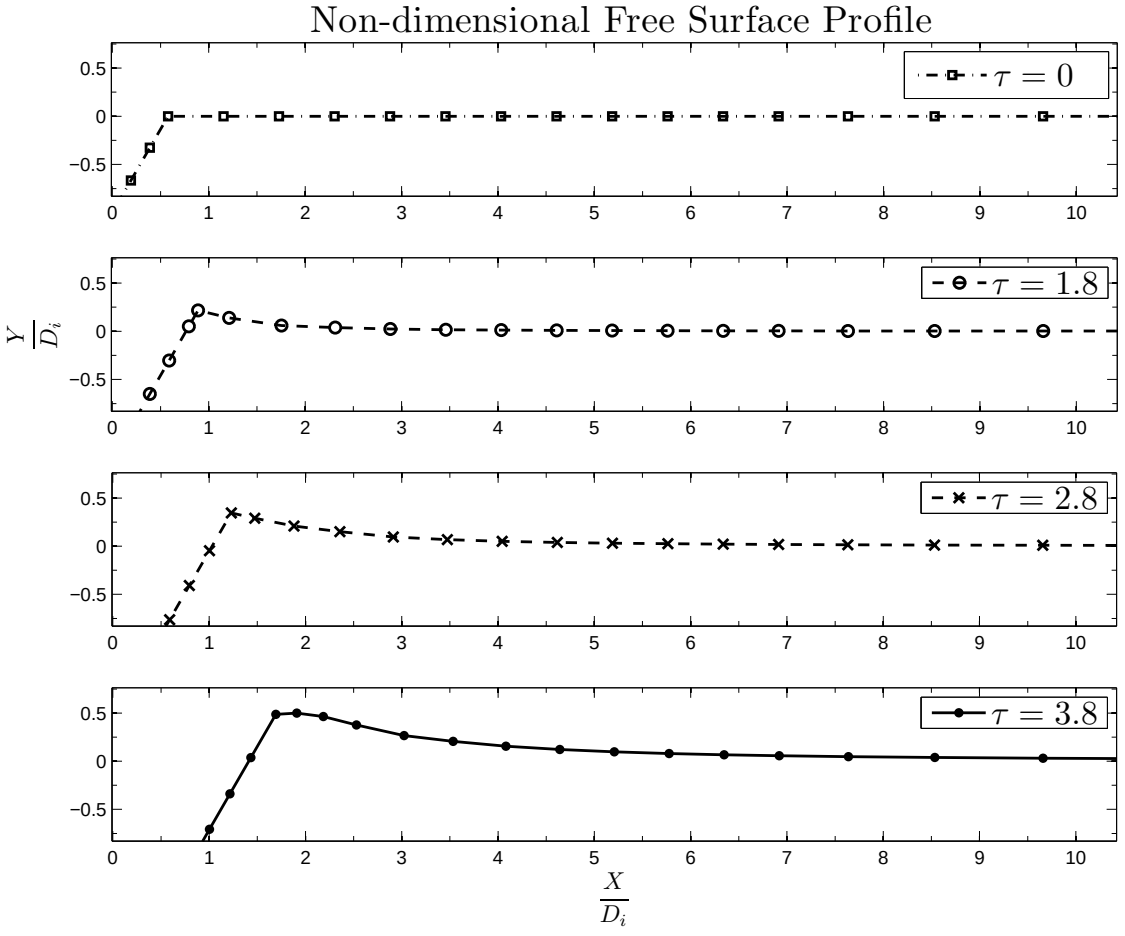

(a)

FIGURE 4.40: Time effect of the symmetric wedge SW30 submerged at a non-dimensional initial depth $\widehat{d_i} = -1$ entering with constant acceleration $G_\tau = 0.2$: plotted at different non-dimensional times τ.

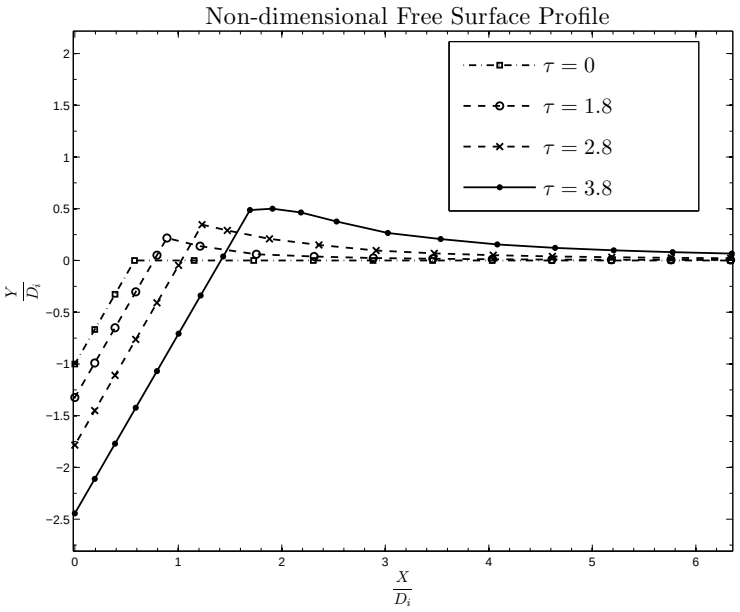

(a)

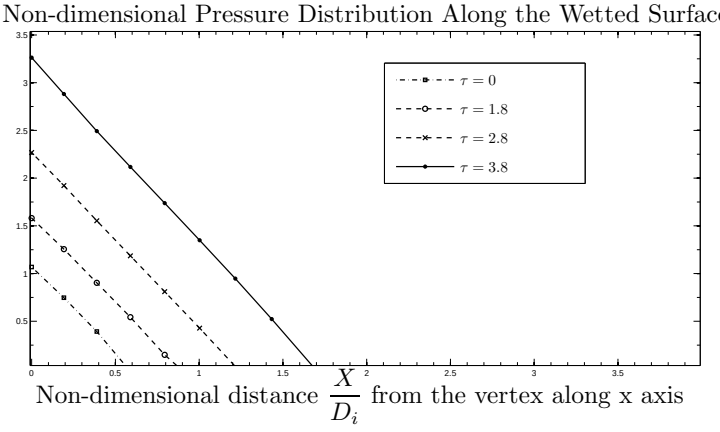

(b)

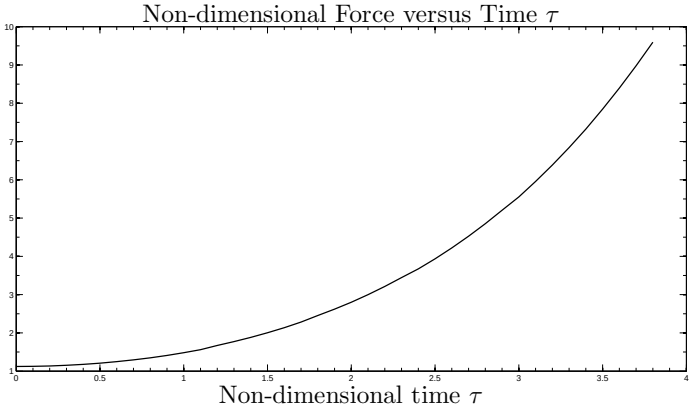

(c)

FIGURE 4.41: Time effect of the symmetric wedge SW30 submerged at a non-dimensional initial depth $\widehat{d_i} = -1$ entering with constant acceleration $G_\tau = 0.2$: (a) and (b) are plotted at different non-dimensional times τ.

4.4.1.2 Acceleration effect

This section for constant acceleration entry of the symmetric wedges presents computed numerical results for free-surface profile, pressure distribution and total force. The results are obtained by running the program with different constant accelerations while attaining the same distance traveled by the symmetric wedges. Fig. (4.42) shows the acceleration effect of the symmetric wedge SW30 entering with different accelerations.

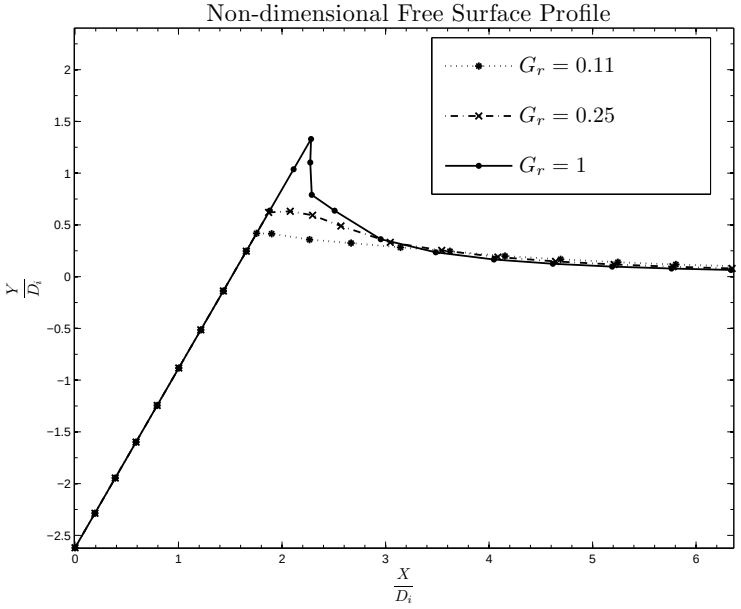

(a)

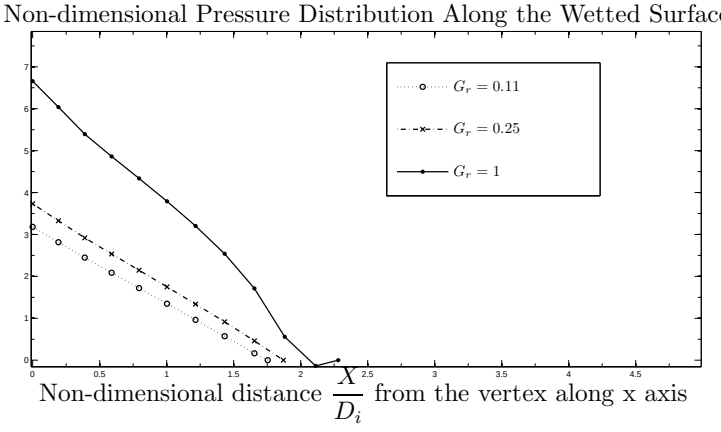

(b)

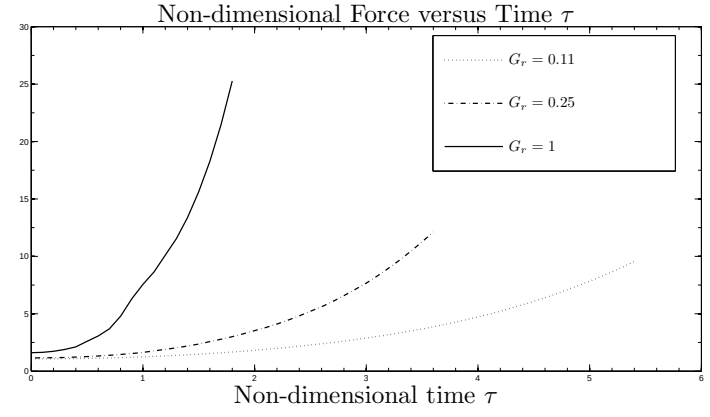

(c)

FIGURE 4.42: Acceleration effect of the symmetric wedge SW30 submerged at a non-dimensional initial depth $\widehat{d_i} = -1$ entering with different constant accelerations G_τ: (a) and (b) are plotted at a non-dimensional time $\tau = 5.4, 3.6, 1.8$ and distance $\widehat{d} = -2.62$.

4.4.1.3 Added mass effect

In an unbounded fluid, particles near to a moving body are accelerated due to the motion executed by the body. The body experiences a great amount of hydrostatic and hydrodynamic pressure on it due to the interaction between the fluid and the body which oppose the motion of the body. These are integrated to calculate total hydrostatic and hydrodynamic forces. The hydrodynamic forces can be thought of in terms of some amount of fluid mass that moves with the body as an added mass (m_a). The motion of the system of the fluid and body can be predicted using Lagrangian dynamics, see Barringer (1996) for more details.

The model we use here takes advantage of the fact that at t=0, the flat free surface is a line of equipotential $\phi = 0$. Thus for heave motion, the fluid flow is initially that in the lower half plane of a double body i.e. a diamond shape of the wedge and it is reflected the free surface, see Newman (1977). This makes it possible to deduce the added masses of the various body shapes moving in heave. In the usual seakeeping theories, this added mass is simply the high-frequency limit of the radiation problem.

In this section, we derive the equation of the system of the fluid and body, the analytical added-mass force for a symmetric wedge and a box body, as explained by Barringer (1996). Then the analytical force is compared with the force difference between the total numerical force computed using the nonlinear theory of Vinje and Bervig (1981a; 1981b) and the buoyancy force, to verify that the forces agree at initial time t=0. The buoyancy force is simply that of the body below the still water line y=0, not the instantaneous water line which is not known a priori.

The equation for the motion of the system of water and the body consists of the hydrostatic force (F_b, buoyancy force) and the hydrodynamic force (F_a, added mass force). The buoyancy force is given by

$$F_b = \rho_w g \forall(t), \tag{4.9}$$

where ρ_w is the fluid density, g is gravitational acceleration, and $\forall(t)$ is submerged volume of the instantaneous portion of the body below the undisturbed free surface level at $y = 0$ and a time t .

The added mass force can be defined from the energy of the system of the fluid and body. The kinetic energy is written as

$$T = \frac{1}{2}(m_a + m_b)v^2. \tag{4.10}$$

The potential energy can be given as

$$V = \int_{-y}^{0} (\rho_w g \forall - m_b g) dy = (\rho_w g \forall - m_b g) y. \tag{4.11}$$

The total energy L of the system is simply sum of the kinetic energy T and the potential energy V:

$$L = T + V = \frac{1}{2}(m_a + m_b)\dot{y}^2 + (\rho_w g \forall - m_b g) y. \tag{4.12}$$

Now we can apply the Lagrange's equation for the motion of the system in a single degree of freedom (vertical motion of the body in heave mode):

$$\frac{\partial L}{\partial y} - \frac{d}{dt}\left(\frac{\partial L}{\partial y}\right) = 0. \tag{4.13}$$

By using Eq. (4.12) and Eq. (4.13), we get

$$\frac{\partial L}{\partial y} - \frac{d}{dt}\left(\frac{\partial L}{\partial y}\right) = \frac{1}{2}\frac{dm_a}{dz}\dot{y}^2 + (\rho_w g \forall - m_b g) - \frac{d}{dt}\left(\frac{1}{2}(m_a + m_b)2\dot{y}\right), \tag{4.14}$$

and

$$\frac{d}{dt}\left(\frac{1}{2}(m_a + m_b)2\dot{y}\right) = (m_a + m_b)\ddot{y} + \frac{dm_a}{dy}\frac{dy}{dt}\dot{y} = (m_a + m_b)\ddot{y} + \frac{dm_a}{dy}\dot{y}^2. \tag{4.15}$$

We find

$$\frac{\partial L}{\partial y} - \frac{d}{dt}\left(\frac{\partial L}{\partial y}\right) = -\frac{1}{2}\frac{dm_a}{dy}\dot{y}^2 + (\rho_w g \forall - m_b g) - (m_a + m_b)\ddot{y} = 0. \tag{4.16}$$

Hence the equation for the motion of the system is

$$m_b\ddot{y} + m_b g - \rho_w g \forall = -m_a\ddot{y} - \frac{1}{2}\frac{dm_a}{dy}\dot{y}^2, \tag{4.17}$$

where the left-hand side is the equation of motion and the right-hand side is the added mass force F_a which can be stated as

$$F_a = \frac{1}{2}\frac{dm_a}{dy}v^2 + m_a\dot{v}, \tag{4.18}$$

where m_a is the added mass, y is the vertical axis, and $\dot{y}$ and $\ddot{y}$ are replaced by v and $\dot{v}$ (the heave velocity and acceleration), respectively. This is exact, but one can not calculate the energy in the fluid easily except at time $t = 0$. In general the added mass would depend on the entire history of motion (i.e. memory), due to wave radiation. Wagner (1932) gives the added mass force for a symmetric wedge as

$$m_a = \rho b^2 G \tan\alpha, \tag{4.19}$$

and the derivative of the added mass is

$$\frac{dm_a}{dy} = \frac{d}{dy}\left\{\rho b^2 G \tan\alpha\right\}, \tag{4.20}$$

where the function G is given in terms of Gamma functions by

$$G = \frac{\Gamma\left(1+\frac{\alpha}{\pi}\right)\Gamma\left(\frac{1}{2}-\frac{\alpha}{\pi}\right)}{\Gamma\left(1-\frac{\alpha}{\pi}\right)\Gamma\left(\frac{1}{2}+\frac{\alpha}{\pi}\right)} - 1, \tag{4.21}$$

and $b = D_i - y$ is the submerged depth of the wedge, where D_i is initial draft and y is change in depth. The $\Gamma(..)$ are Gamma functions, the evaluation of which is performed using the following identities (see Abramowitz and Stegun (1965)):

$$\Gamma(1+x) = x\Gamma(x), \tag{4.22}$$

$$\Gamma(x)\Gamma(1-x) = \frac{\pi}{\sin\pi x}, \tag{4.23}$$

$$\Gamma(1+x) = 1 + a_1x + a_2x^2 + a_3x^3 + a_4x^4 + a_5x^5, \tag{4.24}$$

where Eq. (4.24) is valid for $|x| < 1$ and the coefficients are given by

$$
\begin{aligned}
a_1 &= -0.5748646, \\
a_2 &= 0.9512363, \\
a_3 &= -0.6998588, \\
a_4 &= 0.4245549, \\
a_5 &= -0.1010678.
\end{aligned}
$$

Wagner (1932) states his results for m_a without explanation, and it is worth deriving the result here for comparison with the more complicated body geometry considered later. We consider the Schwartz-Christoffel mapping, see e.g. Milne-Thomson (1968). From the Schwartz-Christoffel theorem, we can state

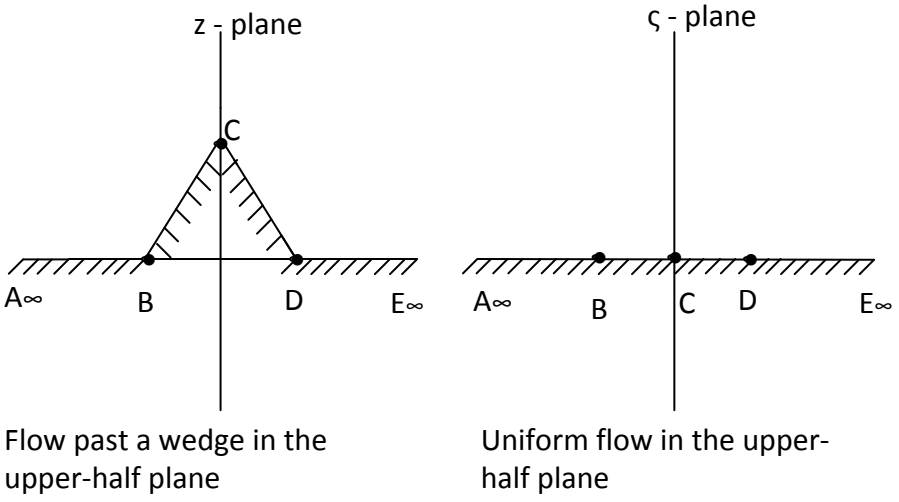

FIGURE 4.43: Definition sketch for the flow mapping in the plane

$$z = K' \int_0^{\zeta} (\zeta+1)^{\frac{\pi-\alpha}{\pi}-1}(\zeta)^{\frac{\pi+2\alpha}{\pi}-1}(\zeta-1)^{\frac{\pi-\alpha}{\pi}-1}d\zeta + L \tag{4.25}$$

$$z = K \int_0^{\zeta} \frac{(\zeta)^{\frac{2\alpha}{\pi}}}{(1-\zeta^2)^{\frac{\alpha}{\pi}}}d\zeta + L. \tag{4.26}$$

At point C: $\zeta = 0,\ z = ai \Rightarrow L = ai.$

At point D: $\zeta = 1,\ z = b \Rightarrow b = K \int_0^1 \frac{(\zeta)^{\frac{2\alpha}{\pi}}}{(1-\zeta^2)^{\frac{\alpha}{\pi}}}d\zeta + ai.$

Using the identity, we get

$$\frac{\Gamma(q)\Gamma(p)}{\Gamma(q+p)} = \int_0^1 t^{q-1}(1-t)^{p-1}dt. \tag{4.27}$$

From Abramowitz & Stegun (1965), and the substitution $\zeta = \sqrt{t}$, we can derive

$$b = K\frac{\Gamma\left(\frac{\alpha}{\pi}-\frac{1}{2}\right)\Gamma\left(1-\frac{\alpha}{\pi}\right)}{\sqrt{\pi}} + ai \Rightarrow K = \frac{(b-ai)\sqrt{\pi}}{\Gamma\left(\frac{\alpha}{\pi}-\frac{1}{2}\right)\Gamma\left(1-\frac{\alpha}{\pi}\right)}. \tag{4.28}$$

We now set $K = |K|e^{-ia}$ where

$$|K| = \frac{b}{\cos\alpha}\frac{\sqrt{\pi}}{\Gamma\left(\frac{\alpha}{\pi}-\frac{1}{2}\right)\Gamma\left(1-\frac{\alpha}{\pi}\right)}. \tag{4.29}$$

So we can express

$$z = |K| \int_0^{\zeta} \left(1-\frac{1}{\zeta^2}\right)^{-\frac{\alpha}{\pi}} d\zeta + ai = |K| \int_1^{\zeta} \left(1+\frac{\alpha}{\pi}\frac{1}{\zeta^2}+...\right) d\zeta + b, \tag{4.30}$$

since

$$|K| \int_0^1 \left(1-\frac{1}{\zeta^2}\right)^{-\frac{\alpha}{\pi}} d\zeta = b - ai. \tag{4.31}$$

Integrating gives

$$z = |K| \left(\zeta - \frac{\alpha}{\pi}\frac{1}{\zeta}+...\right). \tag{4.32}$$

Thus

$$\zeta = z' + \frac{\alpha}{\pi}\frac{1}{z'} + ..., \tag{4.33}$$

where

$$z' = \frac{z}{|K|}$$

by series reversion.

We require $\beta(z) \to z$ as $z \to \infty$ for unit velocity at ∞. So

$$\beta(z) = |K|\zeta = z + |K|^2\frac{\alpha}{\pi}\frac{1}{z} + ... \tag{4.34}$$

The added mass can be derived from the dipole coefficient as explained in Newman (1977) and Appendix B. So taking the coefficient of $1/z$ we can conclude

$$\left(\frac{m_a}{\rho} + \forall\right) = |K|^2\alpha = \frac{(a^2+b^2)\pi\alpha}{\left[\Gamma\left(\frac{\alpha}{\pi} - \frac{1}{2}\right)\Gamma\left(1 - \frac{\alpha}{\pi}\right)\right]^2} \quad , \tag{4.35}$$

where $\forall = b^2 \tan\alpha$ is the body volume. Using further identities defined in Abramowitz and Stegun (1965) we obtain the equation

$$\left(\frac{m_a}{\rho} + \forall\right) = b^2 \tan\alpha \frac{\frac{\alpha}{\pi}\Gamma\left(\frac{\alpha}{\pi}\right)\Gamma\left(\frac{1}{2} - \frac{\alpha}{\pi}\right)}{\Gamma\left(\frac{\alpha}{\pi} + \frac{1}{2}\right)\Gamma\left(\frac{\alpha}{\pi} + \frac{1}{2}\right)}. \tag{4.36}$$

With minor manipulation we finally obtain equations as stated by Wagner (1932). Fig. (4.44) shows the relationship between the added mass, m_a. and the wedge half angle, α. The added mass is non-dimensionalised in two different manners. On the left we non-dimensionalise with respect to the submerged body depth, b. Now we get

$$\frac{m_a}{\rho\pi b^2} = \frac{\tan\alpha}{\pi}G. \tag{4.37}$$

On the right we non-dimensionalise with respect to the body half width, $a^2 = b^2 tan\alpha$. We non-dimensionalise with respect to body half width to allow for comparisons with other body cross sections presented in later sections. We can write

as

$$\frac{m_a}{\rho\pi a^2} = \frac{G}{\pi}. \tag{4.38}$$

We note that the added mass for the wedge approaches $\rho\pi a^2/2$ as α approaches

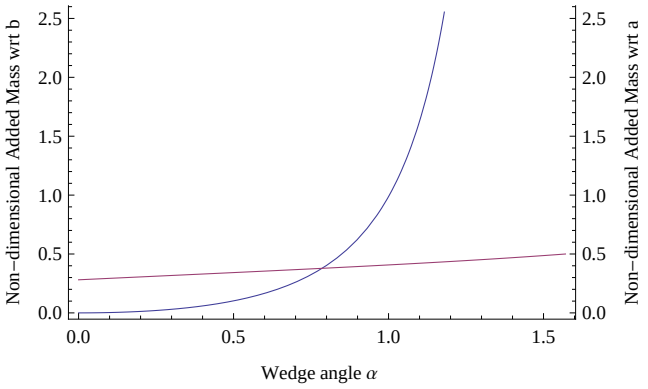

FIGURE 4.44: Non-dimensional added mass (with respect to the depth b and half width a) vs vertical half-wedge angle α

90 degrees. We expect this result since it is the added mass for a flat plate of half width a (equivalent to the displaced mass of a cylinder radius a).
Differentiating the added mass with respect to y and noting that b is a function of y, we get

$$\frac{dm_a}{dy} = -2\rho bG\tan\alpha. \tag{4.39}$$

Hence, by substitution we can obtain the added mass force in a form suitable for comparison with the numerical calculations.

We compare the force difference ($F_d = F_n - F_b$) with the analytic added mass force (F_a) because the numerical force (F_n) which we compute using the numerical method consists of the buoyant force (F_b) and the force due to the pressure on the body (dynamic force), but the computation of the added-mass force does not include the buoyancy force.

Fig. (4.45) and Fig. (4.46) show comparisons of the computed force difference and the analytical added mass force computed for the symmetric wedge SW30 entering water with constant accelerations (G_τ) of 1 and 0.5 respectively. It can be noted that both forces are close to each other at time zero. The added-mass

force (F_a) computed using Eq. (4.18) is positive and increasing as time goes up for entry cases with constant acceleration (see Fig. (4.45) and (4.46)) and constant velocity (see Fig. (4.47)).

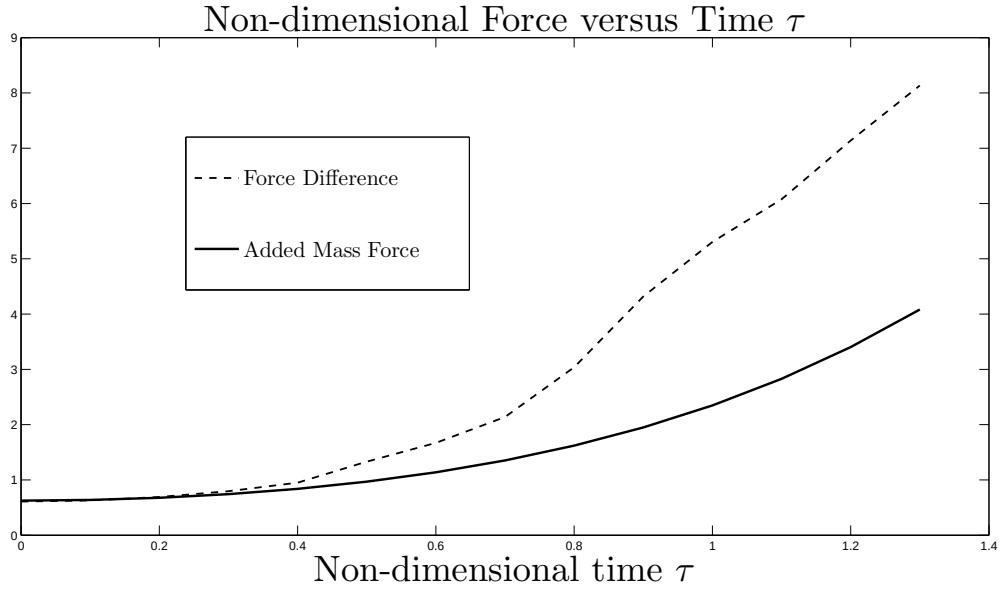

(a)

FIGURE 4.45: Computed numerical force difference and added mass force showing added mass effect for the wedge SW30 entering with constant acceleration $G_\tau = 1$.

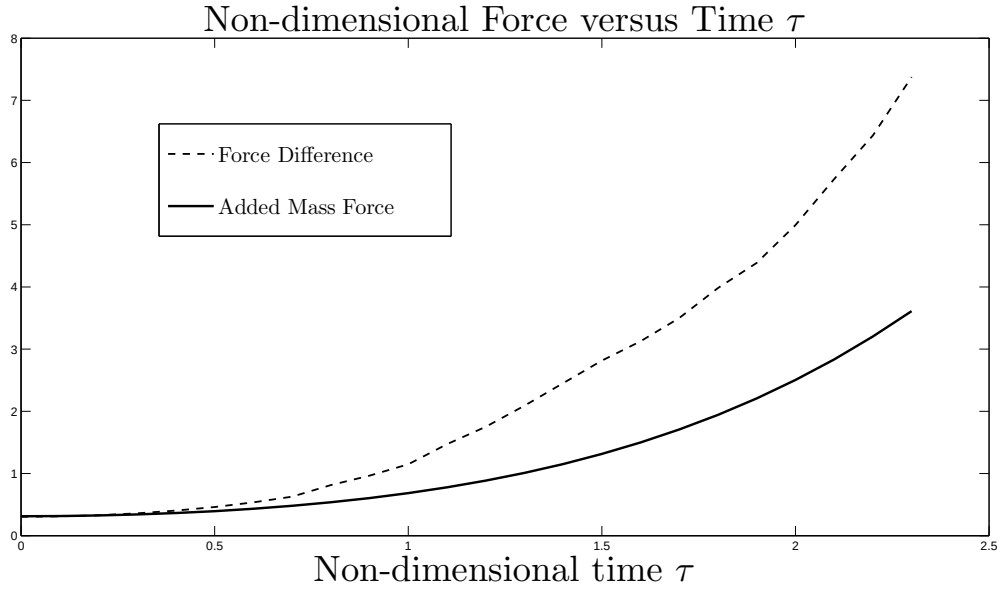

(a)

FIGURE 4.46: Computed numerical force difference and added mass force showing added mass effect for the wedge SW30 entering with constant acceleration $G_\tau = 0.5$.

We also computed the added mass force for the symmetric wedges of various half angles entering water with constant velocity. Fig. (4.47) shows comparison of the computed force difference and the analytical added mass force computed for the symmetric wedge SW30 entering water with a Froude number F_r of 0.5. Results for other wedge angles are given in the CD, see Appendix B.

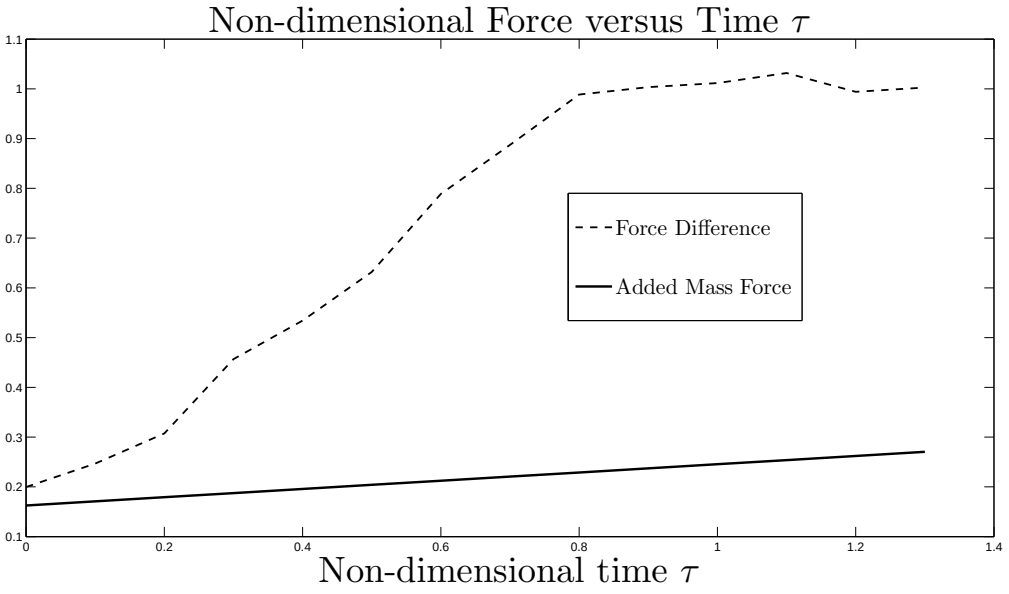

(a)

FIGURE 4.47: Computed numerical force difference and added mass force showing added mass effect for the wedge SW30 entering with constant velocity of Froude number $F_r = 0.5$.

4.4.2 Asymmetric wedge entry

We present numerical results computed using the non-linear time-stepping method for the each asymmetric wedge same as considered in the constant velocity entry. The test cases considered for the asymmetric wedges entering with constant acceleration are explained in this section. For the asymmetric wedges entering with constant acceleration, the results showing the time effect on the stages of the motion with constant acceleration are presented in section (4.4.2.1), whereas the result of changing acceleration is given in section (4.4.2.2).

4.4.2.1 Time effect

As for the constant velocity entry, here we repeat the process for constant acceleration entry of asymmetric wedges. The time effect on free-surface profile, pressure distribution and total force are computed for the asymmetric wedges entering with constant acceleration. The plots are obtained for different time intervals. The length of interval for each asymmetric wedge depends on the angle of the asymmetric wedges and the acceleration of the entry. For each specific interval, the results are plotted at different times. Fig. (4.48) and (4.49) show the time effect of the asymmetric wedge AW4 entering with constant acceleration of 0.5, whereas Figs. (4.50) to (4.53) show the effect for the constant acceleration of 0.25.

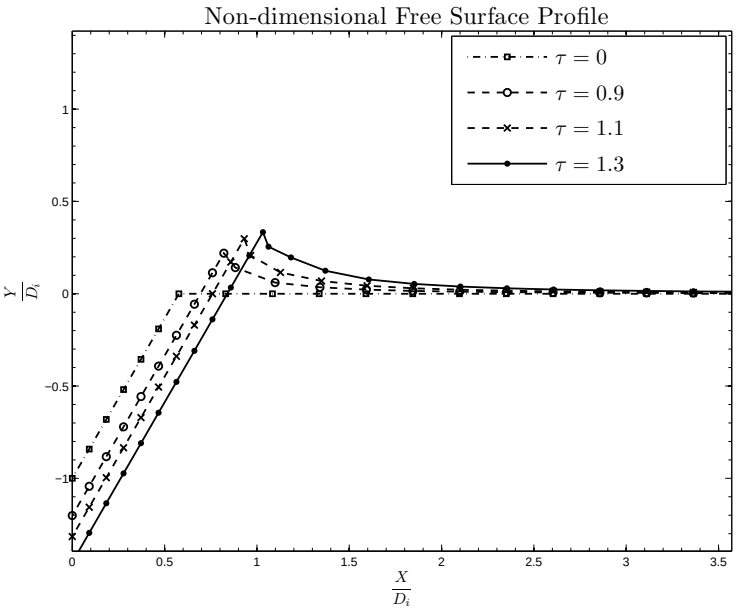

(a) left side of the wedge

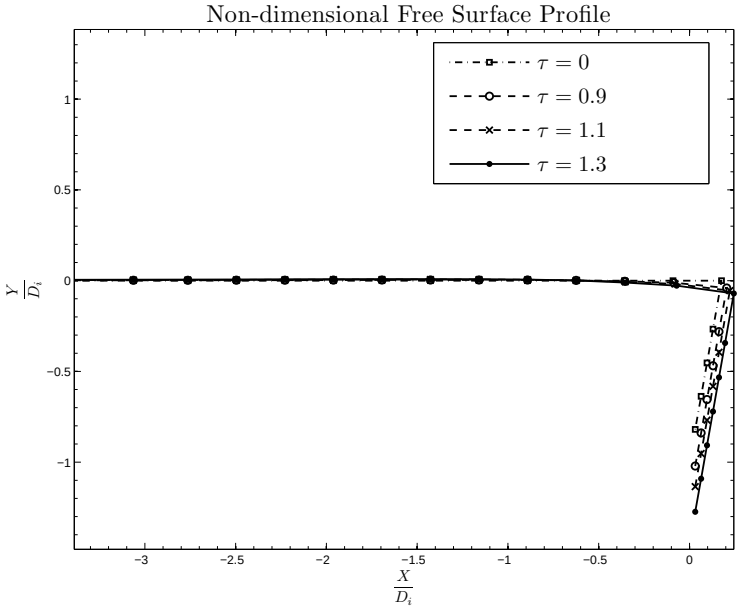

(b) right side of the wedge

FIGURE 4.48: Time effect of the asymmetric wedge AW4 submerged at a non-dimensional initial depth $\widehat{d}_i = -1$ entering with constant acceleration $G_\tau = 0.5$: (a) and (b) are plotted at different non-dimensional times τ.

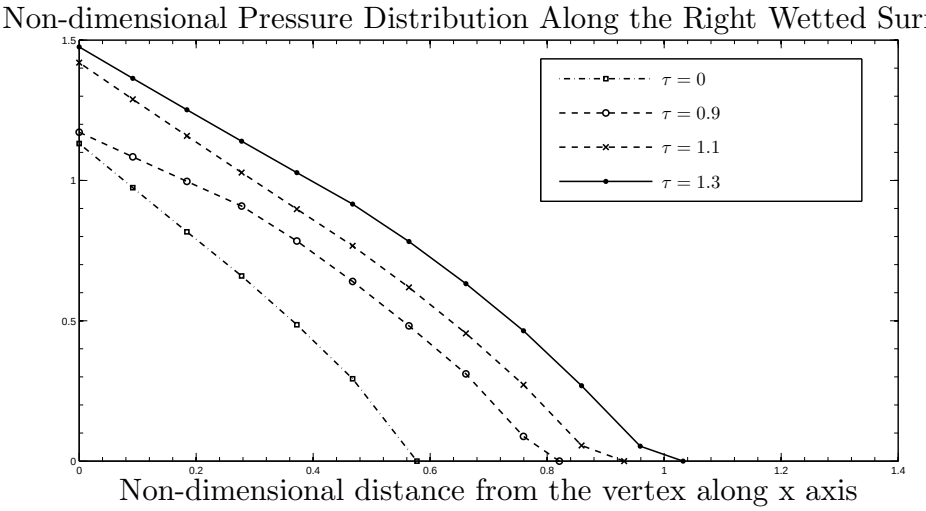

(a)

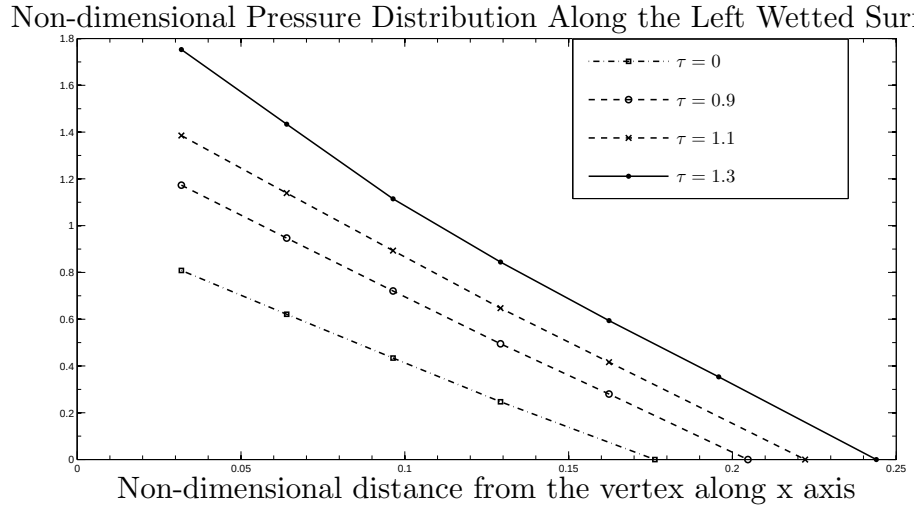

(b)

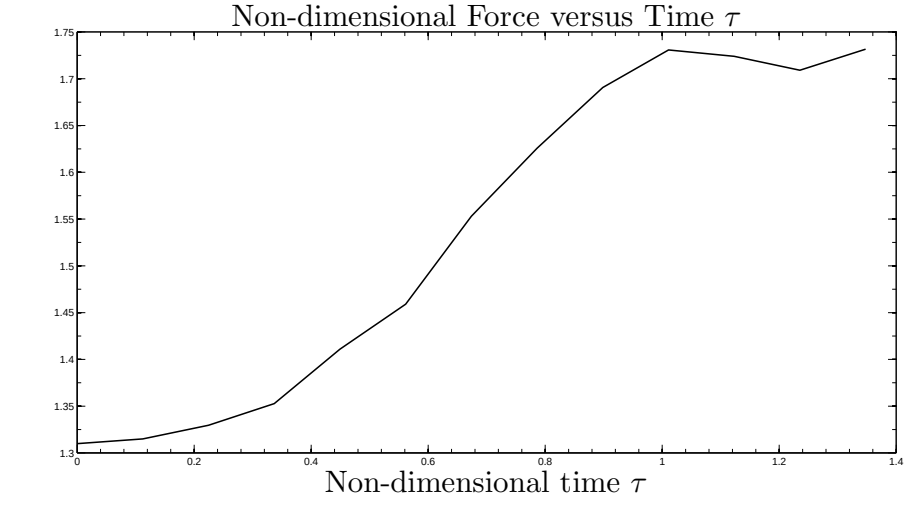

(c)

FIGURE 4.49: Time effect of the asymmetric wedge AW4 submerged at a non-dimensional initial depth $\widehat{d}_i = -1$ entering with constant acceleration $G_\tau = 0.5$: (a) and (b) are plotted at different non-dimensional times τ.

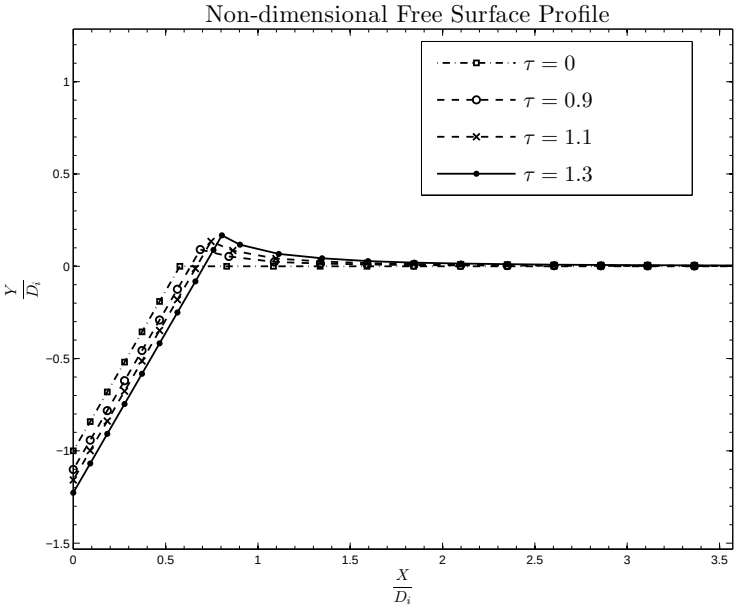

(a) left side of the wedge

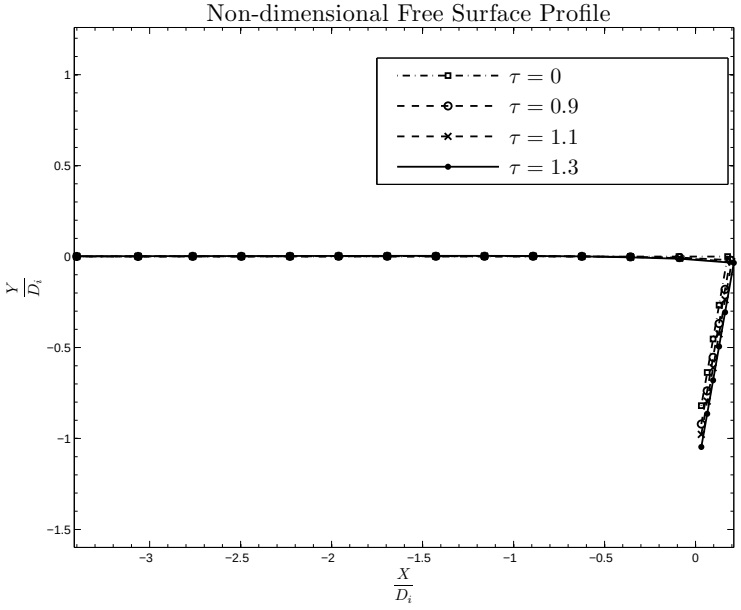

(b) right side of the wedge

FIGURE 4.50: Time effect of the asymmetric wedge AW4 submerged at a non-dimensional initial depth $\widehat{d_i} = -1$ entering with constant acceleration $G_\tau = 0.25$: (a) and (b) are plotted at different non-dimensional times τ.

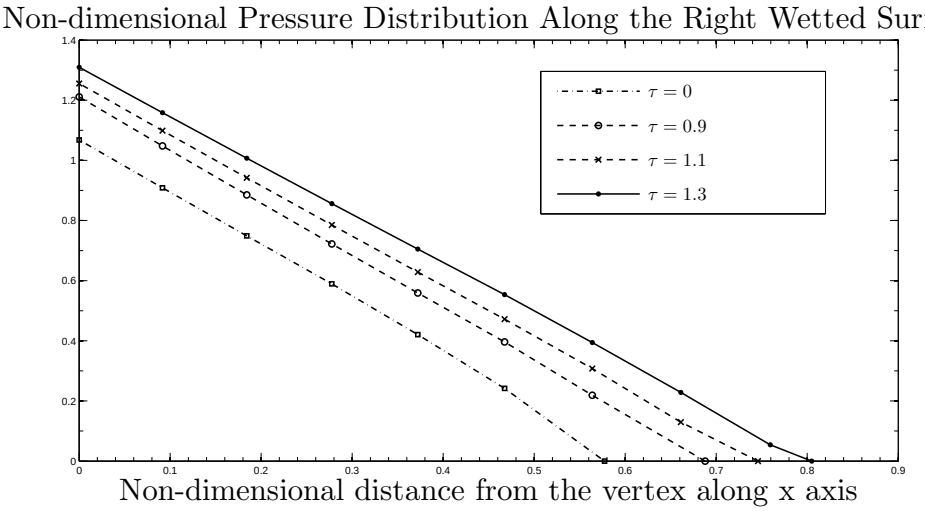

(a)

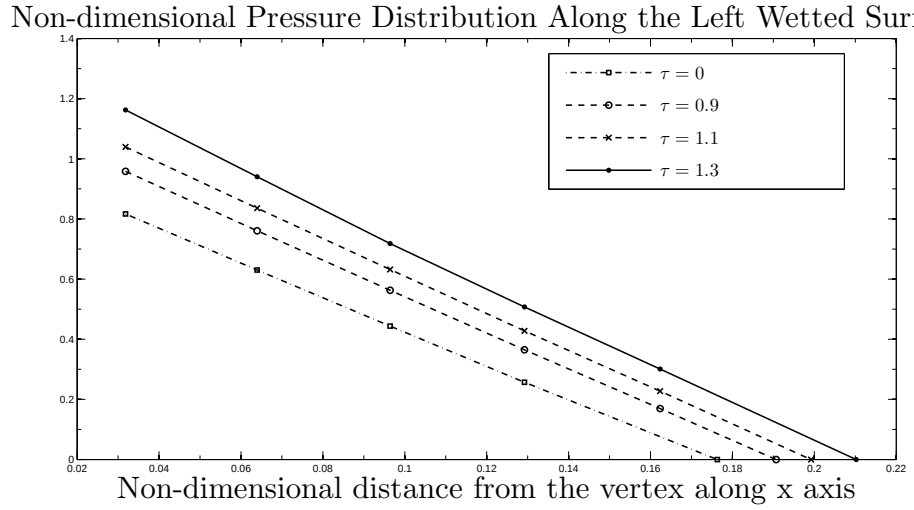

(b)

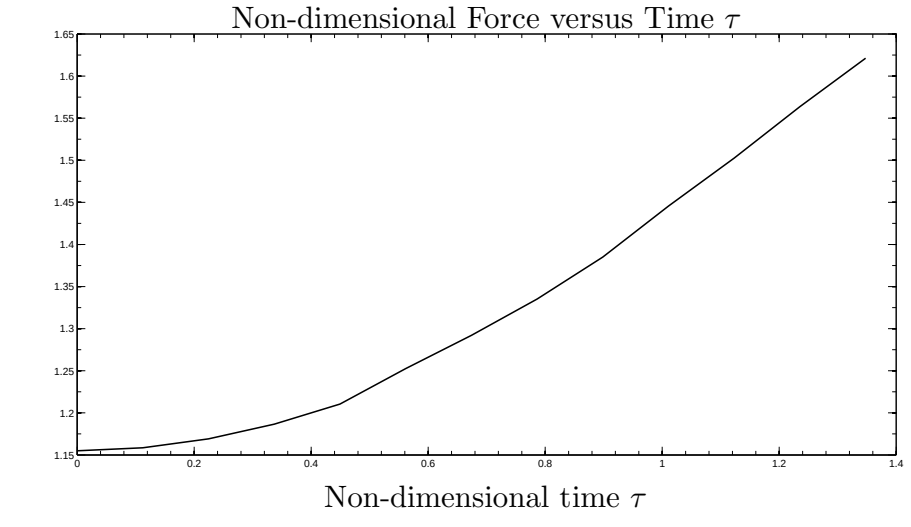

(c)

FIGURE 4.51: Time effect of the asymmetric wedge AW4 submerged at a non-dimensional initial depth $\widehat{d_i} = -1$ entering with constant acceleration $G_\tau = 0.25$: (a) and (b) are plotted at different non-dimensional times τ.

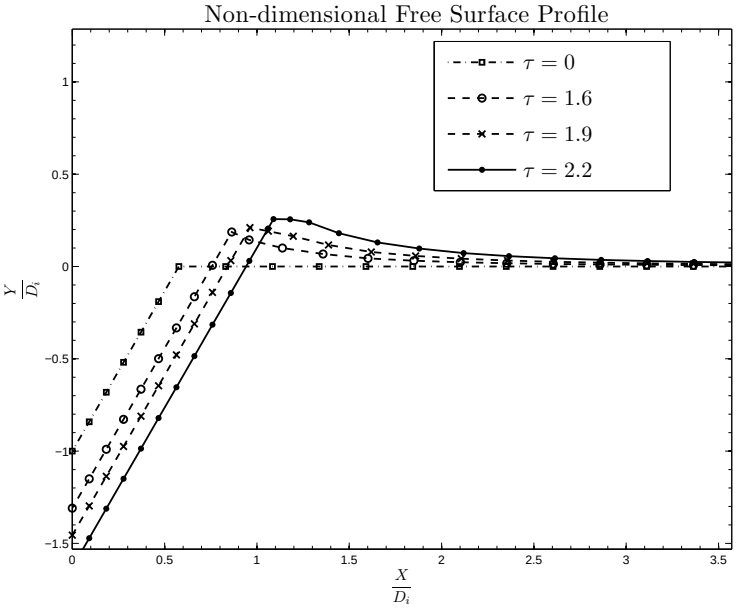

(a) left side of the wedge

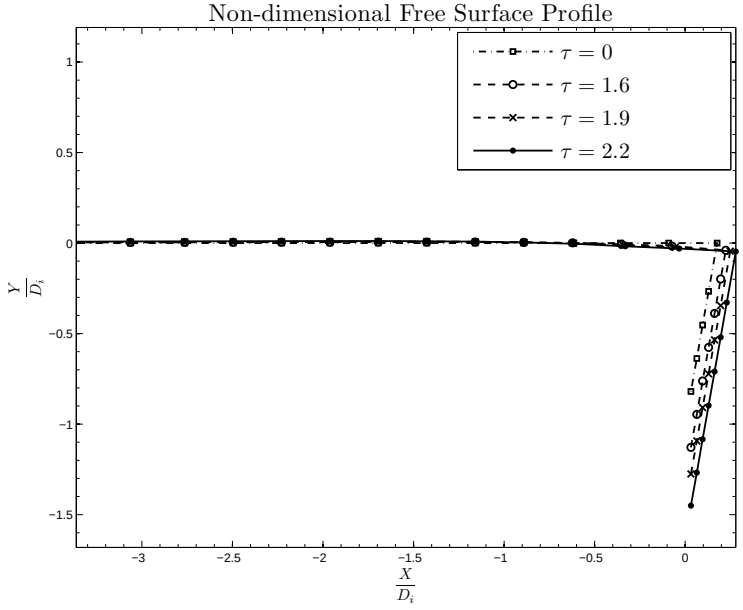

(b) right side of the wedge

FIGURE 4.52: Time effect of the asymmetric wedge AW4 submerged at a non-dimensional initial depth $\widehat{d_i} = -1$ entering with constant acceleration $G_\tau = 0.25$: (a) and (b) are plotted at different non-dimensional times τ.

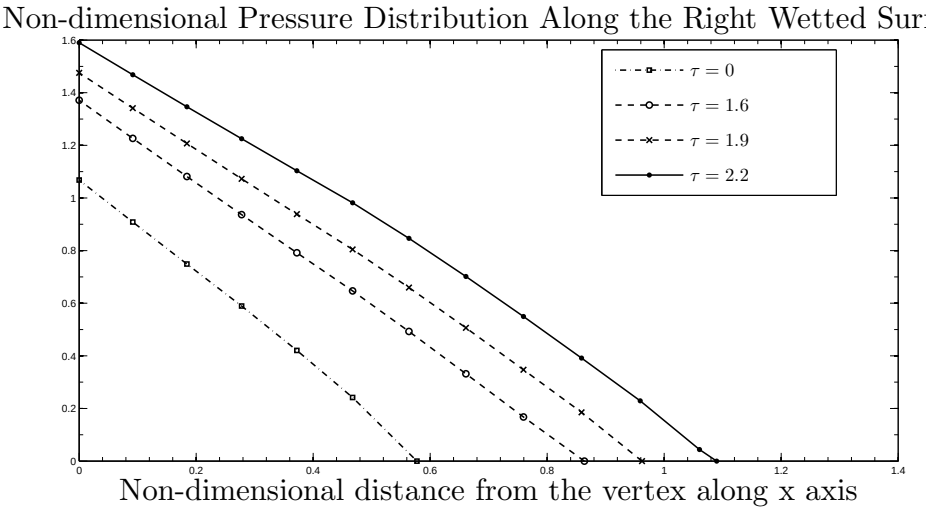

(a)

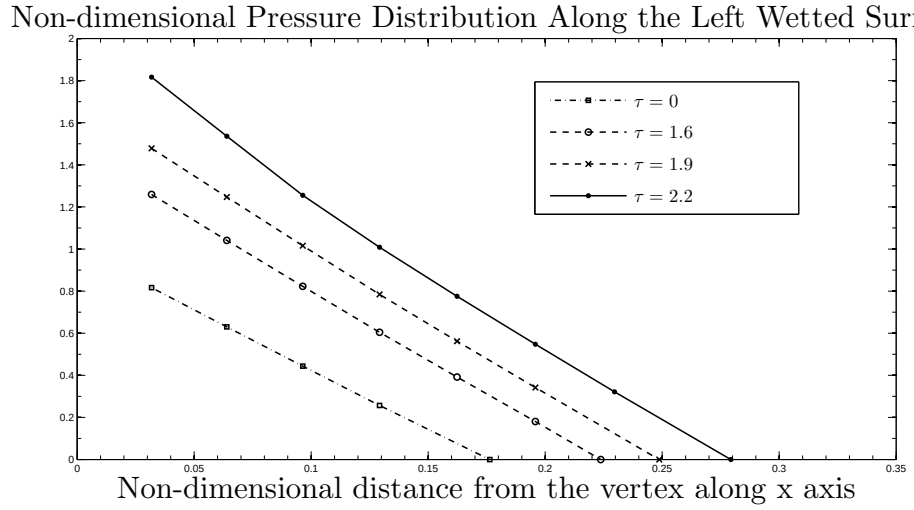

(b)

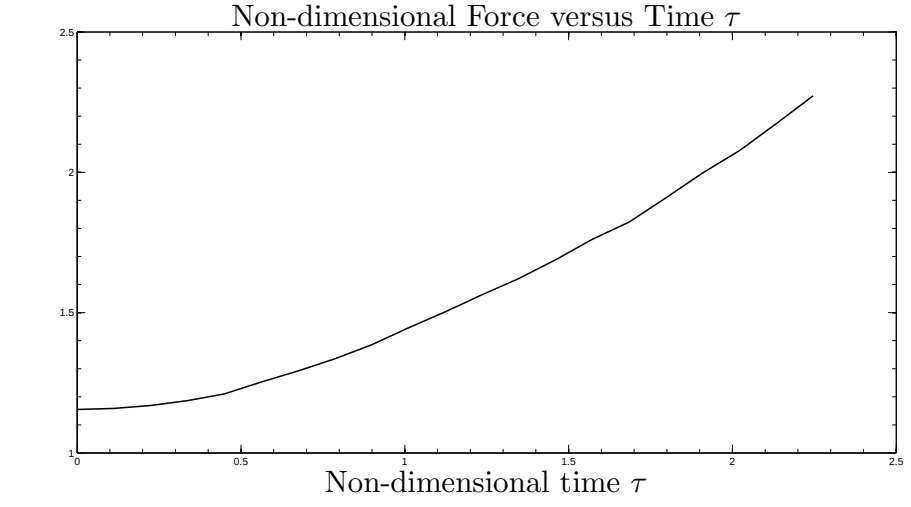

(c)

FIGURE 4.53: Time effect of the asymmetric wedge AW4 submerged at a non-dimensional initial depth $\widehat{d_i} = -1$ entering with constant acceleration $G_\tau = 0.25$: (a) and (b) are plotted at different non-dimensional times τ.

4.4.2.2 Acceleration effect

This section for constant acceleration entry of the asymmetric wedges presents computed numerical results for the free-surface profile, pressure distribution and total force. The results are obtained by running the program with different constant accelerations while attaining the same distance traveled by the asymmetric wedges. Fig. (4.54) and (4.55) show the acceleration of the asymmetric wedge AW4 entering with different accelerations.

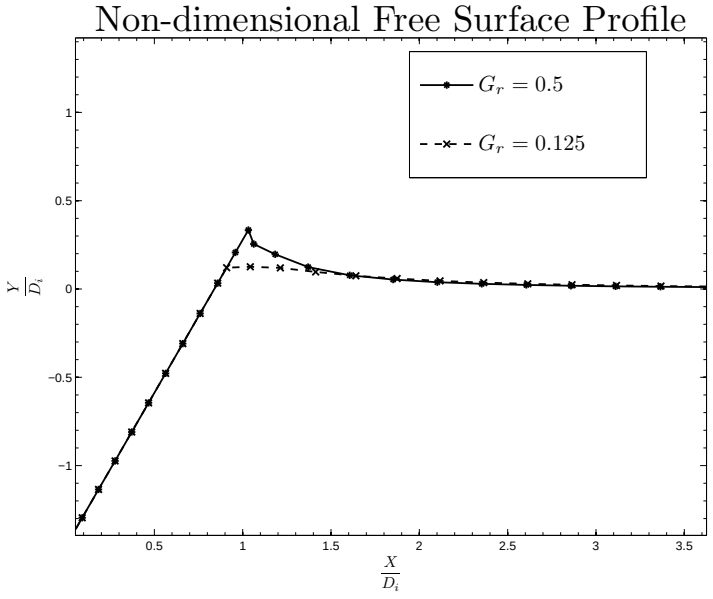

(a)

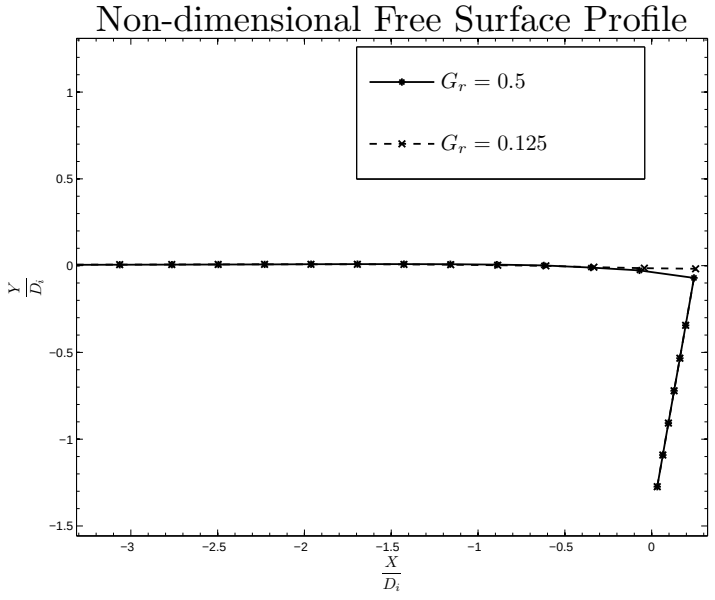

(b)

FIGURE 4.54: Acceleration effect of the asymmetric wedge AW4 submerged at a non-dimensional initial depth $\widehat{d_i} = -1$ entering with different constant accelerations G_τ: (a) and (b) are plotted at different non-dimensional times $\tau = 1.35, 2.67$ and distance $\widehat{d} = -1.45$.

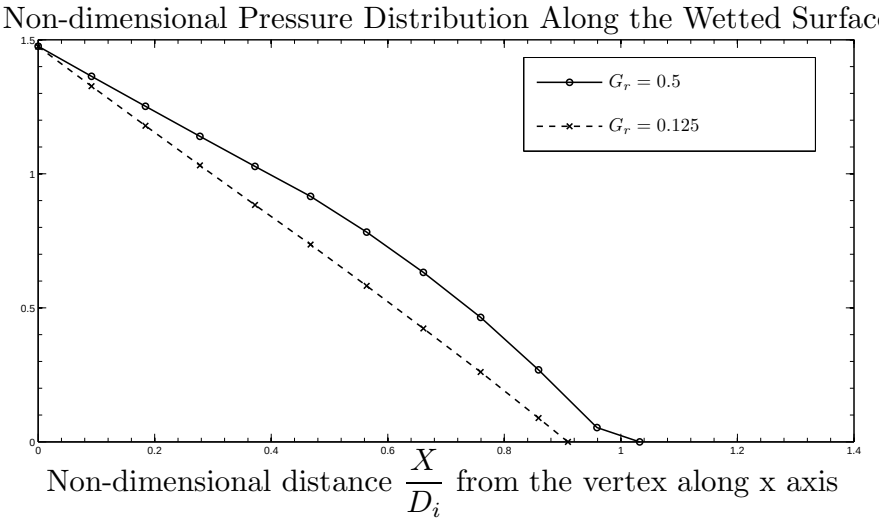

(a)

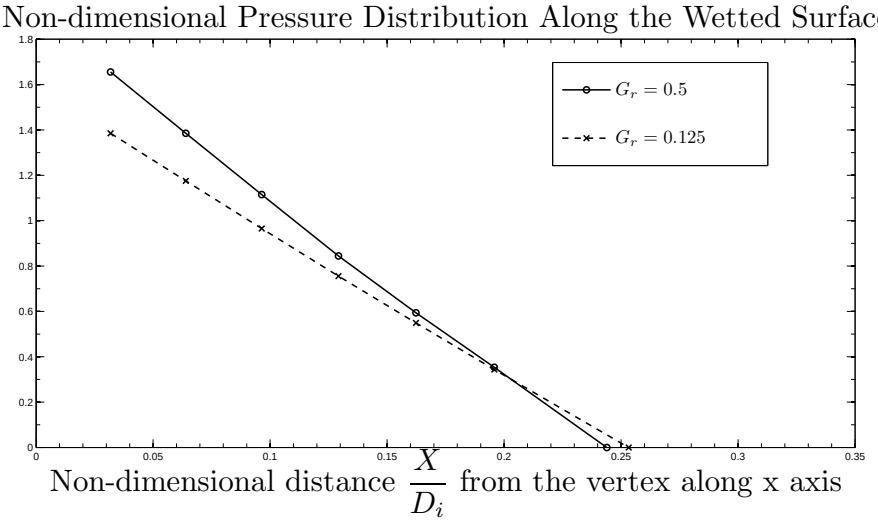

(b)

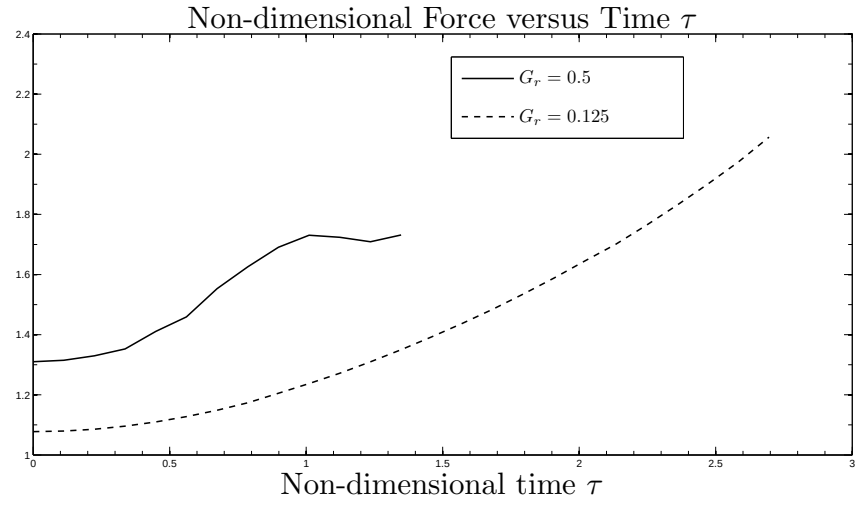

(c)

FIGURE 4.55: Acceleration effect of the asymmetric wedge AW4 submerged at a non-dimensional initial depth $\widehat{d}_i = -1$ entering with different constant accelerations G_τ: (a), (b) and (c) are plotted at different non-dimensional times $\tau = 1.35, 2.67$ and distance $\widehat{d} = -1.45$.

4.4.3 Truncated wedge entry

We present numerical results computed using the non-linear time-stepping method for the same truncated wedges considered in section (4.3.3) for constant velocity entry of the truncated wedges. The test cases considered for the truncated wedges entering with constant acceleration are explained in this section. For the truncated wedge entering with constant acceleration, the results showing time effect are presented in section (4.4.3.1), while the results of changing in acceleration are given in section (4.4.3.2).

4.4.3.1 Time effect

As for the constant velocity entry of the truncated wedges, here we repeat the process for constant acceleration entry of the truncated wedges. The time effect on free-surface profile, pressure distribution and total force are computed for the truncated wedges entering with constant acceleration. The plots are obtained for different time intervals. The length of interval for each truncated wedge depends on the angle of the truncated wedges and the acceleration of the entry. For each specific interval, the results are plotted at different times. Fig. (4.56) and (4.57) show the time effect of the truncated wedge TW3 entering with constant acceleration of 1, whereas Fig. (4.58) and (4.59) show the effect for the constant acceleration of 0.5.

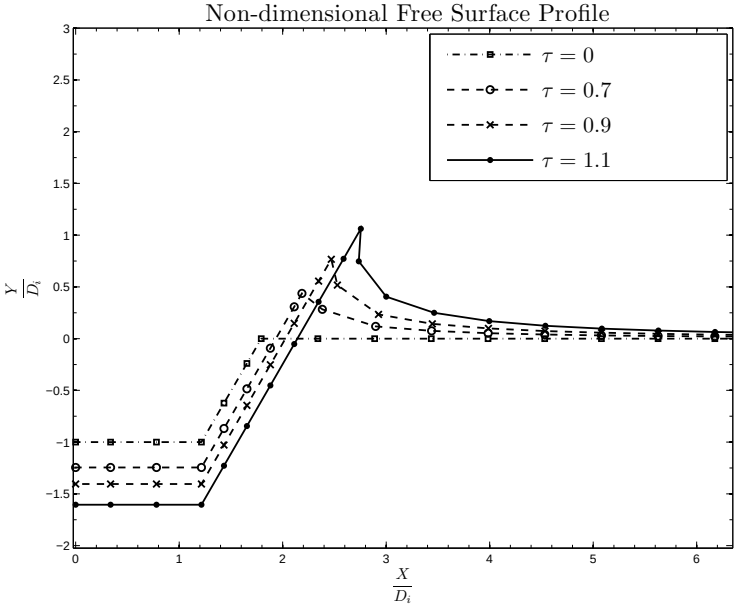

(a)

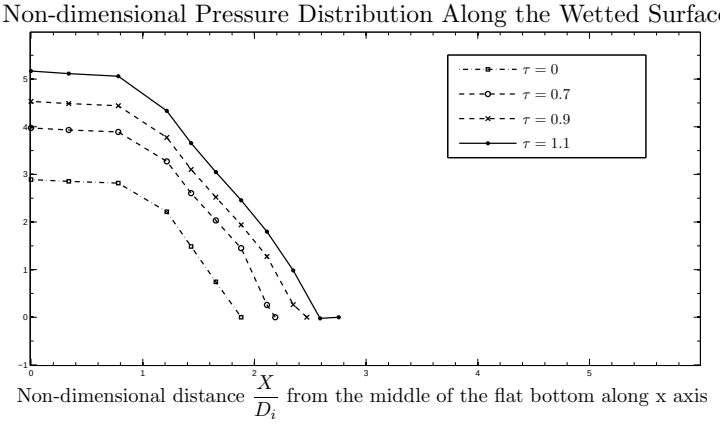

(b)

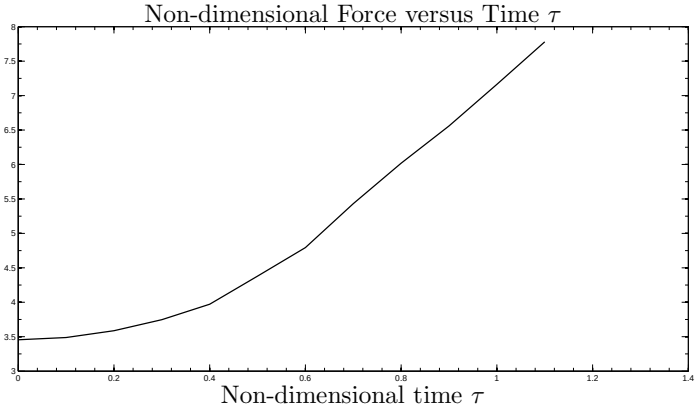

(c)

FIGURE 4.56: Time effect of the truncated wedge TW3 submerged at a non-dimensional initial depth $\widehat{d_i} = -1$ entering with constant acceleration $G_\tau = 1$: (a) and (b) are plotted at different non-dimensional times τ.

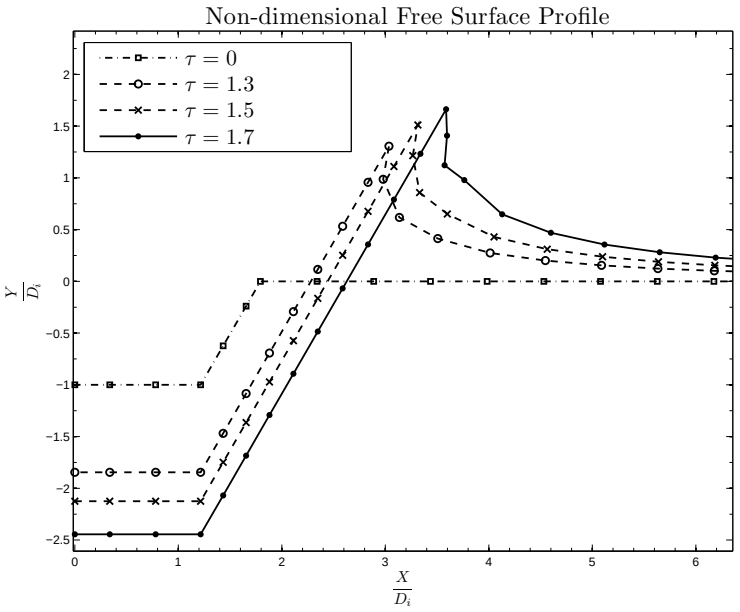

(a)

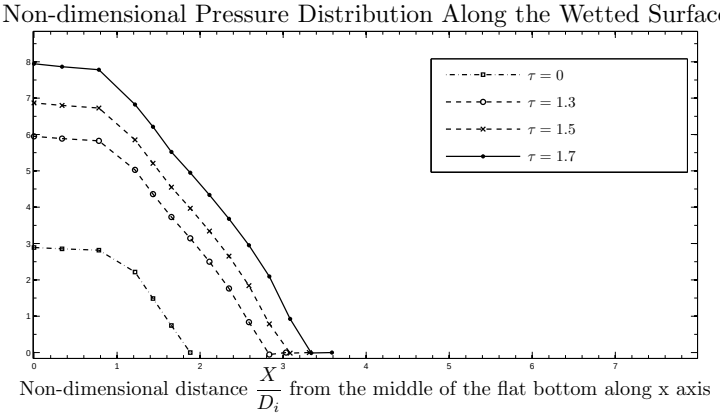

(b)

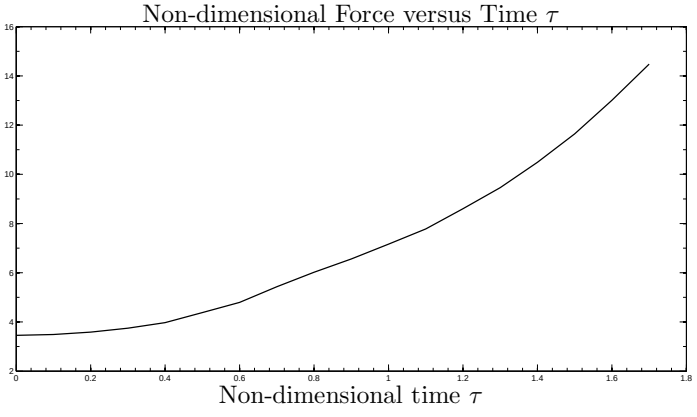

(c)

FIGURE 4.57: Time effect of the truncated wedge TW3 submerged at a non-dimensional initial depth $\widehat{d_i} = -1$ entering with constant acceleration $G_\tau = 1$: (a) and (b) are plotted at different non-dimensional times τ.

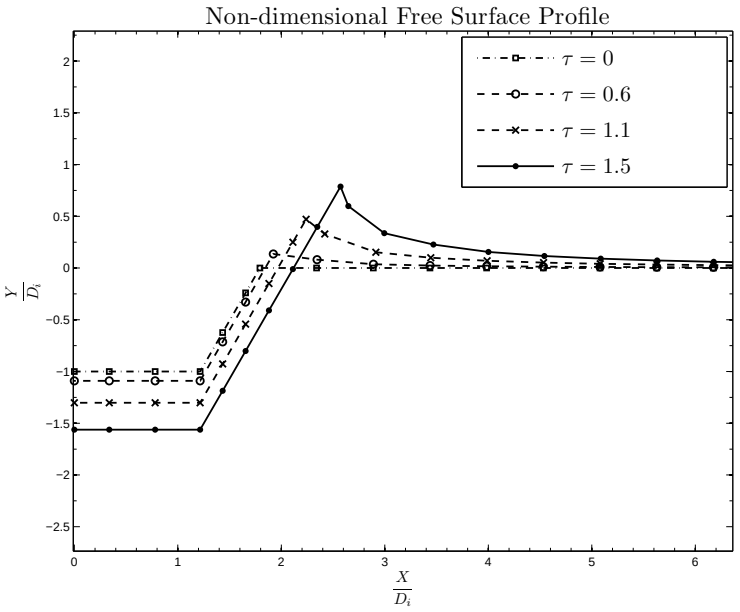

(a)

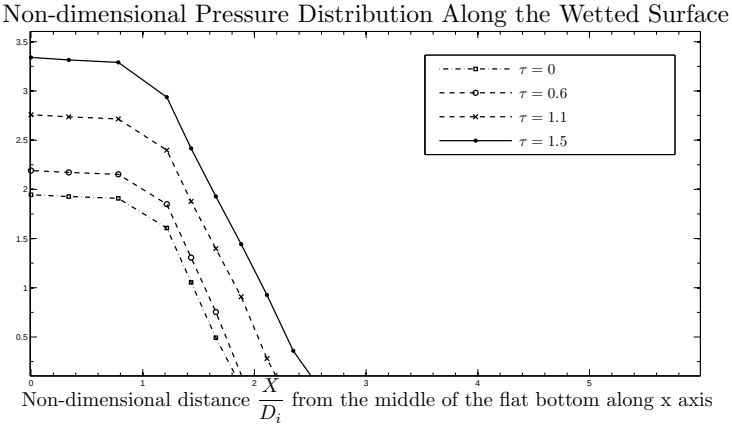

(b)

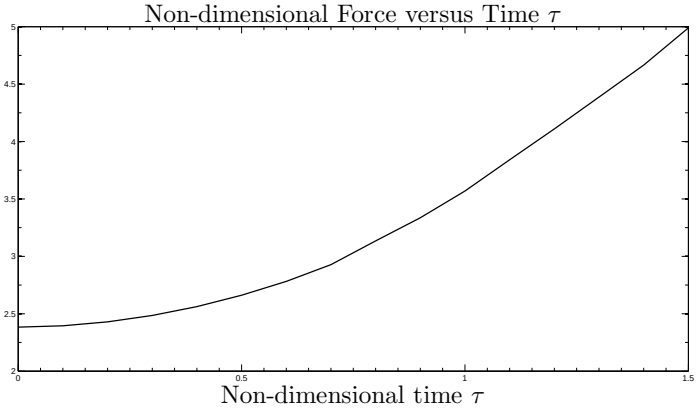

(c)

FIGURE 4.58: Time effect of the truncated wedge TW3 submerged at a non-dimensional initial depth $\widehat{d}_i = -1$ entering with constant acceleration $G_\tau = 0.5$: (a) and (b) are plotted at at different non-dimensional times τ.

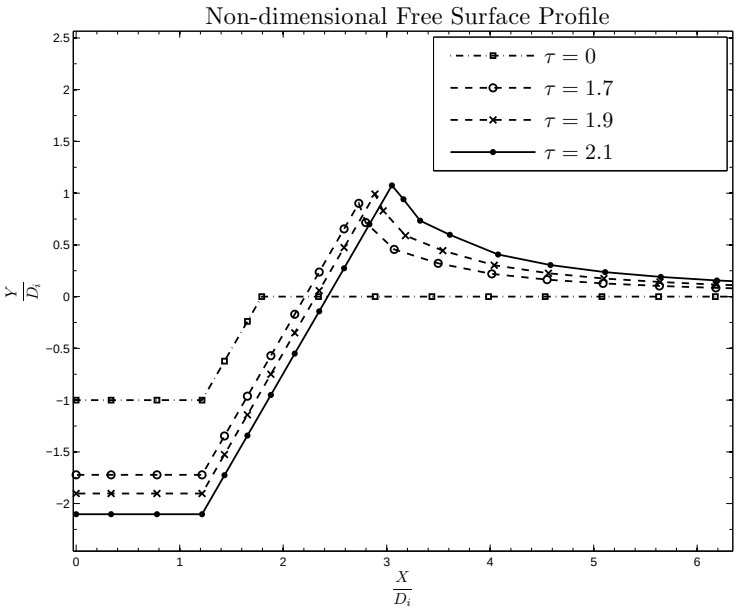

(a)

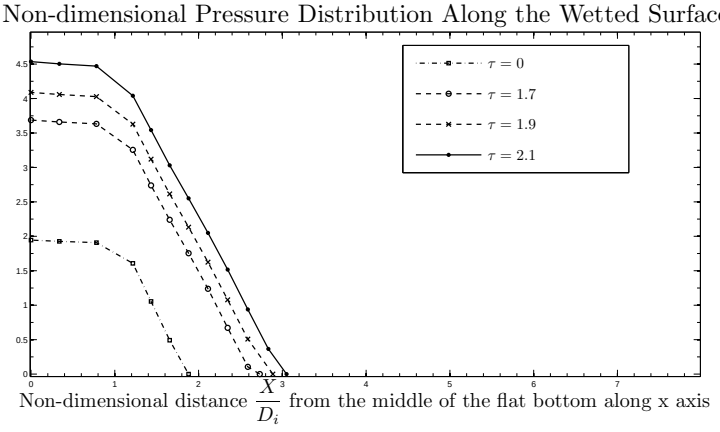

(b)

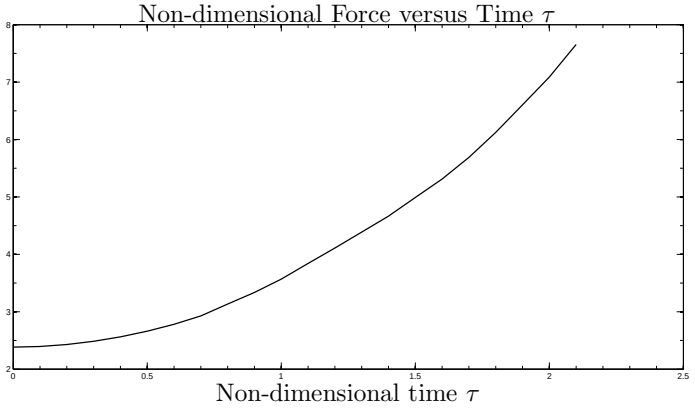

(c)

FIGURE 4.59: Time effect of the truncated wedge TW3 submerged at a non-dimensional initial depth $\widehat{d_i} = -1$ entering with constant acceleration $G_\tau = 0.5$: (a) and (b) are plotted at at different non-dimensional times τ.

4.4.3.2 Acceleration effect

This section for constant acceleration entry of the truncated wedges presents computed numerical results for free-surface profile, pressure distribution and total force. The results are obtained by running the program with different constant accelerations while attaining the same distance traveled by the truncated wedges. Fig. (4.60) shows the acceleration of the truncated wedge TW3 entering with different accelerations.

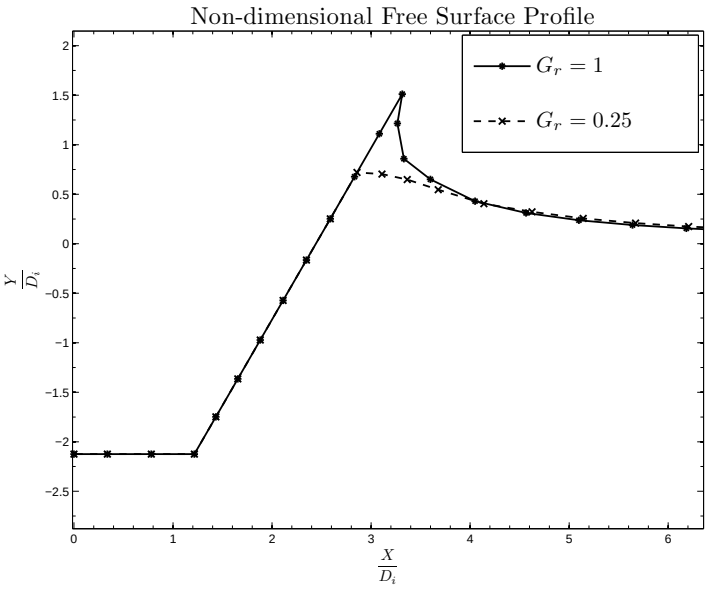

(a)

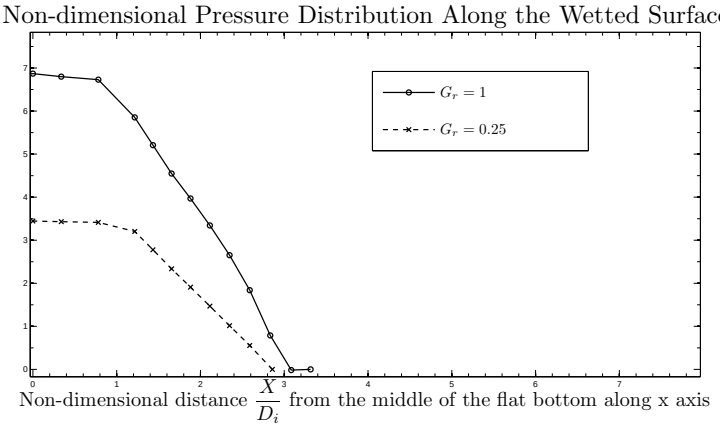

(b)

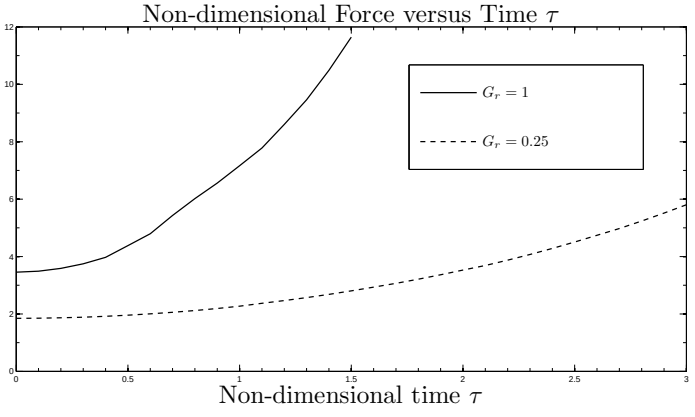

(c)

FIGURE 4.60: Acceleration effect of the truncated wedge TW3 submerged at a non-dimensional initial depth $\widehat{d}_i = -1$ entering with different constant accelerations G_τ: (a) and (b) are plotted at different non-dimensional times $\tau = 1.5, 3$ and distance $\widehat{d} = -2.12$.

4.4.4 Box body entry

We present numerical results computed using the non-linear time-stepping method for the box body same as considered in the constant velocity entry. The test cases considered for the box body entering with constant acceleration are explained in this section. For the box body entering with constant acceleration, the results showing time effect on the stages of the motion with constant acceleration is presented in section (4.4.4.1). The results of changing in acceleration and the comparison of numerical force with the analytical added mass force is given in section (4.4.4.2) and (4.4.4.3) respectively.

4.4.4.1 Time effect

As for the constant velocity entry of the box body, here we repeat the process for constant acceleration entry of the box body. The time effect on free-surface profile, pressure distribution and total force are computed for the box body entering with constant acceleration. The plots are obtained for different time intervals. The length of interval for each box body depends on the aspect ratio of the box body and the acceleration of the entry. For each specific interval, the results are plotted at different times. Fig. (4.61) and (4.62) show the time effect of the box body BX1 entering with constant acceleration of 1, whereas Fig. (4.63) and (4.64) show the effect for the constant acceleration of 0.25.

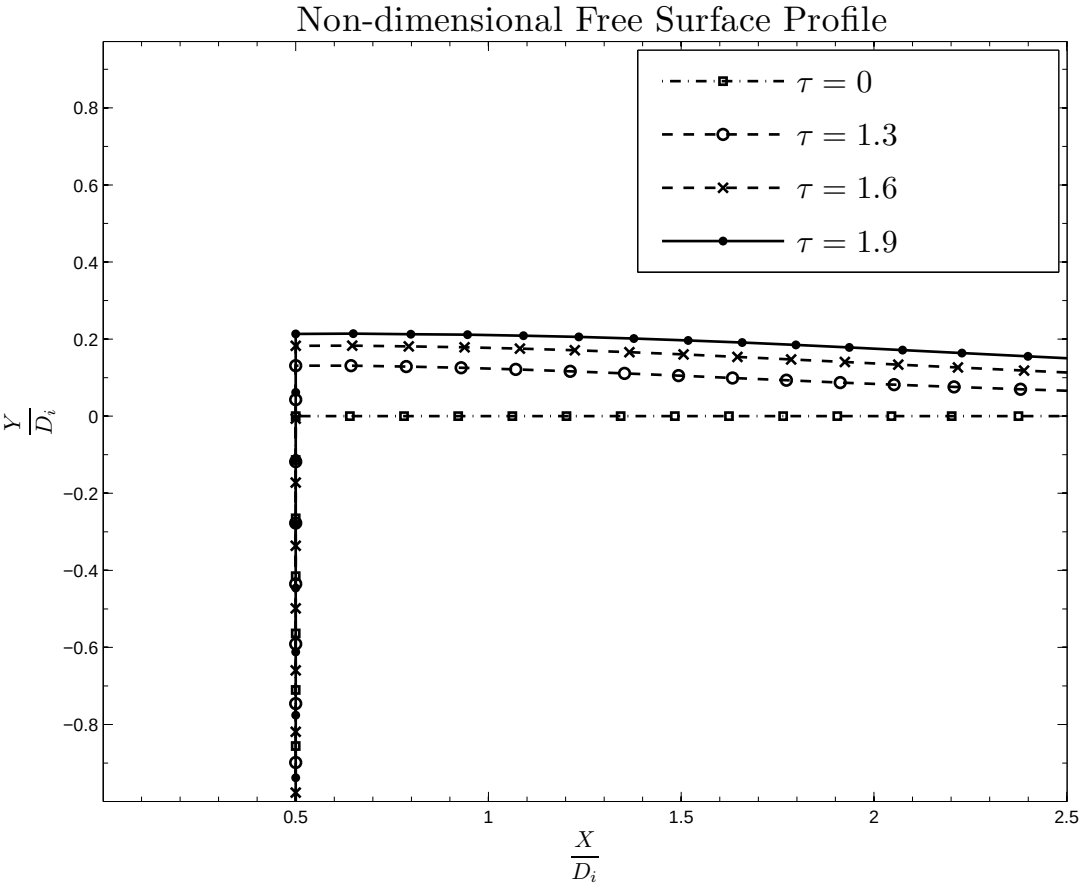

(a)

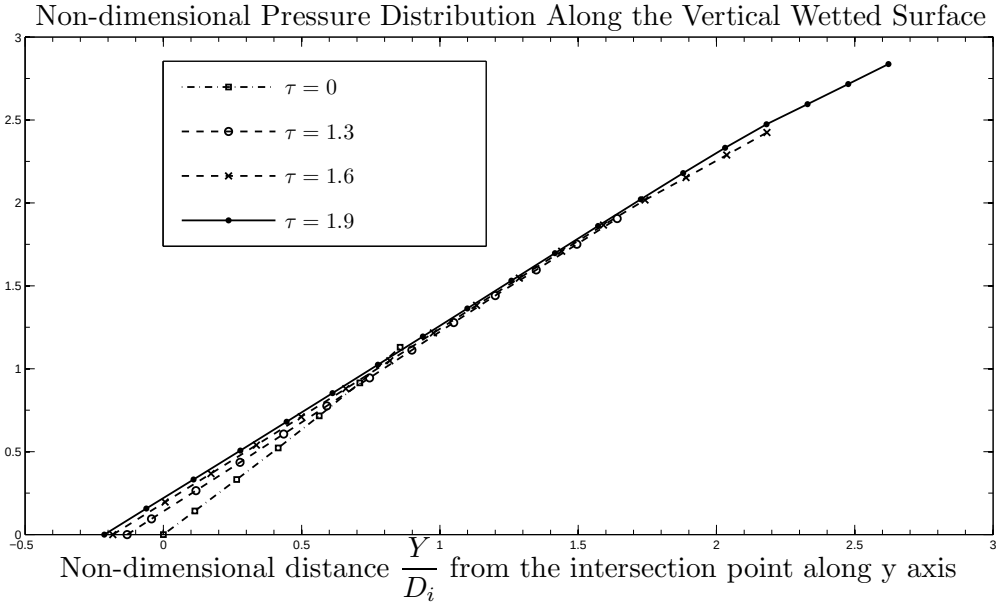

(b)

FIGURE 4.61: Time effect of the box BX1 submerged at a non-dimensional initial depth $\widehat{d_i} = -1$ entering with constant acceleration $G_\tau = 1$: (a) and (b) are plotted at different non-dimensional times τ.

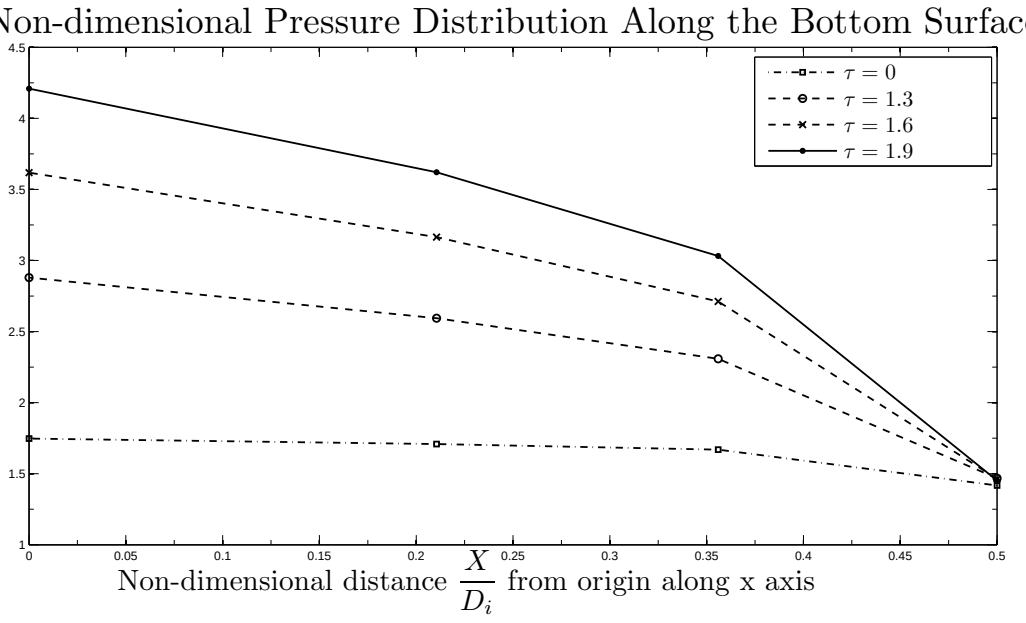

(a)

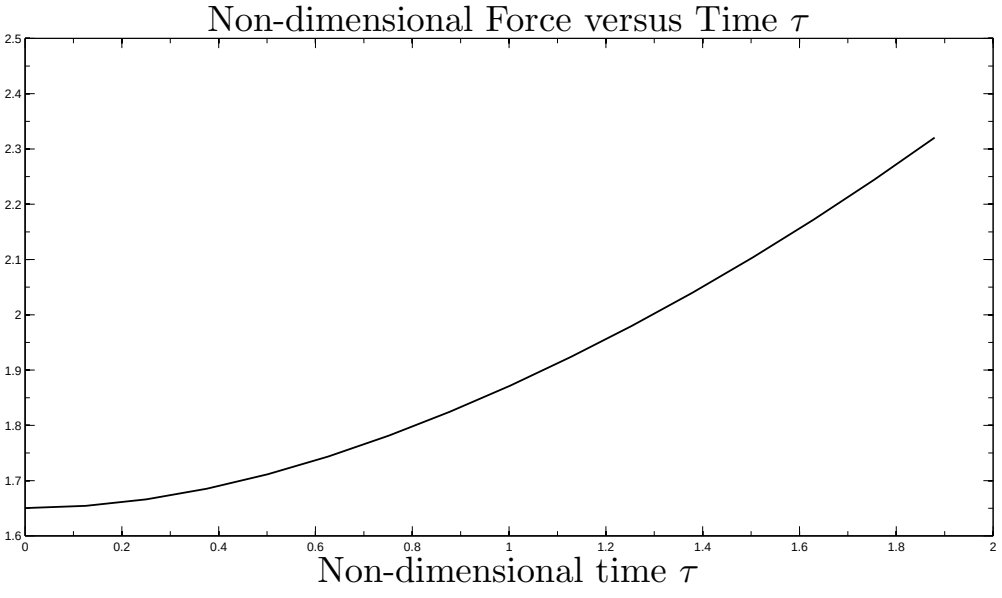

(b)

FIGURE 4.62: Time effect of the box BX1 submerged at a non-dimensional initial depth $\widehat{d}_i = -1$ entering with constant acceleration $G_\tau = 1$: (a) is plotted at different non-dimensional times τ.

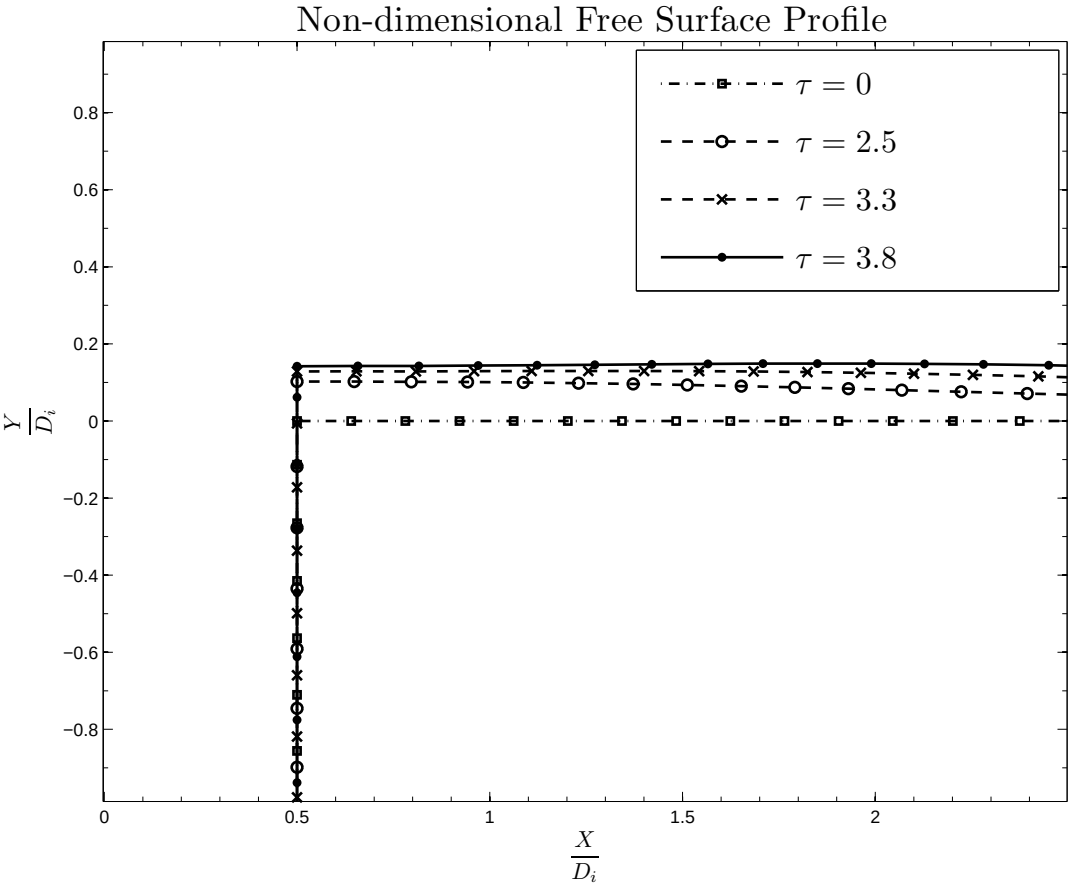

(a)

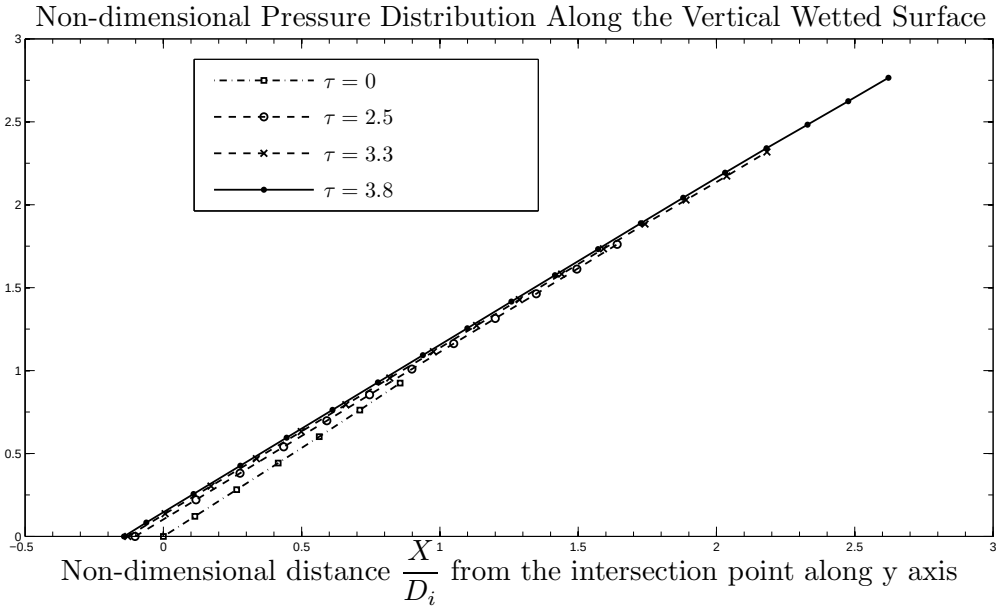

(b)

FIGURE 4.63: Time effect of the box BX1 submerged at a non-dimensional initial depth $\widehat{d_i} = -1$ entering with constant acceleration $G_\tau = 0.25$: (a) and (b) are plotted at different non-dimensional times τ.

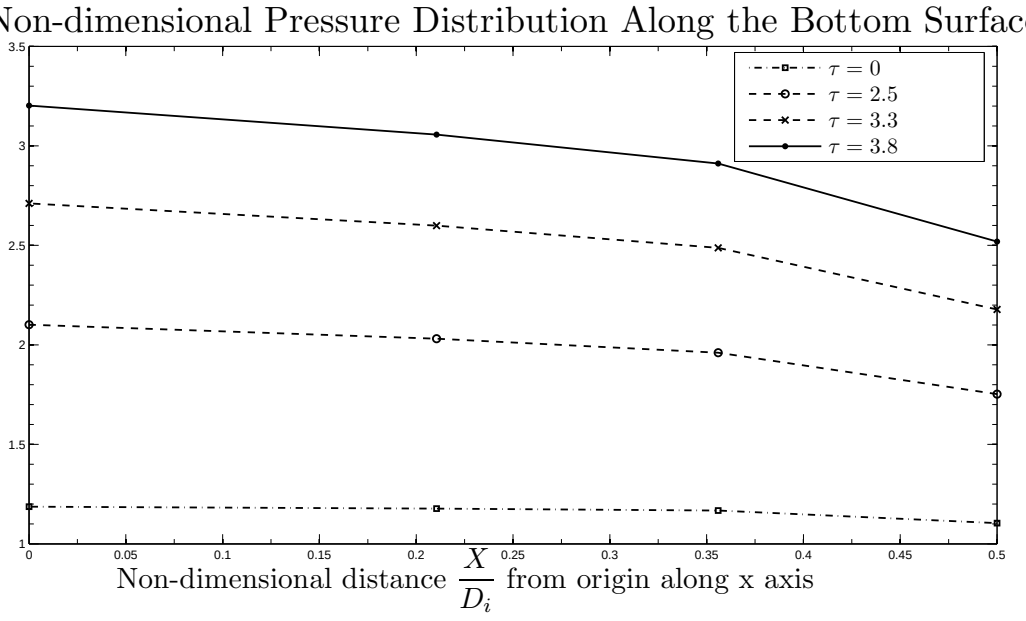

(a)

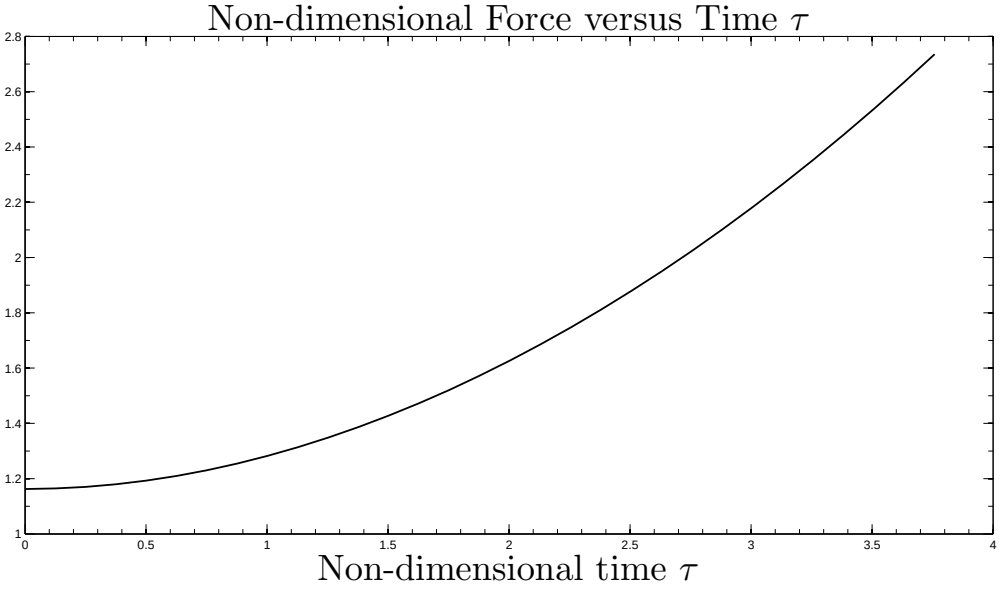

(b)

FIGURE 4.64: Time effect of the box BX1 submerged at a non-dimensional initial depth $\widehat{d_i} = -1$ entering with constant acceleration $G_\tau = 0.25$: (a) is plotted at different non-dimensional times τ.

4.4.4.2 Acceleration effect

This section for constant acceleration entry of the box body presents computed numerical results for free-surface profile, pressure distribution and total force. The results are obtained by running the program with different constant accelerations while attaining the same distance traveled by the box body. Fig. (4.65) and (4.66) show the acceleration of the box body BX1 entering with different accelerations.

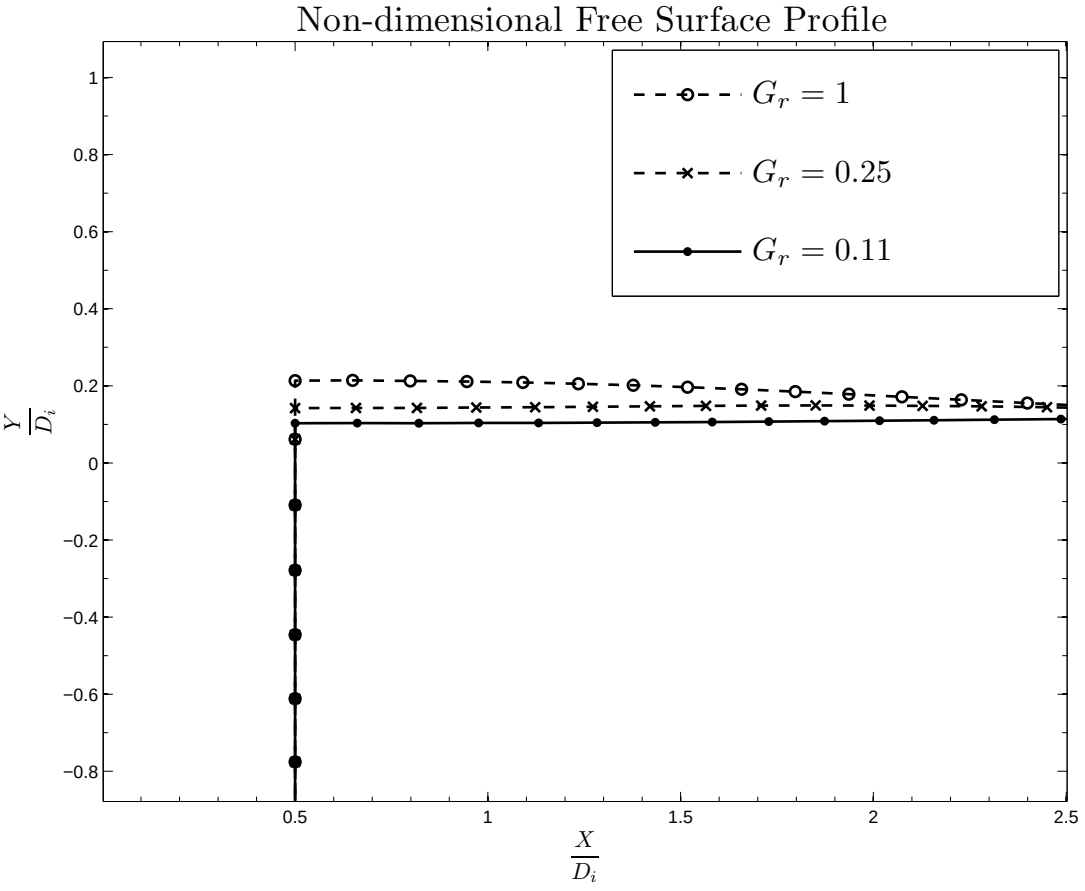

(a)

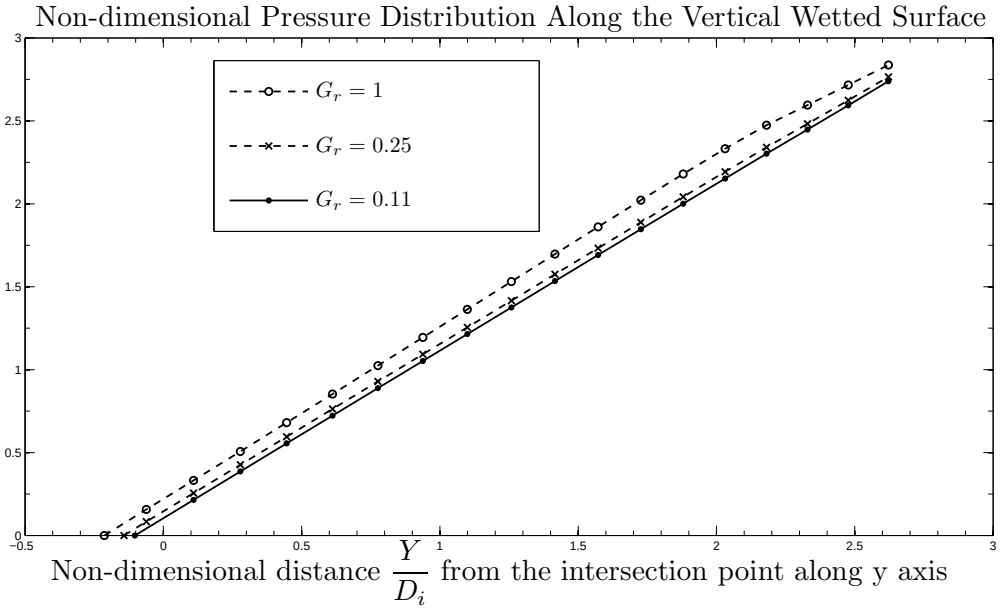

(b)

FIGURE 4.65: Acceleration effect of the box BX1 submerged at a non-dimensional initial depth $\widehat{d_i} = -1$ entering with different constant accelerations G_τ: plotted at different non-dimensional times $\tau = 1.88, 3.76, 5.64$ and distance $\widehat{d} = -2.77$.

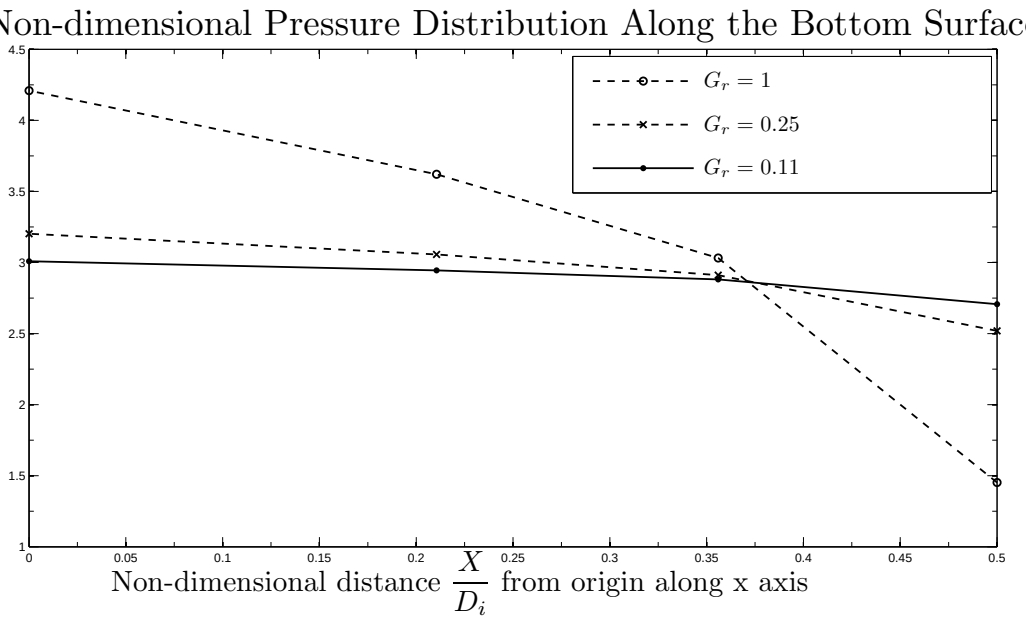

(a)

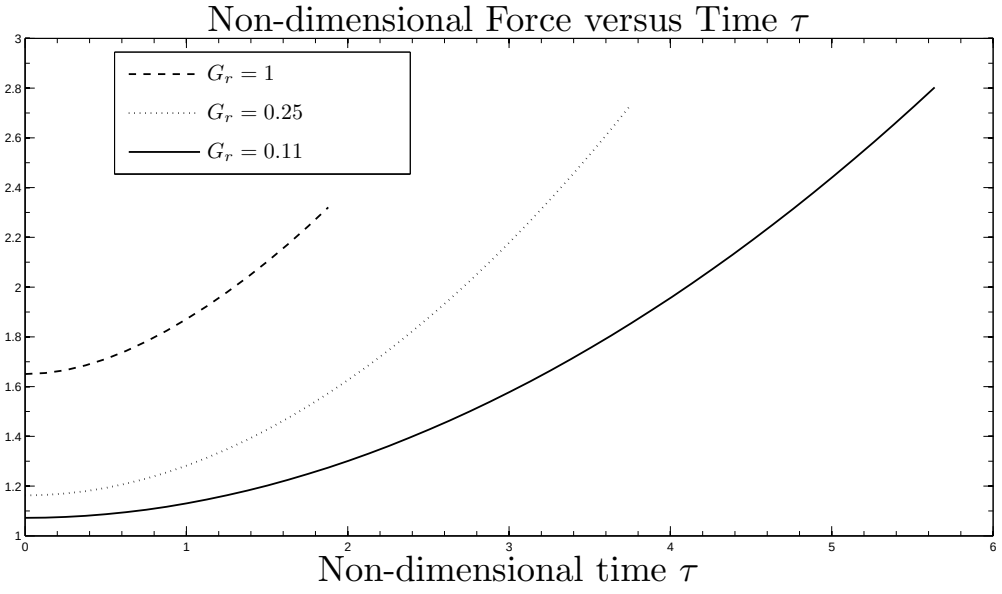

(b)

FIGURE 4.66: Acceleration effect of the box BX1 submerged at a non-dimensional initial depth $\widehat{d}_i$ = entering with different constant acceleration G_τ: plotted at different non-dimensional times $\tau = 1.88, 3.76, 5.64$ and distance $\widehat{d} = -2.77$.

4.4.4.3 Added mass effect

As for symmetric wedges, the added mass of the box body can also be found by conformal mapping, see Barringer (1996). The equation for the analytical added mass and the added mass for a box body taken from the Barringer's derivation is explained.

The force equation of the box body motion is given by complete elliptic integral, giving a curve that can be fitted by the empirical formula:

$$F_a = \frac{1}{2}\frac{dm_a}{dy}\dot{y}^2 + m_a\ddot{y}. \tag{4.40}$$

The added mass force is given by

$$\frac{m_a}{\rho\pi a^2} = 0.50589 + 0.26405\sqrt{\frac{y}{a}} - 0.00104839(\frac{y}{a})^{(\frac{3}{2})} - 0.000014487(\frac{y}{a})^2, \tag{4.41}$$

where a is the bottom half-width of the box and the derivative of the added mass with respect to the depth variable y is given by

$$\frac{1}{\rho\pi a^2}\frac{dm_a}{dy} = 0.132025\frac{1}{\sqrt{ay}} + \frac{0.0251687}{a} + 0.001572585\frac{y}{a} - 0.000028974\frac{y}{a^2}. \tag{4.42}$$

These are compared for the box body with the force difference computed numerically. Fig. (4.67) shows the comparison of the computed force difference and the analytical added mass force computed for the box body BX1. It can be noted that both forces are fairly close to each other at time zero, but here we have resolution problems at the box corners as well as the intersection points.

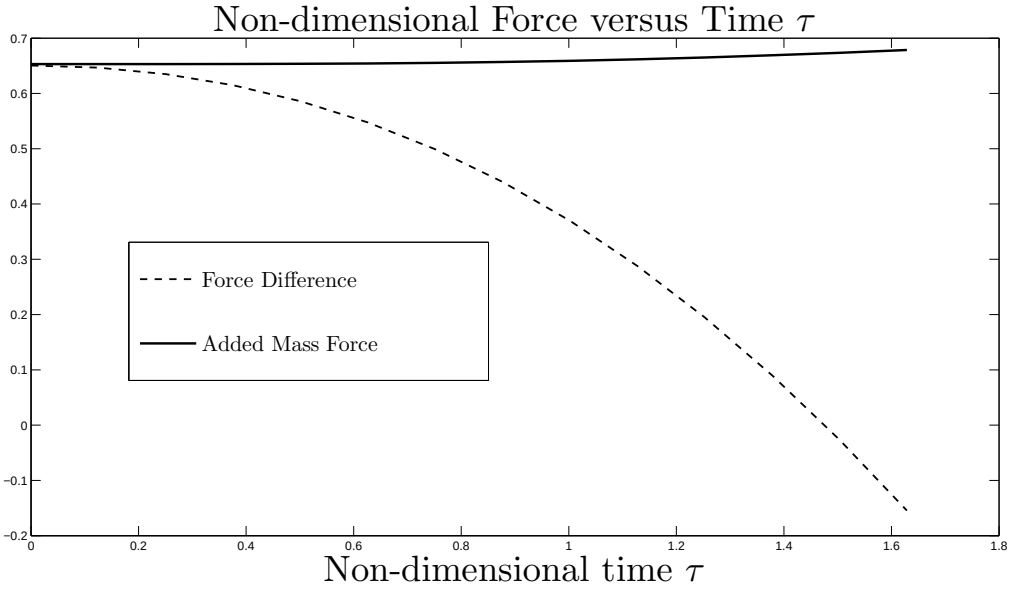

(a)

FIGURE 4.67: Computed numerical force difference and added mass force showing added mass effect for the box BX1 entering with constant acceleration $G_\tau = 1$.

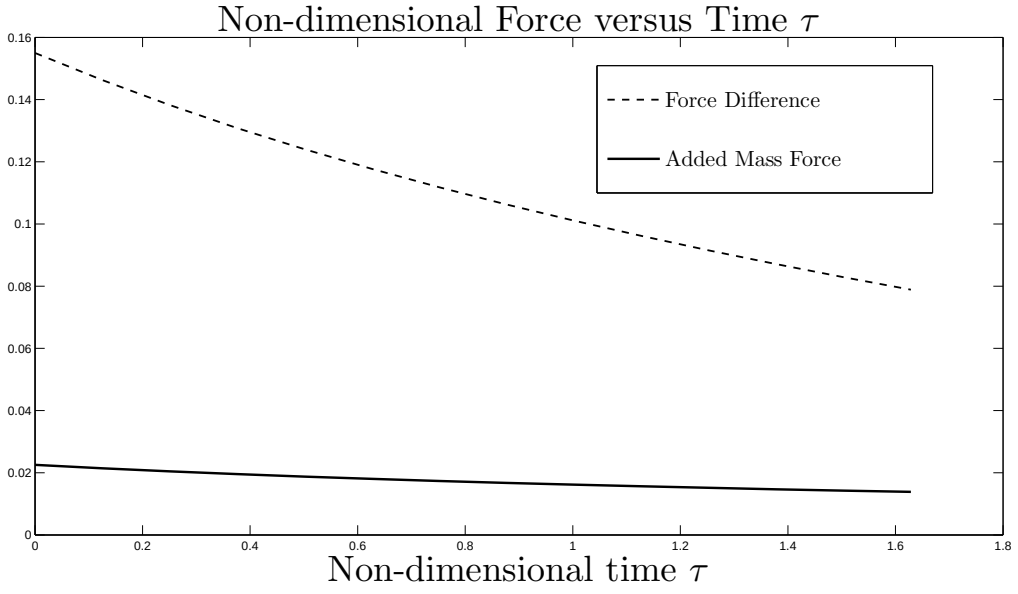

(a)

FIGURE 4.68: Computed numerical force difference and added mass force showing added mass effect for the box BX1 entering with constant velocity of Froude number $F_r = 0.6$.

We also computed the added mass force for the box BX1 entering water with constant velocity. Fig. (4.68) shows comparison of the computed force difference and the analytical added mass force computed for the box BX1 entering water with a Froude number F_r of 0.6. Clearly the added mass theory gives accurate results for small time only for the constant acceleration case. Thus while the value of the added mass given by the simplified added mass model is adequate for small time, its derivative is not. In reality the motion of the free surface will have an effect here.

4.5 Comparison of entry for different wedge angles

In this section, we give a comparison of the computed results for the entry cases with constant velocity and constant acceleration with various angles and shapes. For the constant velocity entry, we present a graph showing the limit of the Froude number which can be used to produce results for a particular shape without breaking the numerical computations. The reason for the breakdown of the numerical computations is the rapid flow created by entry/exit at high Froude number. This causes the fluid particles move fast and creates numerical instability in the computation of the results. This is especially true for the intersection points and also in the derivative of the complex potential at the vertex or corners of the body.

4.5.1 Constant velocity

We numerically studied the entry problem of symmetric wedges, asymmetric wedges, truncated wedges and box by producing extensive results. However, we can only present some results here. Other results are also very useful for future studies of water entry and are included on the CD and explained in Appendix B.

Symmetric wedges

For entry of symmetric wedges, we consider the vertical-half angle varying from 5^o to 55^0. Whilst we selected the angle 30^o to present the computed numerical results, the results for entry of other angles are documented in the CD. As we increase the angles of symmetric wedges for a particular Froude number entry, we can see a significant difference in the results for free-surface profile, pressure and force. We also notice that the change in Froude number for a particular wedge will give noticeable effects on the results. The maximum Froude number that can be used for entry of the symmetric wedges is plotted in Fig. (4.69).

By comparing the computed results for entry given in the CD showing the finite-depth effect, we can see much more effects in the force. It means that the contact surface becomes flatter, which more strongly affects the motion of the particles as we increase the angle of entry.

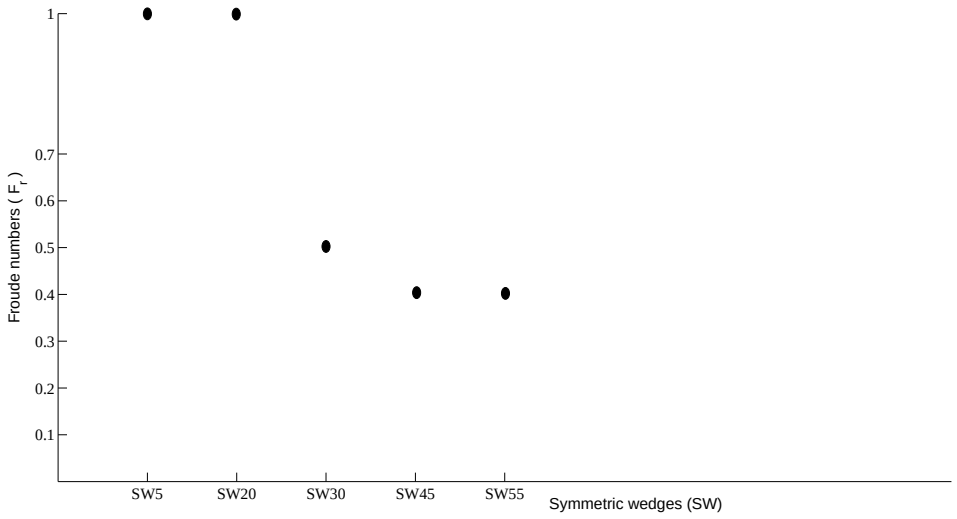

FIGURE 4.69: Froude numbers for the symmetric wedges entering with constant velocity.

The following Table. (4.4) shows the computed value of speed of the intersection point for entry of the symmetric wedges which was computed for the Froude number of 0.4 that is the maximum Froude number that can be used to compute results for the entry of all the symmetric wedges.

Symmetric wedge (SW)	**Speed of intersection point** (v_i)
SW5	0.276
SW20	0.590
SW30	0.963
SW45	1.071
SW55	1.244

TABLE 4.4: Speed of the intersection points for symmetric wedges considered for water entry cases at t=0

We note that at t=0 this non-dimensional speed is independent of the Froude number, suggesting that some sort of extension of Wagner's model for flat wedges (small deadrise angles) might be appropriate. However, Wagner's outer solution relies on the very simple flow around a flat plate; for the diamond-shaped double body here, the corresponding outer solution is far more complicated and so has not been attempted. Finally, by comparing the results for entry using Mackie's theory, we do not see good agreement. It does not work either for entry of slender wedge cases or flatter wedges.

Asymmetric wedges

For entry of asymmetric wedges, we considered three different asymmetric wedges and presented results for asymmetric wedge (AW4) with left-half-wedge angle -10^o and right-half-wedge angle 30^o entering water in section (4.3.2). By comparing the results in the CD for other asymmetric wedges, we notice that the Froude numbers that can be used for asymmetric wedges are not same as for the symmetric wedges. It means that we need low Froude numbers to obtain better numerical results due to the complex flow involving for high Froude number entry of asymmetric wedges. We can also notice that we can see much more effect in the results as we increase the wedge angles. The Froude numbers that can be used to run entry of the asymmetric wedges are given in Fig. (4.70).

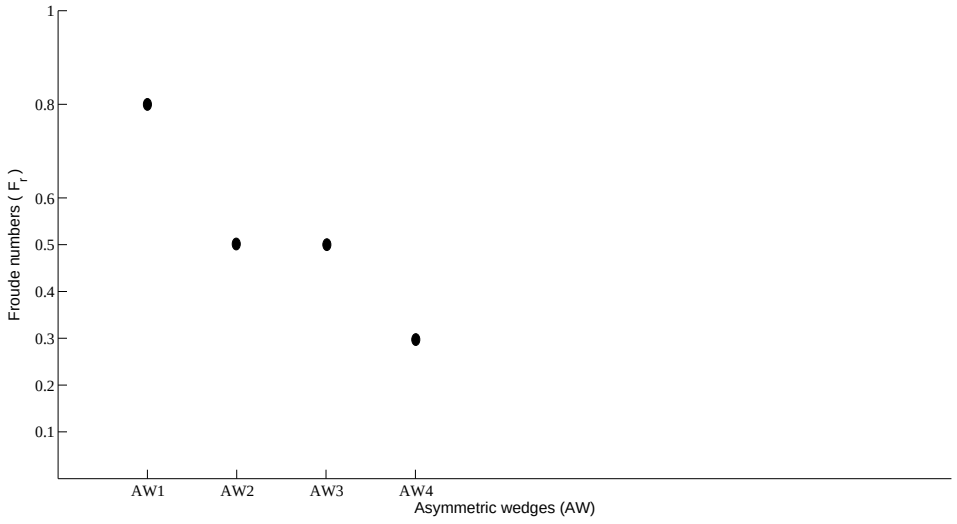

FIGURE 4.70: This figure shows the Froude numbers for the asymmetric wedges entering with constant velocity.

Finally, we can see a significant effect in the finite depth cases of asymmetric wedges compared with the symmetric wedge cases, see the CD for more details.

Truncated wedges

For entry of truncated wedges, we considered three different symmetric wedges of left and right half-wedge angles 10^o, 20^o and 30^o entering with different Froude numbers. We can produce more results by considering different aspect ratios

and asymmetric truncated wedges. However, we only considered some cases for simplicity of the study in this thesis. Similar effects as entry of other wedges can be noticed for the test cases as the angle increases. By comparing with the results for the finite depth effect of entry of symmetric wedges and truncated wedges of same angles, it can be noticed that a small difference in the results of the truncated wedges can be seen due to the flatted bottom surface of the truncated wedges.

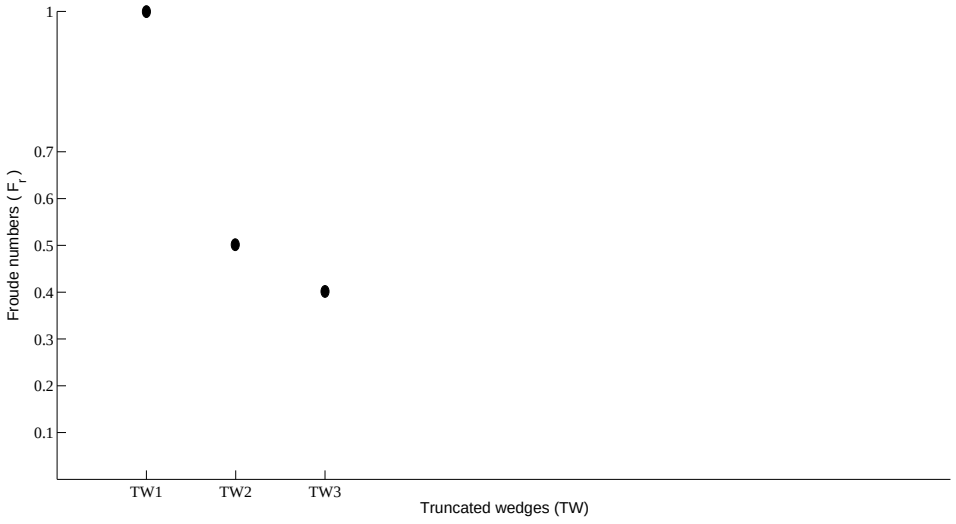

FIGURE 4.71: This figure shows the Froude numbers for the truncated wedges entering with constant velocity.

Box

For entry of box, we only considered one box BX1 because the computed results do not show very significant effects. However, there is a noticeable effect in the finite depth case as it has a flat bottom surface, making it very hard to push the water under it.

4.5.2 Constant acceleration

We considered similar shapes as for constant velocity entry to compute and present numerical results for constant acceleration. The considered test cases for the entry with constant accelerations examine the time effect, acceleration effect and added mass effect for symmetric wedges and box. By increasing the angle of the wedges

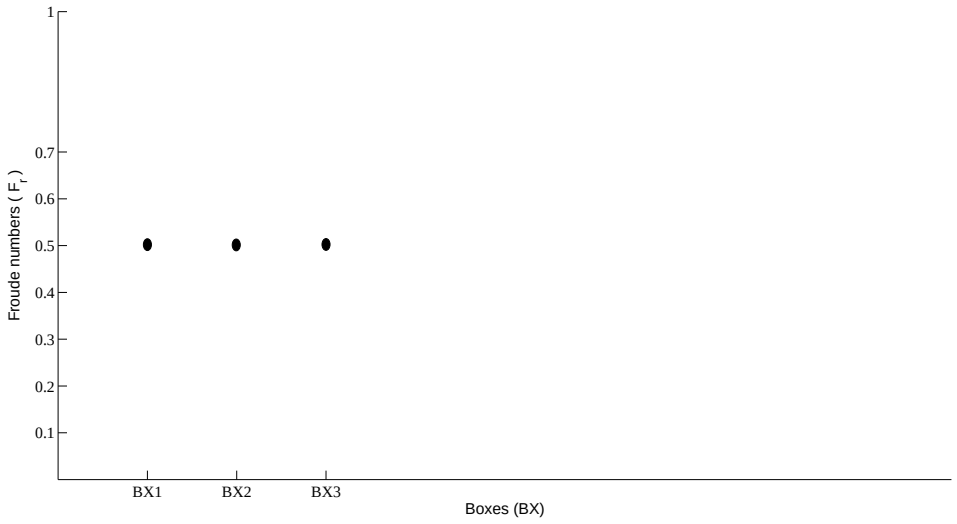

FIGURE 4.72: This figure shows the Froude numbers for the boxes entering with constant velocity.

and accelerations, it is not possible to run the code because the intersection points move rapidly and causes numerical break down.

We presented results by choosing appropriate entry accelerations which vary with the angle of the wedges. By comparing the results for each shape (see the CD), we can see much more effect on the free-surface profile, the pressure distribution and the force as the angles and the constant acceleration of the entry increase for entry of each shape.

For entry of the symmetric wedges and box body, we computed analytical added mass force and compared with the numerical force difference. The results for entry of the symmetric wedge SW30 were presented in section (4.4.1), whereas others are given in the CD. By comparing the results for entry of each shape, we notice that there is generally good agreement of the analytical result with the numerical results initially for constant acceleration cases. However, the result for entry with constant velocity does not give good agreement because the theory can not simply cope when the free surface also moves, thereby affecting the effective submerged volume of the body and hence the force. The added mass theory in general underestimates the hydrodynamic forces, which we believe is to be expected. In addition to that, for the box cases, this may be due to difficulties in calculating the hydrodynamics pressure at corner points on the contour. On the other hand, the added mass theory is generally good for acceleration cases.

Chapter 5

Water Exit of Different Shaped Bodies

In this chapter, we present a set of selected results for water exit of symmetric wedges, asymmetric wedges, truncated wedges and boxes exiting with constant velocity and constant acceleration from water initially at rest. To verify the computed results, we carry out a set of tests such as convergence checks, Froude number effect for the constant velocity cases, time effect on the fluid motion and added mass effect on force for constant acceleration cases. The two-dimensional shapes selected to compute results for water exit are explained in section (5.1). The constant velocity exit and constant acceleration exit are considered in sections (5.2) and (5.3), respectively. We also give some results showing the finite depth effect on exit problems and consider the speed of the intersection points for exit of symmetric wedges. Finally, we present results to compare analytic results computed by using Mackie's (1969, 1965 and 1962) theory (see Greenhow (1990)) for exit of symmetric wedges with the results produced by the present non-linear time-stepping method of Vinje and Brevig (1981a and 1981b).

5.1 Shapes

In addition to the 2D shapes considered to study water entry problems, we consider the following combined body of wedge and thin plate with various angles to compute results for water exit cases with constant velocity or acceleration. The fluid particles follow the bodies exiting water after some time steps. To study

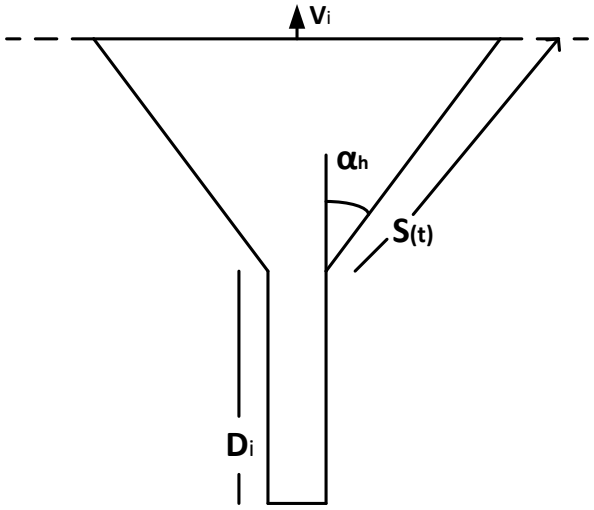

FIGURE 5.1: Combined body of wedge and thin plate for water exit cases

the motion after that stage, we attached a very thin plate shaped body to the symmetric wedge close to the vertex and present some results for the combined body exiting water with constant velocity and constant acceleration. This then allows us to calculate the fluid motion after the wedge has completely exited the fluid. We also assume that there is no vortex shedding around the corners for the combined shape considered as assumed for the symmetric wedge entering fluid in the previous chapter. We do not consider possibility of vortex shedding from the exiting symmetric wedges, the edges of the exiting truncated wedge or the exiting box (where vortex shedding is likely to be important).

5.2 Constant velocity exit

This section, for constant velocity exit of symmetric wedges, asymmetric wedges, truncated wedges and box bodies, reviews the application of the non-linear theory and concerns numerical results computed using the implementation of the equations formulated to study water exit problems in Matlab. For each shape considered for entry cases and shown in Fig. (5.1), we present computed free-surface profile, pressure distribution along the wetted part of the body and numerical total force experienced by the body as it exits through the free surface with constant velocity. To verify the results computed for the bodies, we carry out a set of convergence checks. We examine the Froude number effect, the time effect on motion,

the finite depth effect, and the speed of intersection points between the symmetric wedges and the free surface changing with depths of fluid and Froude number of entry. The symmetric wedges, combined body, asymmetric wedges, truncated wedges and boxes exiting with constant velocity are presented in sections (5.2.1), (5.2.2), (5.2.3), (5.2.4) and (5.2.5) respectively.

5.2.1 Symmetric wedge exit

The main parameters of the problem of symmetric wedge exit are the vertical half wedge angle α_h and the initial submerged depth D_i, see Fig. (4.1(a)). We can compute numerical results for various symmetric wedges, which can be obtained by changing the main parameters of the problem, exiting with different Froude numbers which can be chosen by changing values of the submerged depth and the speed of exit. However, the maximum of the half-wedge angle for high speed of exit is 85^o. In the symmetric-wedge entry case, we present results for various half-wedge angles without breaking numerical computations by carefully selecting the number of points on the boundaries and the velocity of exit. Table (5.1) shows the symmetric wedges (for example, SW30 is a wedge of vertical half-wedge angle 30^0) selected to present results for constant velocity exit and constant acceleration exit. Other results are written on a CD for future studies, see Appendix (B). The results for different Froude numbers are given in section (5.2.1.1). The computed numerical results showing the time effect are presented in sections (5.2.1.2). The finite depth effect and speed of the intersection points for constant velocity exit of symmetric wedges are presented in sections (5.2.1.3) and (5.2.1.4) respectively. Finally, comparison of free-surface profile with Mackie's analytical results for constant velocity of exit of the symmetric wedges is given in section (5.2.1.5).

Symmetric wedge (SW)	**Half wedge angle** (α_h)
SW5	5^o
SW10	10^o
SW20	20^o
SW30	30^o
SW45	45^o
SW85	85^o

TABLE 5.1: Symmetric wedges considered for exit cases

5.2.1.1 Froude number effect

In the study of water exit related problems, the Froude number defined in previous chapter is also a crucial dimensionless physical parameter. To study the effect of Froude number on the motion of exit, we carry out a set of test cases. For a particular symmetric wedge, the test process is to keep all the input variables of a specific run of the program constant, and obtain the Froude numbers by varying the velocity of the exit for the symmetric wedge. We plot the results for the free surface profile, pressure and force at the same distance traveled by the wedge for different exit speeds as time progresses. As we increase the velocity of the exit, we notice much more deformation on the free surface and consequently in the pressure distribution and force as shown in Fig. (5.2) and (5.3) for the symmetric wedge SW30.

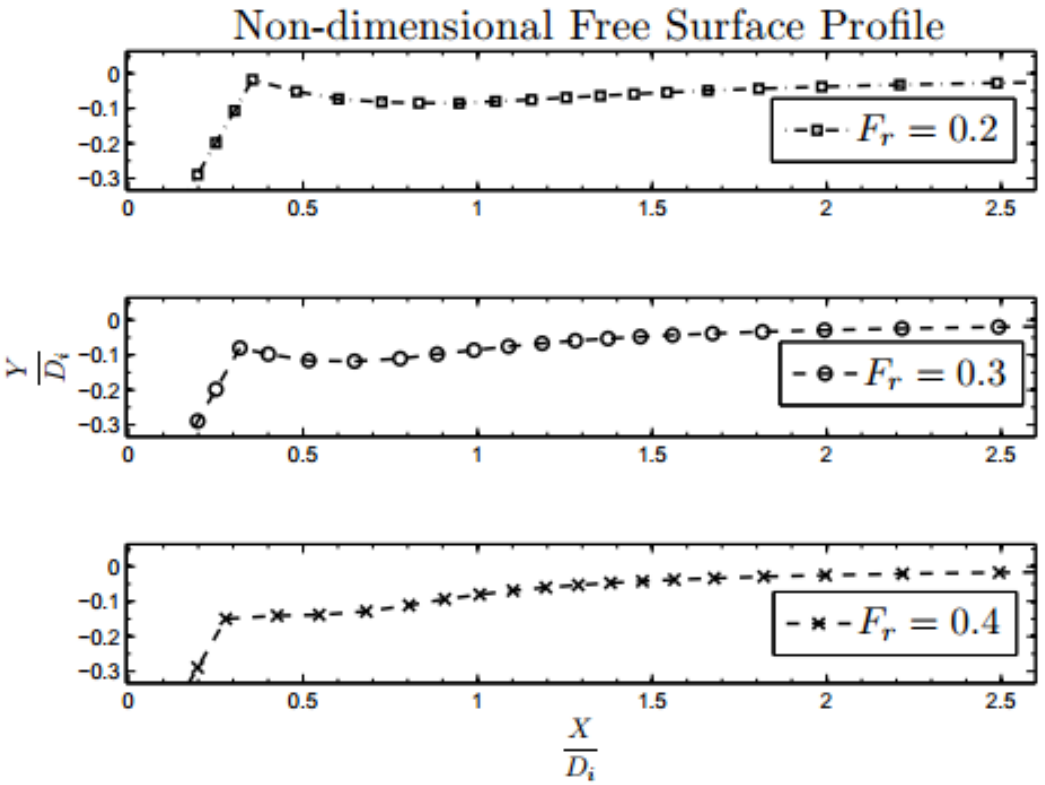

(a)

FIGURE 5.2: Froude number effect of the symmetric wedge SW30 submerged at a non-dimensional initial depth $\widehat{d}_i = -1$ exiting with constant velocity of different Froude numbers: plotted at different non-dimensional times $\tau = 1.8, 1.2, 0.9$ and distance $\widehat{d} = -0.63$.

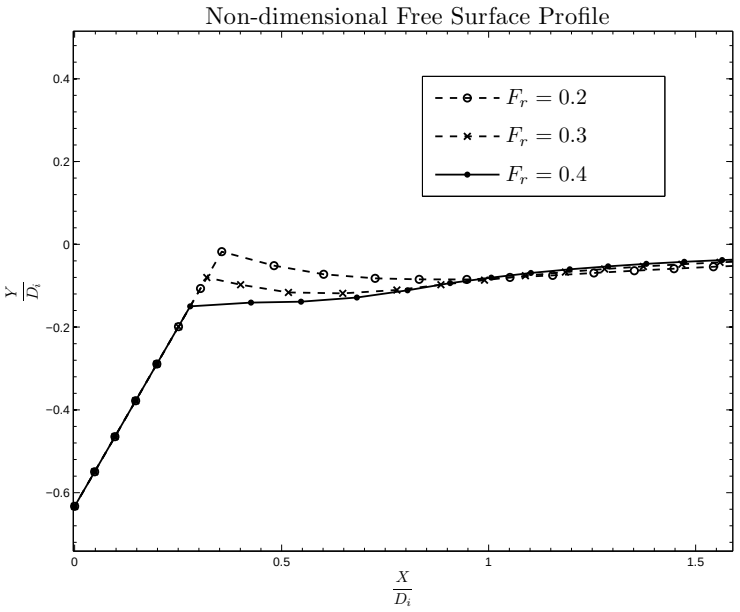

(a)

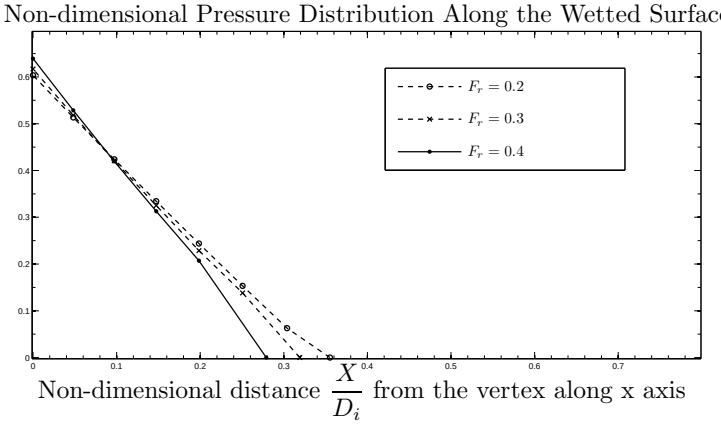

(b)

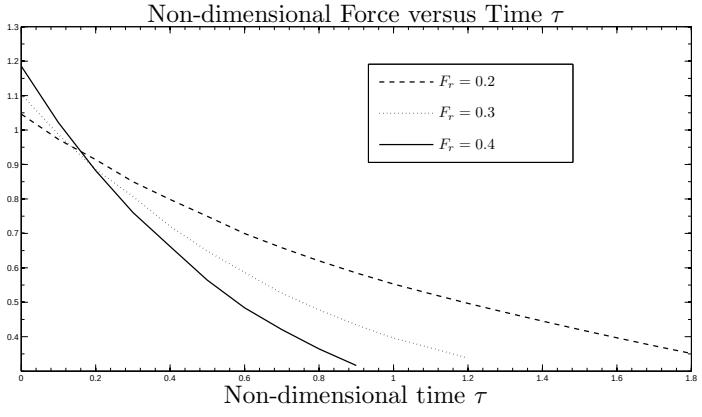

(c)

FIGURE 5.3: Froude number effect of the symmetric wedge SW30 submerged at a non-dimensional initial depth $\widehat{d_i} = -1$ exiting with constant velocity of different Froude numbers F_r: (a) and (b) are plotted at different non-dimensional times $\tau = 1.8, 1.2, 0.9$ and distance $\widehat{d_i} = -0.63$.

5.2.1.2 Time effect

The fluid motion caused by the body exiting water changes as time progresses. We can compute the deformed free-surface profile, pressure along the wetted part of the body and the upward force experienced by the body using the non-linear theory. The computed results showing the time effect on free surface, pressure and force at different stages of the exit with constant velocity are presented in this section. Fig. (5.4) to (5.7) show the time effect of the symmetric wedge SW30 exiting with a Froude number of 0.4.

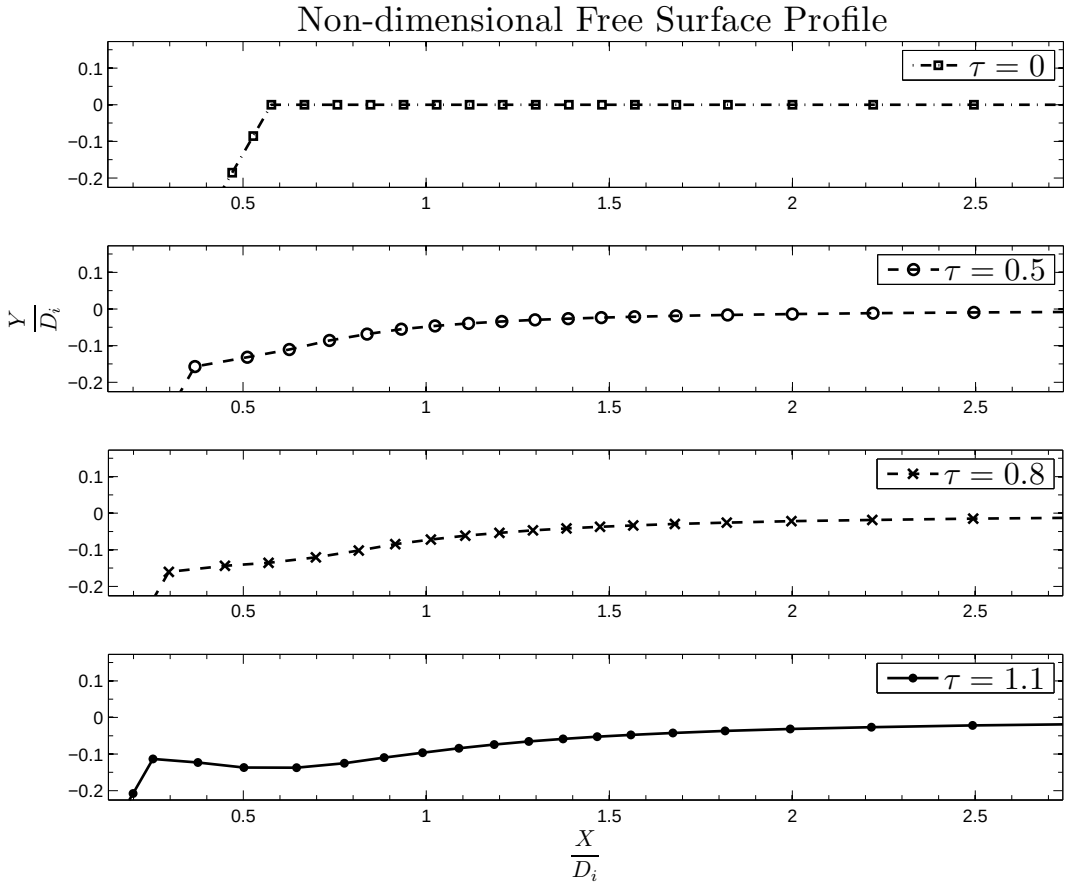

(a)

FIGURE 5.4: Time effect of the symmetric wedge SW30 submerged at a non-dimensional initial depth $\widehat{d_i} = -1$ exiting with constant velocity of Froude number $F_r = 0.4$: plotted at different non-dimensional times τ.

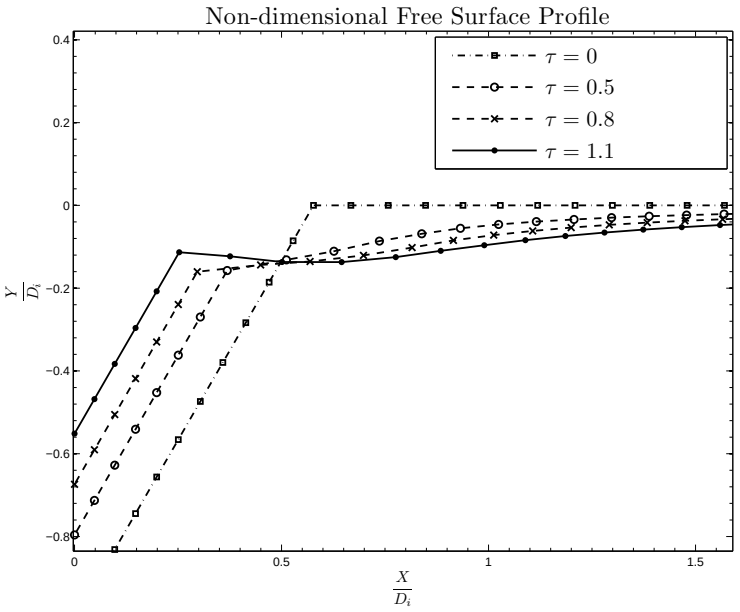

(a)

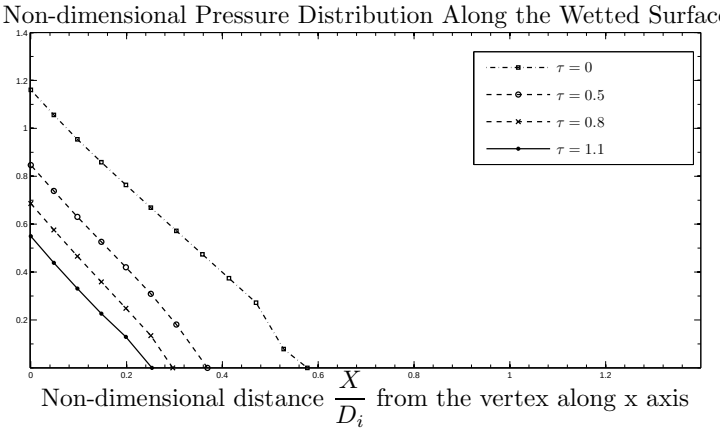

(b)

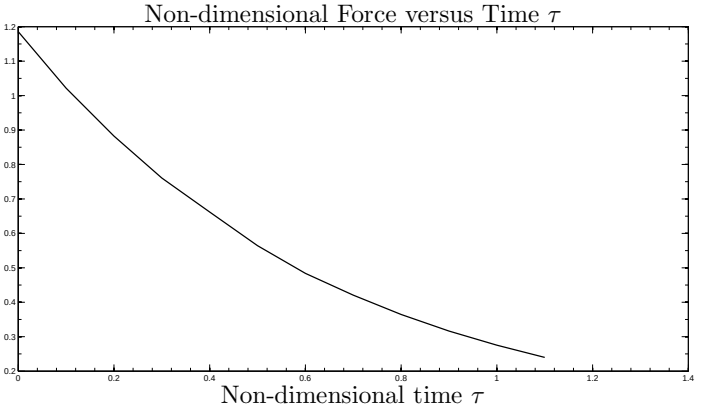

(c)

FIGURE 5.5: Time effect of the symmetric wedge SW30 submerged at a non-dimensional initial depth $\widehat{d_i} = -1$ exiting with constant velocity of Froude number $F_r = 0.4$: (a) and (b) are plotted at different non-dimensional times τ.

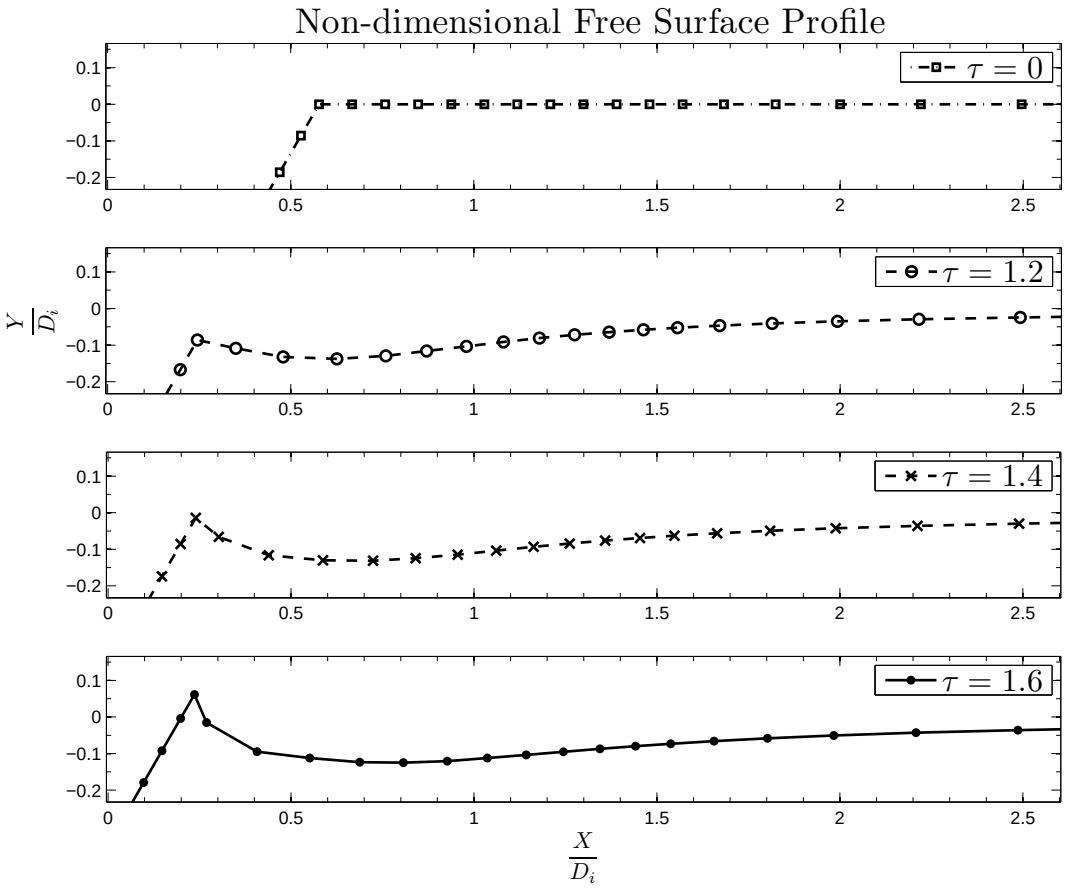

(a)

FIGURE 5.6: Time effect of the symmetric wedge SW30 submerged at a non-dimensional initial depth $\widehat{d_i} = -1$ exiting with constant velocity of Froude number $F_r = 0.4$: plotted at different non-dimensional times τ.

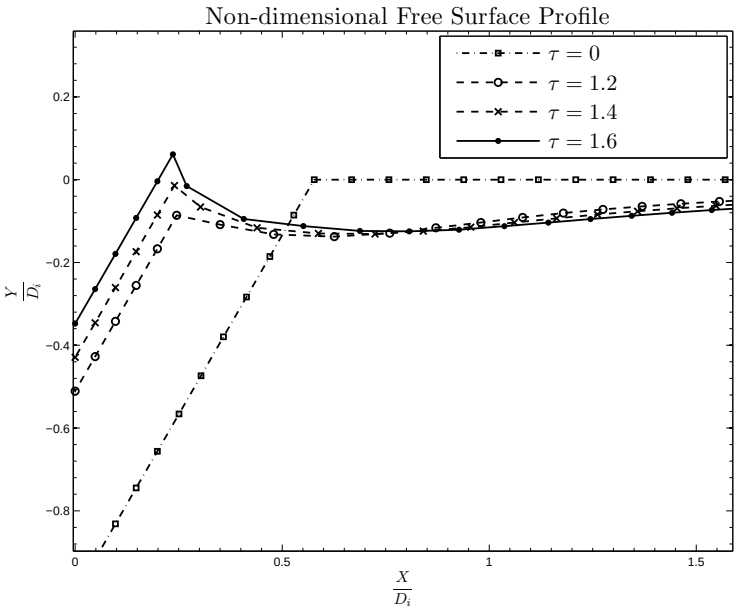

(a)

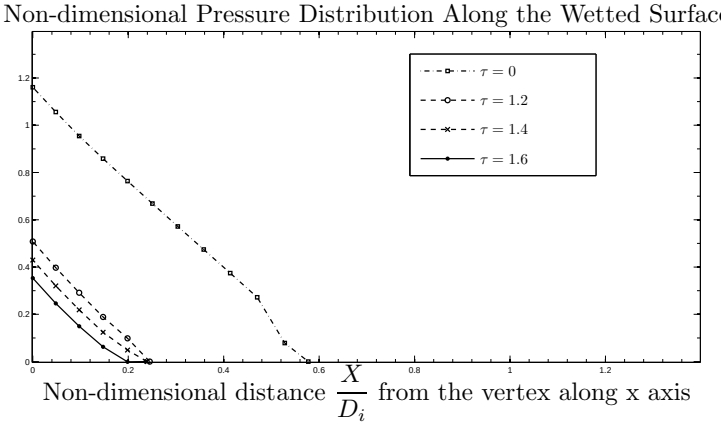

(b)

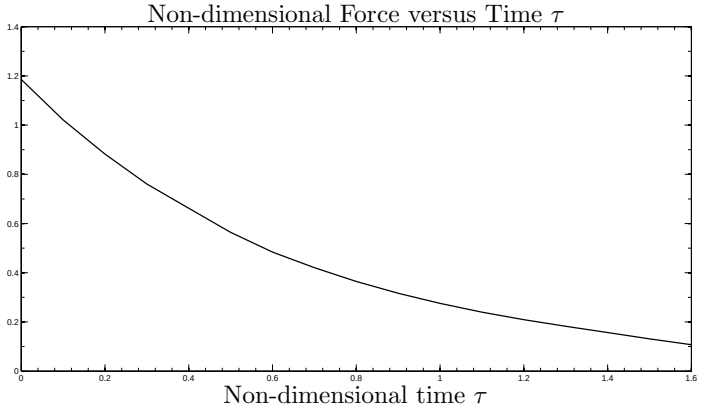

(c)

FIGURE 5.7: Time effect of the symmetric wedge SW30 submerged at a non-dimensional initial depth $\widehat{d_i} = -1$ exiting with constant velocity of Froude number $F_r = 0.4$: (a) and (b) are plotted at different non-dimensional times τ.

5.2.1.3 Finite depth effect

It is very important to predict the motion due to the marine vehicle operations near to the shore (shallow water), as for the water entry of bodies. We present results showing effect on the free-surface profile, pressure and force due to the change in depth of the entry with constant velocity using the non-linear time-stepping method. The results are plotted at the same distance for different depths with the same velocity as it moves with time. Fig. (5.8) represents the computed free-surface profile, pressure distribution and force for the symmetric wedge SW30 entering with a Froude number 0.4, showing the finite depth effect on the motion. We notice, as expected, that for exit of the symmetric wedge SW30, a non-dimensional depth N_d below 1 experiences greater variation of free-surface deformation, pressure and force than that of other depths.

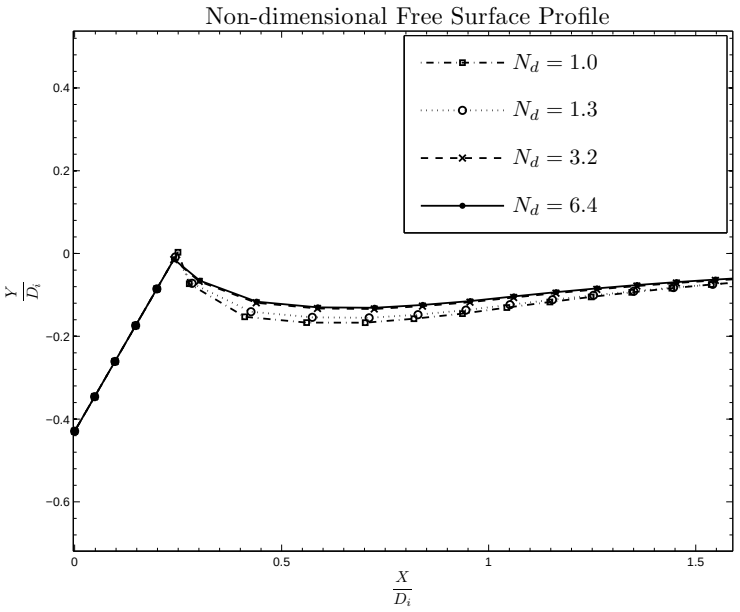

(a)

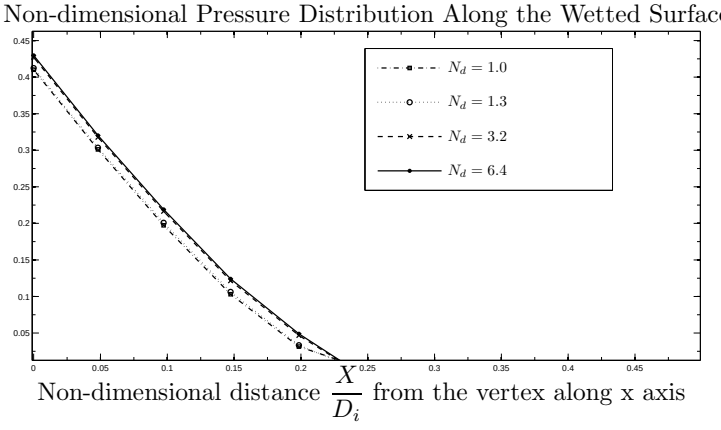

(b)

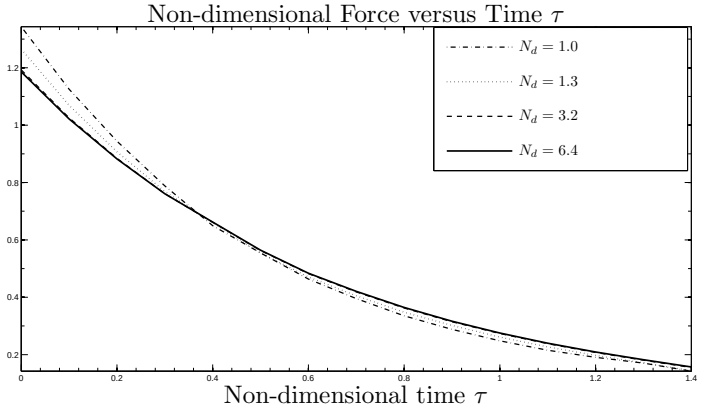

(c)

FIGURE 5.8: Finite depth effect of the symmetric wedge SW30 submerged at a non-dimensional initial depth $\widehat{d_i} = -1$ exiting with constant velocity of Froude number $F_r = 0.4$: (a) and (b) are plotted for different non-dimensional depths N_d at a non-dimensional time $\tau = 1.4$.

5.2.1.4 Speed of intersection point

To study the local flow around the intersection points of exiting symmetric wedges, it is very useful to compute the speed of the intersection points as the body exiting with time. This section presents some results for the speed of intersection points of exiting different symmetric wedges, but it can also be computed for all other shapes.

Speed effect with Froude number

Here we give the computed speed of the intersection points for the symmetric wedges considered showing the effect due to a change in Froude number. The plots are obtained for each shape exiting with different Froude numbers while attaining the same distance traveled by the symmetric wedge as it exits. Fig. (5.9) shows the Froude number effect on the speed of the symmetric wedge SW30. We can see that the initial speed at time zero is same for any velocity of exit, as expected (see the discussion for the entry case, section (4.5)), but that it is substantially higher for exit for the same spatial and temporal resolutions.

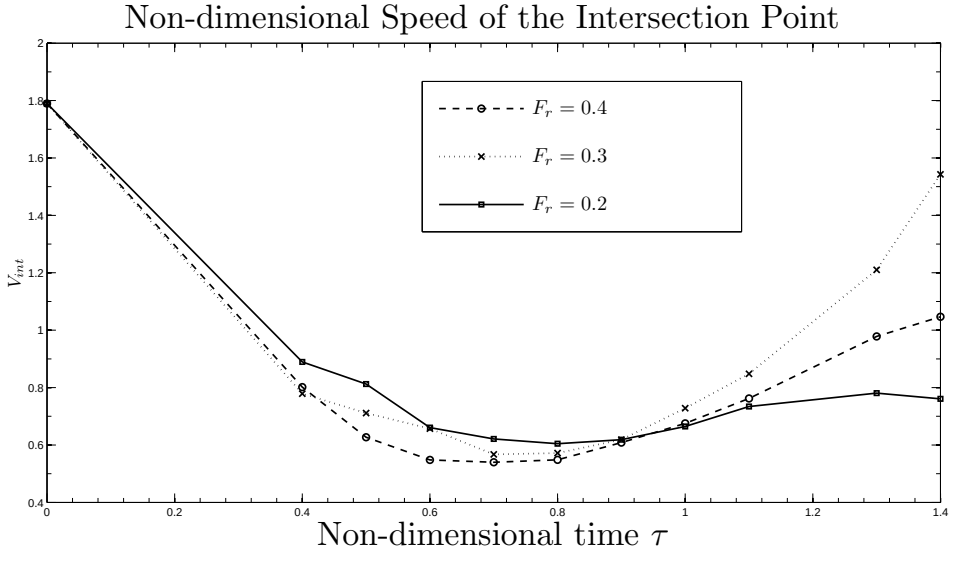

FIGURE 5.9: Froude number in the speed of intersection point for the wedge SW30 exiting with constant velocity.

Speed effect with depth

Here we present the computed speed of the intersection points of the symmetric wedges considered showing effect due to the change in depth of the domain. The plots are obtained for each shape exiting with constant velocity while attaining the same distance traveled by the symmetric wedge as it exits. Fig. (5.10) shows the computed speeds for the symmetric wedge SW30 exiting from the fluid of different depths. Here, we note that starting values of the speed at time zero vary with depth of the fluid.

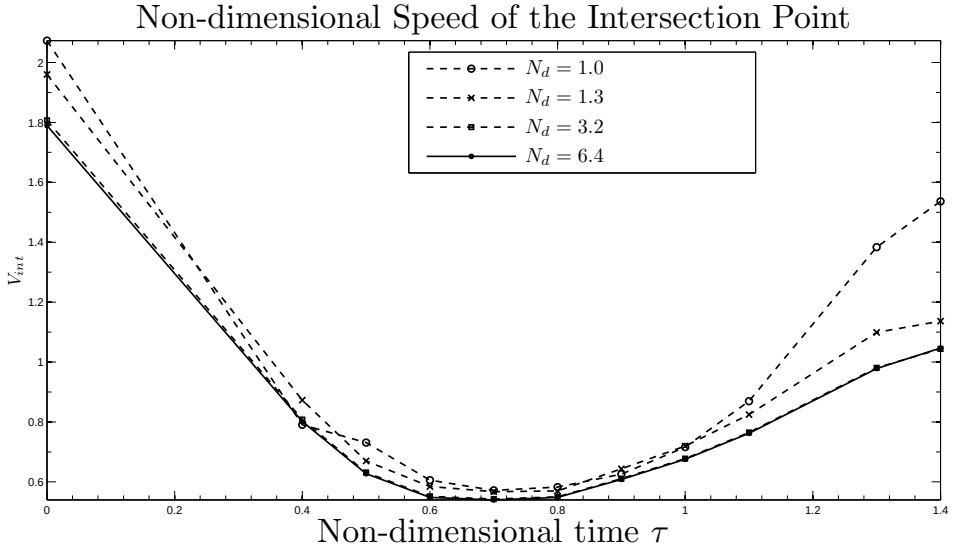

FIGURE 5.10: Effect of depth in the speed of intersection point for the wedge SW30 exiting with constant velocity of Froude number $F_r = 0.4$.

5.2.1.5 Comparison with Mackie's theory

We compare the results for free surface elevation computed using the fully nonlinear time-stepping method with the Mackie's (1969, 1965 and 1962) theory based on time-dependent wave-maker theory for slender body. The linearised free surface profile can be expressed as, see Greenhow (1990),

$$\eta(x,t) = \frac{2}{\pi}\int_0^\infty \bar{\eta}(\lambda,t)\cos\lambda x d\lambda. \tag{5.1}$$

For exit, we have

$$\begin{aligned}\bar{\eta}(\lambda,t) = {} & \alpha_h U^2 e^{-\lambda D}\left[\frac{\cos(\sqrt{\lambda g}t) - e^{-\lambda U t}}{\lambda(\lambda U^2+g)}\right] \\ & - \frac{\alpha_h U e^{-\lambda D}\sin(\sqrt{\lambda g}t)}{\lambda(\lambda U^2+g)\sqrt{\lambda g}}\left[\lambda U^2 e^{\lambda D} + g(e^{\lambda D}-1)\right],\end{aligned} \tag{5.2}$$

where U is velocity, D is initial draft for exit and α_h is the wedge half-angle. Based on the formulation, we present computed results showing moderate agreement with the non-linear time-stepping theory of Vinje and Brevig (1981a; 1981b) for some symmetric wedges exiting with constant velocities. Fig. (5.11) shows the comparison for the symmetric wedge SW5 exiting with Froude number 0.4. However, for larger angles the agreement in free surface profiles (see Appendix B) is not as good as expected.

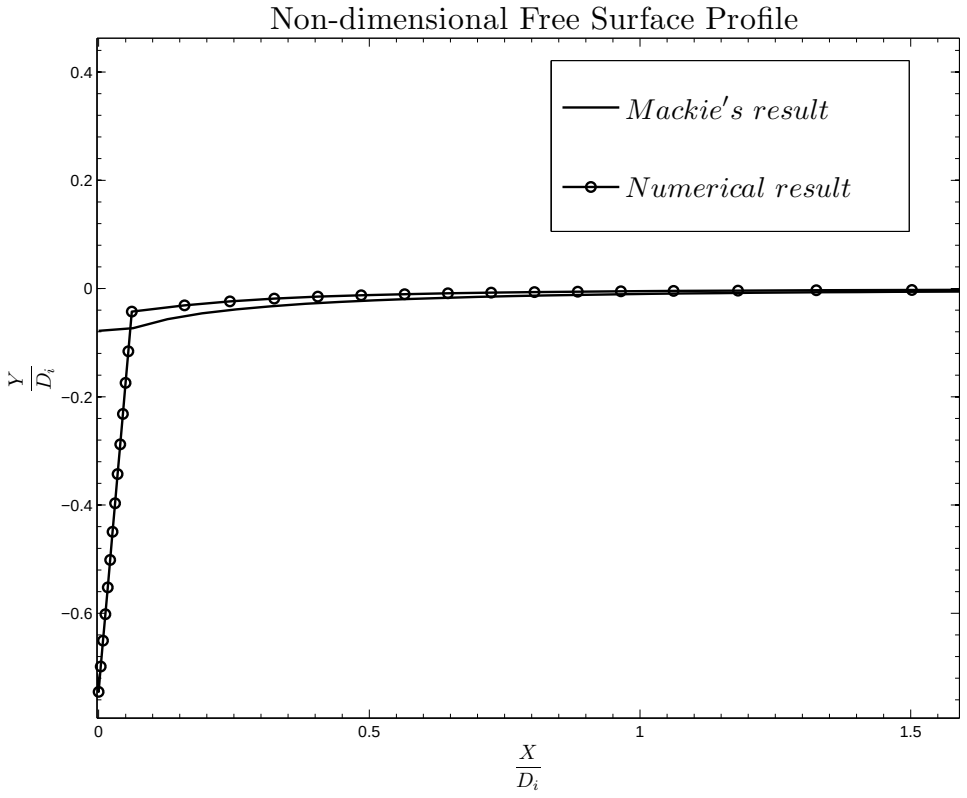

(a) at a non-dimensional time $\tau = 0.5$

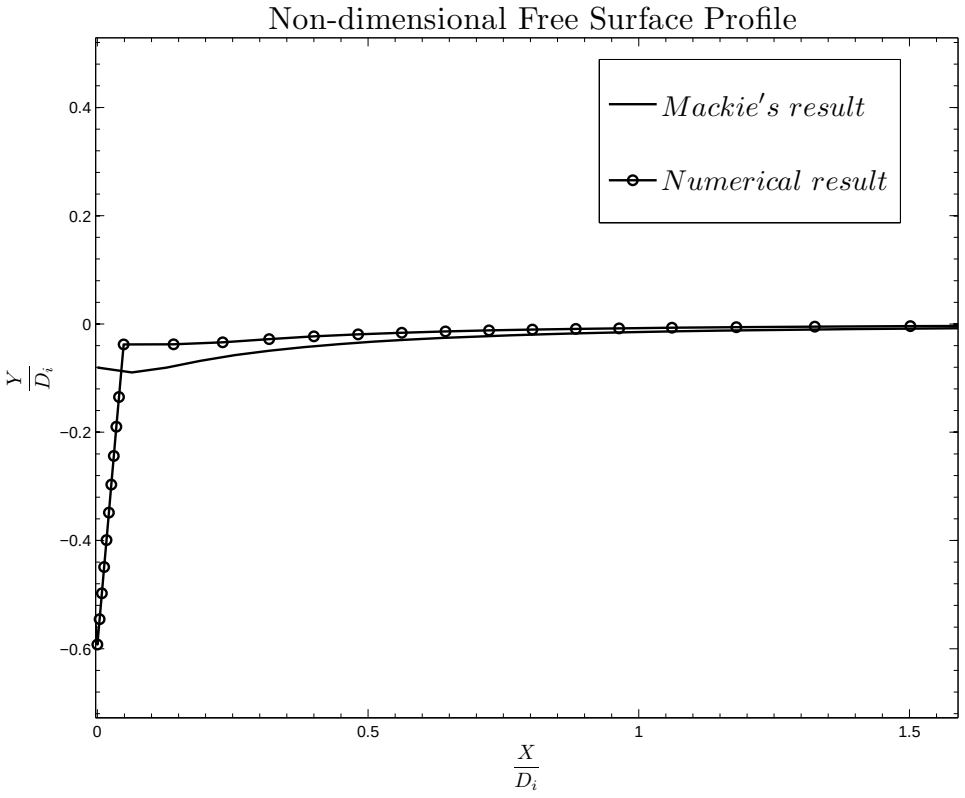

(b) at a non-dimensional time $\tau = 0.8$

FIGURE 5.11: Comparison of computed free surface profile with Mackie's resuls for the wedge SW5 exiting with constant velocity of $F_r = 0.5$.

5.2.2 Combined body exit

This section presents computed results for the combined body exiting with constant velocity. Section (5.2.2.1), (5.2.2.2) and (5.2.2.3) give some results for the combined body CW30 of half-wedge angle 30 attached to a thin plate showing Froude number effect, time effect on the motion and finite depth effect, respectively.

Fig. 5.12(a) and 5.12(b) show the comparison between the symmetric wedge (SW30) and the combined body (CB30) plotted at the same non-dimensional time intervals. From Fig. (5.12), we can see there is no difference in the free-surface profile at different times. We also checked the results for the wedge SW30 combined body CB30 exiting with different Froude numbers and noticed no changes between the results of the two bodies.

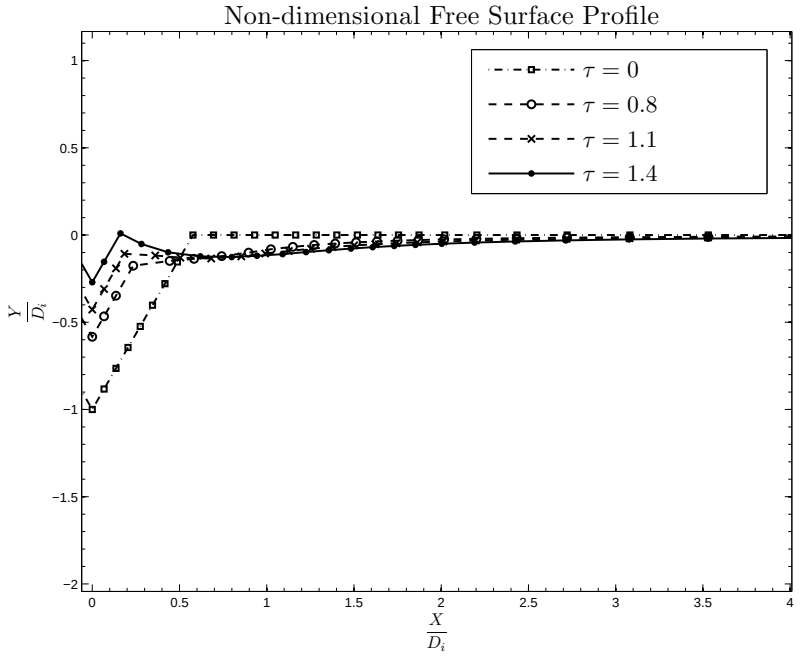

(a) symmetric wedge SW30

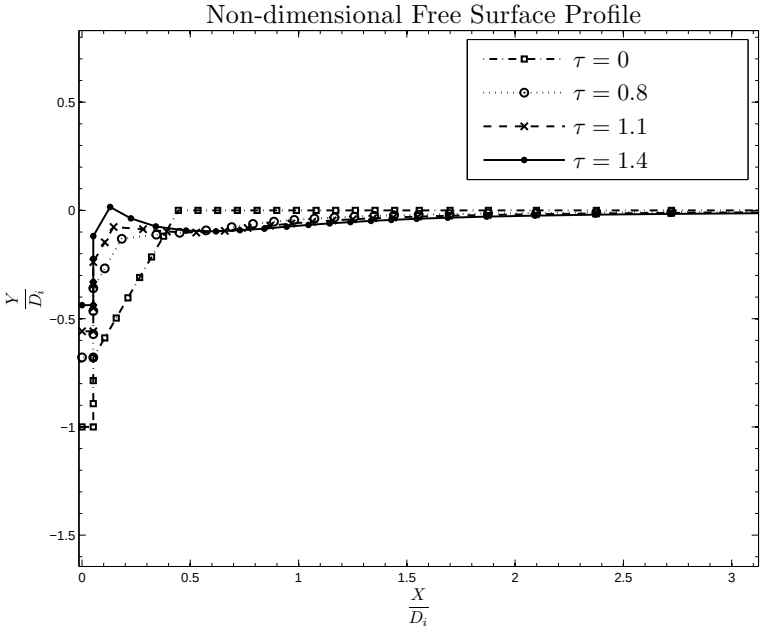

(b) combined body CB30

FIGURE 5.12: Time effect of the combined body CB30 and the symmetric wedge SW30 submerged at a non-dimensional initial depth $\widehat{d_i} = -1$ exiting with constant velocity of Froude number $F_r = 0.4$: plotted at different non-dimensional times τ.

5.2.2.1 Froude number effect

To study the effect of Froude number on the results, we carry out a set of test cases. For a particular combined wedge, the test process is to keep all the input variables of a specific run of the program constant, and obtain the Froude numbers by varying the velocity of the exit for the combined wedge. We plot the results for the free-surface profile, pressure and force at the same distance traveled by the combined wedge for different exit speeds as time progresses. As we increase velocity of the exit, we notice much more deformation on the free surface and consequently in the pressure distribution and force as shown in Fig. (5.13) and (5.14) for the combined wedge CW30.

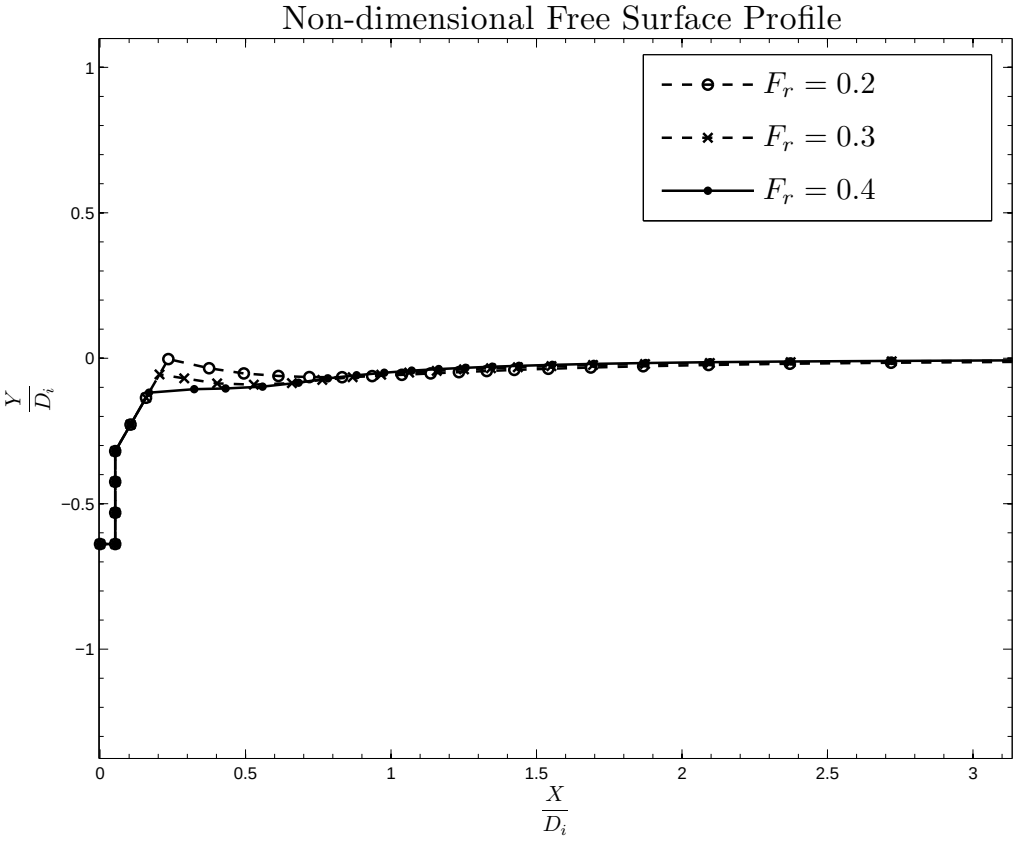

(a)

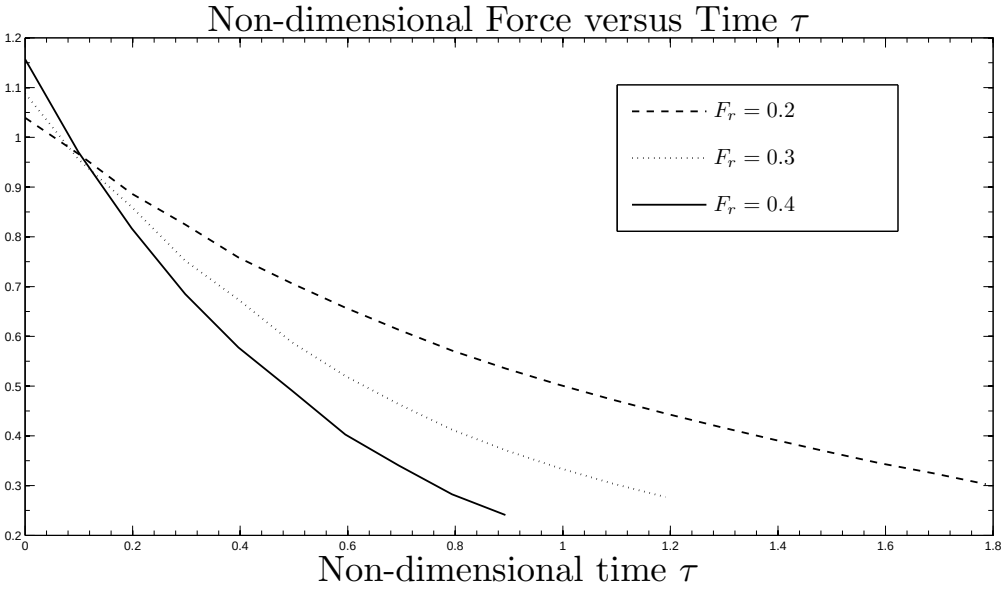

(b)

FIGURE 5.13: Froude number effect of the combined body CB30 submerged at a non-dimensional initial depth $\widehat{d}_i = -1$ exiting with constant velocity of different Froude numbers F_r: plotted at different non-dimensional times $\tau = 1.79, 1.19, 0.89$ and distance $\widehat{d} = -0.639$.

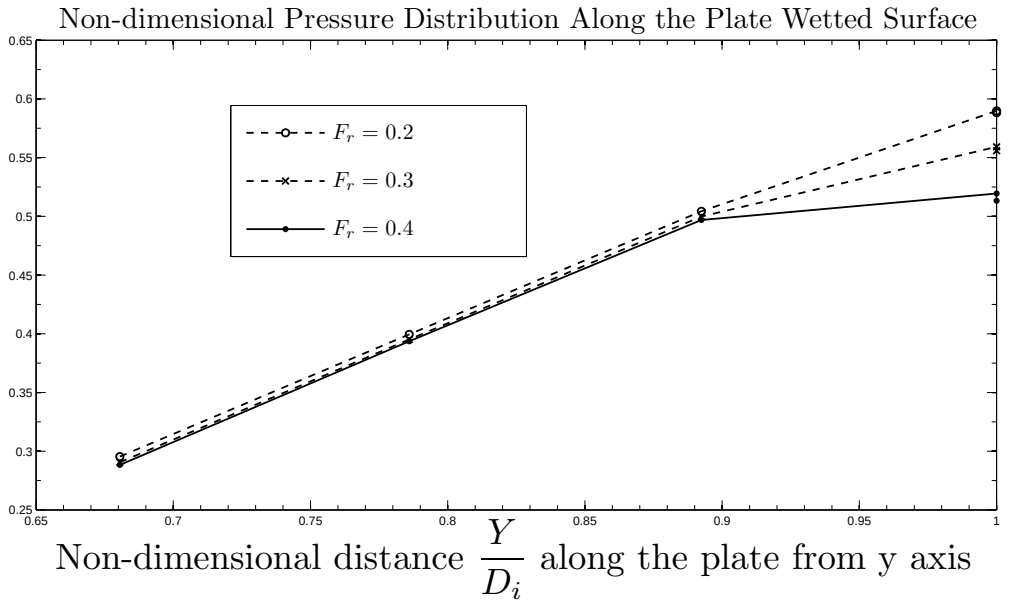

(a)

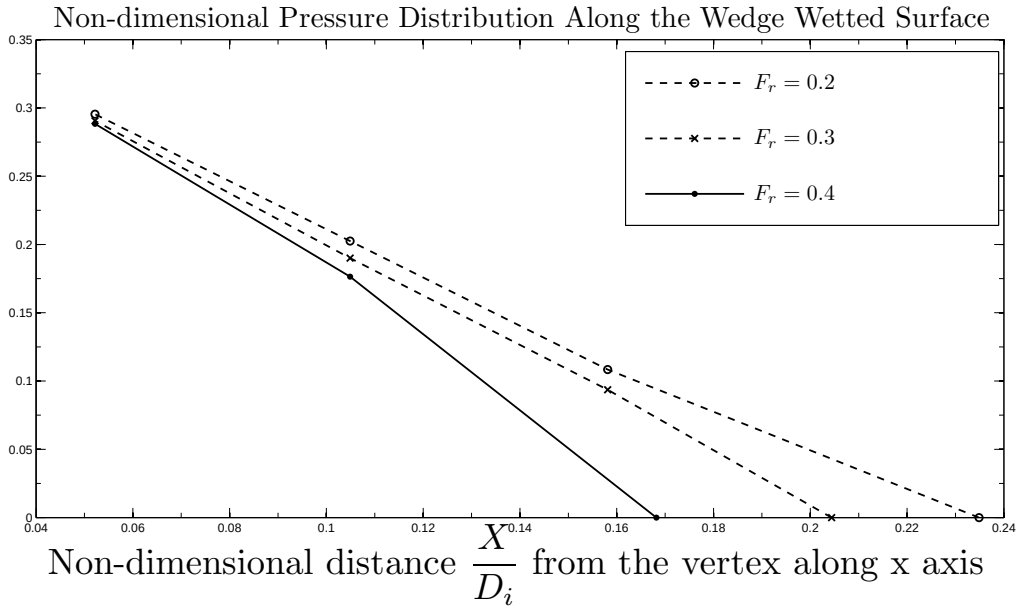

(b)

FIGURE 5.14: Froude number effect of the combined body CB30 submerged at a non-dimensional initial depth $\widehat{d}_i = -1$ exiting with constant velocity of different Froude numbers F_r: plotted at different non-dimensional times $\tau = 1.79, 1.19, 0.89$ and distance $\widehat{d} = -0.639$.

5.2.2.2 Time effect

The computed results showing time effect on free surface, pressure and force at different stages of the exit with constant velocity are presented in this section. Figs. (5.15) to (5.18) show time effect of the combined wedge CW30 exiting with Froude number of 0.4.

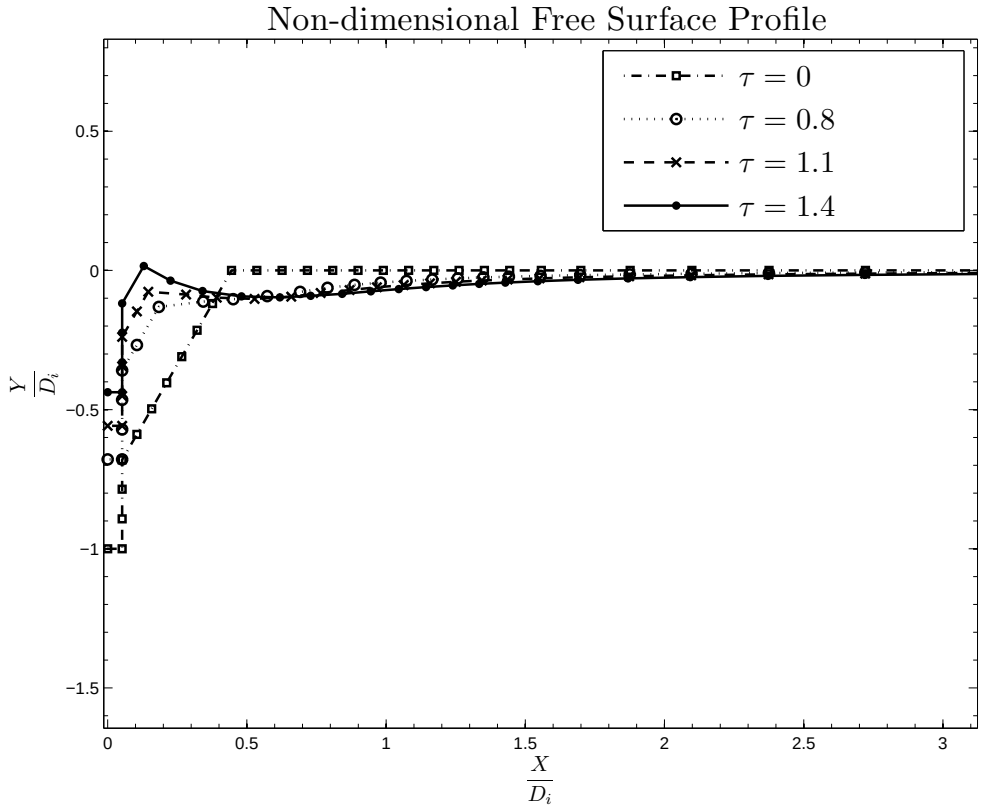

(a)

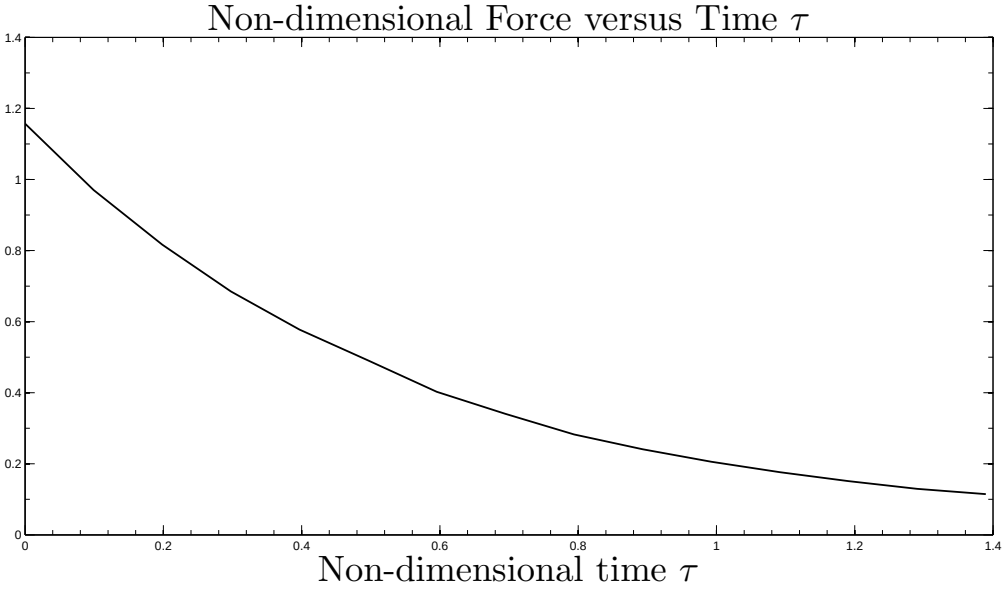

(b)

FIGURE 5.15: Time effect of the combined body CB30 submerged at a non-dimensional initial depth $\widehat{d_i} = -1$ exiting with constant velocity of Froude number $F_r = 0.4$: plotted at different non-dimensional times τ.

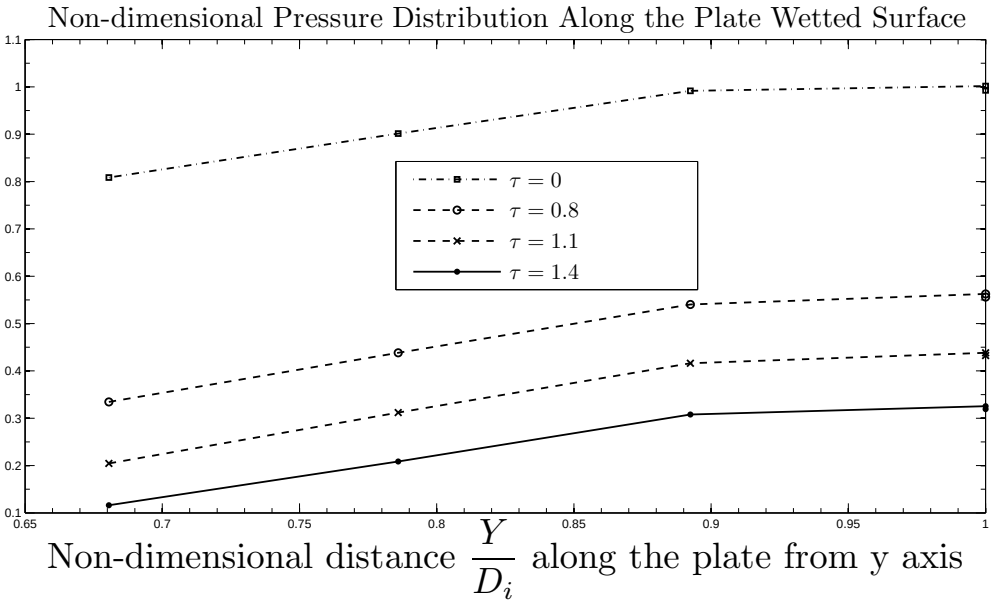

(a)

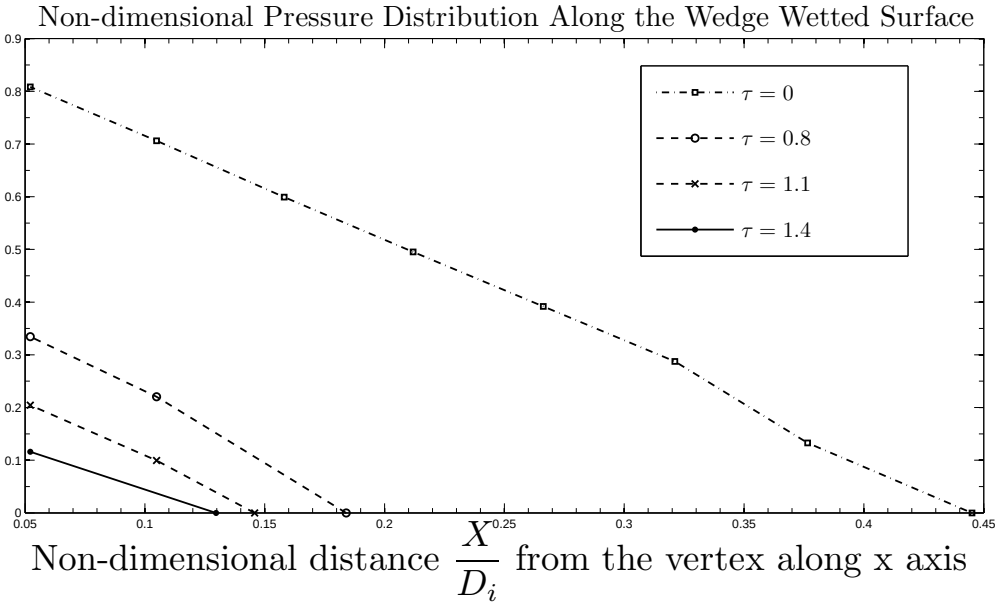

(b)

FIGURE 5.16: Time effect of the combined body CB30 submerged at a non-dimensional initial depth $\widehat{d_i} = -1$ exiting with constant velocity of Froude number $F_r = 0.4$: plotted at different non-dimensional times τ.

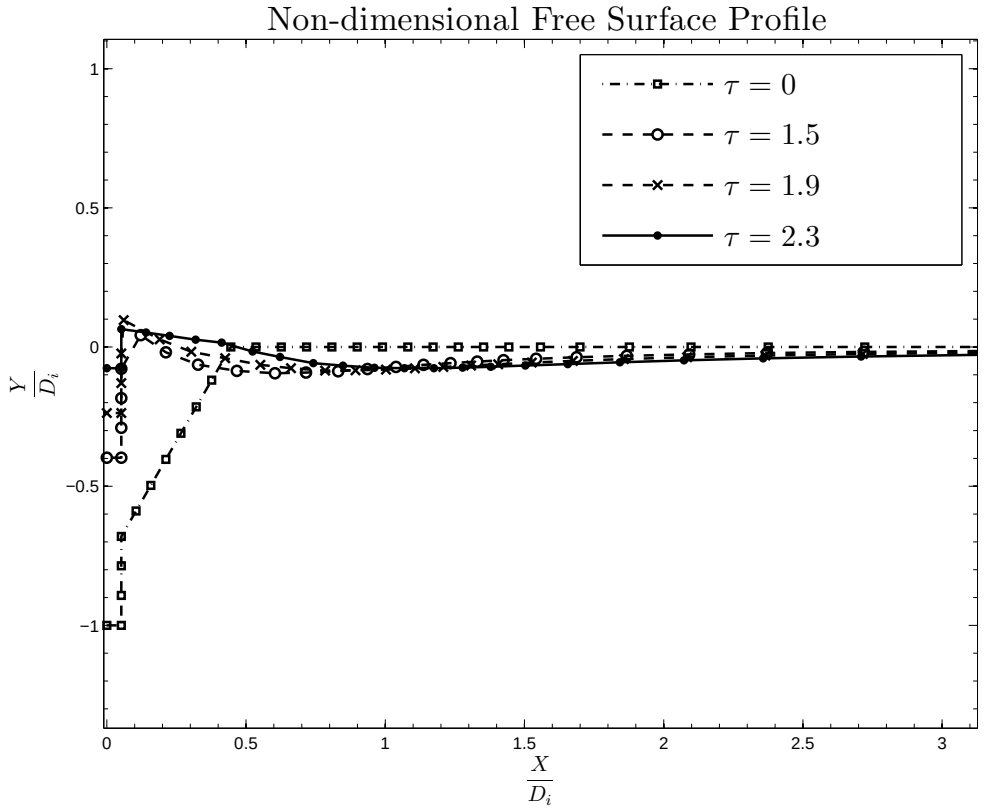

(a)

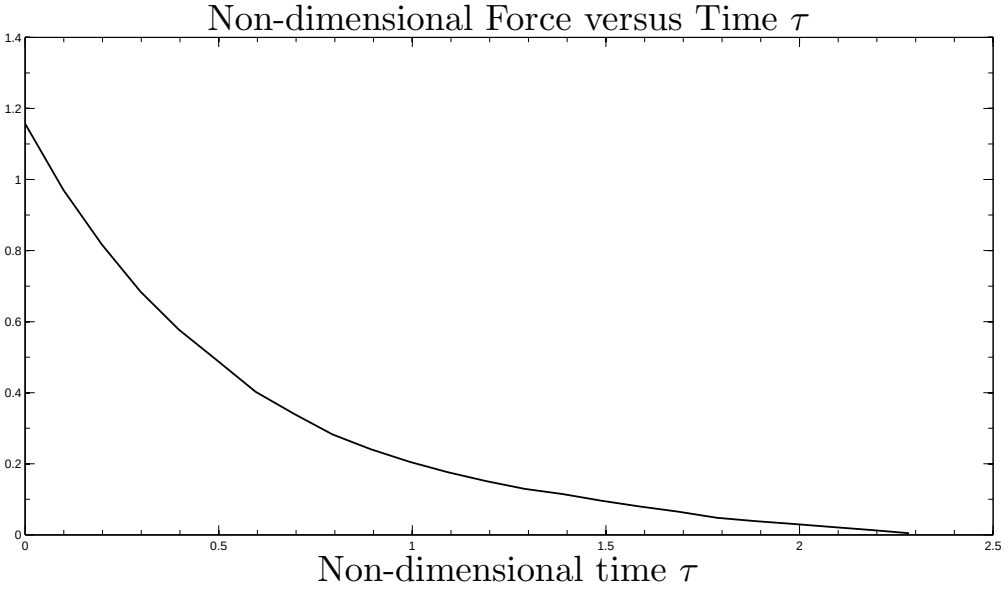

(b)

FIGURE 5.17: Time effect of the combined body CB30 submerged at a non-dimensional initial depth $\widehat{d_i} = -1$ exiting with constant velocity of Froude number $F_r = 0.4$: plotted at different non-dimensional times τ.

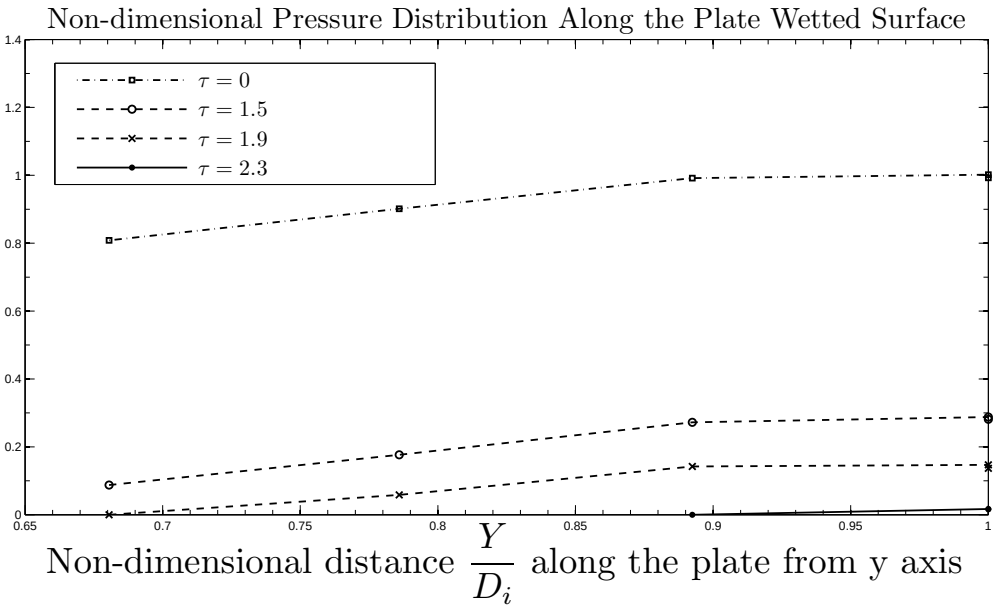

(a)

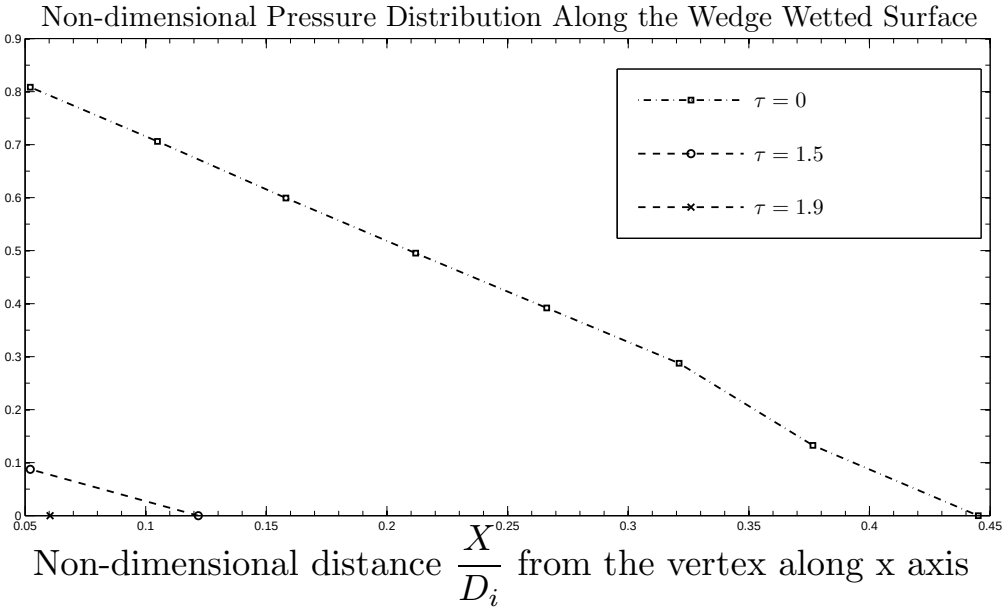

(b)

FIGURE 5.18: Time effect of the combined body CB30 submerged at a non-dimensional initial depth $\widehat{d_i} = -1$ exiting with constant velocity of Froude number $F_r = 0.4$: plotted at different non-dimensional times τ.

5.2.2.3 Finite depth effect

We present results showing effect on the free-surface profile, pressure and force due to the change in depth of the entry with constant velocity using the non-linear time-stepping method. The results are plotted at the same distance moved by the body for different depths of exit with the same velocity. Fig. (5.19) and (5.20) represent the computed free-surface profile, pressure distribution and force for the combined wedge CW30 exiting with Froude number 0.4 showing finite depth effect on the motion. We notice, as expected, that for exiting of the combined wedge CW30 the non-dimensional depth N_d below 1 experiences a greater difference in free-surface deformation, pressure and force than that of other depths.

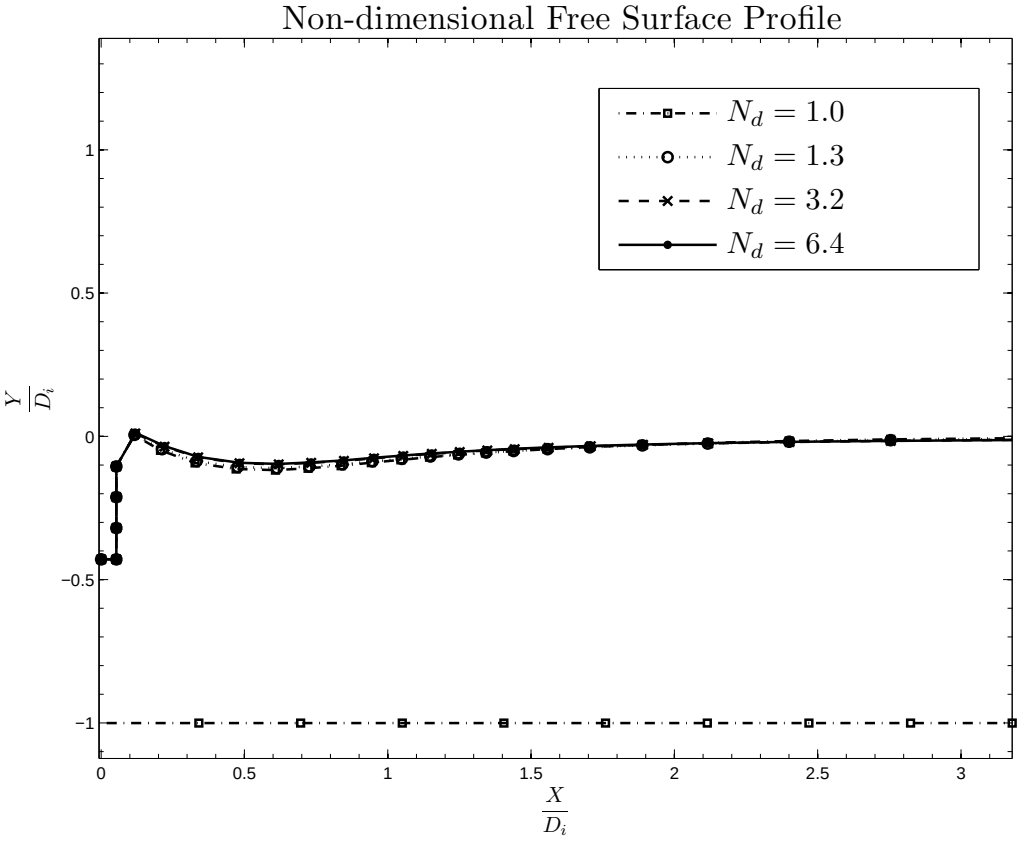

(a)

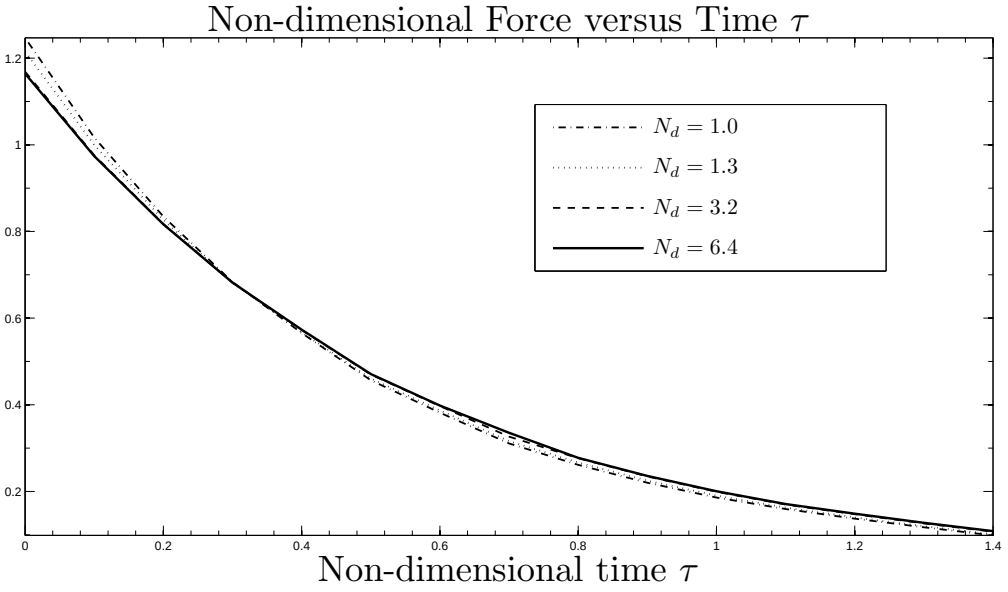

(b)

FIGURE 5.19: Finite depth effect of the combined body CB30 submerged at a non-dimensional initial depth $\widehat{d_i} = -1$ exiting with constant velocity of Froude number $F_r = 0.4$: (a) and (b) are plotted for different non-dimensional depths N_d at a non-dimensional time $\tau = 1.4$.

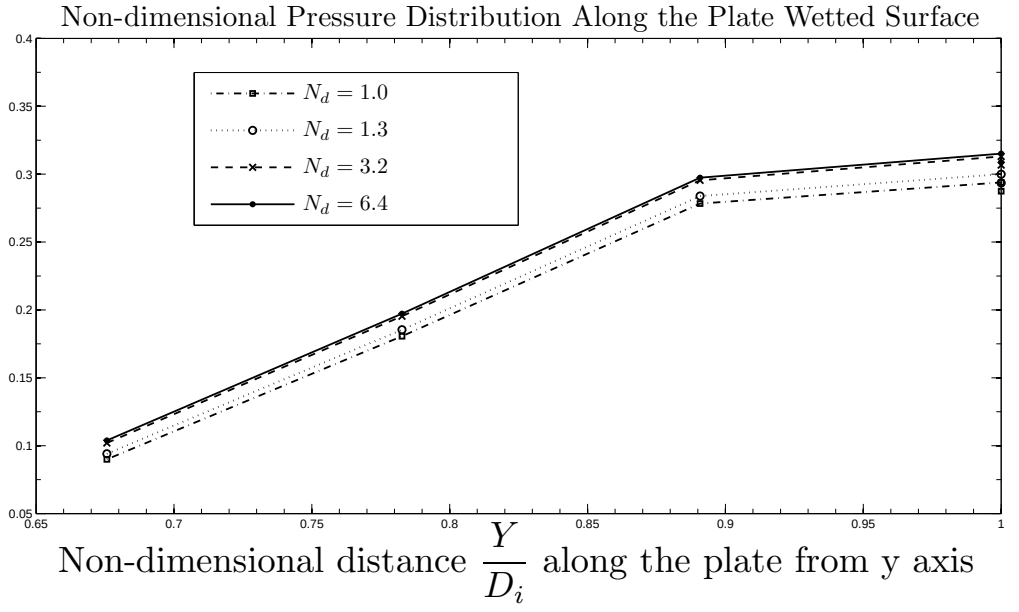

(a)

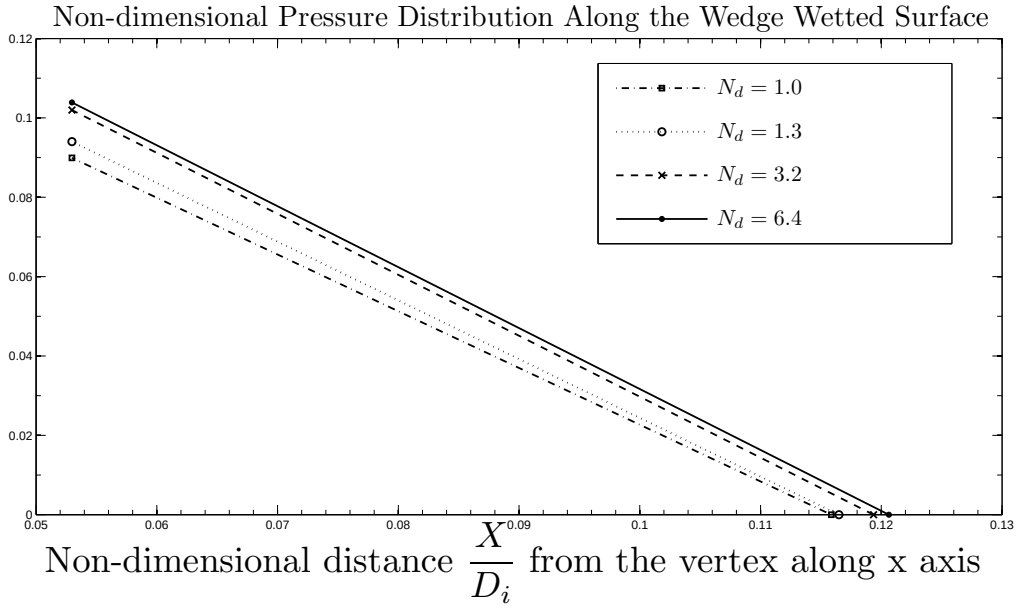

(b)

FIGURE 5.20: Finite depth effect of the combined body CB30 submerged at a non-dimensional initial depth $\widehat{d_i} = -1$ exiting with constant velocity of Froude number $F_r = 0.4$: (a) and (b) are plotted for different non-dimensional depths N_d at a non-dimensional time $\tau = 1.4$.

5.2.3 Asymmetric wedge exit

The parameters for an asymmetric wedge is same as those for a symmetric wedge except the left half angle β_h. Tab. (5.2) gives the details for the test cases carried out for the wedge. The results for different Froude numbers of exit with constant velocity are given in section (5.2.3.1). The computed numerical results for the asymmetric wedges show the time effect and finite depth effect in sections (5.2.3.2) and (5.2.3.3) respectively. The convergence of the asymmetric wedge exit also checked and results are given on the CD, see Appendix (B).

Asymmetric wedge	**Half wedge angle**	
(AW)	(β_h)	(α_h)
AW1	5^o	10
AW2	0^o	30
AW3	-20^o	30
AW4	-10^o	30

TABLE 5.2: Asymmetric wedges considered for water exit cases

5.2.3.1 Froude number effect

To study the effect of Froude number on exiting asymmetric wedges, we carry out a set of test cases. For a particular asymmetric wedge, the test process is to keep all the input variables of a specific run of the program constant, and obtain the Froude numbers by varying the velocity of the exit for the asymmetric wedge. We plot the results for the free-surface profile, pressure and force at the same distance traveled by the asymmetric wedge for different exit speeds as time progresses. The same process is repeated for the asymmetric wedges shown in Table (5.2). As we increase velocity of the exit, we can notice much more deformation on the free surface and consequently in the pressure distribution and force as shown in Fig. (5.21) and (5.22).

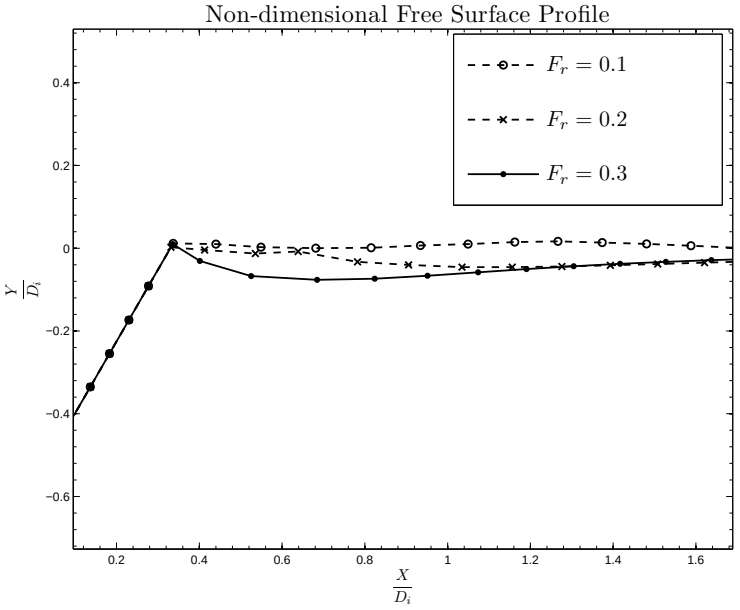

(a)

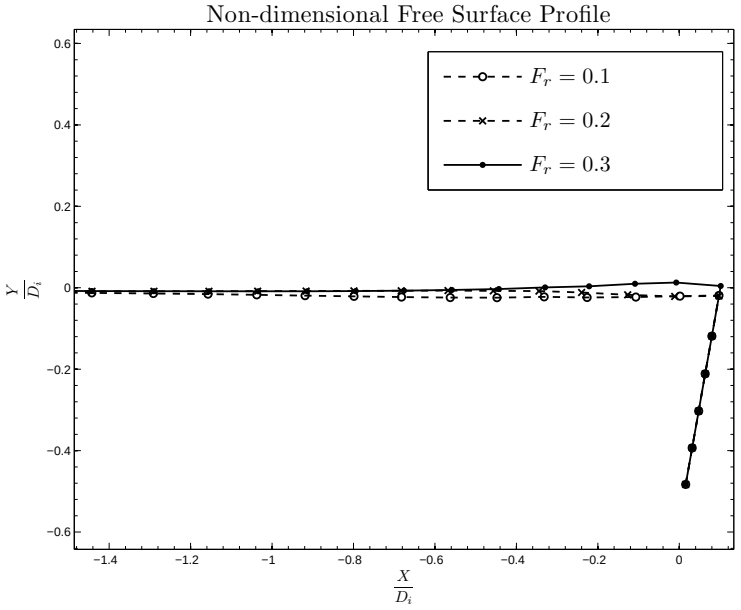

(b)

FIGURE 5.21: Froude number effect of the asymmetric wedge AW4 submerged at a non-dimensional initial depth $\widehat{d_i} = -1$ exiting with constant velocity of different Froude numbers F_r: plotted at different non-dimensional times $\tau = 4.2, 2.1, 1.4$ and distance $\widehat{d} = -0.57$.

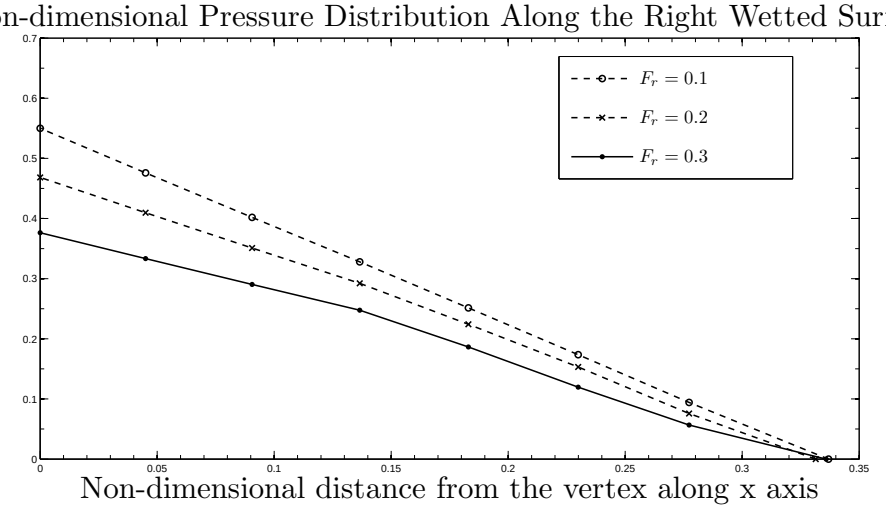

(a)

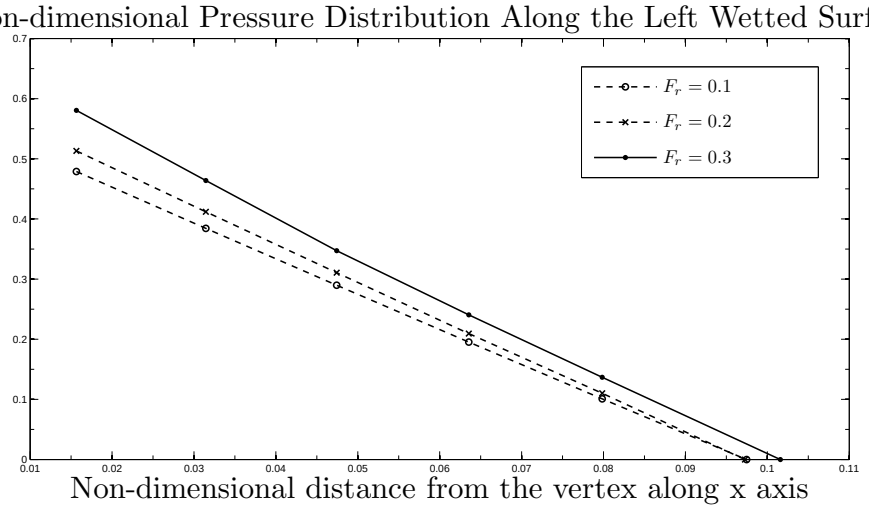

(b)

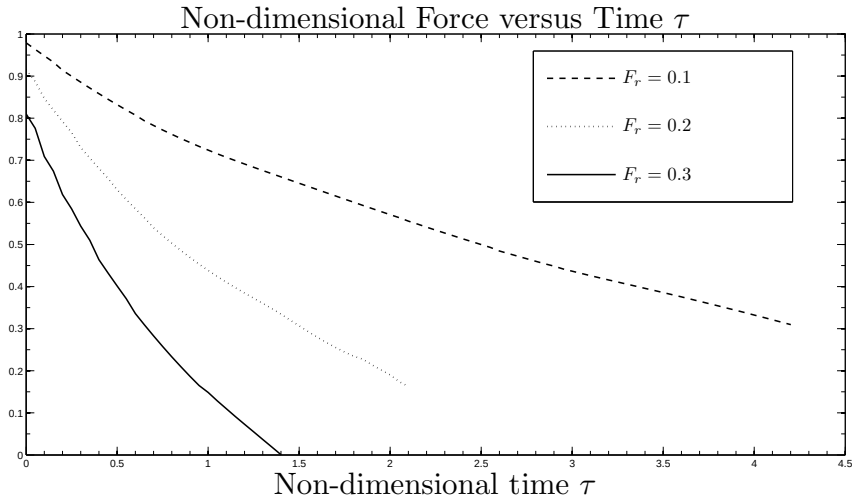

(c)

FIGURE 5.22: Froude number effect of the asymmetric wedge AW4 submerged at a non-dimensional initial depth $\widehat{d}_i = -1$ exiting with constant velocity of different Froude numbers: plotted at different non-dimensional times $\tau = 4.2, 2.1, 1.4$ and distance $\widehat{d} = -0.57$.

5.2.3.2 Time effect

The motion of the asymmetric wedge changes as time progresses. We can compute the deformed free-surface profile, pressure along the wetted part of the body and the upward force experienced by the body using the non-linear theory. The computed results showing time effect on free surface, pressure and force at different stages of the exit with constant velocity are presented in this section. Fig. (5.23) to (5.26) show the time effect of the asymmetric wedge AW4 exiting with a Froude number of 0.3.

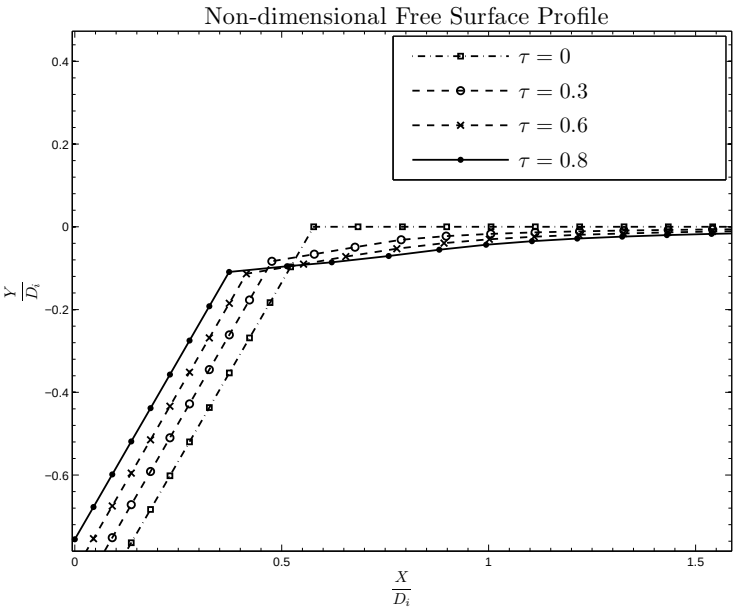

(a)

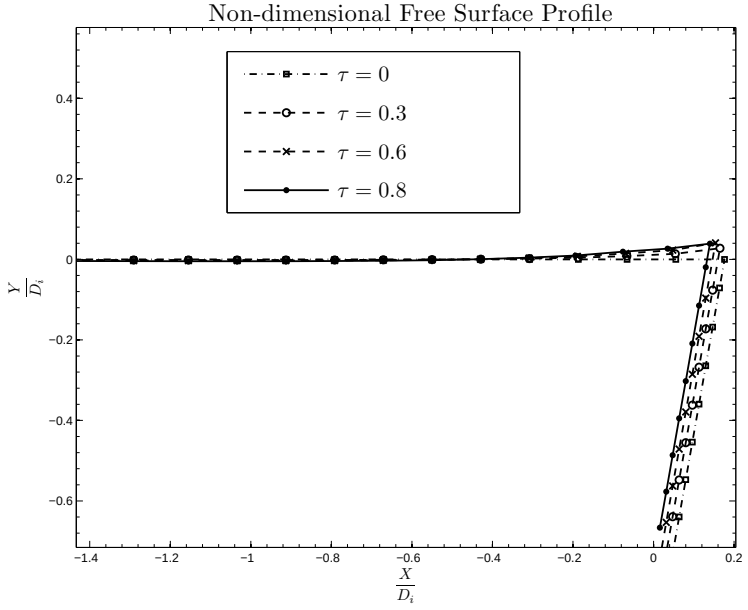

(b)

FIGURE 5.23: Time effect of the asymmetric wedge AW4 submerged at a non-dimensional initial depth $\widehat{d_i} = -1$ exiting with constant velocity of Froude number $F_r = 0.3$: plotted at different non-dimensional times τ.

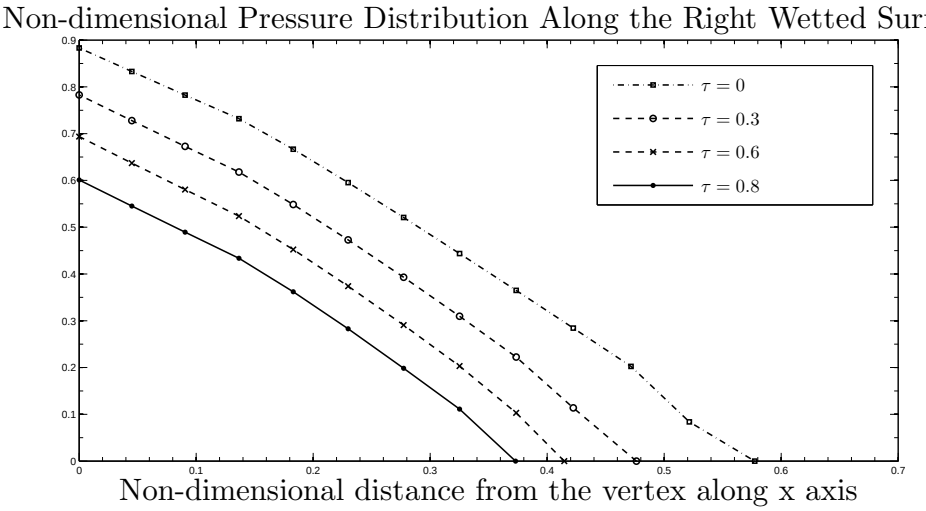

(a)

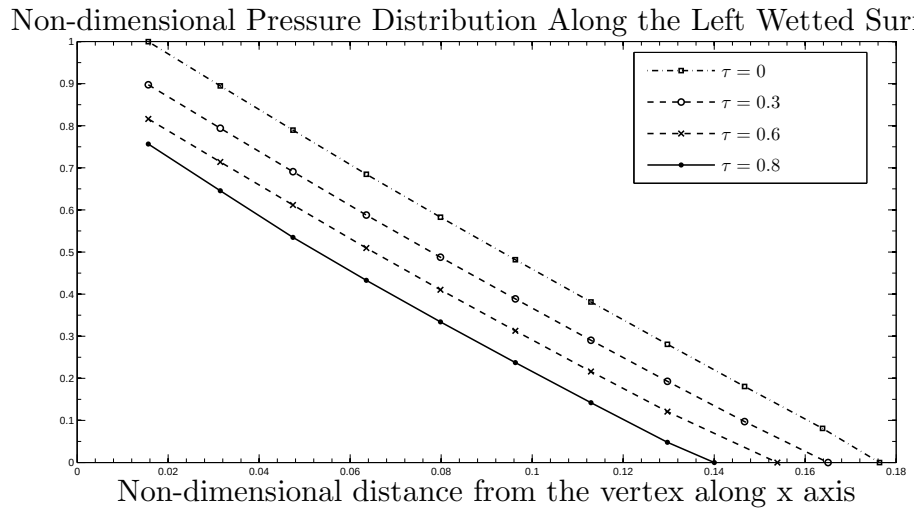

(b)

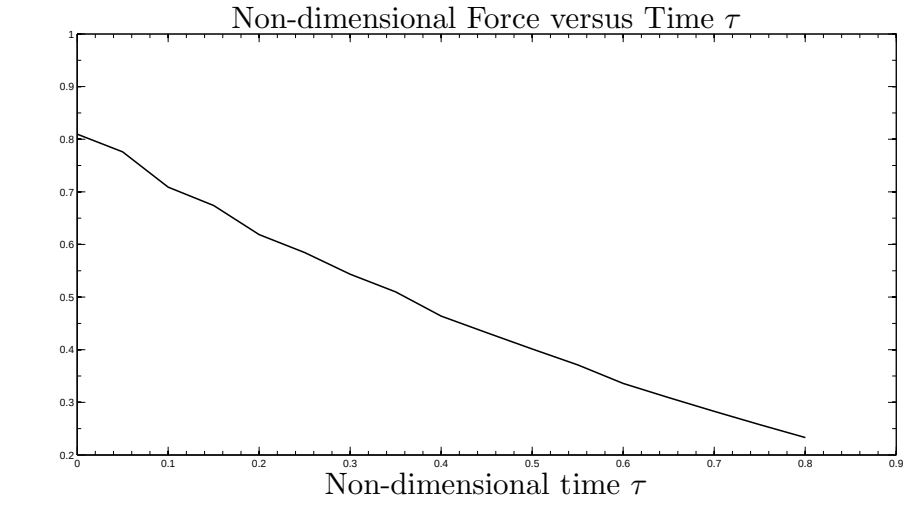

(c)

FIGURE 5.24: Time effect of the asymmetric wedge AW4 submerged at a non-dimensional initial depth $\widehat{d}_i = -1$ exiting with constant velocity of Froude number $F_r = 0.3$: plotted at different non-dimensional times τ.

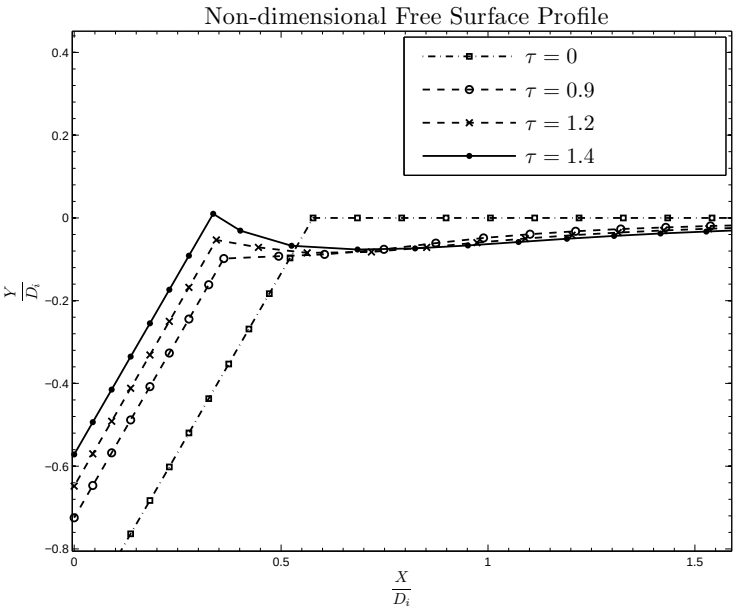

(a)

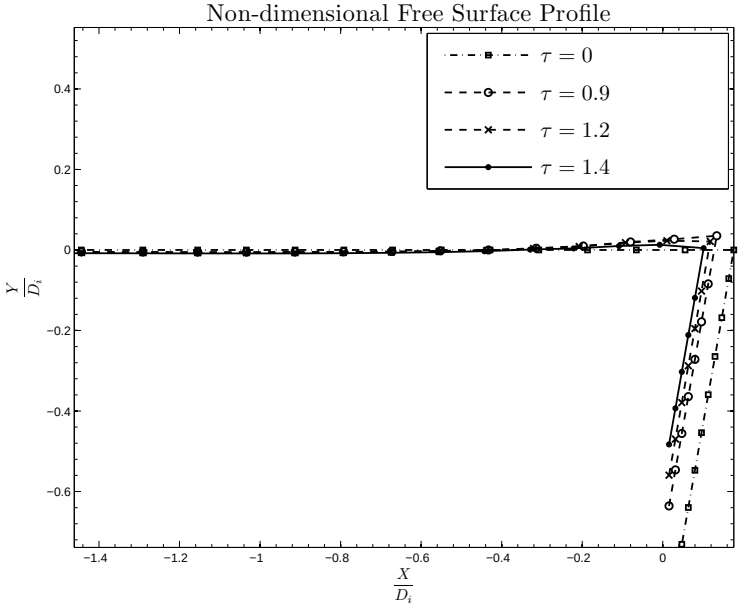

(b)

FIGURE 5.25: Time effect of the asymmetric wedge AW4 submerged at a non-dimensional initial depth $\widehat{d_i} = -1$ exiting with constant velocity of Froude number $F_r = 0.3$: plotted at different non-dimensional times τ.

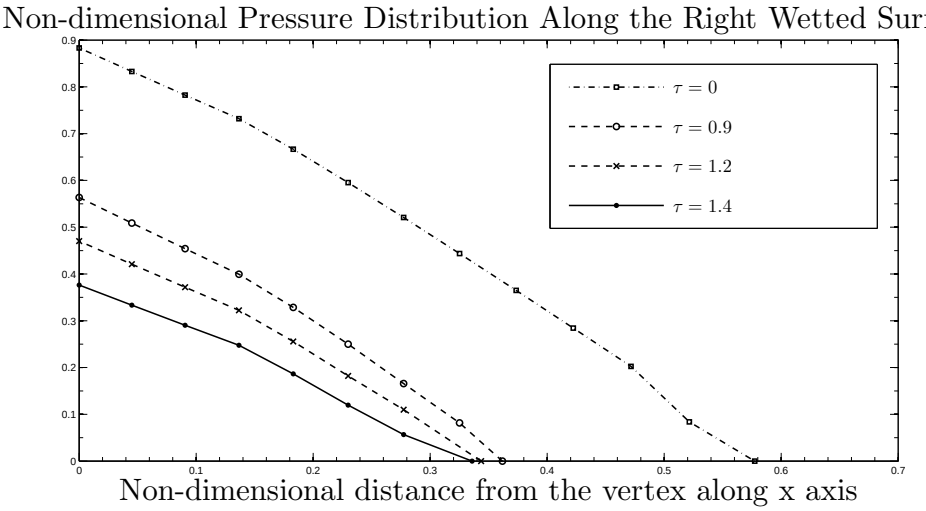

(a)

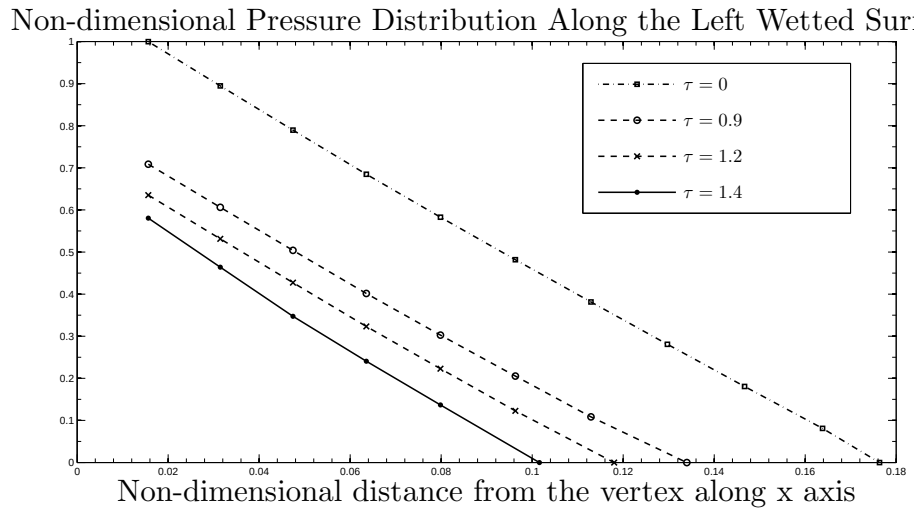

(b)

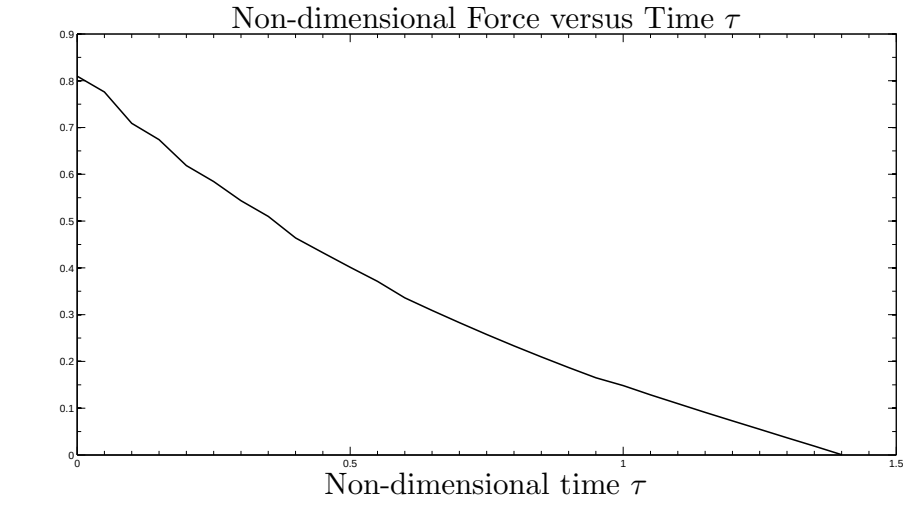

(c)

FIGURE 5.26: Time effect of the asymmetric wedge AW4 submerged at a non-dimensional initial depth $\widehat{d_i} = -1$ exiting with constant velocity of Froude number $F_r = 0.3$: plotted at different non-dimensional times τ.

5.2.3.3 Finite depth effect

As for the computation for finite depth effect of symmetric wedges exiting with constant velocity, we present computed results for the asymmetric wedges exiting with constant velocity showing the finite depth effect on free surface, pressure and force. Fig. (5.27) and (5.28) give the computed free-surface profile, pressure distribution and force for the asymmetric wedge AW4 exiting with Froude number 0.3 showing the finite depth effect on the motion. We notice, as expected, that for exiting of the asymmetric wedge AW4 that the non-dimensional depth N_d below 1 experiences a greater difference in free-surface deformation, pressure and force than that of other depths.

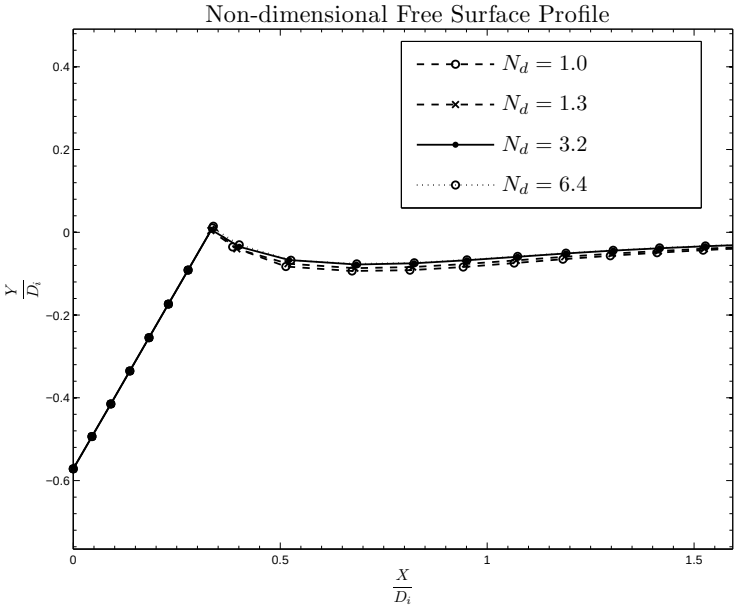

(a)

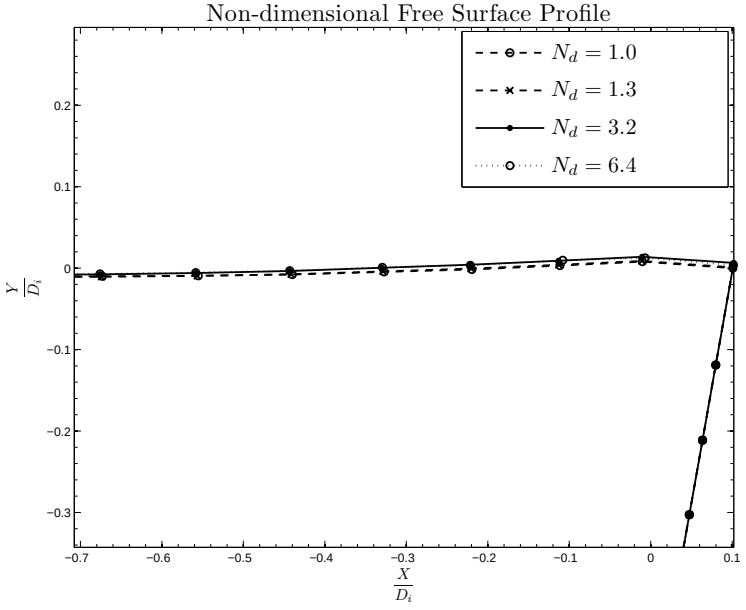

(b)

FIGURE 5.27: Finite depth effect of the asymmetric wedge AW4 submerged at a non-dimensional initial depth $\widehat{d_i} = -1$ exiting with constant velocity of Froude number $F_r = 0.3$: (a) and (b) are plotted for different non-dimensional depths N_d at a non-dimensional time $\tau = 1.4$.

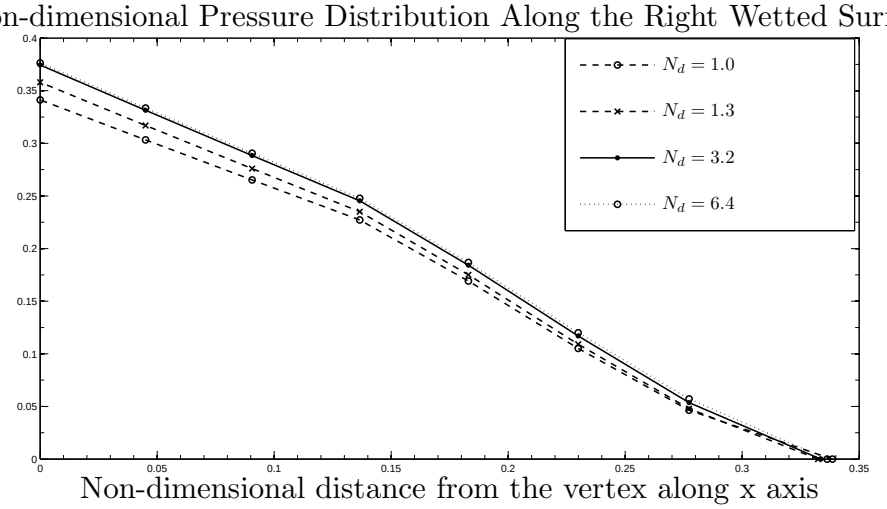

(a)

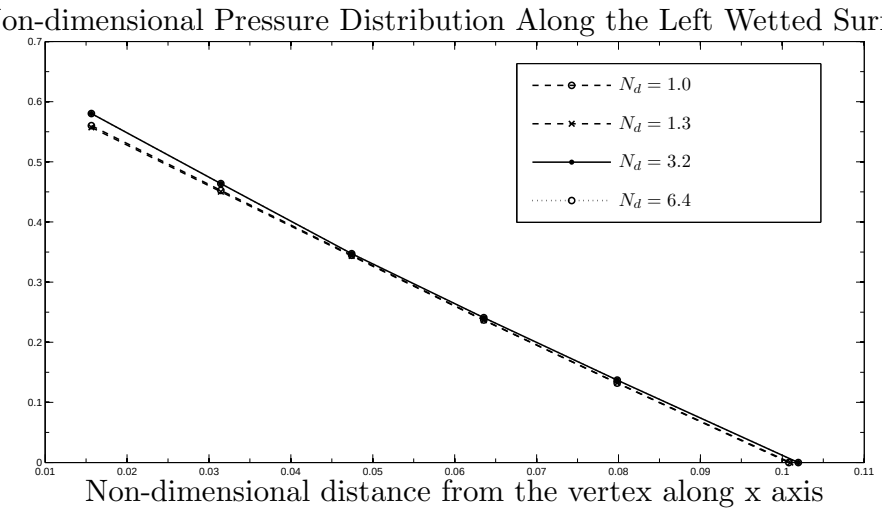

(b)

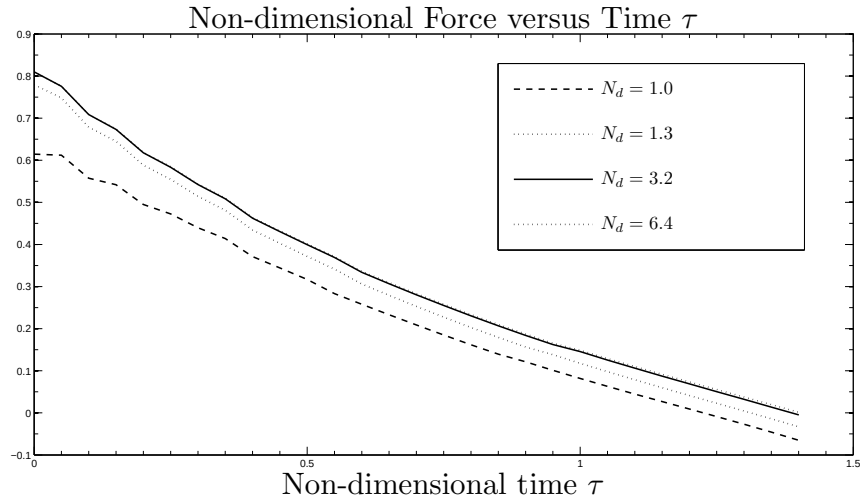

(c)

FIGURE 5.28: Finite depth effect of the asymmetric wedge AW4 submerged at a non-dimensional initial depth $\widehat{d}_i = -1$ exiting with constant velocity of Froude number $F_r = 0.3$: (a) and (b) are plotted for different non-dimensional depths N_d at a non-dimensional time $\tau = 1.4$.

5.2.4 Truncated wedge exit

Control parameters on the truncated wedge shown on Fig.(4.1(c)) are left half angle β_h, right half angle α_h, height of the wedge h, bottom width of the wedge b and the aspect ratio T_a. We produce results for the test cases given in Table (5.3) by considering various aspect ratios T_a and wedge angles. The results for different Froude numbers of exit with constant velocity are given in section (5.2.4.1). The computed numerical results for the truncated wedges show the time effect and finite depth effect in sections (5.2.4.2) and (5.2.4.3) respectively.

Truncated wedge (TW)	**Left angle** (β_h)	**Right angle** (α_h)
TW1	10^o	10^o
TW2	20^o	20^o
TW3	30^o	30^o

TABLE 5.3: Truncated wedges for exit cases

5.2.4.1 Froude number effect

To study the effect of Froude number on the results the truncated wedges, we carry out a set of test cases. For a particular truncated wedge, the test process is to keep all the input variables of a specific run of the program constant, and obtain the Froude numbers by varying the velocity of the exit for the truncated wedge. We plot the results for the free-surface profile, pressure and force at the same distance traveled by the truncated wedge for different exit speeds as time progresses. The same process is repeated for the truncated wedges as shown in Table (5.3). As we increase velocity of the exit, we can notice much more deformation on the free surface and consequently in the pressure distribution and force as shown in Fig. (5.29).

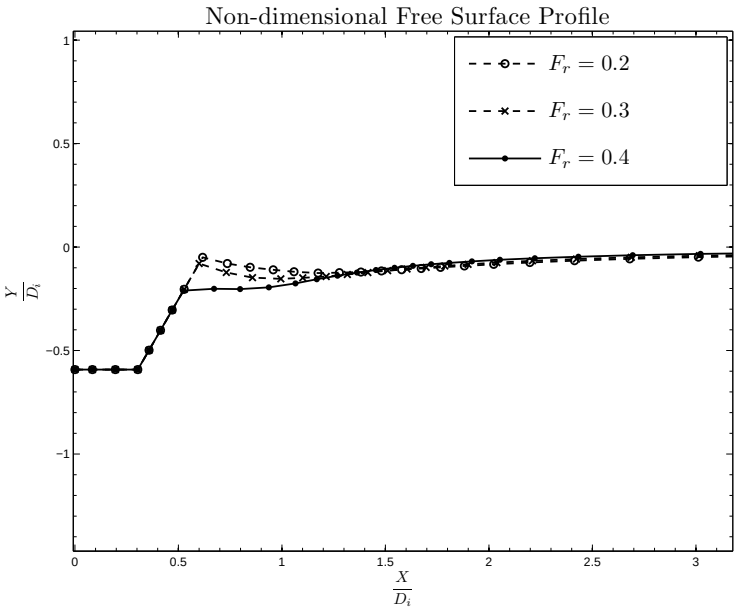

(a)

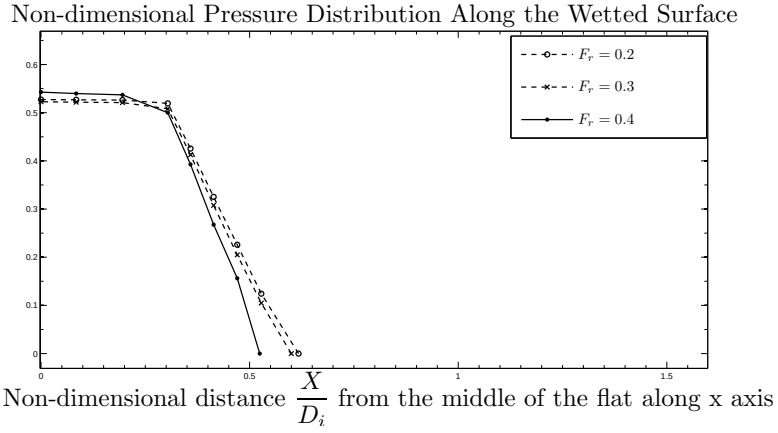

(b)

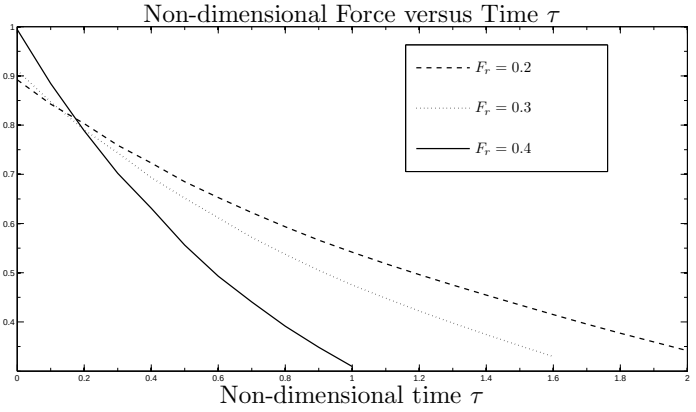

(c)

FIGURE 5.29: Froude number effect of the truncated wedge TW3 submerged at a non-dimensional initial depth $\widehat{d}_i = -1$ exiting with constant velocity of different Froude numbers F_r: (a) and (b) are plotted at different non-dimensional times $\tau = 2, 1.6, 1$ and distance $\widehat{d} = -0.592$.

5.2.4.2 Time effect

The computed results for the truncated wedges showing time effect on free surface, pressure and force at a set of three different intervals of the exit with constant velocity are presented in this section. Fig. (5.30) and (5.31) show the time effect of the truncated wedge TW3 exiting with Froude number of 0.4.

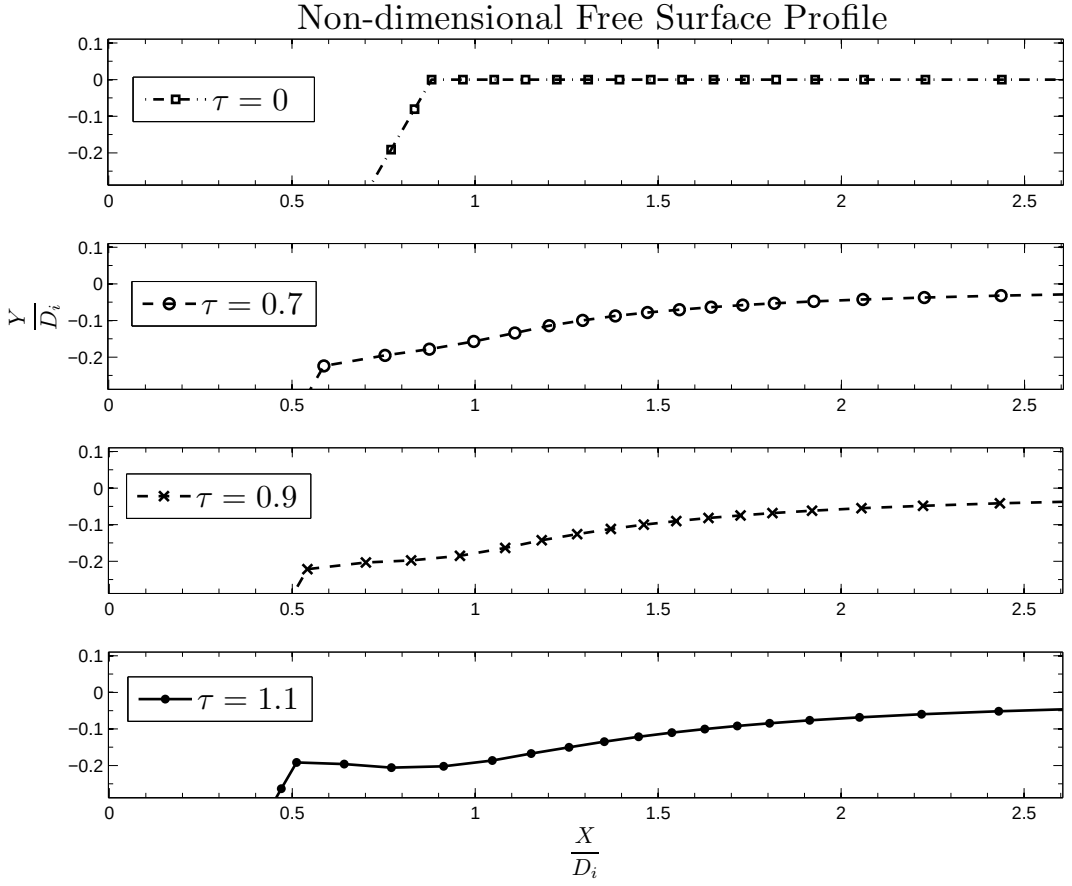

(a)

FIGURE 5.30: Time effect of the truncated wedge TW3 submerged at a non-dimensional initial depth $\widehat{d_i} = -1$ exiting with constant velocity of Froude number $F_r = 0.4$: plotted at different non-dimensional times τ.

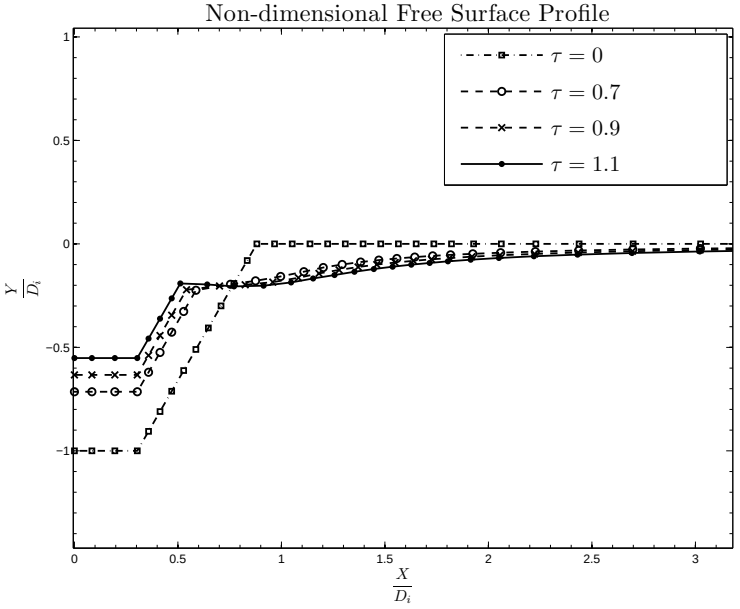

(a)

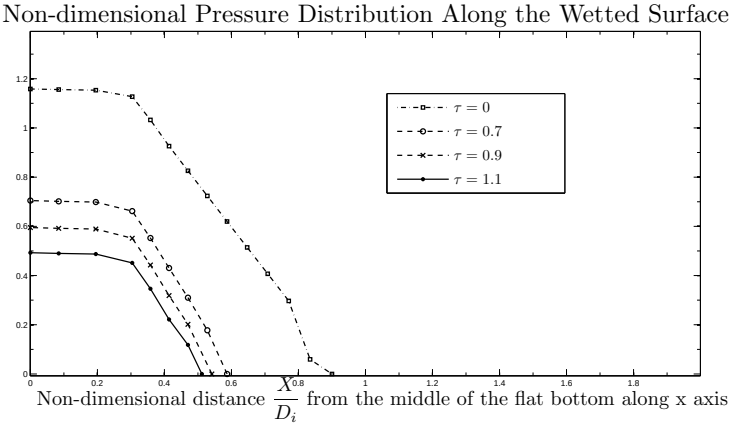

(b)

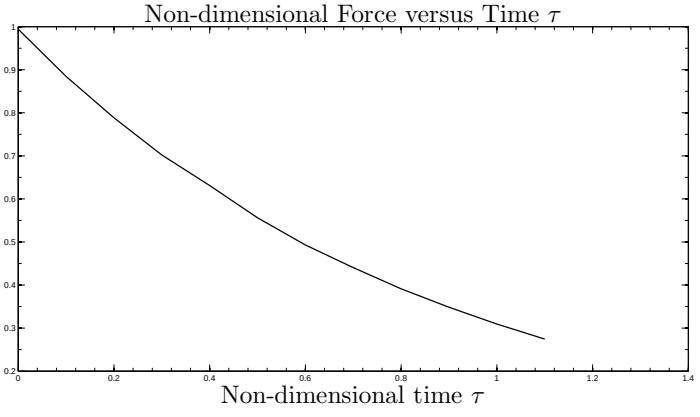

(c)

FIGURE 5.31: Time effect of the truncated wedge TW3 submerged at a non-dimensional initial depth $\widehat{d_i} = -1$ exiting with constant velocity of Froude number $F_r = 0.4$: (a) and (b) are plotted at different non-dimensional times τ.

5.2.4.3 Finite depth effect

As for the computation for finite depth effect of truncated wedges exiting with constant velocity, we present computed results for the truncated wedges exiting with constant velocity showing finite depth effect on free surface, pressure and force. Fig. (5.32) presents the computed free-surface profile, pressure distribution and force for the truncated wedge TW3 exiting with Froude number 0.4 showing the finite depth effect on the motion. We notice, as expected, for exiting of the truncated wedge TW3 that the non-dimensional depth N_d below 1 experiences a greater difference in the free-surface deformation, pressure and force than that of other depths.

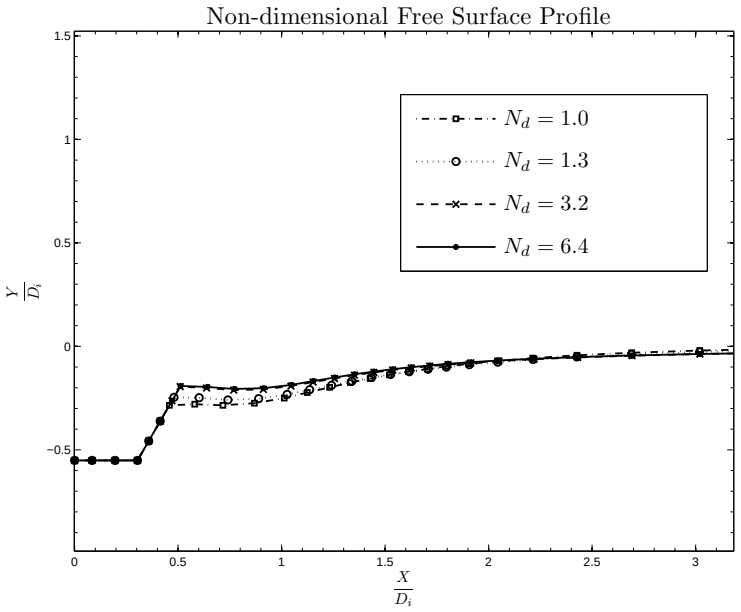

(a)

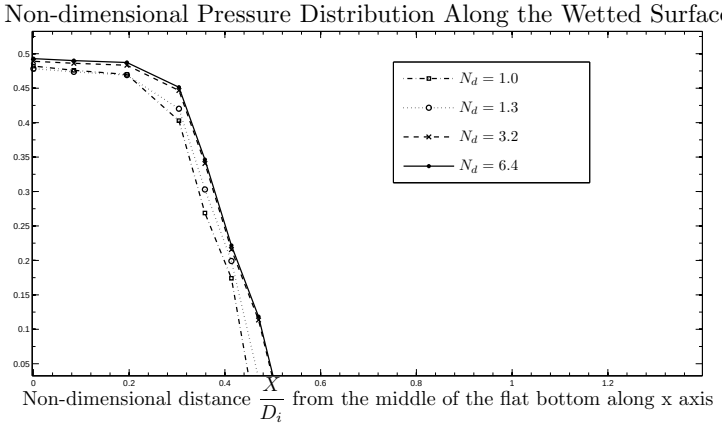

(b)

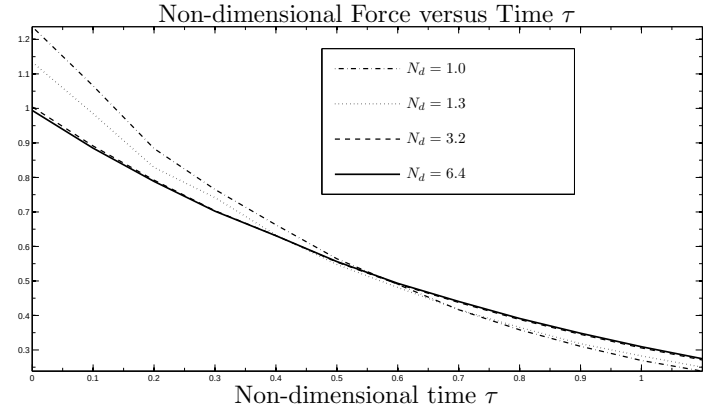

(c)

FIGURE 5.32: Finite depth effect of the truncated wedge TW2 submerged at a non-dimensional initial depth $\widehat{d_i} = -1$ exiting with constant velocity of Froude number $F_r = 0.4$: (a) and (b) are plotted for different non-dimensional depths N_d at a non-dimensional time $\tau = 1.1$.

5.2.5 Box exit

As in the previous sections, the main parameter for a box body as considered for entry cases is the aspect ratio R_a which is the ratio of the initial depth to the width of the box. As an example, we present some results showing Froude number effect and time effect on the motion of the box BX2 with the aspect ratio 0.7. The results for different Froude numbers of exit with constant velocity are given in section (5.2.5.1). The computed numerical results for the box body show the time effect and finite depth effect in sections (5.2.5.2) and (5.2.5.3) respectively.

Box (BX)	**Aspect ratio** (R_a)
BW1	1
BW2	0.5
BW3	0.25

TABLE 5.4: Box bodies considered for exit cases

5.2.5.1 Froude number effect

To study the effect of Froude number on the results the box body exit, we carry out a set of test cases. For a particular box body, the test process is to keep all the input variables of a specific run of the program constant, and obtain the Froude numbers by varying the velocity of the exit for the box body. We plot the results for the free-surface profile, pressure and force at the same distance traveled by the box body for different exit speeds as time progresses. The same process is repeated for the box body as shown in Table (5.4). As we increase velocity of the exit, we notice much more deformation on the free surface and consequently in the pressure distribution and force, as shown in Fig. (5.33) and (5.34).

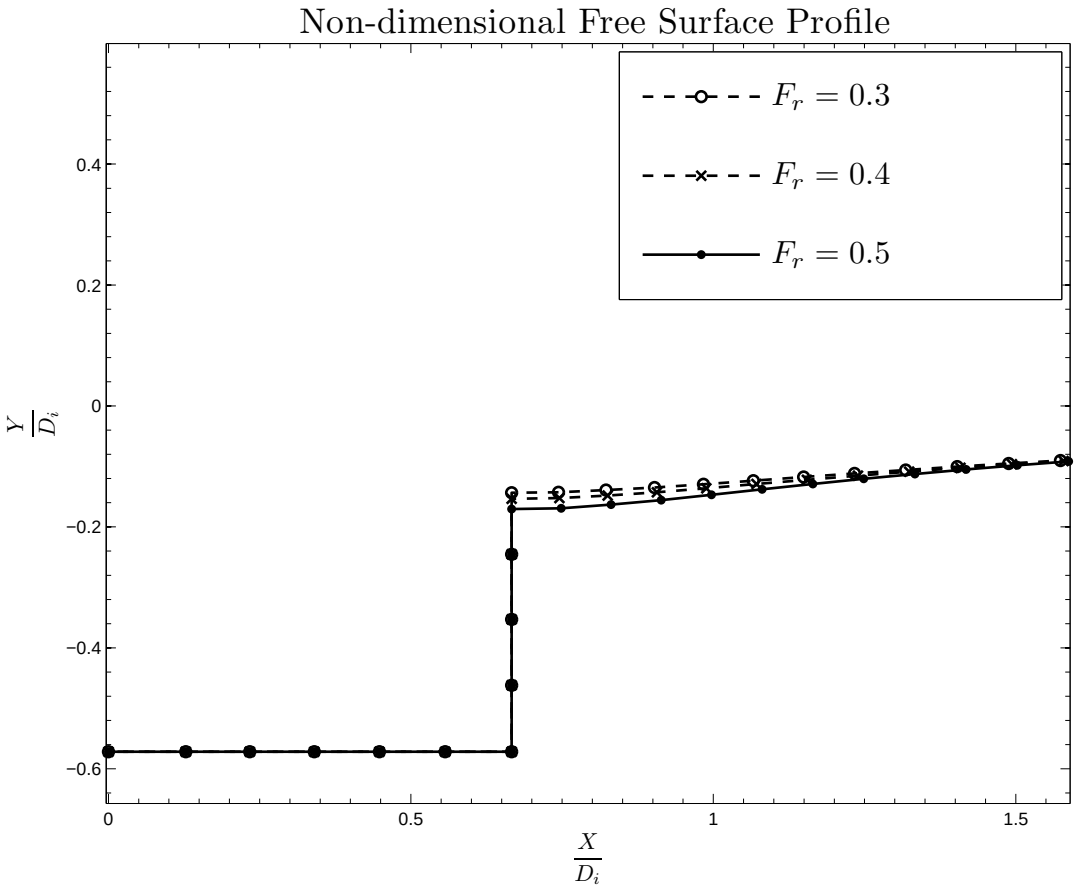

(a)

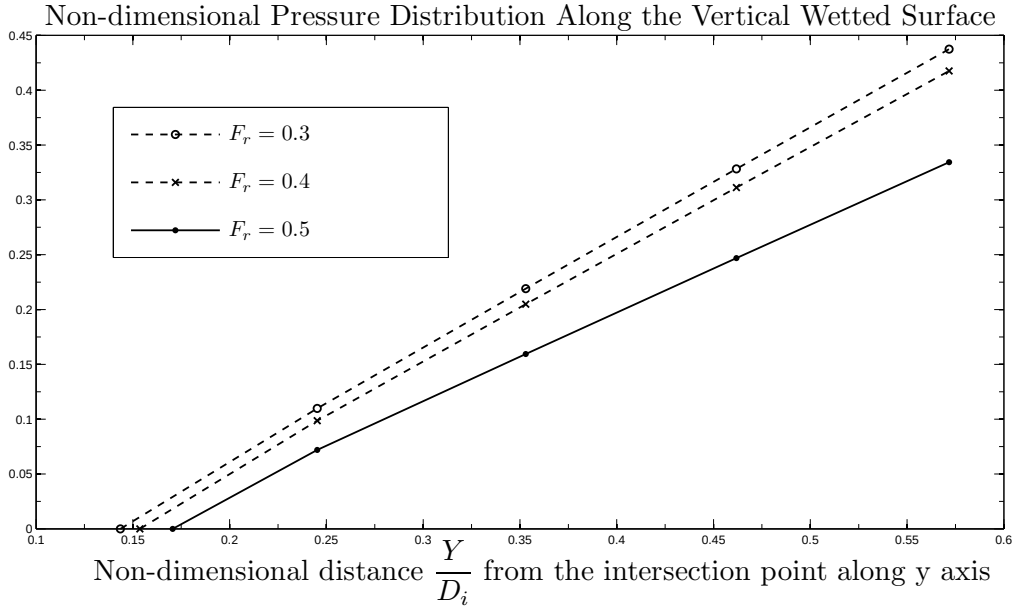

(b) along vertical surface

FIGURE 5.33: Froude number effect of the box BX2 submerged at a non-dimensional initial depth $\widehat{d}_i = -1$ exiting with constant velocity of different Froude numbers F_r: (a) and (b) are plotted at different non-dimensional times $\tau = 1.4, 1.2, 0.8$ and distance $\widehat{d} = -0.572$.

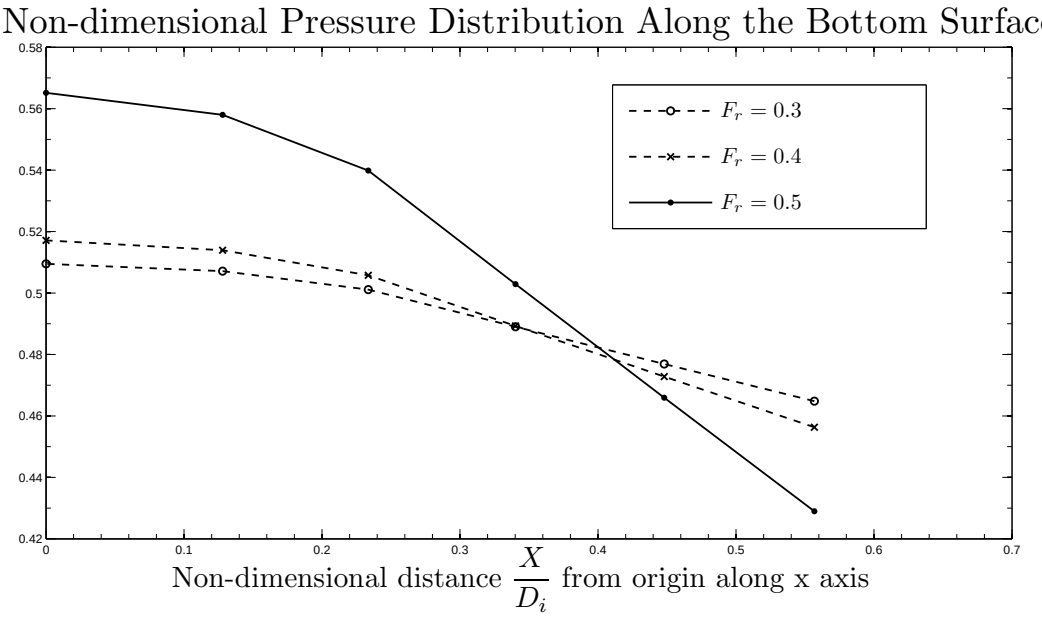

(a)

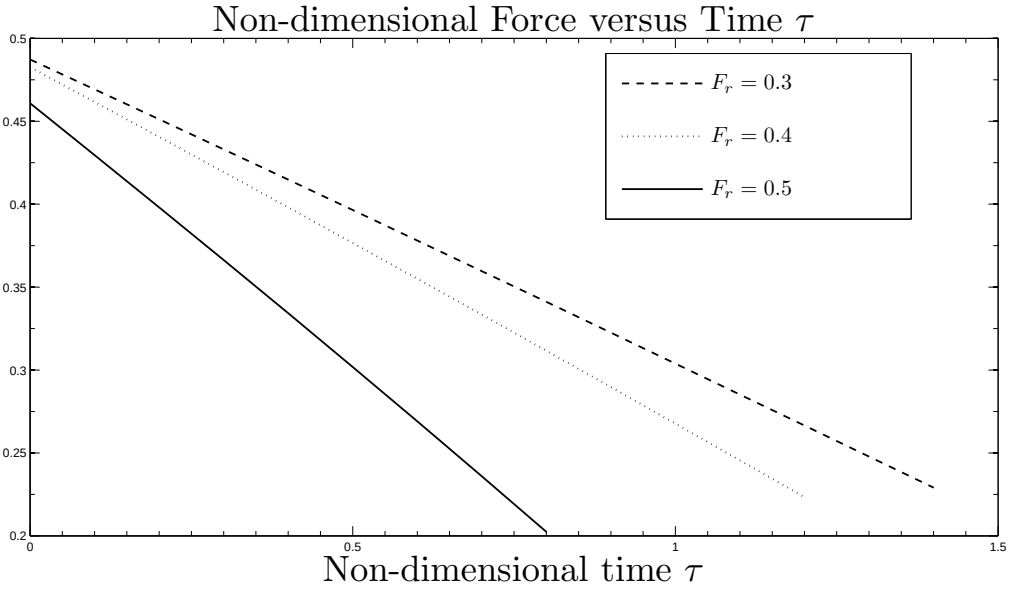

(b)

FIGURE 5.34: Froude number effect of the box BX2 submerged at a non-dimensional initial depth $\widehat{d_i} = -1$ exiting with constant velocity of different Froude numbers F_r: (a) is plotted at different non-dimensional times $\tau = 1.4, 1.2, 0.8$ and distance $\widehat{d} = -0.572$.

5.2.5.2 Time effect

The computed results for the box body showing time effect on free surface, pressure and force at a set of three different intervals of the exit with constant velocity are presented in this section. Fig. (5.35) and (5.36) show time effect of the box BX2 exiting with Froude number of 0.5.

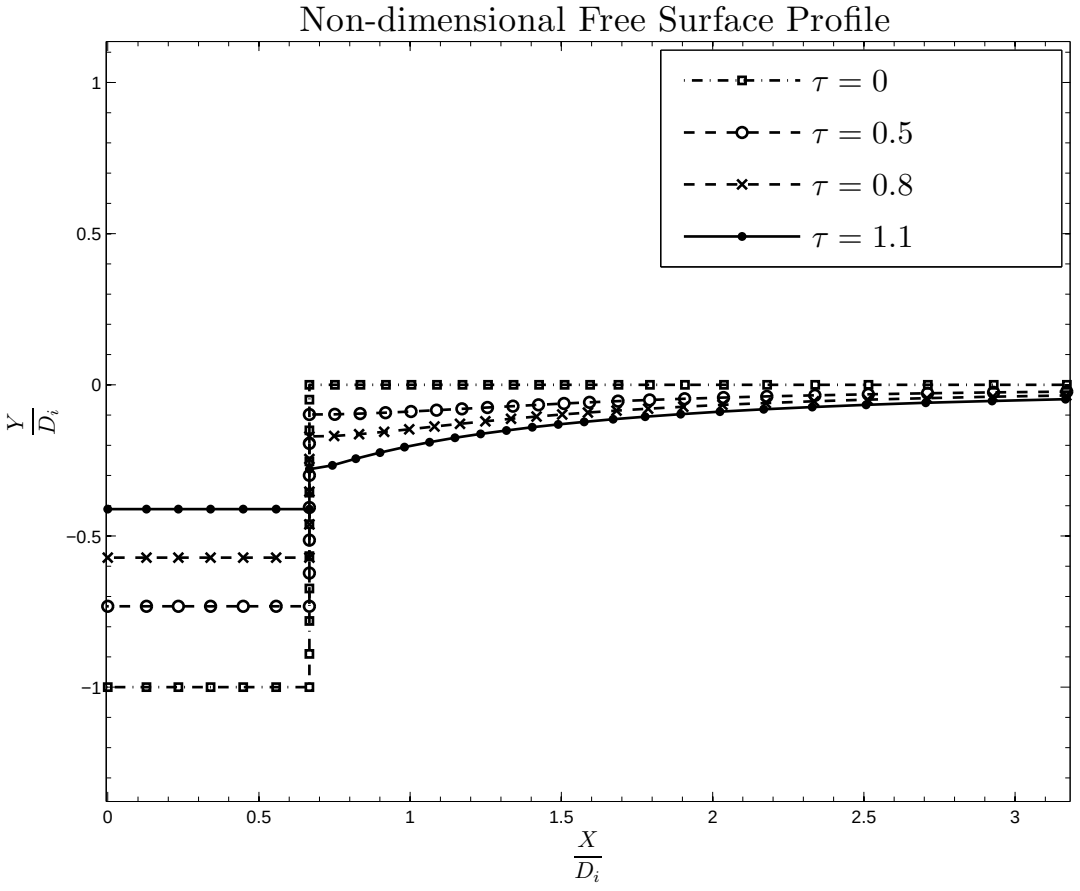

(a)

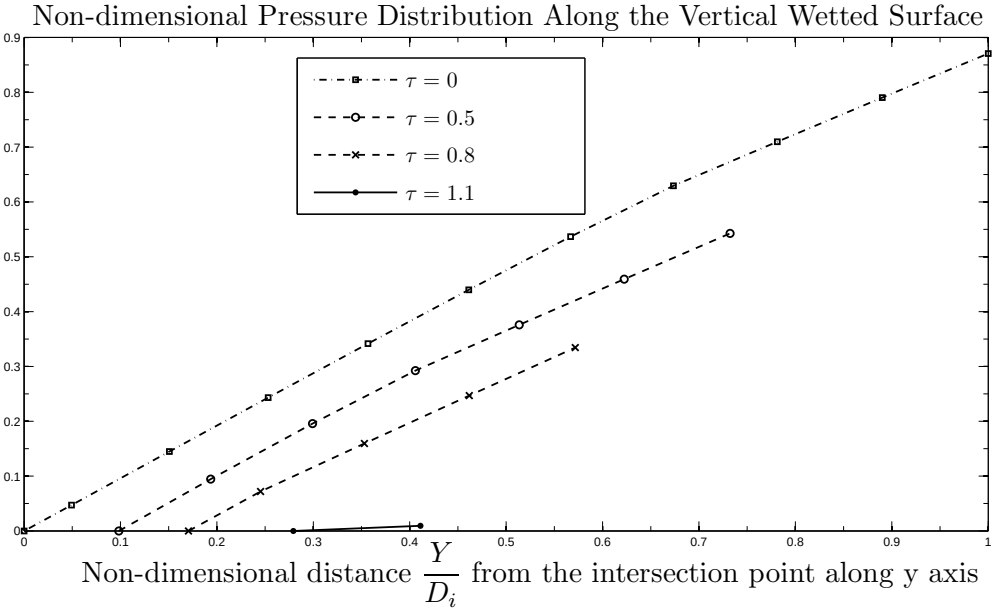

(b) along vertical surface

FIGURE 5.35: Time effect of the box BX2 submerged at a non-dimensional initial depth $\widehat{d_i} = -1$ exiting with constant velocity of Froude number $F_r = 0.5$: (a) and (b) are plotted at different non-dimensional times τ.

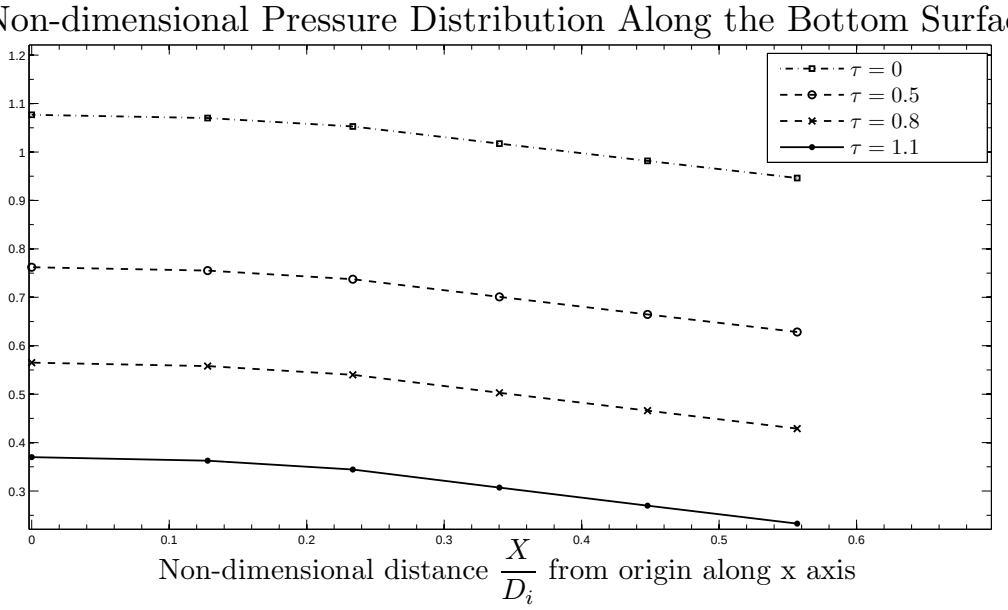

(a)

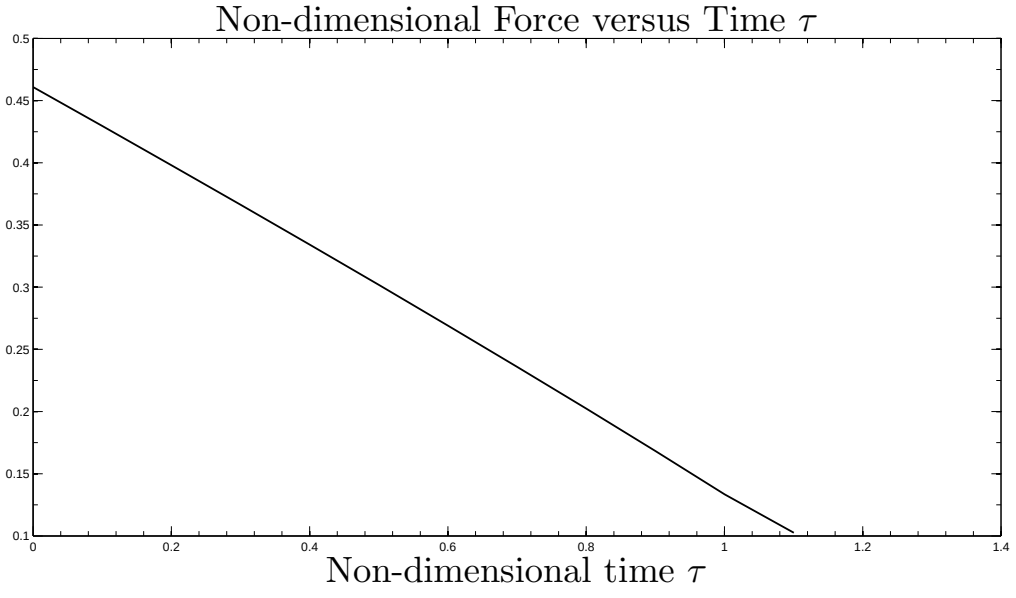

(b)

FIGURE 5.36: Time effect of the box BX2 submerged at a non-dimensional initial depth $\widehat{d}_i = -1$ exiting with constant velocity of Froude number F_r =0.5: (a) is plotted at different non-dimensional times τ.

5.2.5.3 Finite depth effect

We here present computed results for the box body entering with constant velocity showing the finite depth effect on free surface, pressure and force in this section. Fig. (5.37) and (5.38) represent the computed free-surface profile, pressure distribution and force for the box BX2 exiting with Froude number 0.5 showing finite depth effect. We notice, as expected, for exiting of the box BX2 that the non-dimensional depth N_d 1.1 experiences a greater difference in the free-surface deformation, pressure and force than that of other depths. It is not possible to compute results for the non-dimensional depth N_d below 1.1 due to numerical problems.

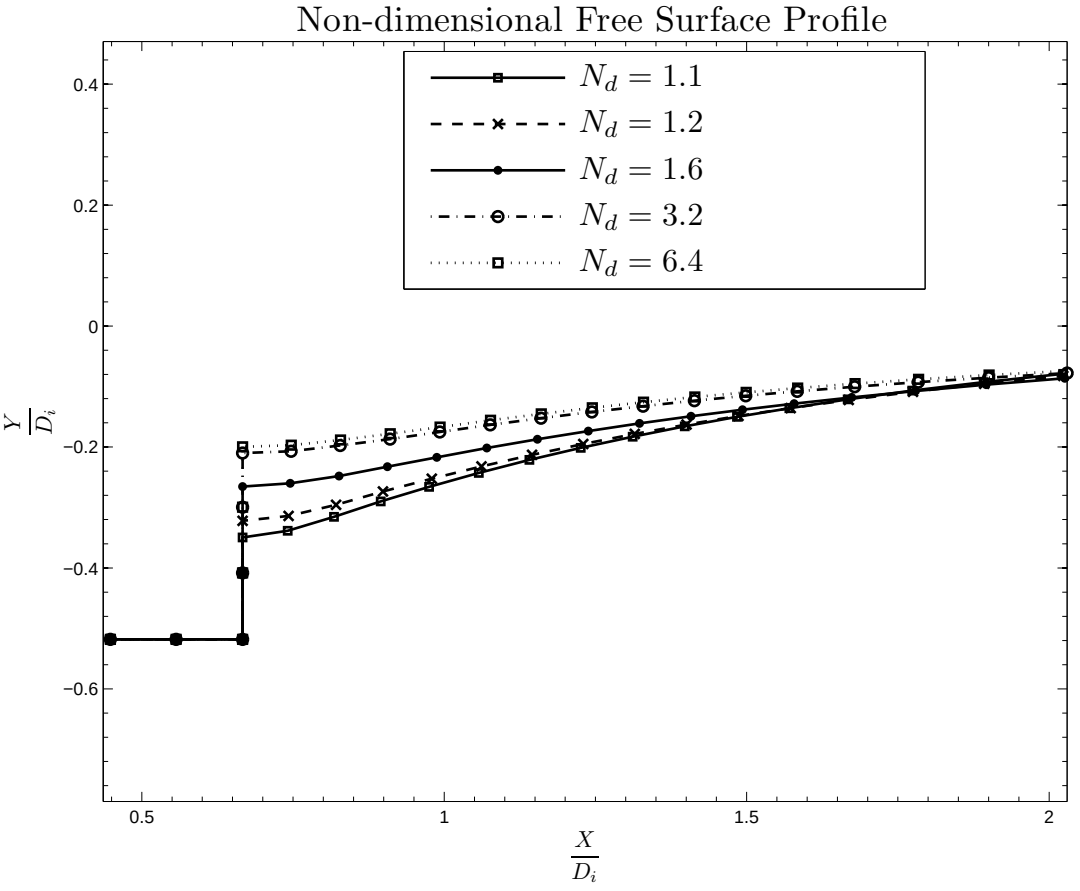

(a)

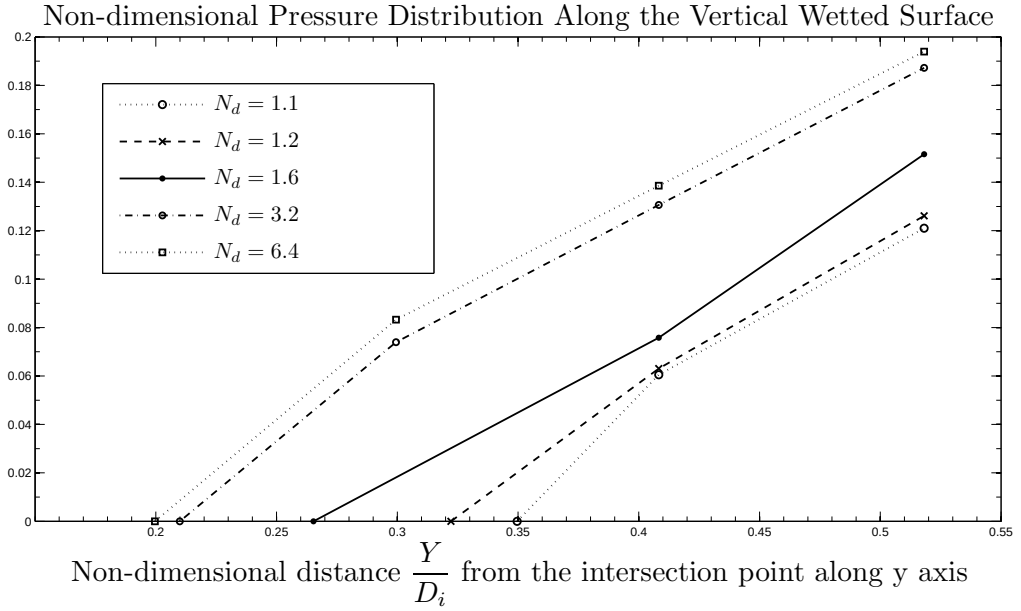

(b) along vertical surface

FIGURE 5.37: Finite depth effect of the box BX2 submerged at a non-dimensional initial depth $\widehat{d_i} = -1$ exiting with constant velocity of Froude number $F_r = 0.5$: (a) and (b) are plotted for different non-dimensional depths N_d at a non-dimensional time $\tau = 0.9$.

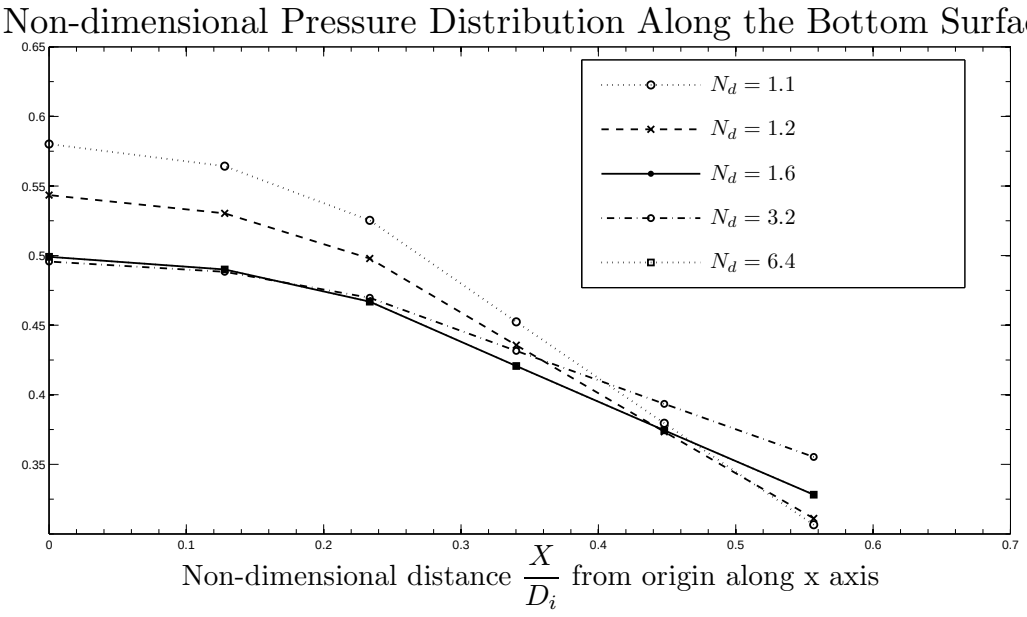

(a)

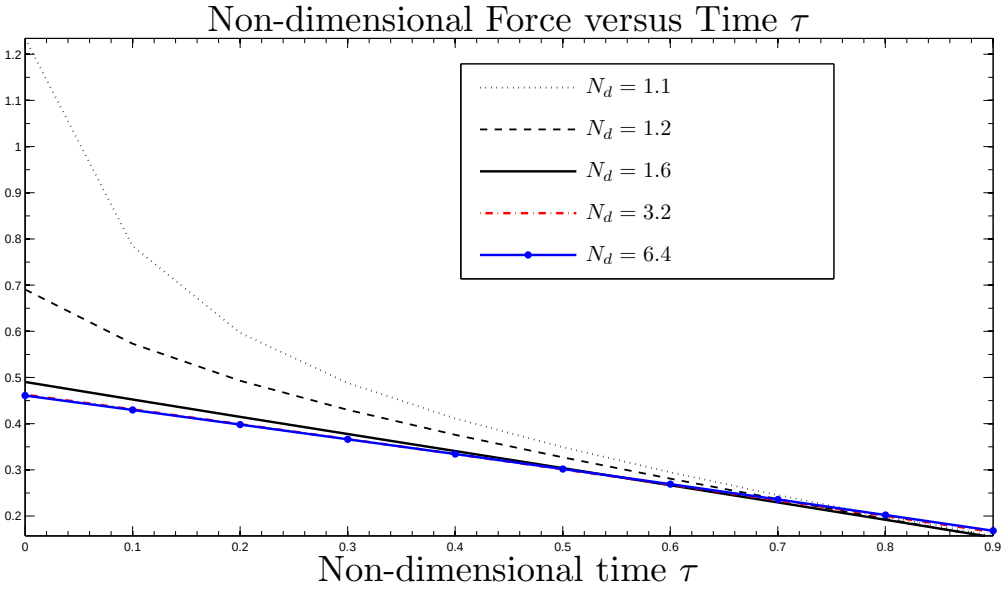

(b)

FIGURE 5.38: Finite depth effect of the box BX2 submerged at a non-dimensional initial depth $\widehat{d_i} = -1$ exiting with constant velocity of Froude number $F_r = 0.5$: (a) is plotted for different non-dimensional depths N_d at a non-dimensional time $\tau = 0.9$.

5.3 Constant acceleration exit

This section, for constant acceleration exit of symmetric wedges, asymmetric wedges, truncated wedges and box bodies, reviews the application of the non-linear theory and presents numerical results. For each shape considered in the study of constant velocity exit, we present computed free-surface profile, pressure distribution along the wetted part of the body and numerical total force experienced by the body as it exits through the free surface with constant velocity. The symmetric wedges, combined body, asymmetric wedges, truncated wedges and boxes exiting with constant acceleration are presented in section (5.3.1), (5.3.2), (5.3.3), (5.3.4) and (5.3.5) respectively.

5.3.1 Symmetric wedge exit

We present numerical results computed using the non-linear time-stepping method for the each symmetric wedge, as in the constant velocity exit cases. The test cases considered for the symmetric wedges exiting with constant acceleration are explained in this section. For the symmetric wedges exiting with constant acceleration, the results showing the time effect on the stages of the motion with constant acceleration are presented in section (5.3.1.1). The results of changing the acceleration and the comparison of numerical force with the analytical added mass force is given in section (5.3.1.2) and (5.3.1.3) respectively.

5.3.1.1 Time effect

As we did for the constant velocity exit, here we repeat the process for constant acceleration exit. The time effect on free-surface profile, pressure distribution and total force are computed for the symmetric wedges considered exiting with constant acceleration. The plots are obtained for different time intervals. The length of interval for each symmetric wedge depends on the angle of the symmetric wedges and the acceleration of the exit. For each specific interval, the results are plotted at different times. Fig. (5.39) and (5.40) show the time effect over the time intervals for the symmetric wedge SW30 exiting with constant acceleration of 1, while Fig. (5.41) and (5.42) show plots for the wedge exiting with constant acceleration of 0.5.

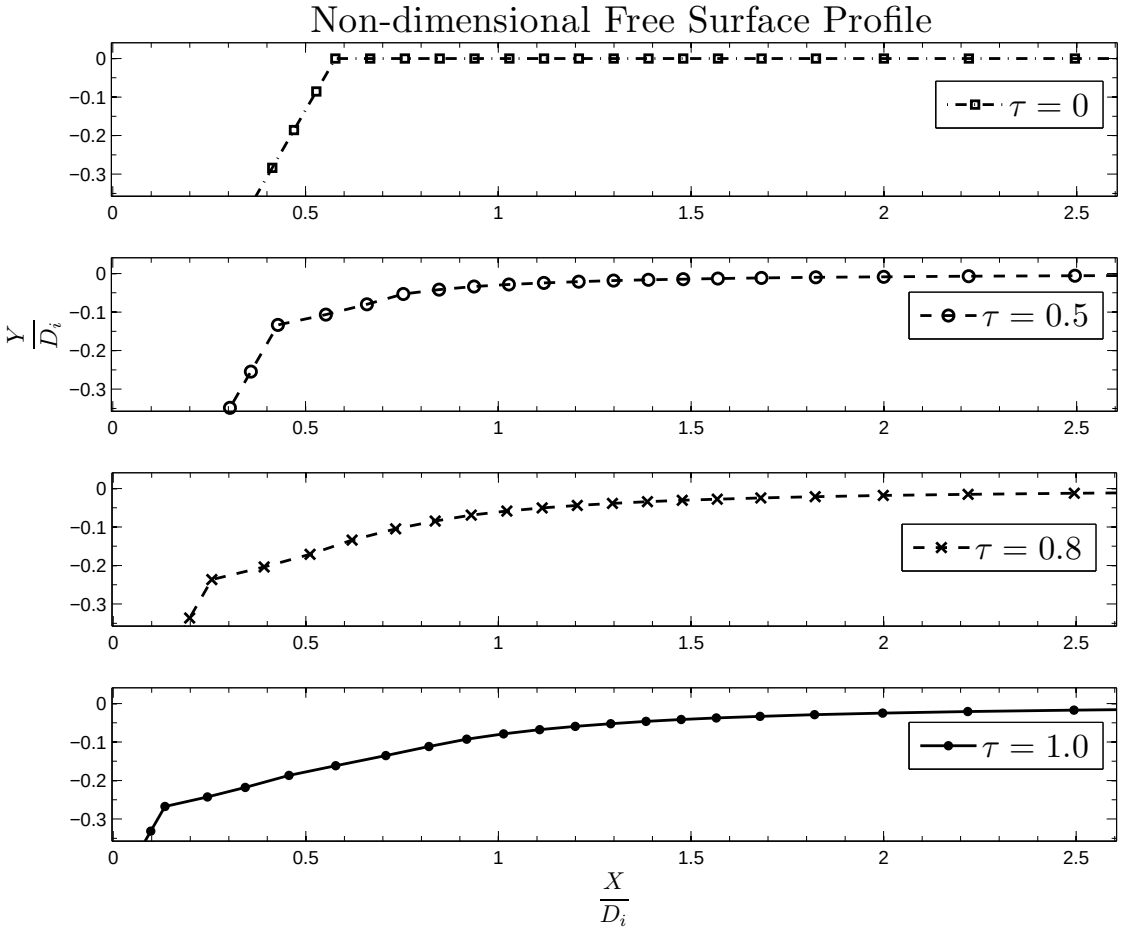

(a)

FIGURE 5.39: Time effect of the symmetric wedge SW30 submerged at a non-dimensional initial depth $\widehat{d}_i = -1$ exiting with constant acceleration $G_\tau = 1$: plotted at different non-dimensional times $\tau =$.

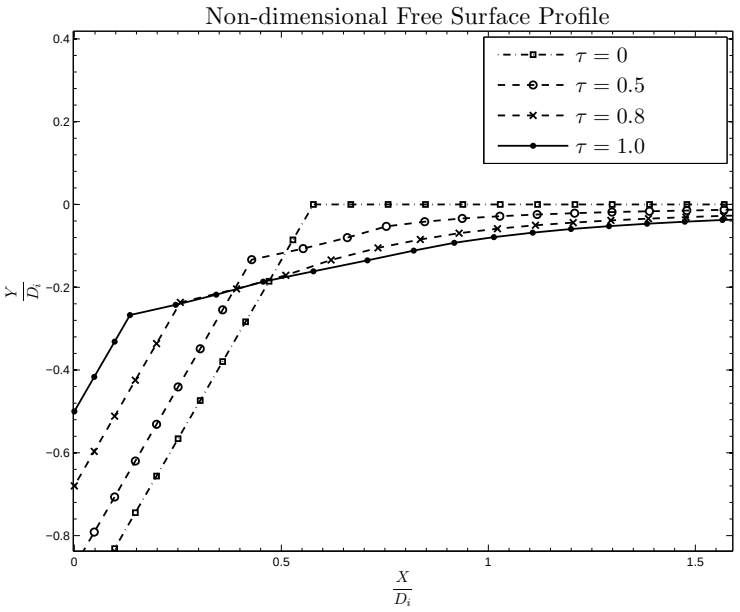

(a)

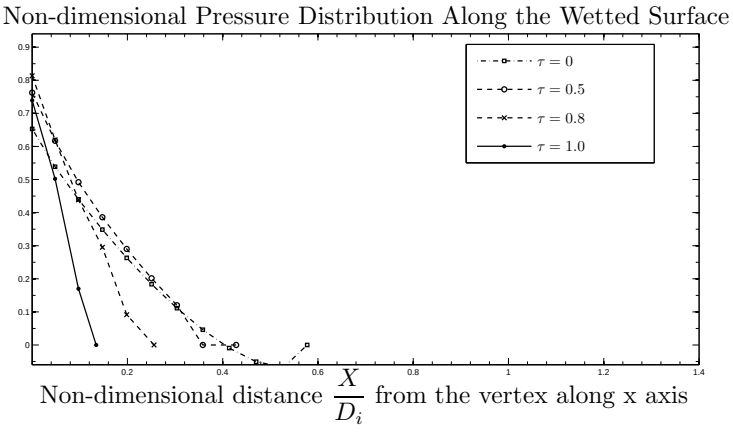

(b)

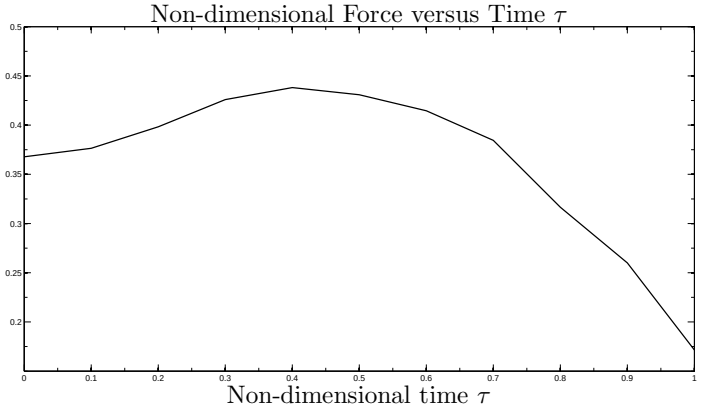

(c)

FIGURE 5.40: Time effect of the symmetric wedge SW30 submerged at a non-dimensional initial depth $\widehat{d_i} = -1$ exiting with constant acceleration $G_\tau = 1$: (a) and (b) are plotted at a non-dimensional time τ.

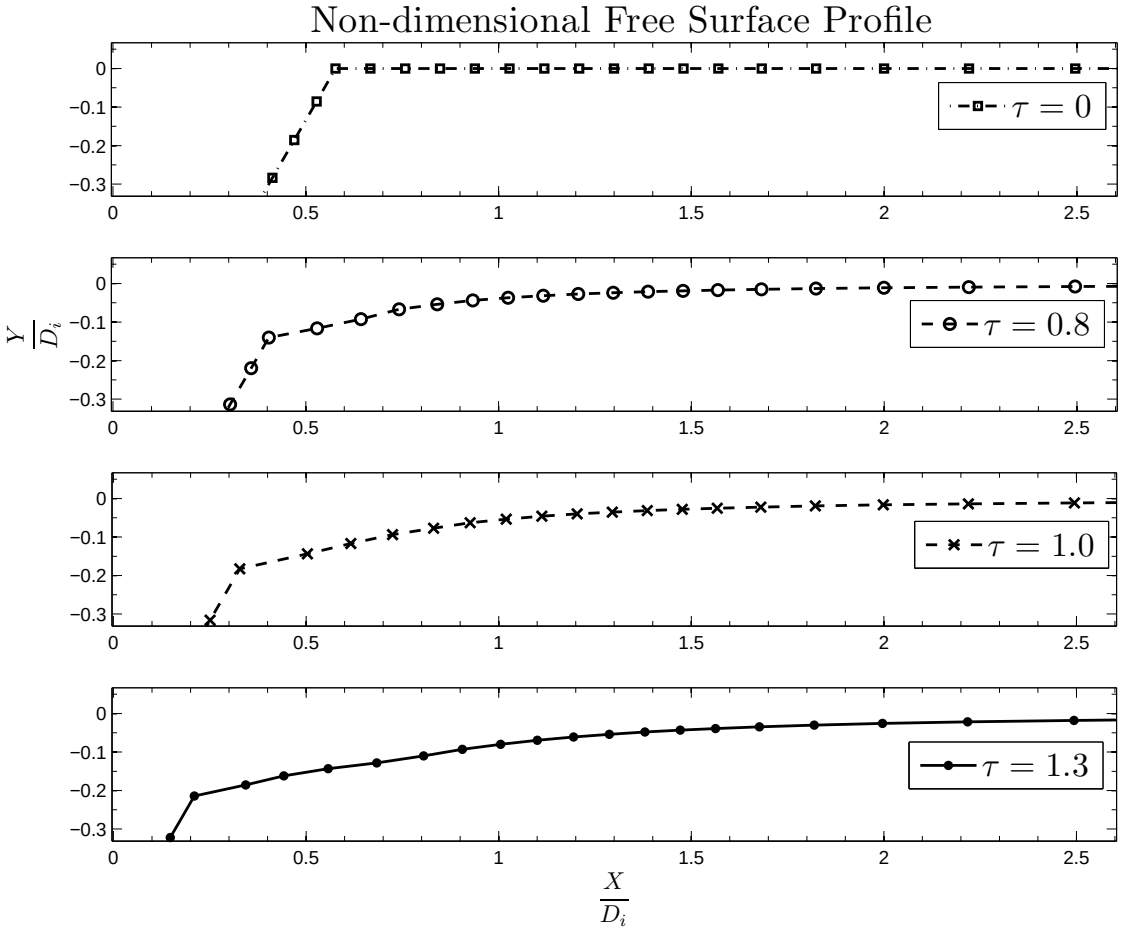

(a)

FIGURE 5.41: Time effect of the symmetric wedge SW30 submerged at a non-dimensional initial depth $\widehat{d_i} = -1$ exiting with constant acceleration $G_\tau = 0.5$: plotted at different non-dimensional times τ.

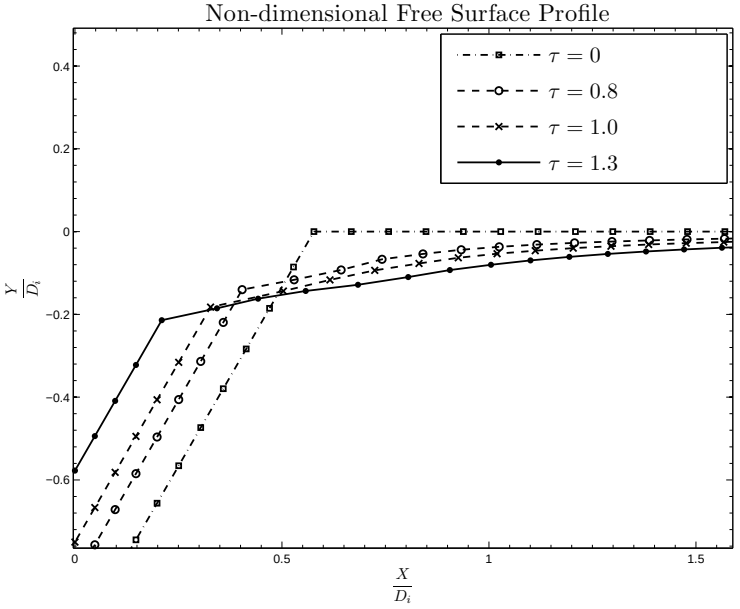

(a)

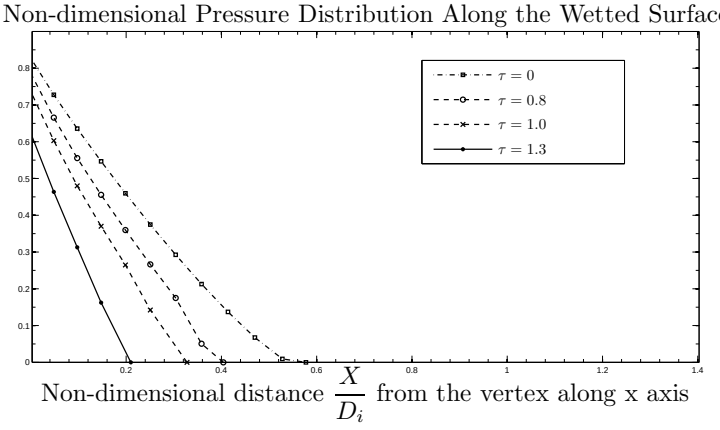

(b)

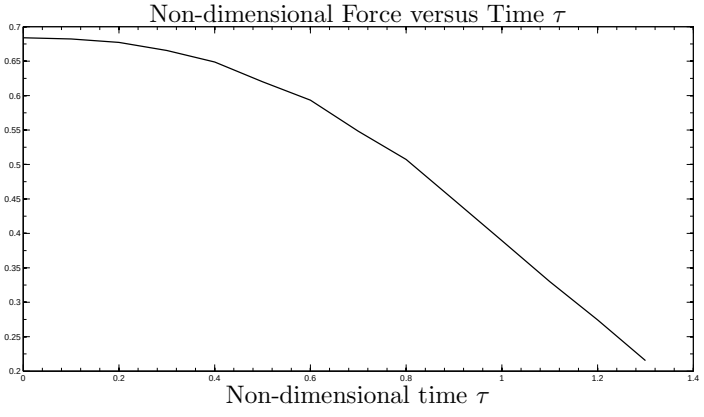

(c)

FIGURE 5.42: Time effect of the symmetric wedge SW30 submerged at a non-dimensional initial depth $\widehat{d_i} = -1$ exiting with constant acceleration $G_\tau = 0.5$: (a) and (b) are plotted at different non-dimensional times τ.

5.3.1.2 Acceleration effect

This section presents computed numerical results for free-surface profile, pressure distribution and total force. The results are obtained by running the program with different constant accelerations while attaining the same distance traveled by the symmetric wedges. Fig. (5.43) shows the acceleration effect of the symmetric wedge SW30 exiting with different accelerations.

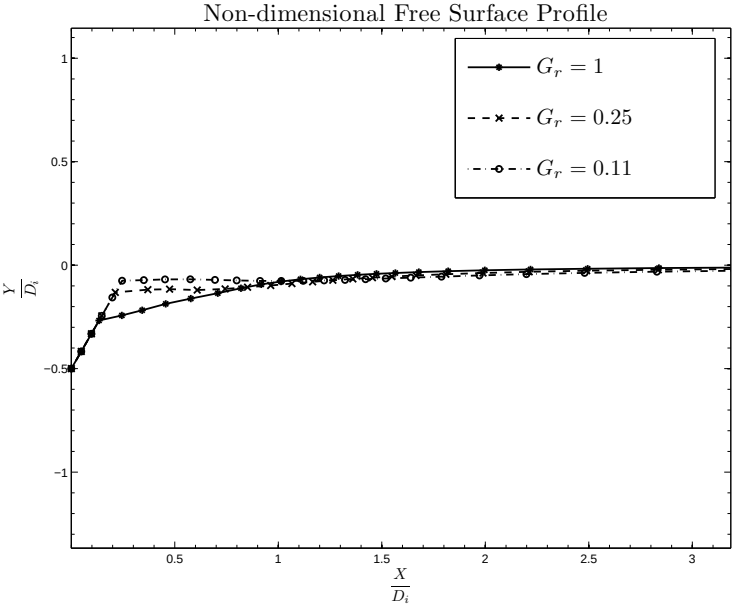

(a)

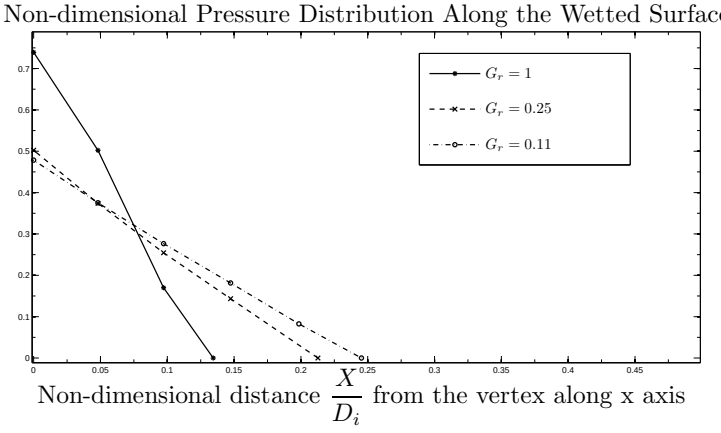

(b)

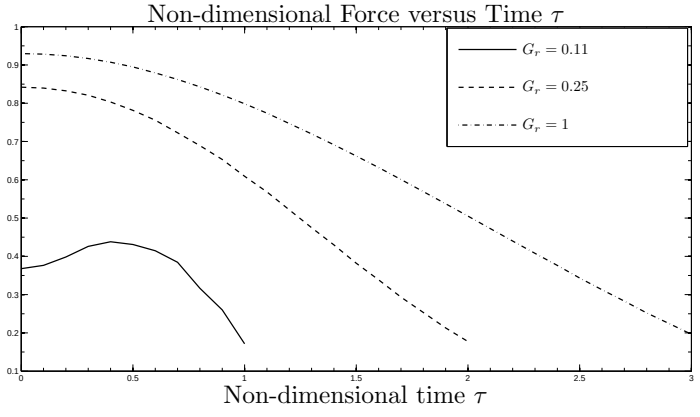

(c)

FIGURE 5.43: Acceleration effect of the symmetric wedge SW30 submerged at a non-dimensional initial depth $\widehat{d}_i = -1$ exiting with different constant accelerations G_τ: (a) and (b) are plotted at different non-dimensional times $\tau = 1, 2, 3$ and distance $\widehat{d} = -0.5$.

5.3.1.3 Added mass effect

As for entry cases, the analytical force computed for water exit of symmetric wedge is compared with the force difference between the total numerical force computed using the nonlinear theory of Vinje and Brevig and the buoyancy force to verify whether the forces agree at initial time t=0.

Fig. (5.44) and (5.45) show comparison of the computed force difference and the analytical added mass force computed for the symmetric wedge SW30 exiting with constant accelerations of 1 and 0.5, respectively. The computed added-mass force using Eq. (4.18) is negative and decreases in absolute magnitude as time increases for exit with constant acceleration (see Fig. (5.44) and (5.45)), but it is positive and decreases as time increases for exit with constant velocity (see Fig. (5.46)).

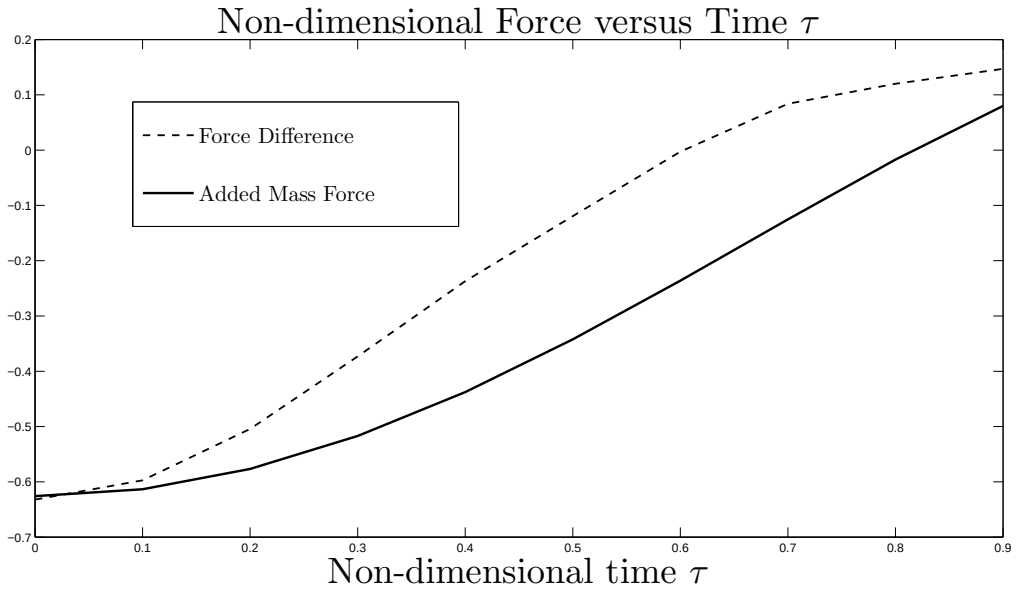

(a)

FIGURE 5.44: Computed numerical force difference and added mass force showing added mass effect for the wedge SW30 exiting with constant acceleration $G_\tau = 1$.

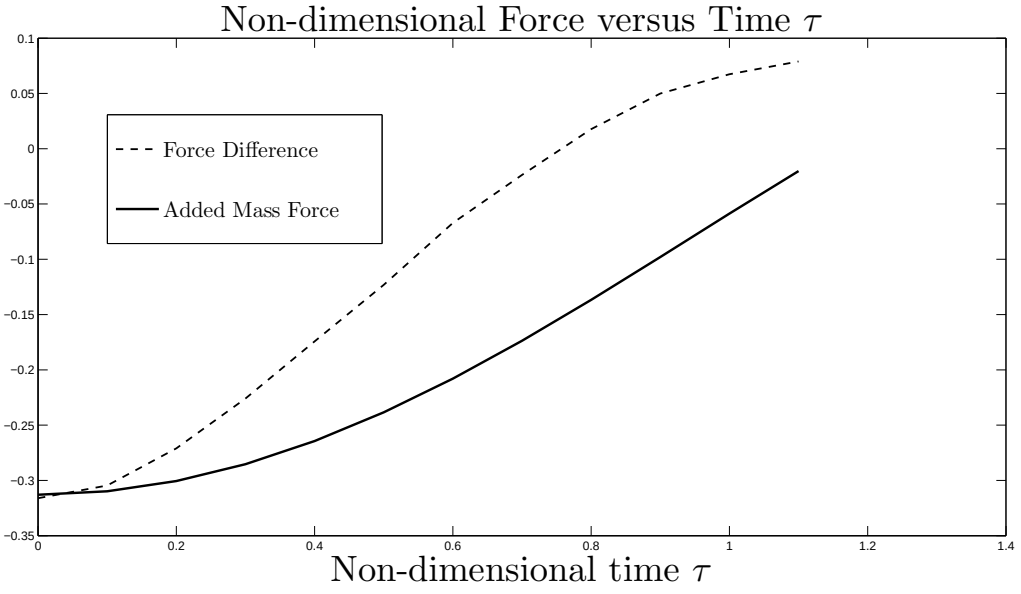

(a)

FIGURE 5.45: Computed numerical force difference and added mass force showing added mass effect for the wedge SW30 exiting with constant acceleration $G_\tau = 0.5$.

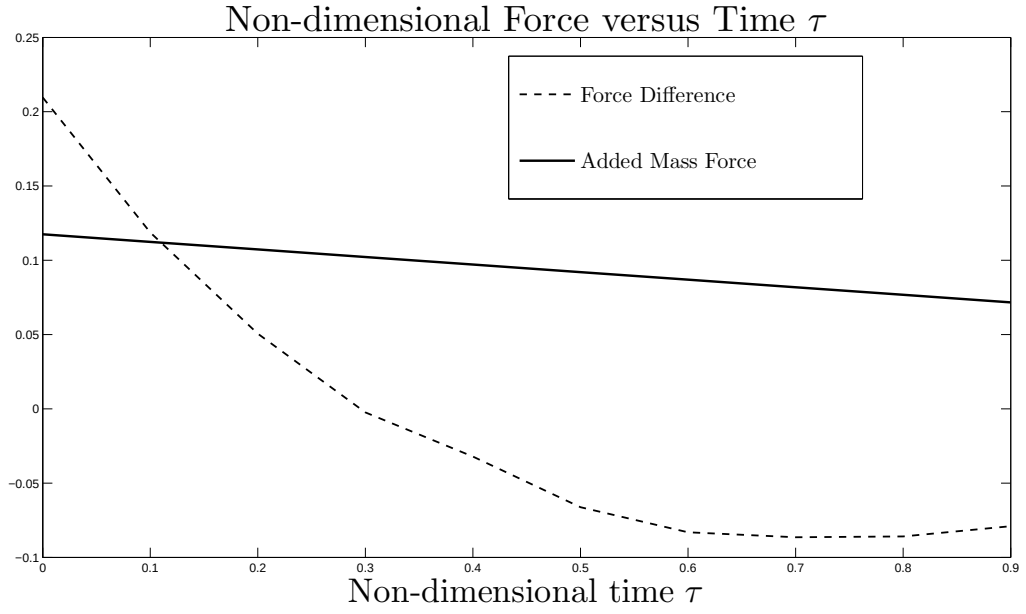

(a)

FIGURE 5.46: Computed numerical force difference and added mass force showing added mass effect for the wedge SW30 exiting with constant velocity of Froude number $F_r = 0.4$.

We also computed the added mass force for the symmetric wedges of various half angles exiting water with constant velocity. Fig. (5.46) shows comparison of the computed force difference and the analytical added mass force computed for the symmetric wedge SW30 exiting water with a Froude number F_r of 0.4. Results for other wedge angles are given in the CD, see Appendix B.

It is perhaps surprising that the added mass force and force difference is positive for the constant velocity exit case since one would expect a negative force when extracting a body from a fluid. However, in reality this would involve an period of acceleration which is missing from these idealised calculations. The main implication of the above results is that the upwards v^2 force in the added mass theory does in fact agree with the force difference, at least approximately, and is in the correct direction. Hence it should be included in more general motions for example those involving both acceleration and velocity terms, as in Fig. (5.45).

5.3.2 Combined body exit

The test cases considered for the combined body exiting with constant acceleration are explained in this section. For the combined body exiting with constant acceleration, results showing time effect on the motion with constant acceleration are presented in section (5.3.2.1), while the results of changing the acceleration are given in section (5.3.2.2).

5.3.2.1 Time effect

As for the constant velocity exit of the combined body, here we repeat the process for constant acceleration exit. The time effect on free-surface profile, pressure distribution and total force are computed for the combined body exiting with constant acceleration. The plots are obtained for different time intervals. For each specific interval, the results are plotted at different time. Fig. (5.47) to (5.50) show the time effect of the combined body CB30 exiting with constant acceleration of 0.5.

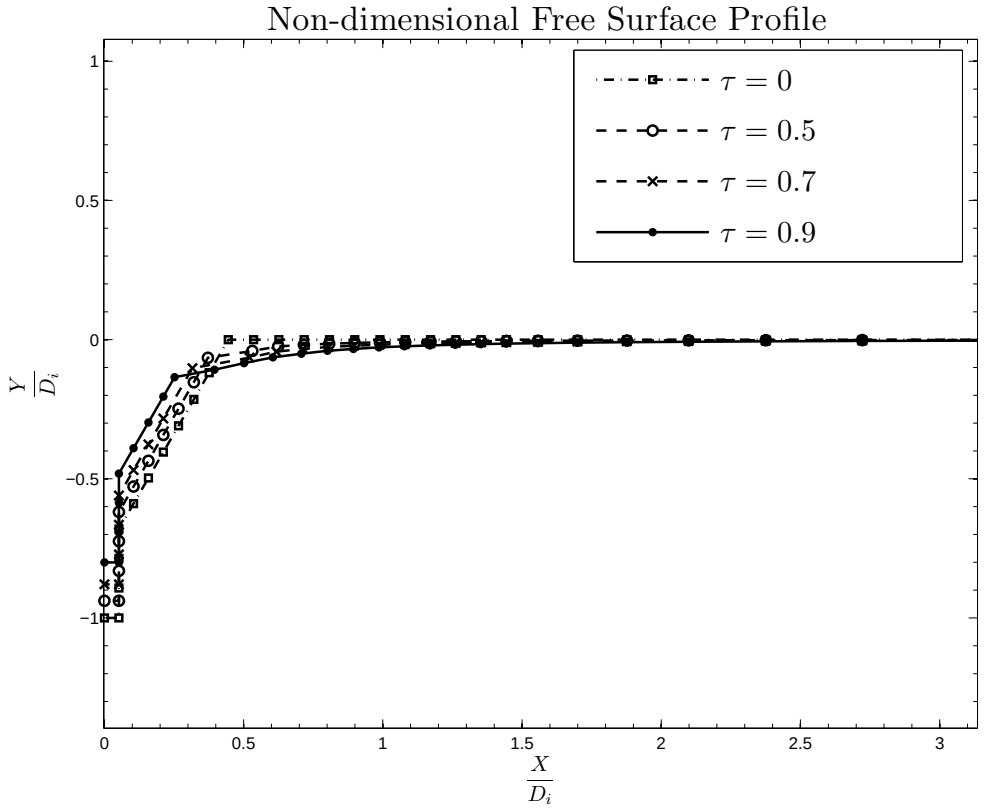

(a)

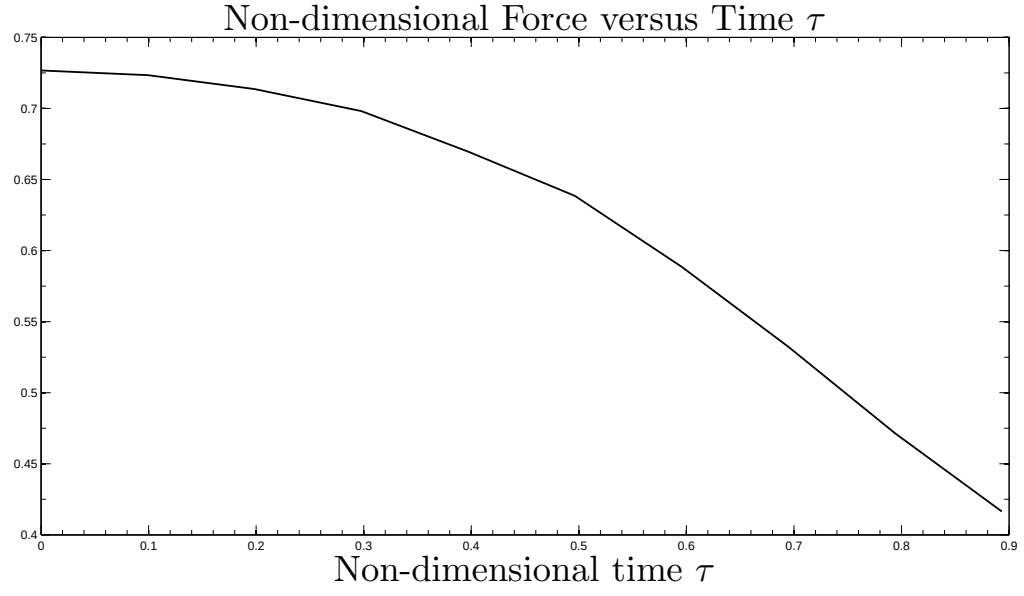

(b)

FIGURE 5.47: Time effect of the combined body CB30 submerged at a non-dimensional initial depth $\widehat{d_i} = -1$ exiting with constant acceleration $G_\tau = 0.5$: (a) is plotted at different non-dimensional times τ.

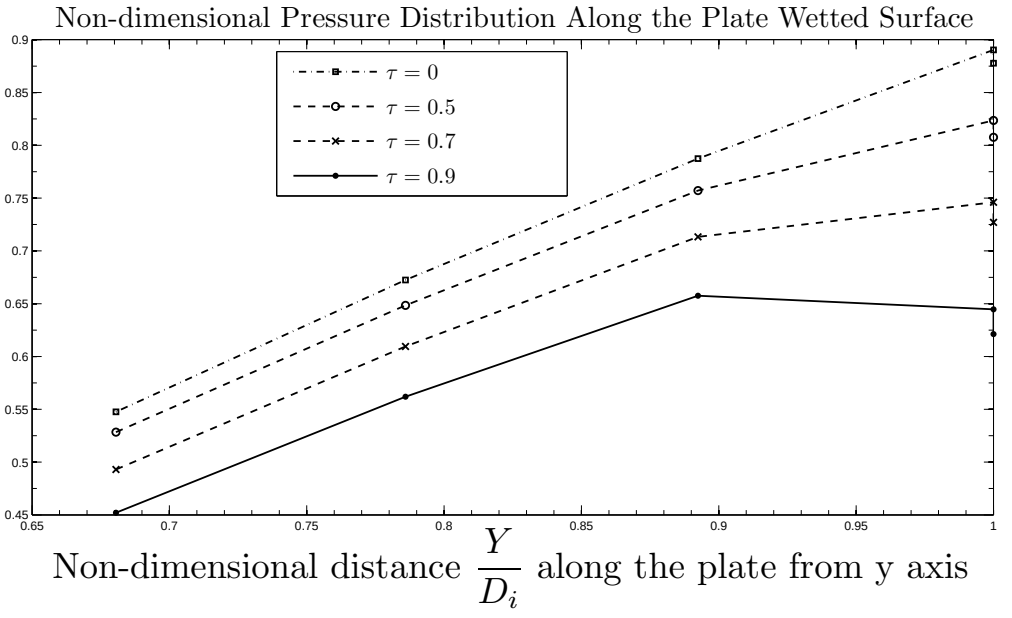

(a)

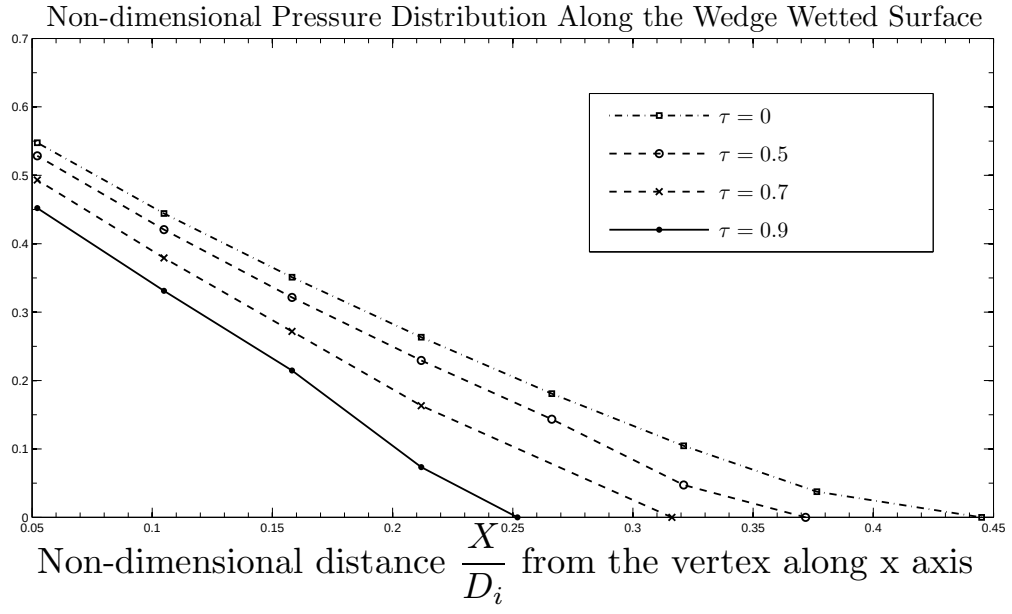

(b)

FIGURE 5.48: Time effect of the combined body CB30 submerged at a non-dimensional initial depth $\widehat{d_i} = -1$ exiting with constant acceleration $G_\tau = 0.5$: (a) and (b) are plotted at different non-dimensional times τ.

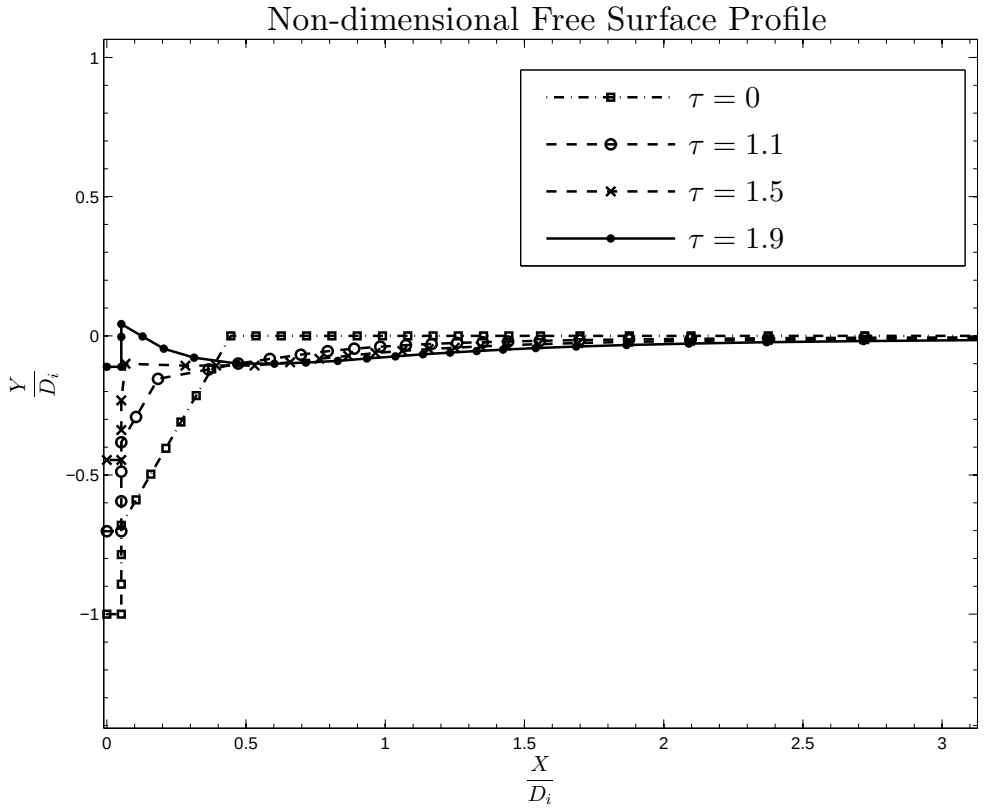

(a)

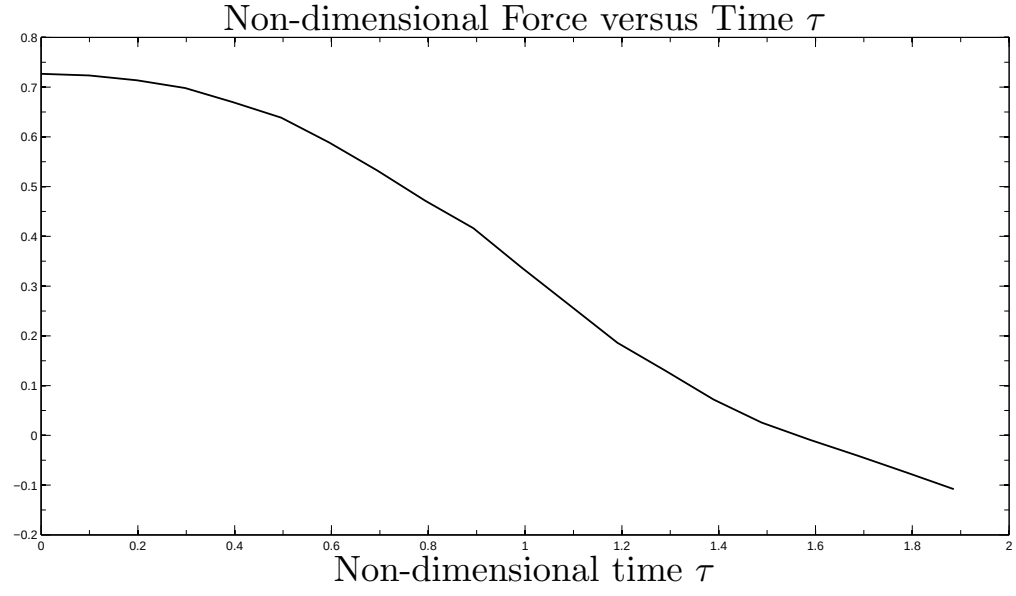

(b)

FIGURE 5.49: Time effect of the combined body CB30 submerged at a non-dimensional initial depth $\widehat{d_i} = -1$ exiting with constant acceleration $G_\tau = 0.5$: (a) is plotted at different non-dimensional times τ.

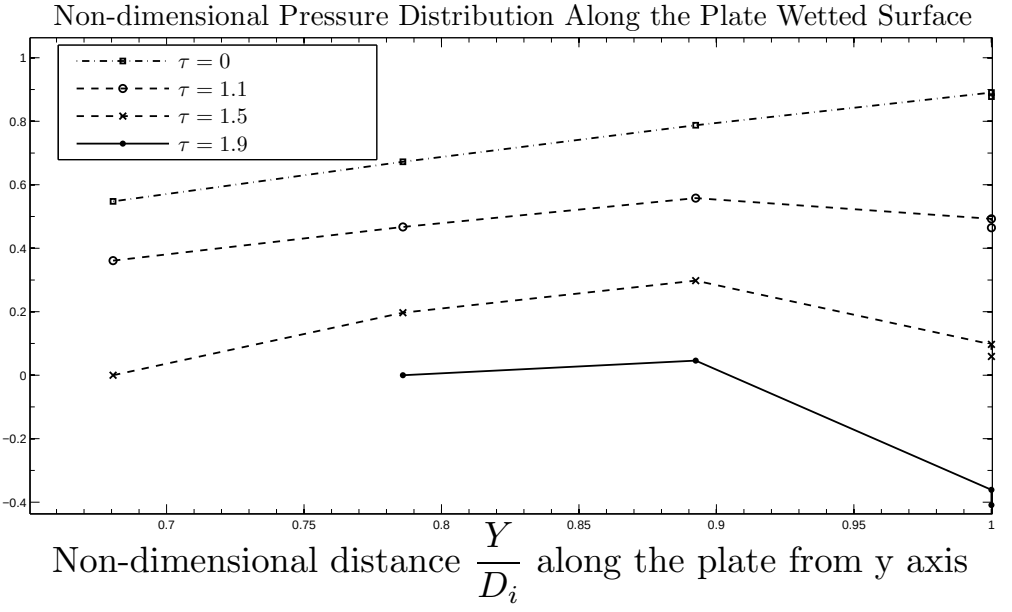

(a)

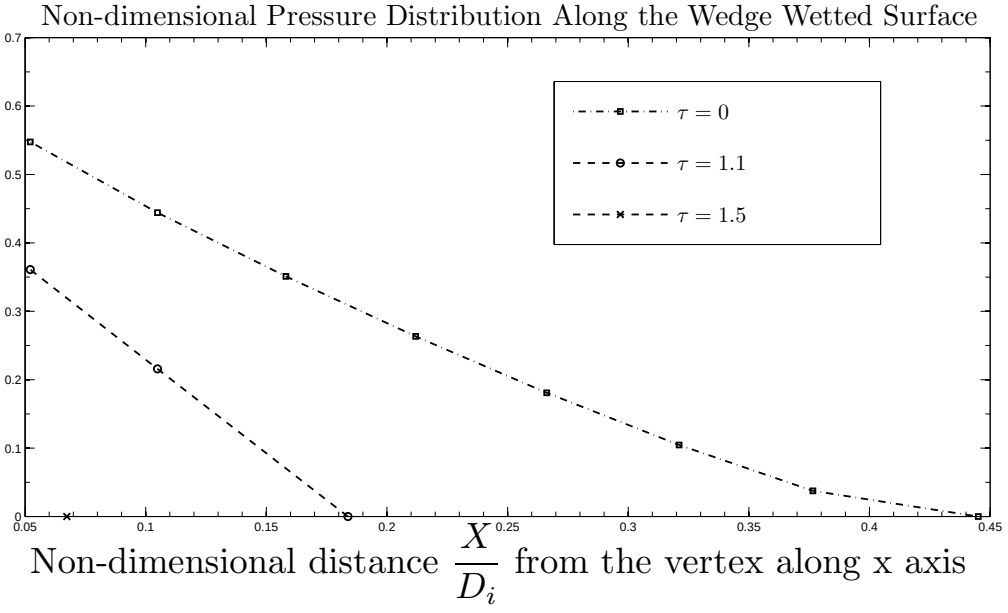

(b)

FIGURE 5.50: Time effect of the combined body CB30 submerged at a non-dimensional initial depth $\widehat{d_i} = -1$ exiting with constant acceleration $G_\tau = 0.5$: (a) and (b) are plotted at different non-dimensional times τ.

5.3.2.2 Acceleration effect

This section for constant acceleration exit of the combined body presents numerical results for free-surface profile, pressure distribution and total force. The results are obtained by running the program with different constant accelerations while attaining at a same distance traveled by the combined body. Fig. (5.51) shows the acceleration effect of the combined body CB30 exiting with different accelerations.

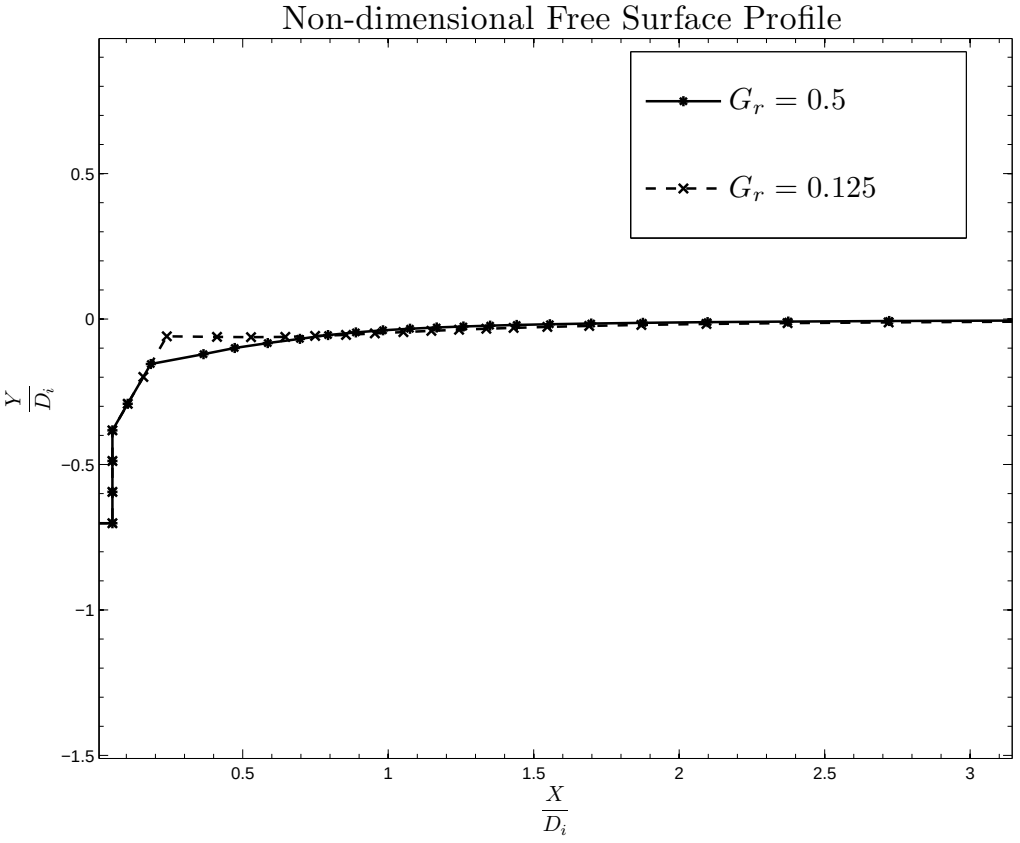

(a)

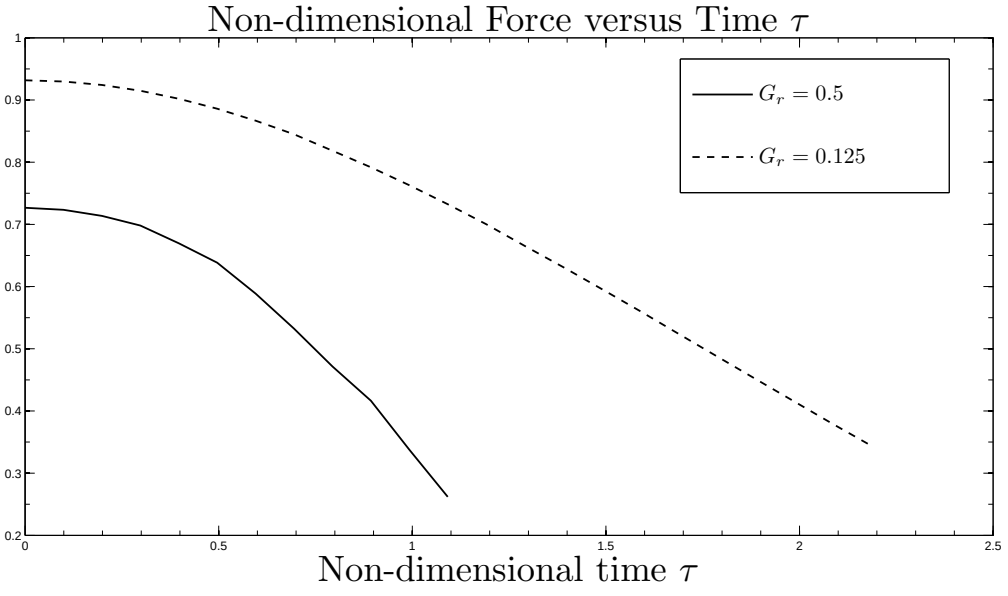

(b)

FIGURE 5.51: Acceleration effect of the combined body CB30 submerged at a non-dimensional initial depth $\widehat{d_i} = -1$ exiting with different constant accelerations G_τ: (a) is plotted at different non-dimensional times $\tau = 1.09, 2.18$ and distance $\widehat{d} = -0.7$.

5.3.3 Asymmetric wedge exit

We here present numerical results for the same asymmetric wedges. The test cases considered for the asymmetric wedges exiting with constant acceleration are explained in this section. For the asymmetric wedges exiting with constant acceleration, the results showing the time effect on the stages of the motion with constant acceleration is presented in section (5.3.3.1), while the results of changes in acceleration is given in section (5.3.3.2).

5.3.3.1 Time effect

As for the constant velocity exit, here we repeat the process for constant acceleration entry of asymmetric wedges. The time effect on free-surface profile, pressure distribution and total force are computed for the asymmetric wedges entering with constant acceleration. The plots are obtained for different time intervals. The length of interval for each asymmetric wedge depends on the angle of the asymmetric wedges and the acceleration of the entry. For each specific interval, the results are plotted at different time and it repeats with the intervals. Fig. (5.52) and (5.53) show the time effect of the asymmetric wedge AW4 exiting with constant acceleration of 0.5, whereas Fig. (5.54) to (5.55) show the effect for the constant acceleration of 0.125.

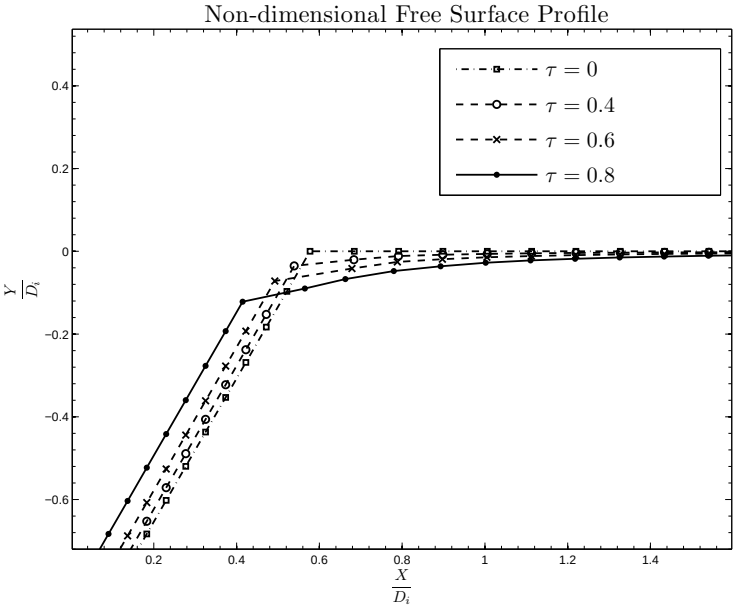

(a)

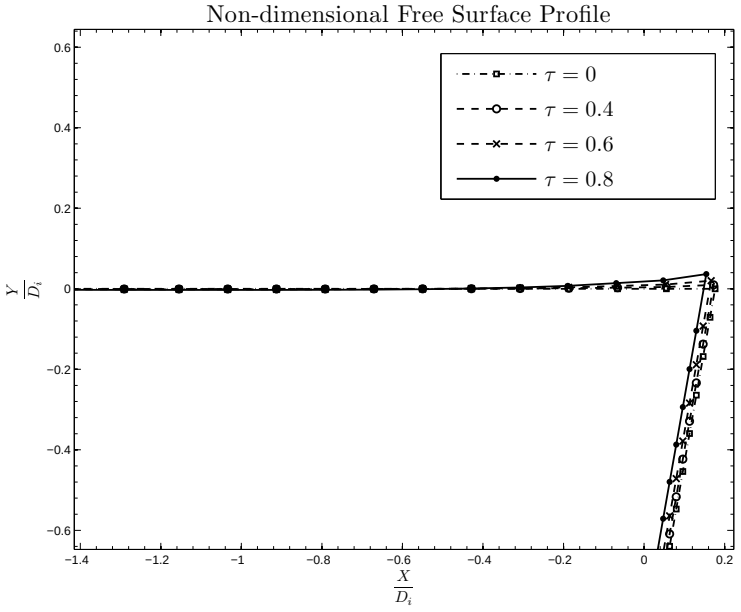

(b)

FIGURE 5.52: Time effect of the asymmetric wedge AW4 submerged at a non-dimensional initial depth $\widehat{d_i} = -1$ exiting with constant acceleration $G_\tau = 0.5$: (a) and (b) are plotted at different non-dimensional times τ.

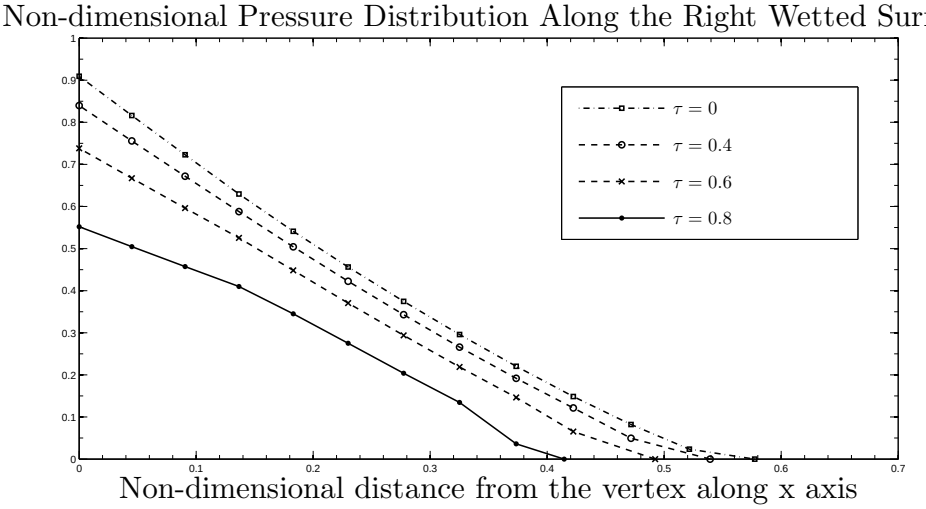

(a)

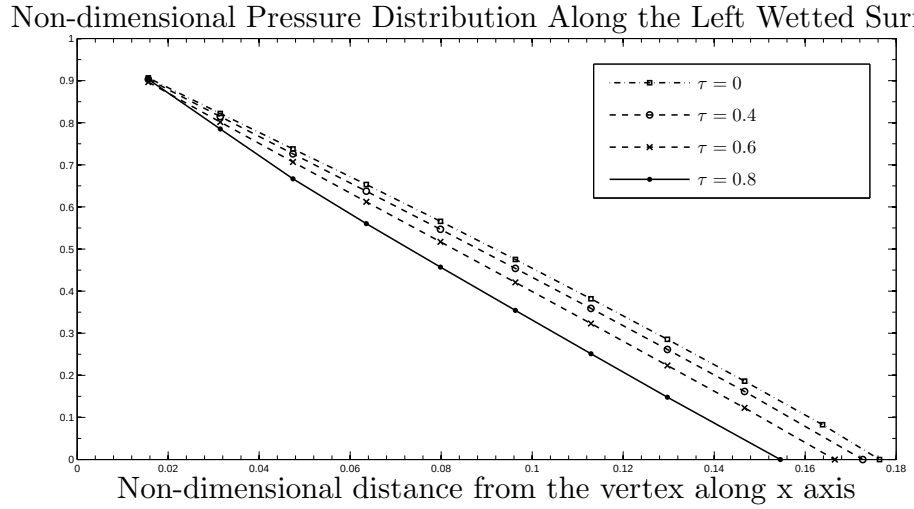

(b)

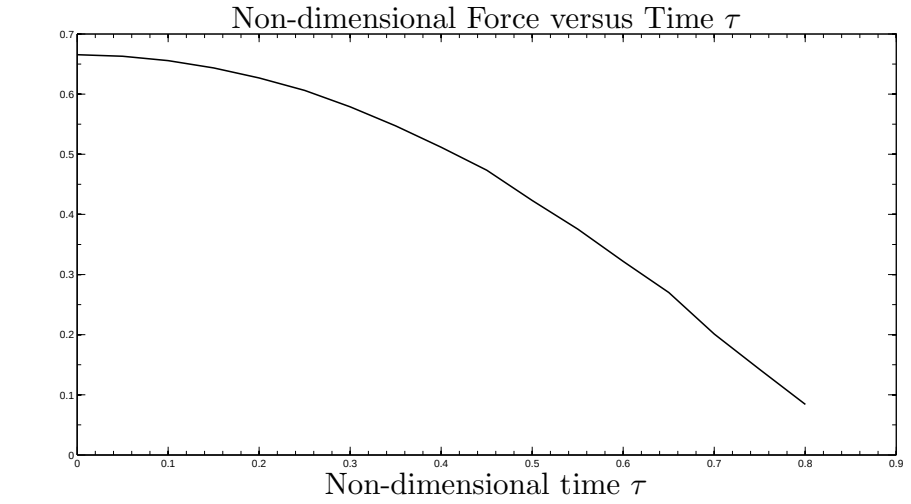

(c)

FIGURE 5.53: Time effect of the asymmetric wedge AW4 submerged at a non-dimensional initial depth $\widehat{d}_i = -1$ exiting with constant acceleration $G_\tau = 0.5$: (a) and (b) are plotted at different non-dimensional times τ.

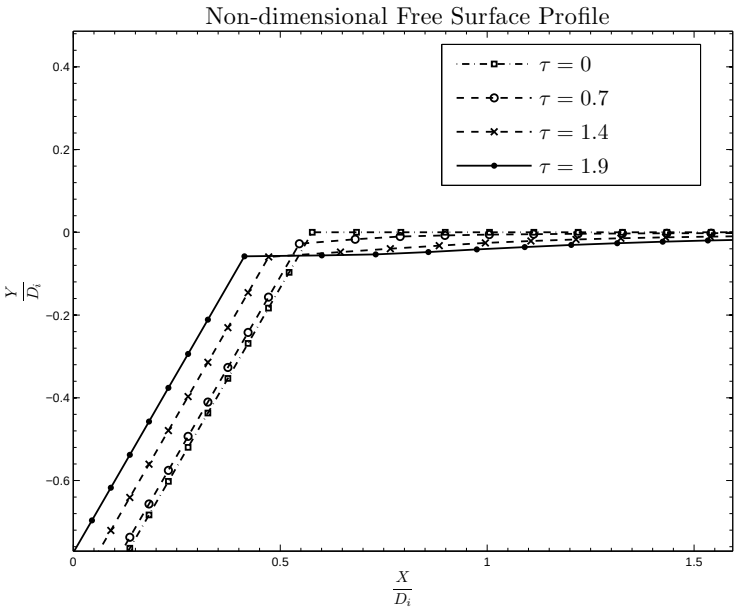

(a)

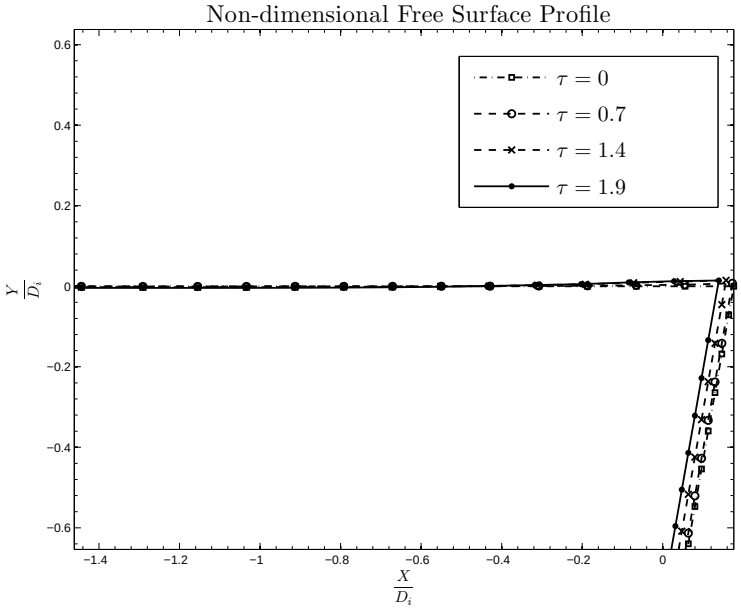

(b)

FIGURE 5.54: Time effect of the asymmetric wedge AW4 submerged at a non-dimensional initial depth $\widehat{d_i} = -1$ exiting with constant acceleration $G_\tau = 0.125$: (a) and (b) are plotted at different non-dimensional times τ.

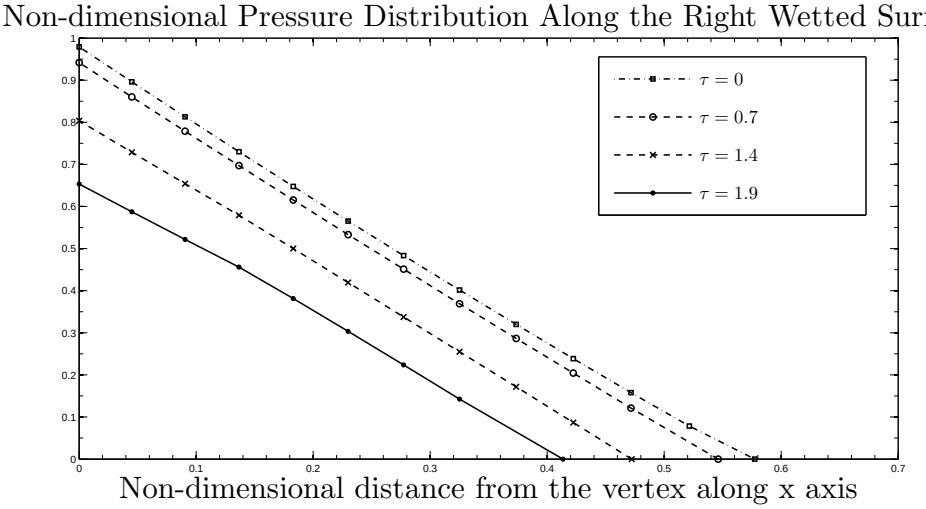

(a)

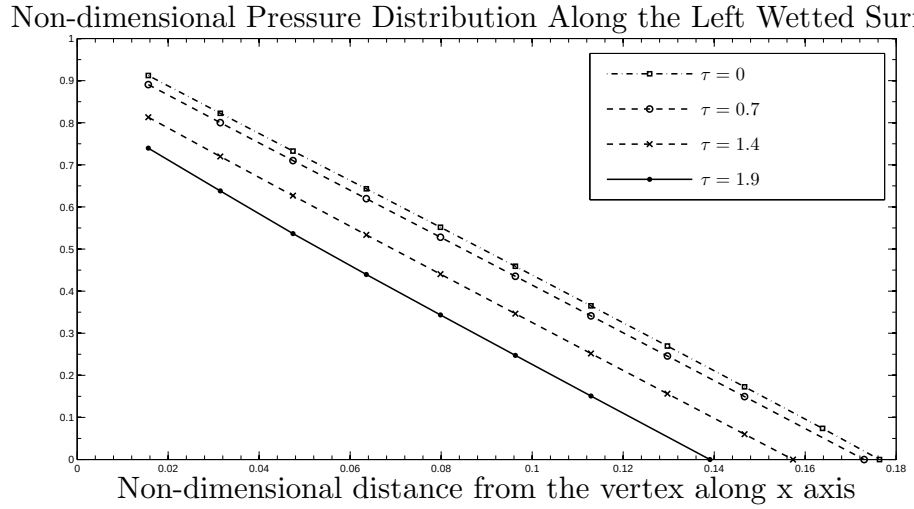

(b)

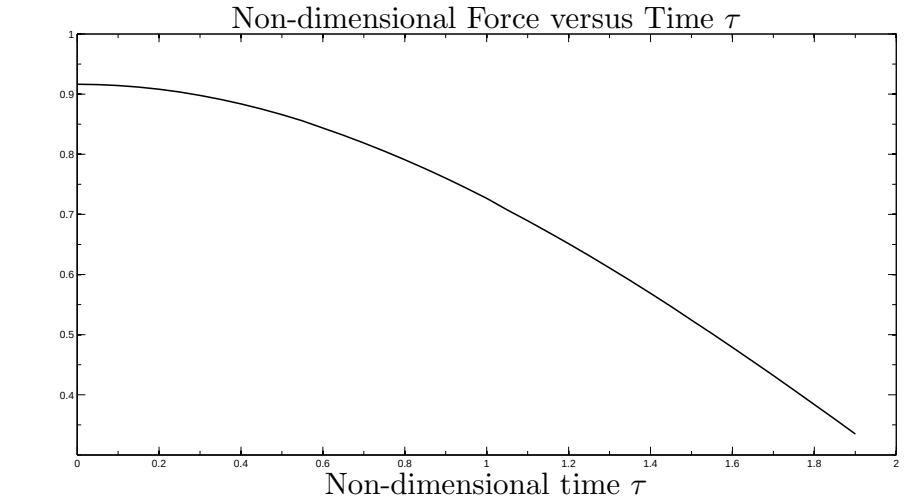

(c)

FIGURE 5.55: Time effect of the asymmetric wedge AW4 submerged at a non-dimensional initial depth $\widehat{d}_i = -1$ exiting with constant acceleration $G_\tau = 0.125$: (a) and (b) are plotted at different non-dimensional times τ.

5.3.3.2 Acceleration effect

This section for constant acceleration exit of asymmetric wedges presents numerical results for free-surface profile, pressure distribution and total force. The results are obtained by running the program with different constant accelerations while attaining the same distance traveled by the asymmetric wedges. Fig. (5.56) and (5.57) show the acceleration of the asymmetric wedge AW4 exiting with different accelerations.

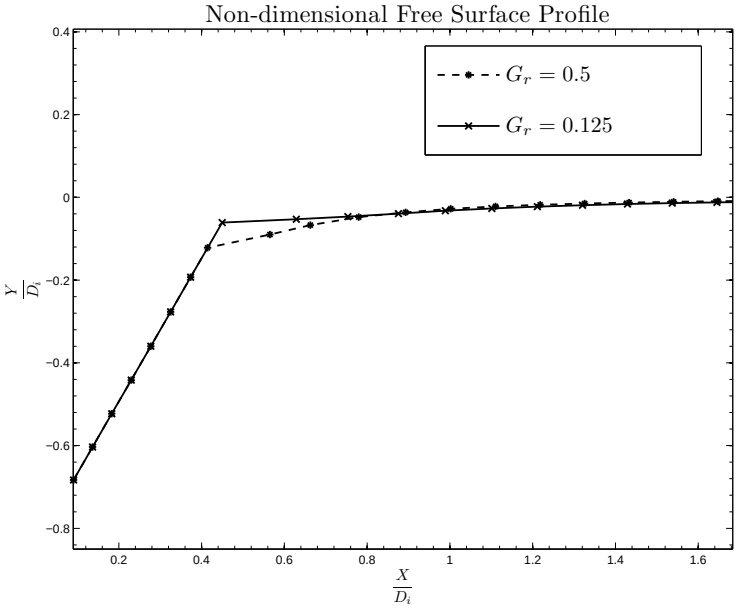

(a)

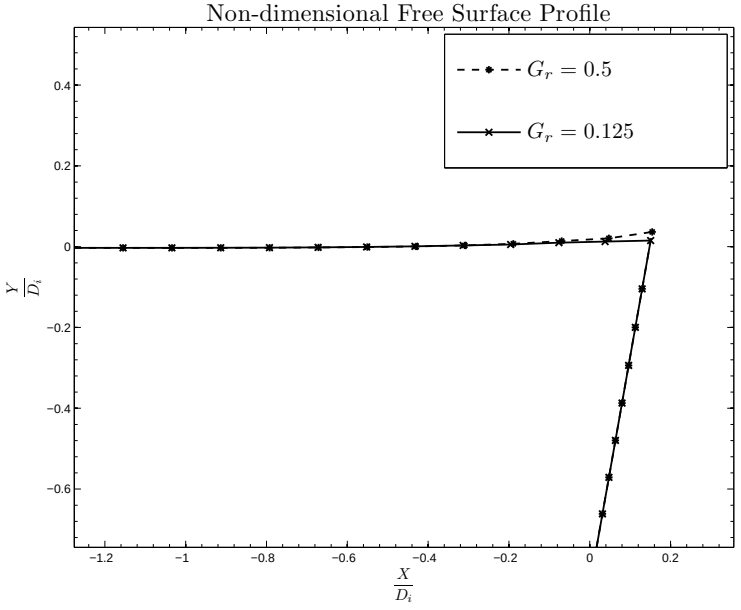

(b)

FIGURE 5.56: Acceleration effect of the symmetric wedge AW4 submerged at a non-dimensional initial depth $\widehat{d_i} = -1$ exiting with different constant accelerations G_τ: (a) and (b) are plotted at different non-dimensional times $\tau = 0.8, 1.6$ and distance $\widehat{d} = -0.84$.

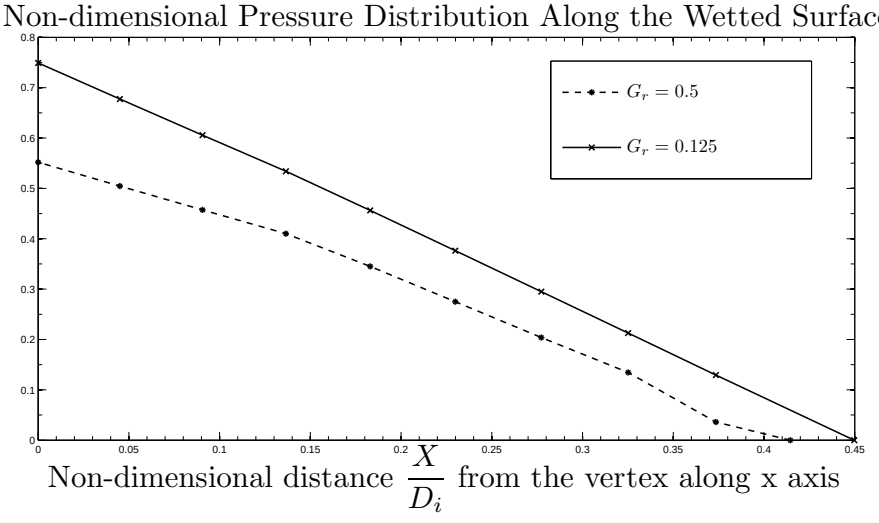

(a)

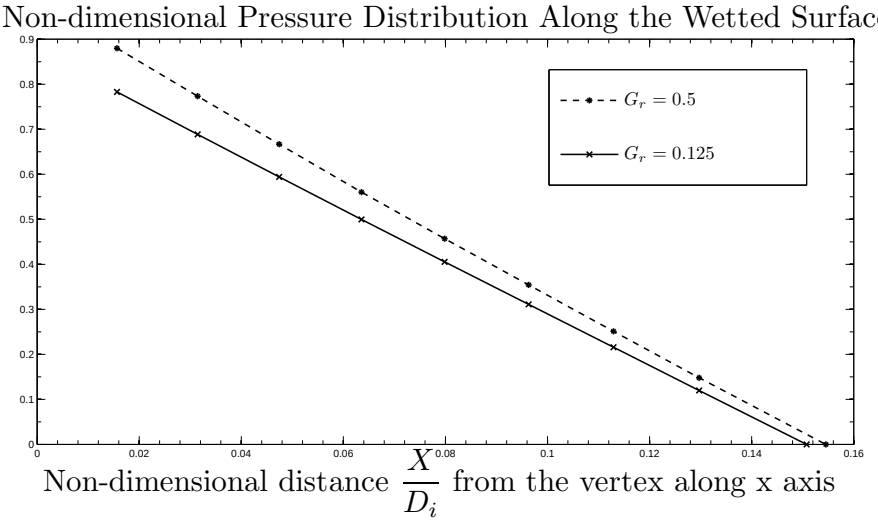

(b)

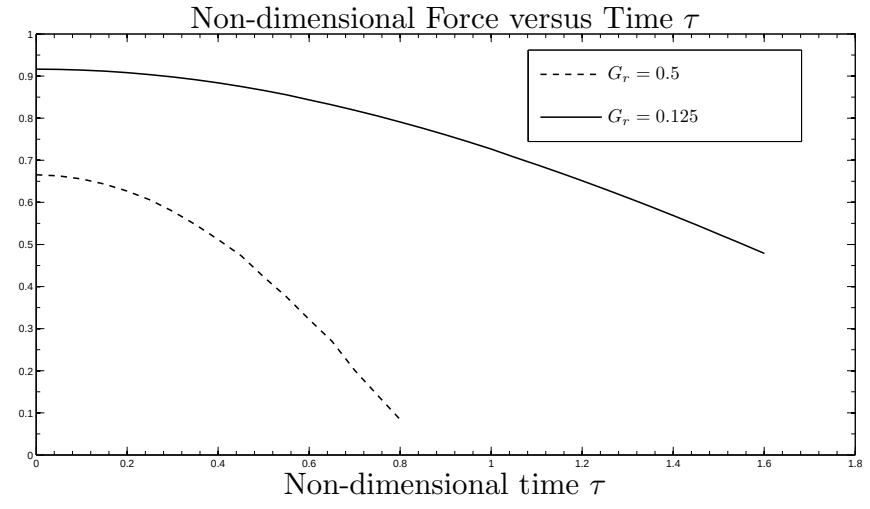

(c)

FIGURE 5.57: Acceleration effect of the symmetric wedge AW4 submerged at a non-dimensional initial depth $\widehat{d_i} = -1$ exiting with different constant accelerations G_τ: (a) and (b) are plotted at different non-dimensional times $\tau = 0.8, 1.6$ and distance $\widehat{d} = -0.84$.

5.3.4 Truncated wedge exit

We present numerical results computed using the non-linear time-stepping method for the truncated wedges as in the constant velocity exit of the truncated wedges. For the truncated wedge exiting with constant acceleration, results showing the time effect with constant acceleration are presented in section (5.3.4.1), while the results of changes in acceleration are given in section (5.3.4.2).

5.3.4.1 Time effect

As for the constant velocity exit of the truncated wedges, here we repeat the process for constant acceleration exit of the truncated wedges. The time effect on free-surface profile, pressure distribution and total force are computed for the truncated wedges exiting with constant acceleration. The plots are obtained for different time intervals. The length of interval for each truncated wedge depends on the angle of the truncated wedges and the acceleration of the exit. For each specific interval, the results are plotted at different time. Fig. (5.58) shows the time effect of the truncated wedge TW3 exiting with constant acceleration of 0.5.

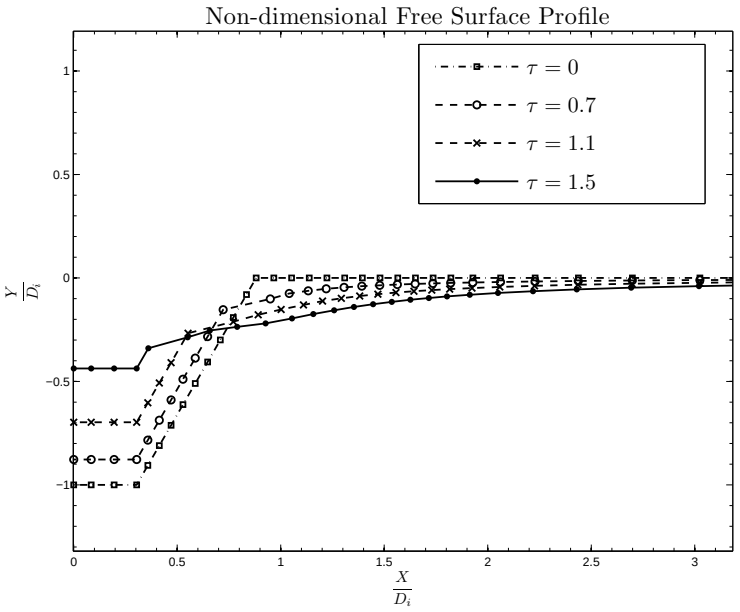

(a)

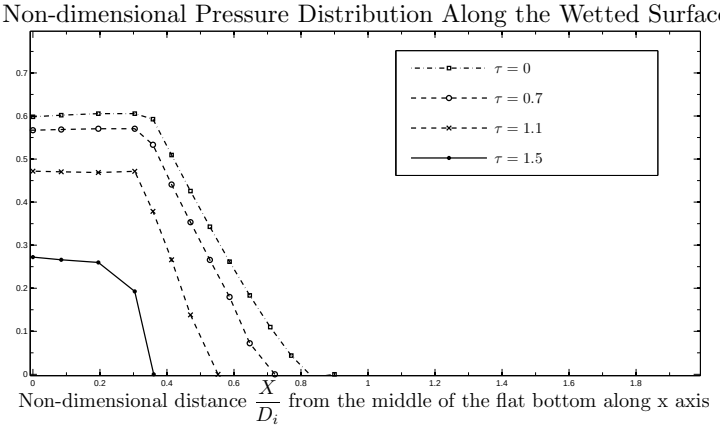

(b)

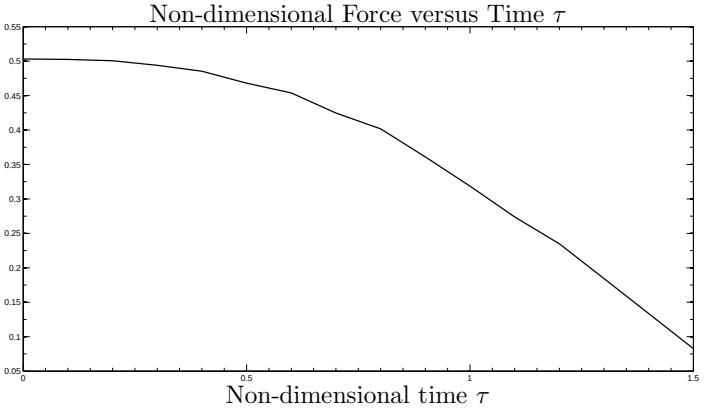

(c)

FIGURE 5.58: Time effect of the truncated wedge TW3 submerged at a non-dimensional initial depth $\widehat{d_i} = -1$ exiting with constant acceleration $G_\tau = 0.5$: (a) and (b) are plotted at different non-dimensional times τ.

5.3.4.2 Acceleration effect

This section for constant acceleration exit of the truncated wedges presents numerical results for free-surface profile, pressure distribution and total force. The results are obtained by running the program with different constant accelerations while attaining the same distance traveled by the truncated wedges. Fig. (5.59) shows the acceleration of the truncated wedge TW3 exiting with different accelerations.

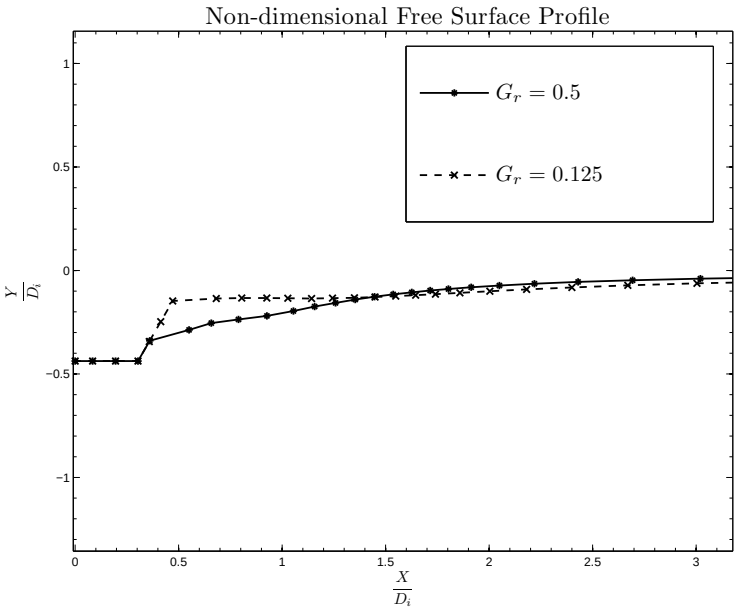

(a)

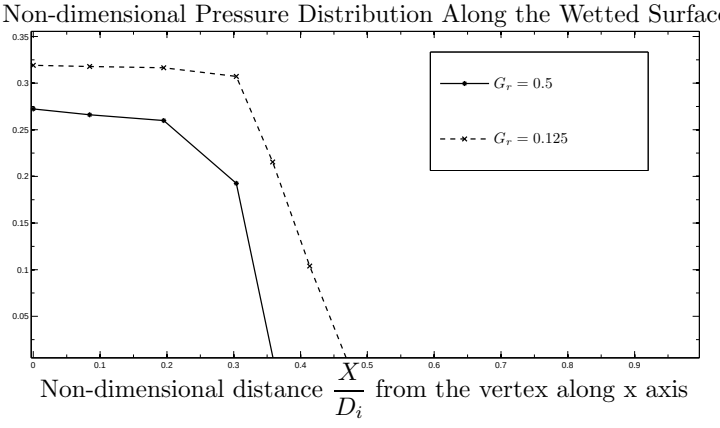

(b)

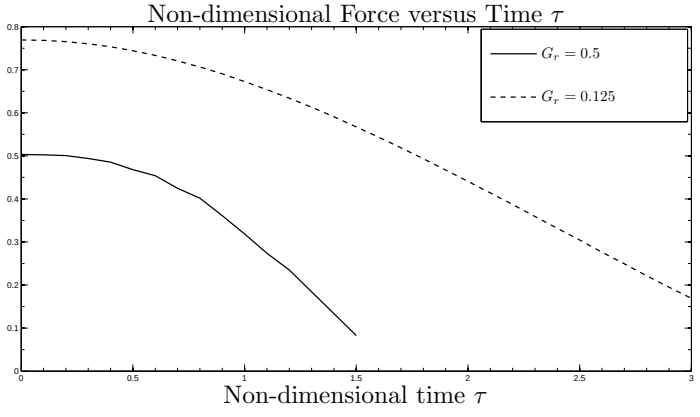

(c)

FIGURE 5.59: Acceleration effect of the truncated wedge TW3 submerged at a non-dimensional initial depth $\widehat{d_i} = -1$ exiting with different constant accelerations G_τ: (a) and (b) are plotted at different non-dimensional times $\tau = 1.5, 3$ and distance $\widehat{d} = -0.437$.

5.3.5 Box body exit

We present numerical results computed using the non-linear time-stepping method for the box body same as considered in the constant velocity exit. For the box body exiting with constant acceleration, the results showing time effect on the stages of the motion with constant acceleration are presented in section (5.3.5.1). The results of changes in acceleration and the comparison of numerical force with the analytical added mass force are given in section (5.3.5.2) and (5.3.5.3) respectively.

5.3.5.1 Time effect

As for the constant velocity exit of the box body, here we repeat the process for constant acceleration exit of the box body. The time effect on free-surface profile, pressure distribution and total force are computed for the box body exiting with constant acceleration. The plots are obtained for different time intervals. The length of interval for each box body depends on the aspect ratio of the box body and the acceleration of the exit. For each specific interval, the results are plotted at different time. Fig. (5.60) and (5.61) show the time effect of the box body BX2 exiting with constant acceleration of 0.5, whereas Fig. (5.62) and (5.63) show the effect for the constant acceleration of 0.125.

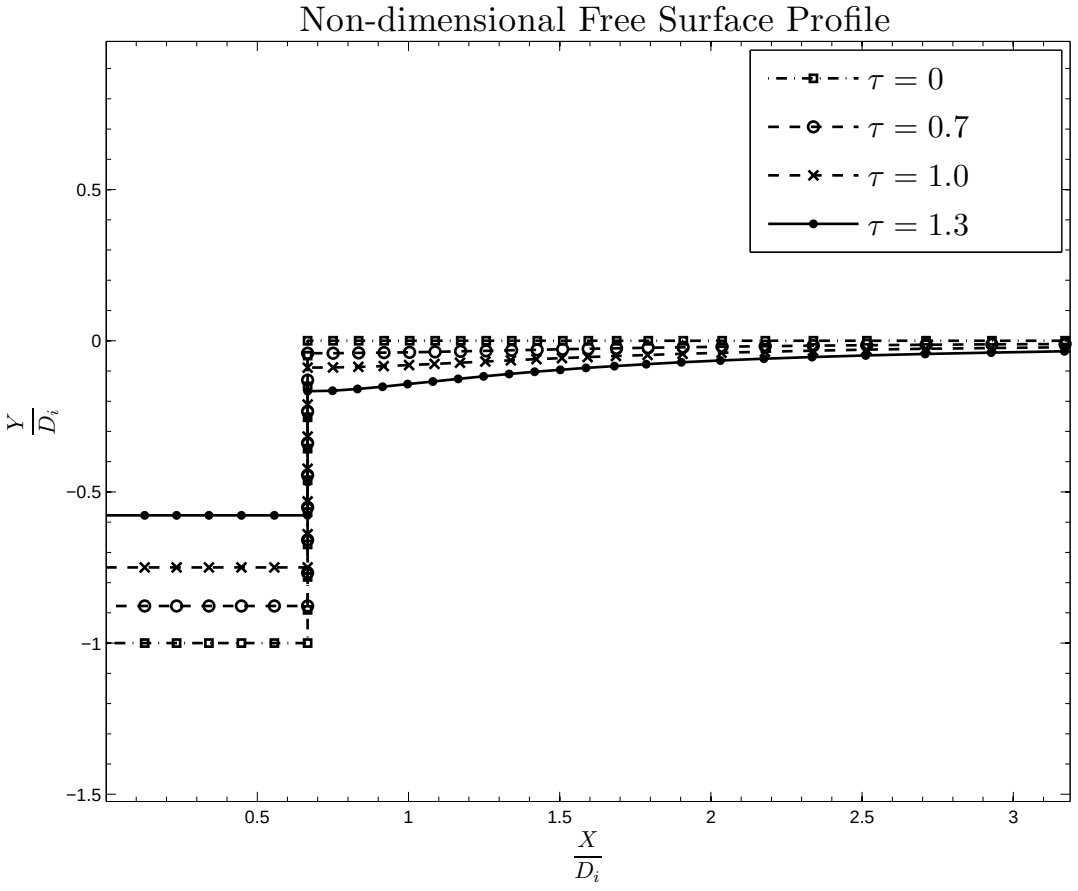

(a)

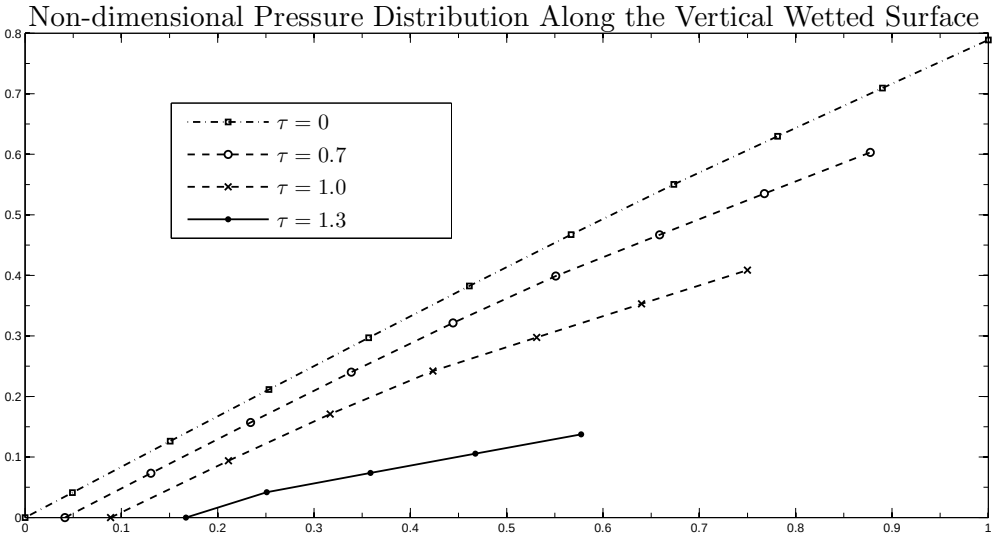

(b) along vertical surface

FIGURE 5.60: Time effect of the box BX2 submerged at a non-dimensional initial depth $\widehat{d_i} = -1$ exiting with constant acceleration $G_\tau = 0.5$: (a) and (b) are plotted at different non-dimensional times τ.

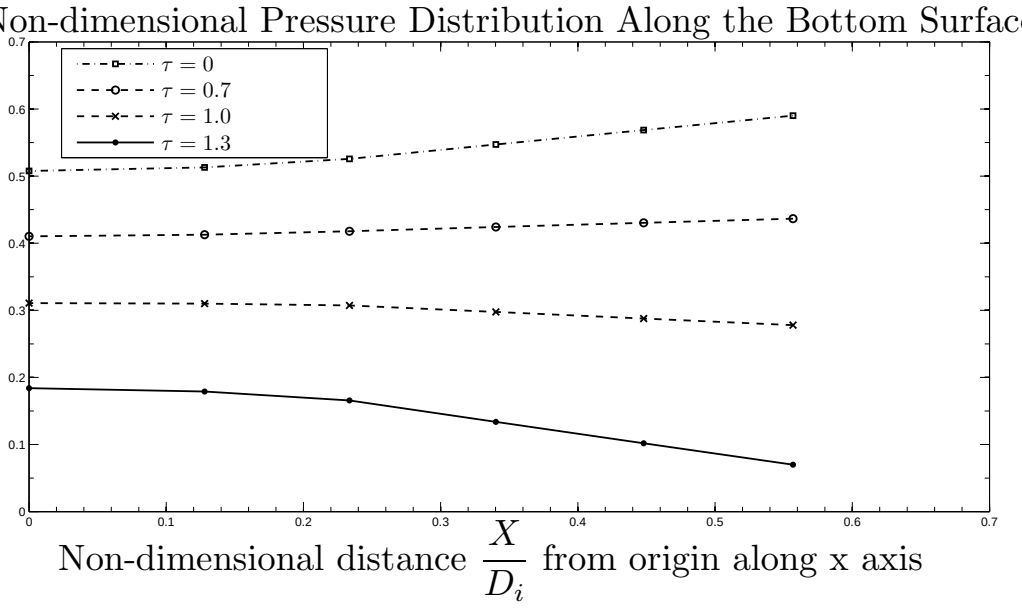

(a)

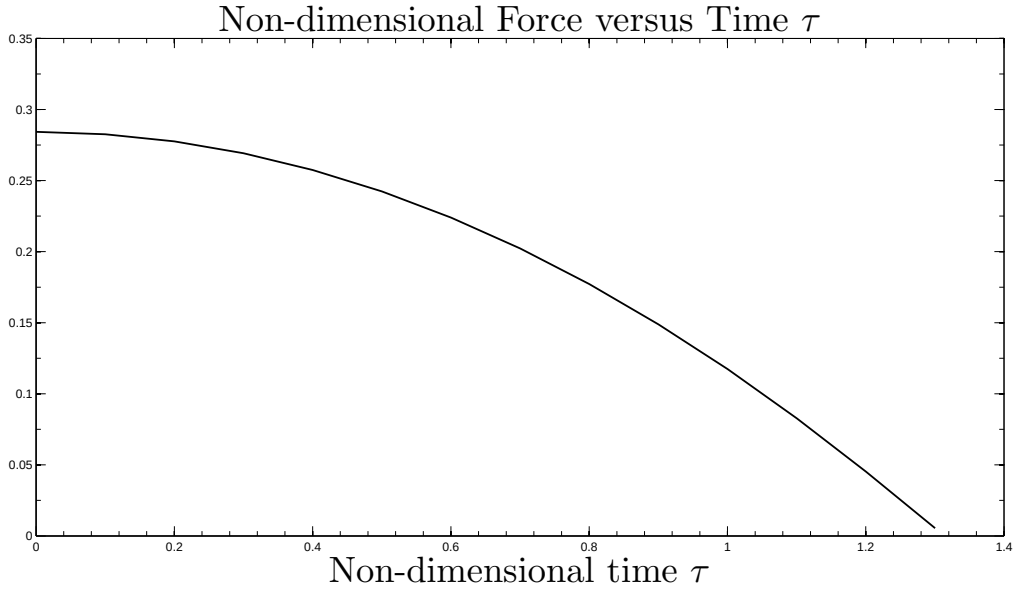

(b)

FIGURE 5.61: Time effect of the box BX2 submerged at a non-dimensional initial depth $\widehat{d}_i = -1$ exiting with constant acceleration $G_\tau = 0.5$: (a) is plotted at different non-dimensional times τ.

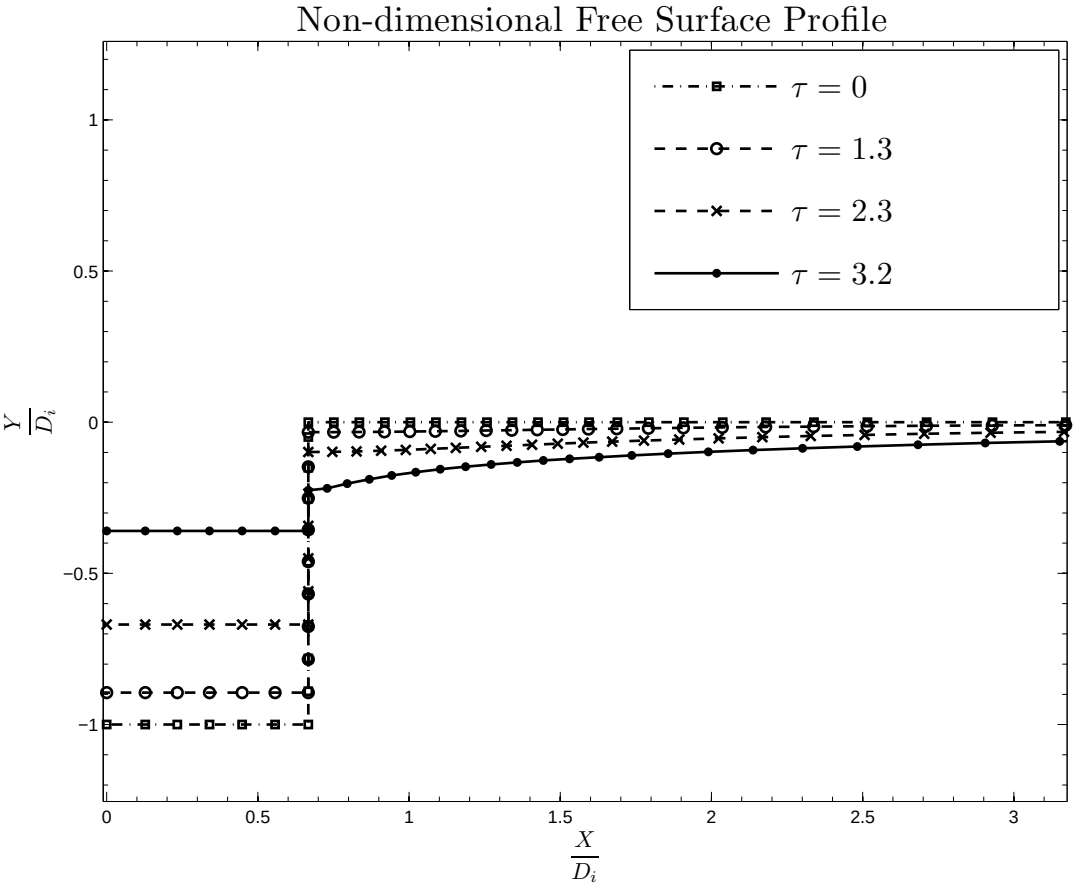

(a)

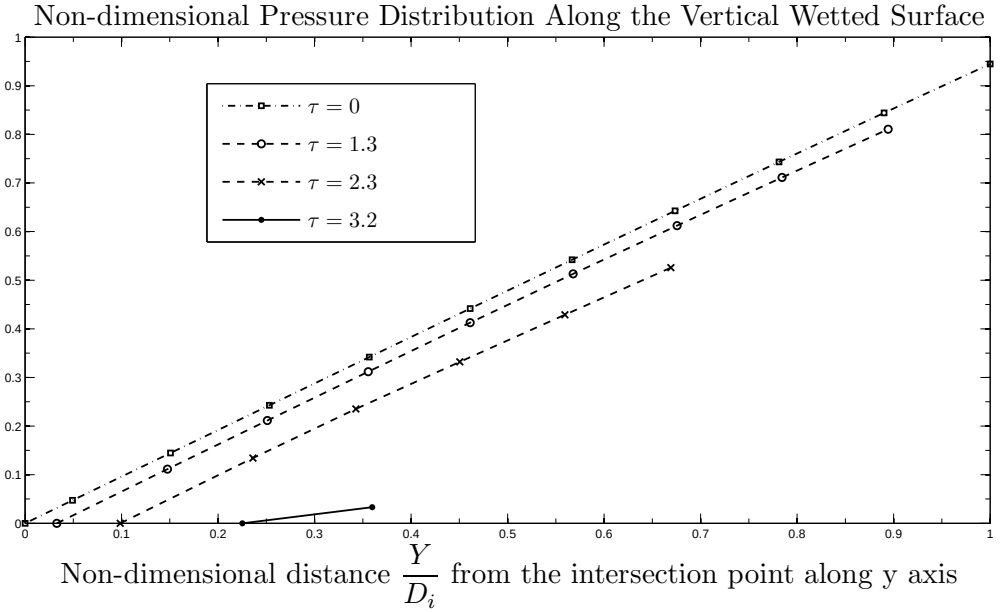

(b) along vertical surface

FIGURE 5.62: Time effect of the box BX2 submerged at a non-dimensional initial depth $\widehat{d_i} = -1$ exiting with constant acceleration $G_\tau = 0.125$: (a) and (b) are plotted at different non-dimensional times τ.

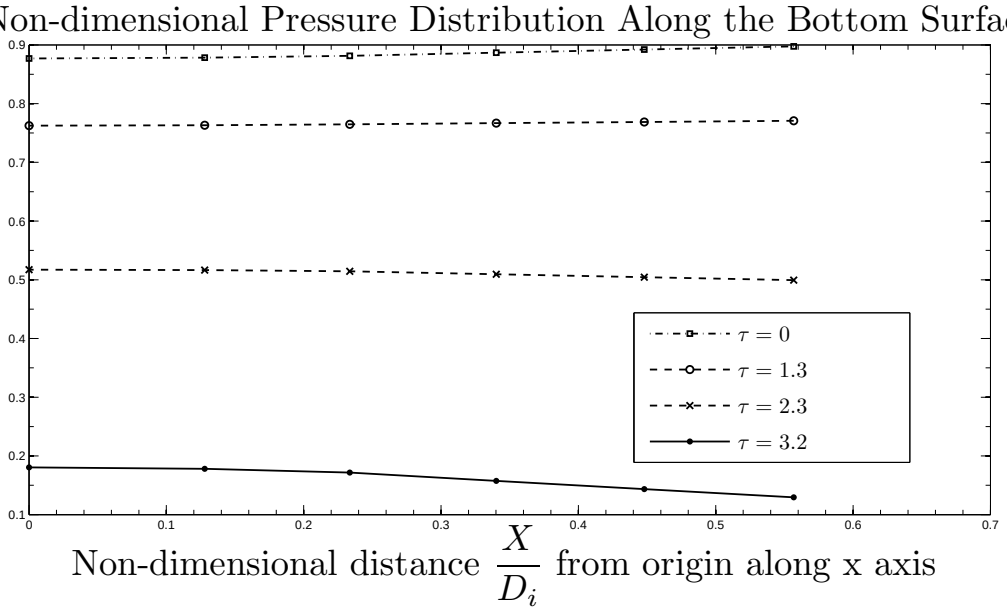

(a)

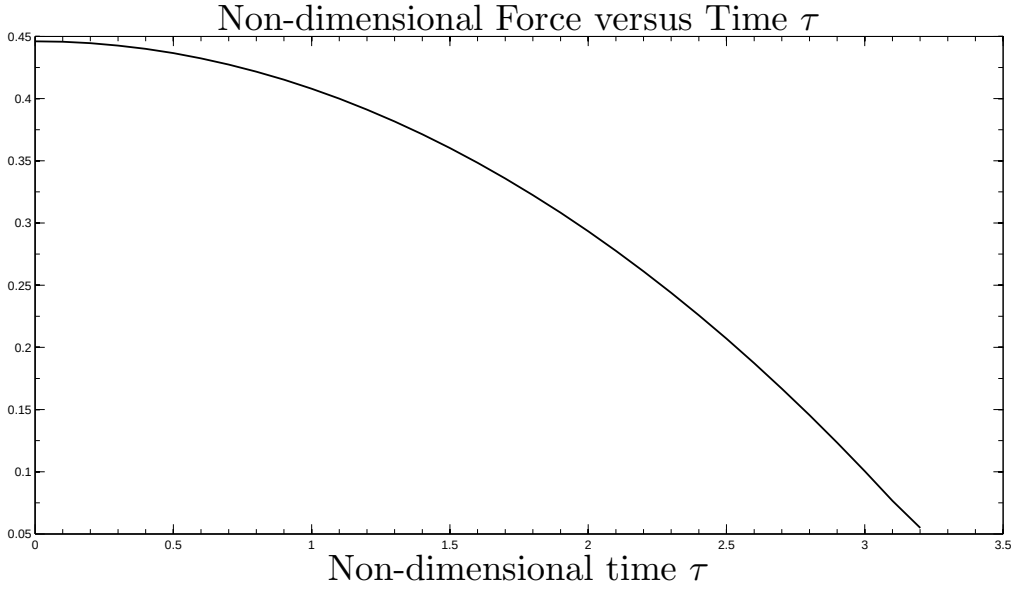

(b)

FIGURE 5.63: Time effect of the box BX2 submerged at a non-dimensional initial depth $\widehat{d_i} = -1$ exiting with constant acceleration $G_\tau = 0.125$: (a) is plotted at different non-dimensional times τ.

5.3.5.2 Acceleration effect

This section for constant acceleration exit of the box body presents computed numerical results for free-surface profile, pressure distribution and total force. The results are obtained by running the program with different constant accelerations while attaining the same distance traveled by the box body. Fig. (5.64) and (5.65) show the box body BX2 exiting with different accelerations.

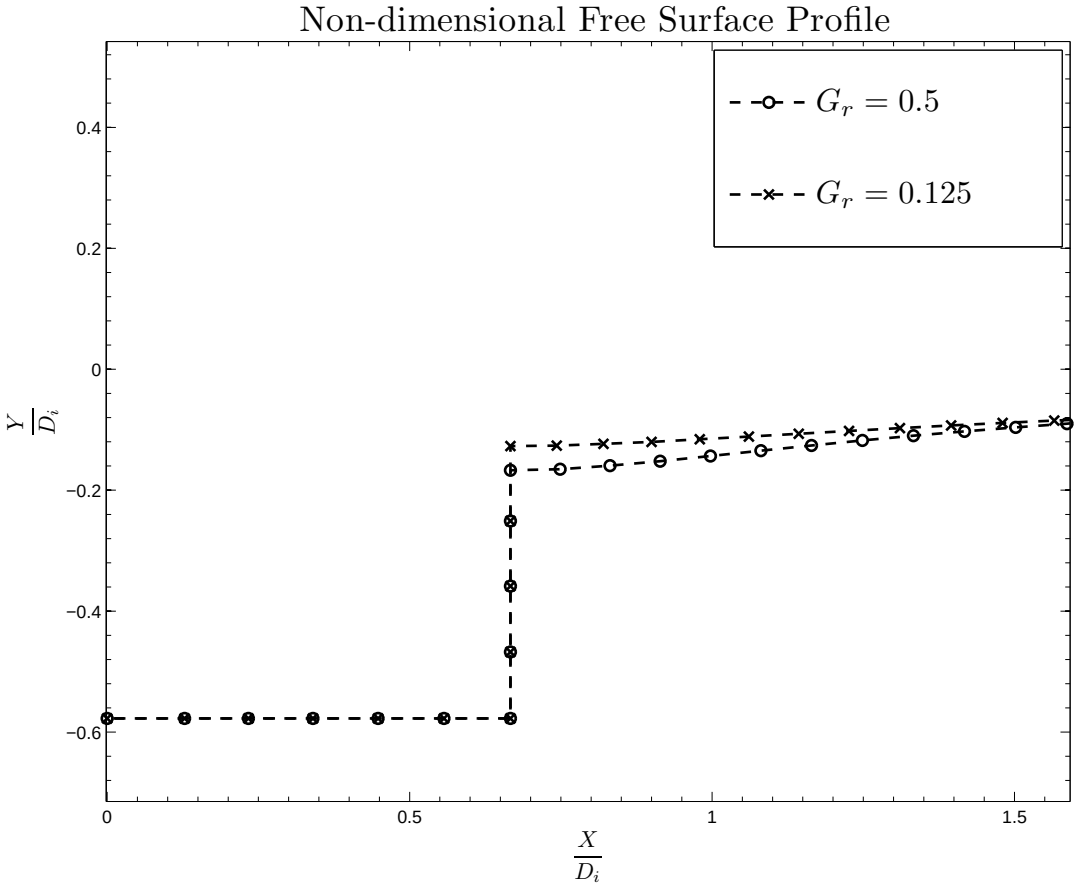

(a)

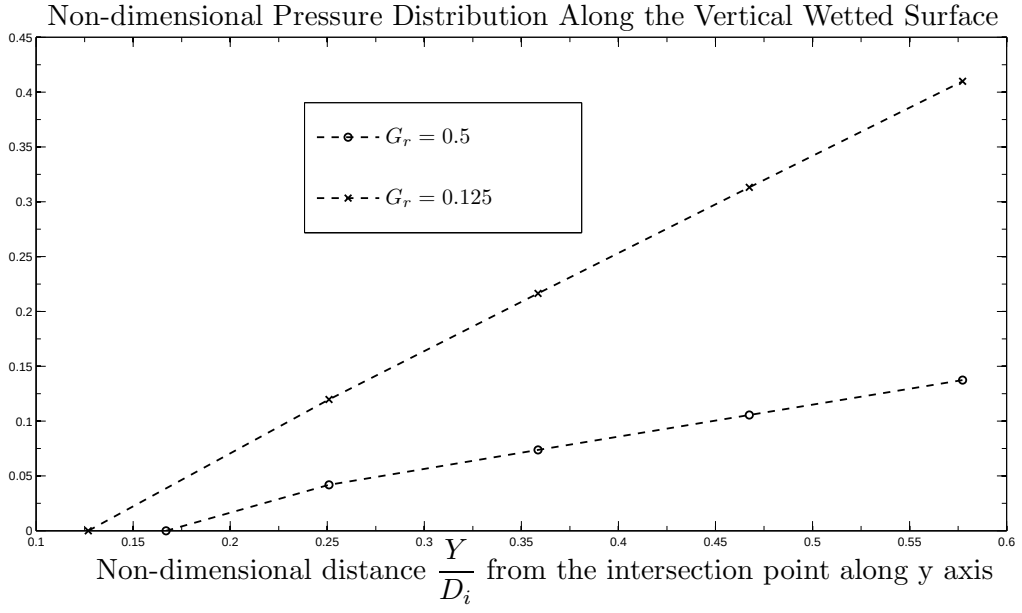

(b) along vertical surface

FIGURE 5.64: Acceleration effect of the box BX2 submerged at a non-dimensional initial depth $\widehat{d_i} = -1$ exiting with different constant accelerations G_τ: plotted at different non-dimensional $\tau = 1.3, 2.6$ and distance $\widehat{d} = -0.577$.

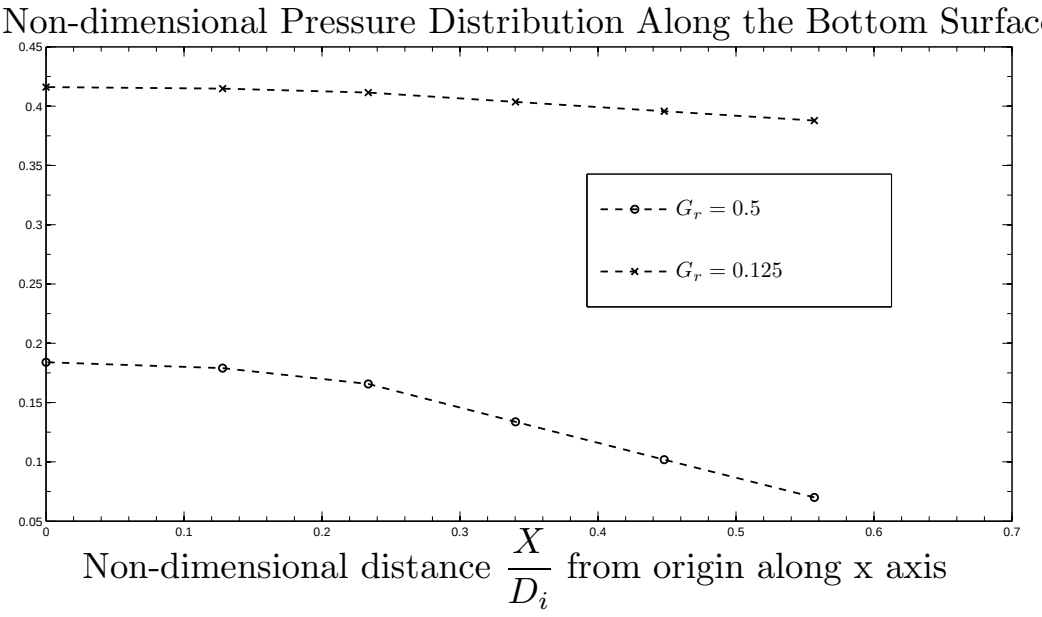

(a)

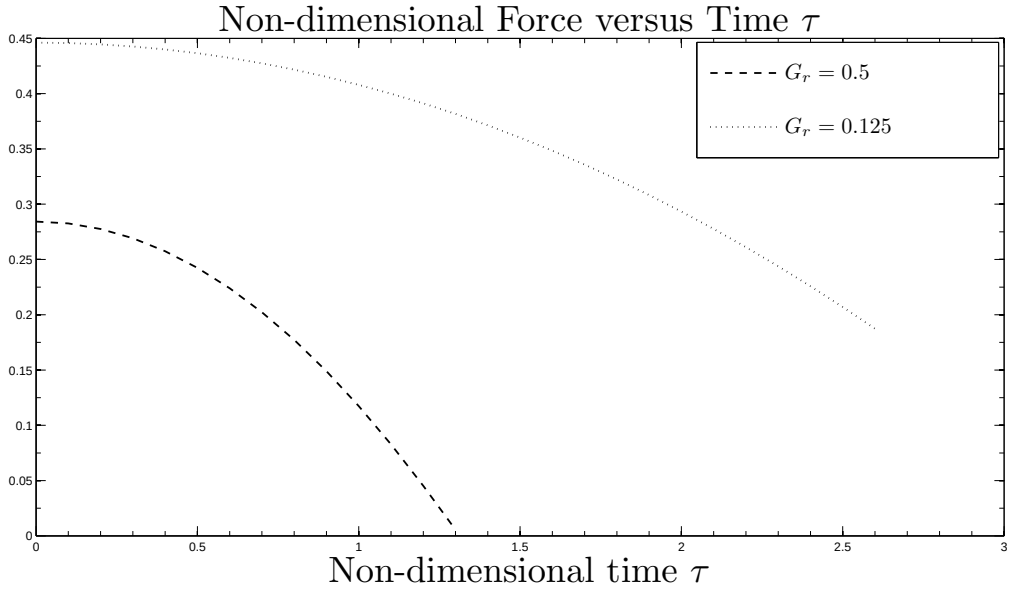

(b)

FIGURE 5.65: Acceleration effect of the box BX2 submerged at a non-dimensional initial depth $\widehat{d}_i = -1$ exiting with different constant accelerations G_τ: (a) is plotted at different non-dimensional times $\tau = 1.3, 2.6$ and distance $\widehat{d} = -0.577$.

5.3.5.3 Added mass effect

The analytical added mass force for box body exiting is compared with the force difference computed numerically using the non-linear time-stepping method. Fig. (5.66) shows the comparison of the computed force difference and the analytical added mass force computed for the box body BX2 with constant accelerations.

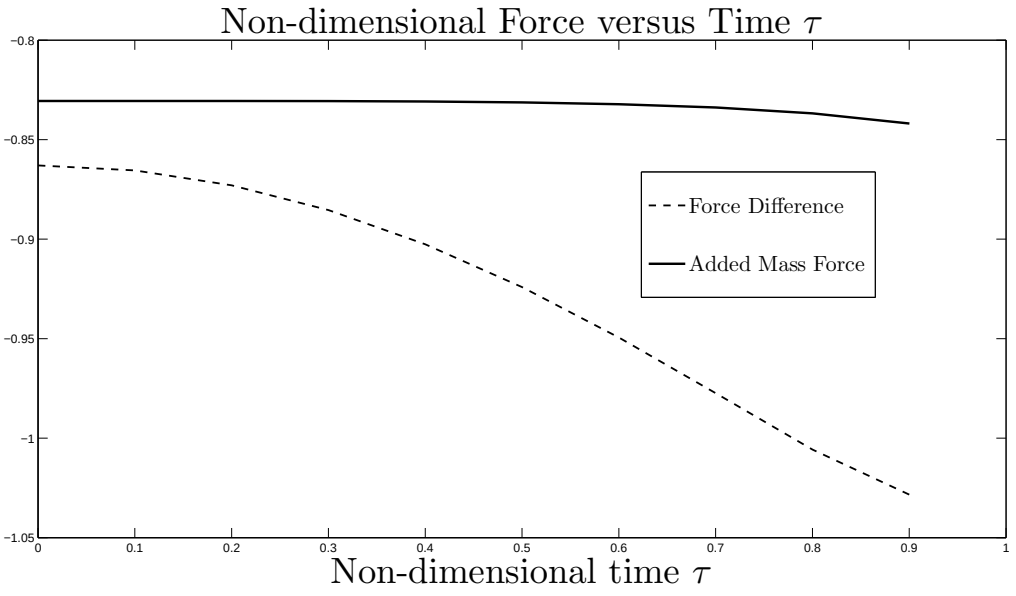

(a)

FIGURE 5.66: Computed numerical force difference and added mass force showing added mass effect for the box BX2 exiting with constant acceleration $G_\tau = 1$.

We also computed the added mass force for the box BX2 exiting water with constant velocity. Fig. (5.67) shows comparison of the computed force difference and the analytical added mass force computed for the box BX2 exiting water with a Froude number F_r of 0.5.

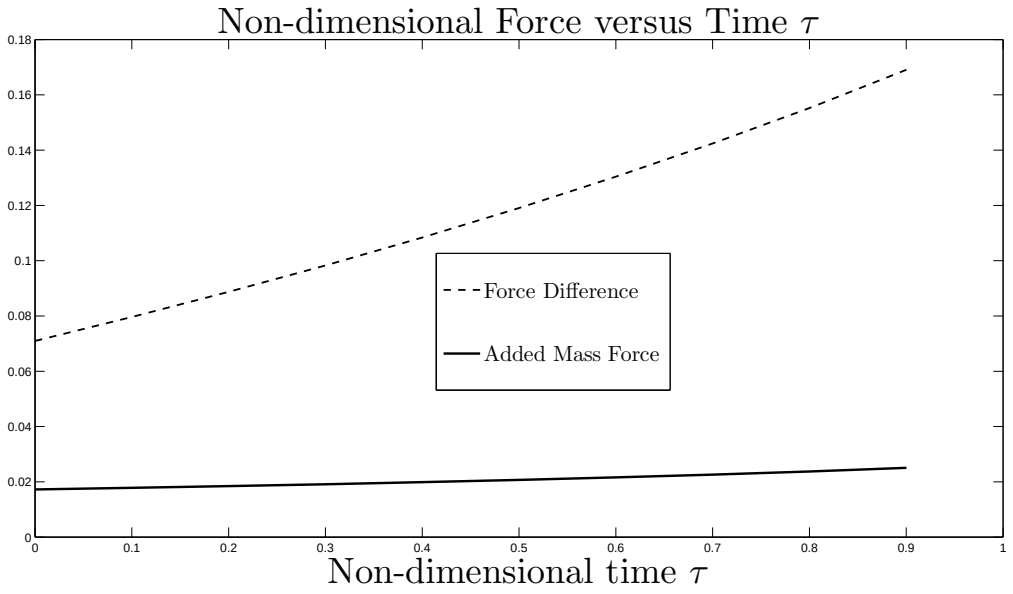

(a)

FIGURE 5.67: Computed numerical force difference and added mass force showing added mass effect for the box BX2 exiting with constant velocity of Froude number $F_r = 0.5$.

5.4 Comparison of exit for different wedge angles

In this section, we give a comparison of the computed results for the exit cases with constant velocity and constant acceleration varying with angles and shapes. For the constant velocity exit, we present a graph showing the limit of the Froude number which can be used to produce results for a particular shape without breaking the numerical computations.

5.4.1 Constant velocity

We numerically studied the exit problem of symmetric wedges, combined body, asymmetric wedges, truncated wedges and box by producing extensive results. However, we can only present some results here. Other results are also very useful for future studies in this field of water exit and are specified in Appendix B.

Symmetric wedges

For exit of symmetric wedges, we take the vertical-half angle varying from 5^o to 85^0. We selected the angle 30^o to present the numerical results, but results for other angles are documented on the CD. As we increase the angles of symmetric wedges for a particular Froude number, we can see a significant difference in the results for free-surface profile, pressure and force. We also notice that the change in Froude number for a particular wedge will give noticeable effects on the results. The maximum Froude number that can be used for exit of the symmetric wedges is plotted in Fig. (5.68).

By comparing the computed results given in the CD for the finite-depth effect, we can see much more the effects in the force as the contact surface becomes flatter which affects the motion of the particles below the body more strongly.

Table (5.5) shows the computed value of speed of the intersection point for exit of the symmetric wedges which was computed for the Froude number of 0.4. This is the maximum Froude number (common for all shapes) that can be used to compute results for the exit of the symmetric wedges.

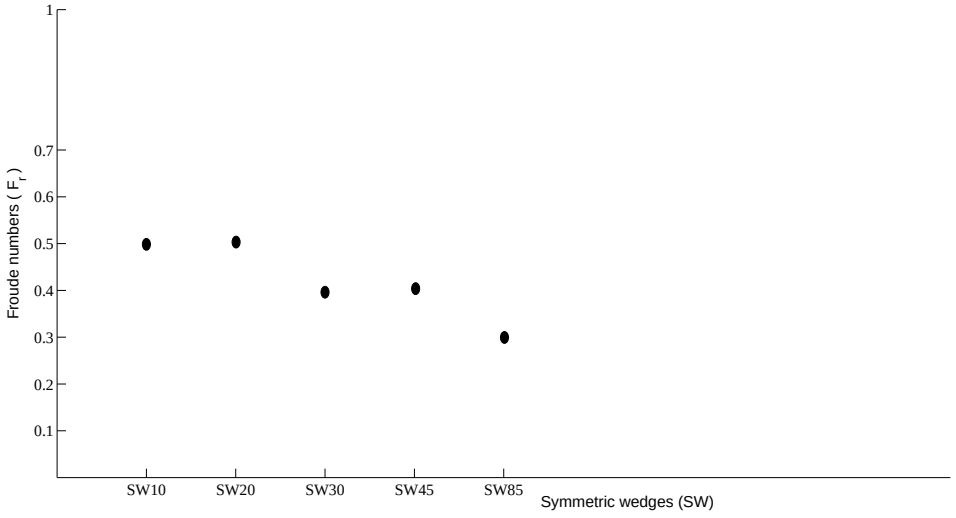

FIGURE 5.68: This figure shows the Froude numbers for symmetric wedges exiting with constant velocity.

Symmetric wedge (SW)	**Speed of intersection point** (α_h)
SW10	0.573
SW20	1.440
SW30	1.790
SW45	1.936

TABLE 5.5: Speed of the intersection points for symmetric wedges considered for water exit cases at t=0

As for entry, we note that at t=0 this non-dimensional speed is independent of Froude number. Here, however, no extension of Wagner's theory is possible, even in principle. Finally, by comparing the results for exit of Mackie's theory, we can see reasonable agreement between numerical and the analytical results for the free surface.

Combined body

For exit of combined body CB30, we presented numerical results. By comparing the results with the symmetric wedge SW30, we can see that the particles following the combined wedge and the intersection points continue to move along the vertical surface of the combined body until reaching last point close to the corner of the

box extension. There is also a significant change in the finite depth effect with the attached wedge compared with the symmetric wedge.

Asymmetric wedges

For exit of asymmetric wedges, we considered three different asymmetric wedges and presented results for asymmetric wedge (AW4) with left-half-wedge angle -10^o and right-half-wedge angle 30^o exiting water in section (5.2.3). By comparing the results on the CD for exit of other asymmetric wedges, we notice that the Froude numbers that can be used for asymmetric wedges are not same as for the symmetric wedges. It means that we need low Froude numbers to obtain good numerical results due to the rapid flow around the vertex for high Froude number exit of asymmetric wedges. We also notice strong effects in the results as we increase the wedge angles. The Froude numbers that can be used to run exit of the asymmetric wedges are given in Fig. (5.69).

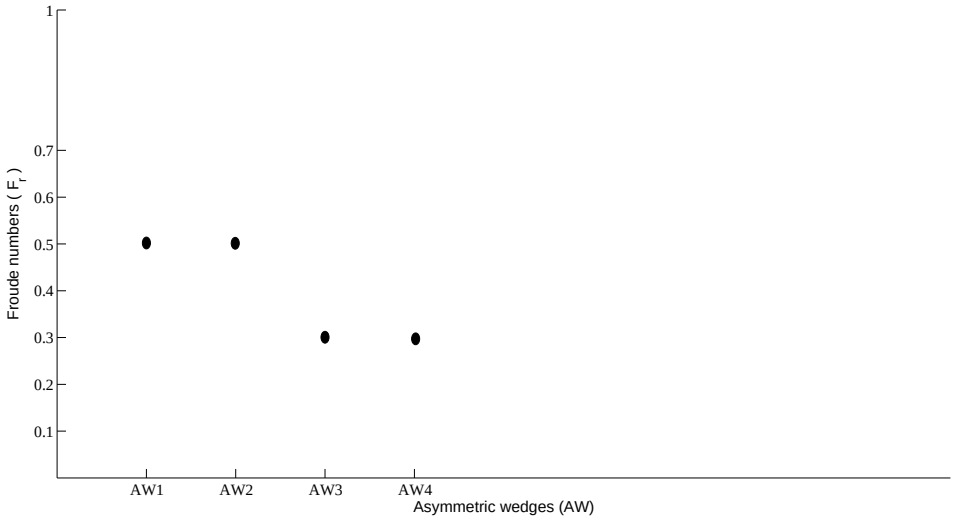

FIGURE 5.69: This figure shows the Froude numbers for the asymmetric wedges exiting with constant velocity.

Finally, we can see a significant effect in the finite depth cases of exit of asymmetric wedges compared with exit of the symmetric wedge cases, see the CD.

Truncated wedges

For exit of truncated wedges, we considered three different symmetric wedges of left and right half-wedge angles 10^o, 20^o and 30^o exiting with different Froude numbers. We can produce more results by considering different aspect ratios and asymmetric truncated wedges. However, we only considered some cases for this thesis. Similar effects as other wedges can be noticed for the test cases as the angle increases. By comparing with the results for the finite depth effect of exit of symmetric wedges and truncated wedges of same angles, it can be noticed that a small difference in the results of the truncated wedges can be seen due to the flatted bottom surface of the truncated wedges.

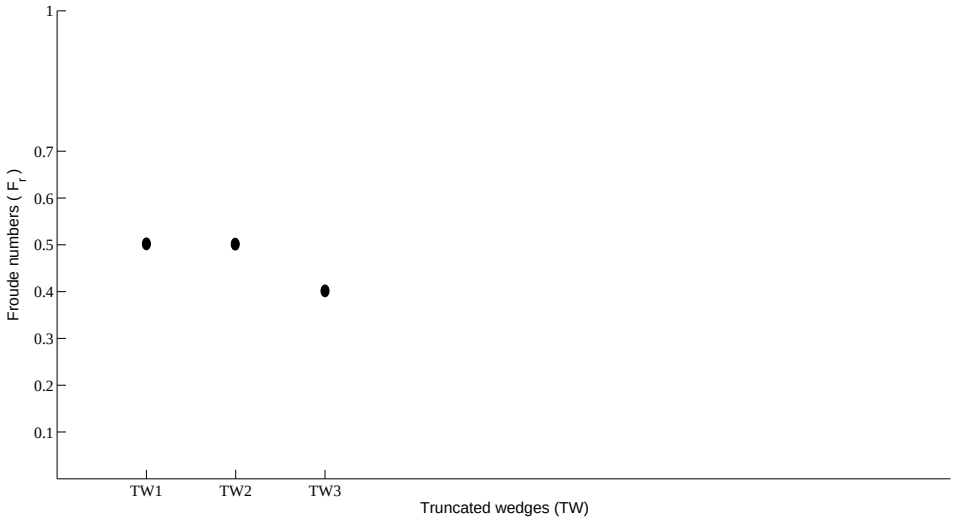

FIGURE 5.70: This figure shows the Froude numbers for the truncated wedges exiting with constant velocity.

Box

We considered three different boxes and presented results for the exit of box BX2 in section (5.2.5). We can produce more results by considering different aspect ratios of the box. However, we only considered some cases for simplicity of the study in this thesis. As we increase aspect ratio and Froude number of exit, we can notice much more effect on the results. There is a noticeable effect in the finite depth case that has a flat bottom surface.

5.4.2 Constant acceleration

We considered similar shapes as for constant velocity exit to compute and present numerical results for constant acceleration exit. The considered test cases for exit with constant accelerations are the time effect, acceleration effect and added mass effect for symmetric wedges and boxes. By increasing the angle of the wedges and accelerations, it is not possible to run the code because the intersection points move rapidly as body leaves the water and this causes numerical break down in the computations.

We presented results by choosing appropriate accelerations which vary with the angle of the wedges. By comparing the results for exit of each shape (see the CD), we can see strong effects on the free-surface profile, the pressure distribution and the force as the angles and the value of the constant acceleration of the exit increase for each shape.

As for entry of the symmetric wedges and box body, we computed analytical added mass force and compared with the numerical force difference for exit cases. The results for exit of the symmetric wedge SW30 were presented in section (5.3.1), whereas others are given in the CD. By comparing the results for exit of each shape, we notice that there is only moderate agreement of the analytical result with the numerical results initially for constant acceleration cases. However, the result for exit with constant velocity does not give better agreement because of the difficulties in applying the theory when the free surface also moves and in calculating the hydrodynamic pressure at corner points on the contour, see section (5.5.2).

Chapter 6

Conclusion

This chapter briefly reviews the work done in this thesis to study forced water entry and exit of symmetric, asymmetric, truncated wedges and boxes, and exit of combined body through a free surface. A summary and main conclusions are given in sections (6.1) and (6.2) respectively, while discussions of the results and recommendations for future work are detailed in section (6.3).

6.1 Thesis Summary

We started by introducing some very important applications (slamming causing effects in coastal and offshore structures) of structure-fluid interaction in the field of coastal and marine engineering, and explained water entry and exit phases involved in real problems. Earlier contributions to the study of water entry and exit and the recent research relevant to this study of water entry and exit were reviewed. In the literature review we looked at theoretical, numerical, and experimental aspects of water entry and exit problems, especially noting few contributions exist for the study of water exit related problems (see Greenhow (1990)).

In chapter 2, detailed explanation was given on the formulation of the two-dimensional initial boundary-value problem (IBVP) using description of mixed Eulerian and Lagrangian formulation of Vinje and Brevig (1981a; 1981b), which was further developed by Greenhow (see also, Barringer (1996) and Moyo (1996)). The model assumptions, boundary conditions and initial conditions were clearly explained.

The solution method for the IBVP using the boundary element method (BEM) giving integral equation was precisely specified.

In chapter 3, the numerical formulation to the IBVP which was used to implement the equations in Matlab was explained. The time-stepping algorithms (Runge-Kutta and Hamming predictor corrector methods) commonly used in the numerical methods of ordinary differential equations (ODE) were also given for the Matlab implementation.

In chapter 4, the method for derivation of non-dimensional parameters and computed dimensionless numerical results using the numerical formulation of the IBVP were presented for water entry of symmetric wedge of half-wedge angle 30^o (SW30), asymmetric wedge of half-left and right angles of -10^o and 30^o (AW4), truncated wedge of half-left and right angles of 30^o (TW3) and a box body (BX1) with constant velocity and constant accelerations. For constant velocity entry, some test cases examined the time effect, the Froude number effect, and speed of the intersection points varying with depths and Froude numbers was investigated numerically. Moreover, the numerical results computed for the symmetric wedges using the IBVP were compared with the analytical theory developed by Mackie (1965) and numerically formulated by Greenhow (1990).

For constant acceleration entry, derivation of added mass theory based on Barringer's thesis (1996) and some test cases such as time effect on the motion, acceleration effect and comparison of added mass force with numerical force difference for symmetric wedge (SW30) and box body (BX1) were presented.

In chapter 5, computed dimensionless numerical results using the numerical formulation of the IBVP were presented for water exit of symmetric wedge of half-wedge angle 30^o (SW30), combined body (CB30), asymmetric wedge of half-left and right angles of -10^o and 30^o (AW4) respectively, truncated wedge of half-left and right angles of 30^o (TW3) and a box body (BX1) with constant velocity and constant accelerations. For constant velocity exit, some test cases examined the time effect in entry, the Froude number effect, and speed of the intersection points varying with depths and Froude numbers was investigated numerically. Moreover, the numerical results computed for the symmetric wedges using the IBVP were compared with the analytical theory developed by Mackie (1965) and applied by Greenhow (1990).

For constant acceleration exit, some test cases examining the time effect on the motion, acceleration effect and comparison of added mass force with numerical force difference for symmetric wedge (SW30) and box body (BX2) were presented.

6.2 Main conclusions

We noticed that the results obtained for both entry and exit which were presented in the chapter 4 and 5 showed good agreement with the test cases explained in the chapter 4 such as convergence checks for entry and exit, self-similarity test for entry, time effect of initial and late stages of entry and exit and Froude number effect for entry and exit. However, results obtained by Mackie's theory for entry of symmetric wedges did not show very good agreement for different Froude numbers, but better agreement than that of the entry cases for exit of slender wedges. Calculations on the speed of intersection points for entry and exit were presented. It was observed that the increase or decrease in the initial velocity of the body did not affect the non-dimensional initial velocity of the intersection points as expected. It was also observed that there was a considerable effect on the free surface, pressure and total force computation for entry and exit due to the change in the depth of the fluid. It was also noticed that the analytical force computed using the added mass theory and the force difference computed using the nonlinear time-stepping method of Vinje and Brevig (1981a; 1981b) agreed quite well at the initial stage of entry and exit with constant accelerations (time τ=0).

6.3 Discussions and Recommendations

The problem of water entry and exit was formulated as mathematical equations by assuming that the fluid is incompressible, irrotational and the potential theory can be used to solve the problem. Moreover, for the simplification of the model, we can avoid surface tension, air cushioning effects at initial stage, ventilation effect for exit problems and the effect on the solution due to the vortex shedding near the corners. However, in reality, we can not usually avoid these effects. As we pointed out in Chapter 4 on water entry, the avoidance of the presence of vortex shedding from the vertex of asymmetric wedges, truncated wedges and boxes makes the

computation of water entry and exit easier. However, avoiding the vortex shedding may consequently lead to inaccuracy of the results due to flow separation of the vortex shedding. It should be taken into account to compute results for water entry and exit of asymmetric wedges and box bodies accurately. The method presented in this thesis based on the assumption of no vortex shedding along the vertex of the wedge was explained by Barringer (1996) for a knuckle-shaped body. One can further develop this model to include a mathematical formulation to study the effects causing by vortex shedding, especially for the case of asymmetric and box bodies.

For constant velocity entry and exit, we produced results for a limited range of Froude numbers, but it was noticed that this model can not be used to compute pressure and force for high Froude number cases due to the presence of the singularity in the computation of the pressure at the corner of the box and vertex of the wedge. It is not clear if this model can be modified to tackle high speed entry and exit cases too.

We also studied convergence of the results. The model can be used to compute accurate results for the non-dimensional time-step size lower than 0.1 and the point spacing should be chosen carefully to avoid numerical inaccuracies in the results.

We did not consider shapes which are curved or have low deadrise angles (below 15^o). For entry, we presented good results vertical half-wedge angle below 45^o. However, we tried to produce results for the angle of 55^o entering with low Froude number. The results did not show interesting effects because of the low Froude number and rapid movement of the fluid particles and the body points. It may be possible for one to resolve this problem by investigating the model further, and possibly removing the jet flow as in Zhao and Faltinsen (1993).

Another possibility for further development is to do more calculations on curve-shaped bodies (small dead-rise angle; parabolic or elliptic shapes) with a consideration of the effects on the pressure load of the presence of air cushioning in the initial stage of entry.

It is also possible to look into the computation of an upside-down-shaped wedge in entry and exit with constant velocity and constant acceleration by considering the strong effects due to the vortex shedding and flow separation from the trailing corners. As for low deadrise angle cases, there may be strong effects due to a

change in depth. For high-speed exit, we can possibly expect cavitation effects. We did not consider this effect too.

Finally, from the literature, we can see that there has been considerable number of contributions on the study of water entry related problems numerically and experimentally. However, for exit, much more research needs to be carried out in the future, numerically and experimentally. We have tried to present some results to study exit problems numerically. However, we need experimental results to validated the results computed numerically. Workers should produce experimental results for exit problem which could be useful for future research.

Appendix A

Matlab Graphical User Interface (GUI)

The water entry and exit problem was formulated as mathematical equations using physical properties. It was then solved by formulating the mathematical equations as numerical equations. The formulated problem was implemented in Matlab package to produce numerical and graphical results. To verify the computed result and produce more results by considering different test cases, the code was edited manually for each run of the test cases. It is very difficult to modify the input data each time. To avoid the complication of giving input manually by opening each file of the test cases, we designed a graphical user interface in Matlab which can be used to interact with the code directly through the windows by clicking each button.

In this chapter, we explain the graphical user interface designed in Matlab to study water entry and exit problem. The interface is called as Water Entry Exit Study Tool (WEEST) which has been developed in an efficient manner to analyse the results by changing the variables. In addition to that, WEEST can be installed as a package on any computer even if Matlab is not installed. It is very user friendly to use and speeds up user's work. Moreover, it might be used as a teaching tool to teach undergraduate students. Researchers in this field can use it for their studies. The following sections clearly explain the structure of WEEST.

A.1 WEEST windows

WEEST consists of several logically connected windows such as the WEEST main window, the WEEST shape window, WEEST graph window and the WEEST results window. It is easy to study exit and entry problems separately by selecting different shaped objects. By running WEEST, we can first see the main window which has two buttons named as Entry and Exit as shown in the Fig (A.1).

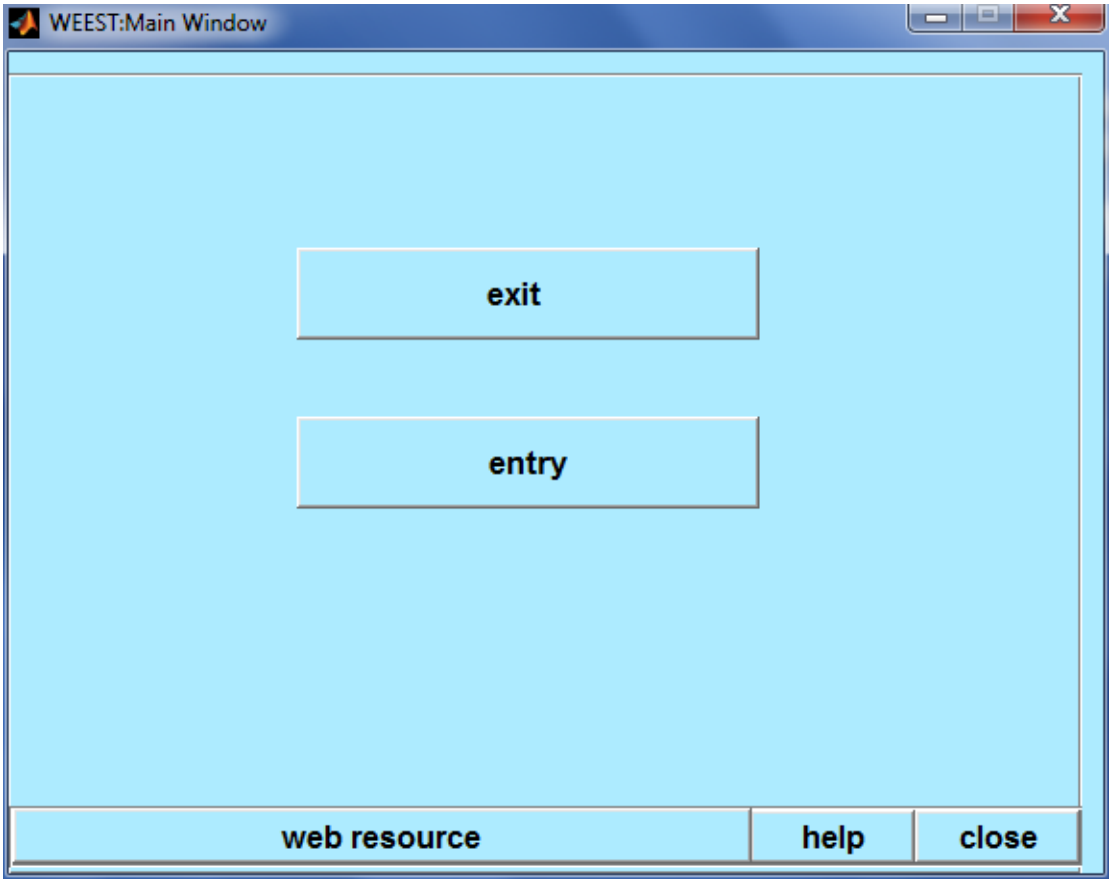

FIGURE A.1: Main window of WEEST

By clicking a button on the main window, we can go to another window as shown in Fig. (A.2) in which we can choose a shape of the object such as wedge, box and others interested in studying.

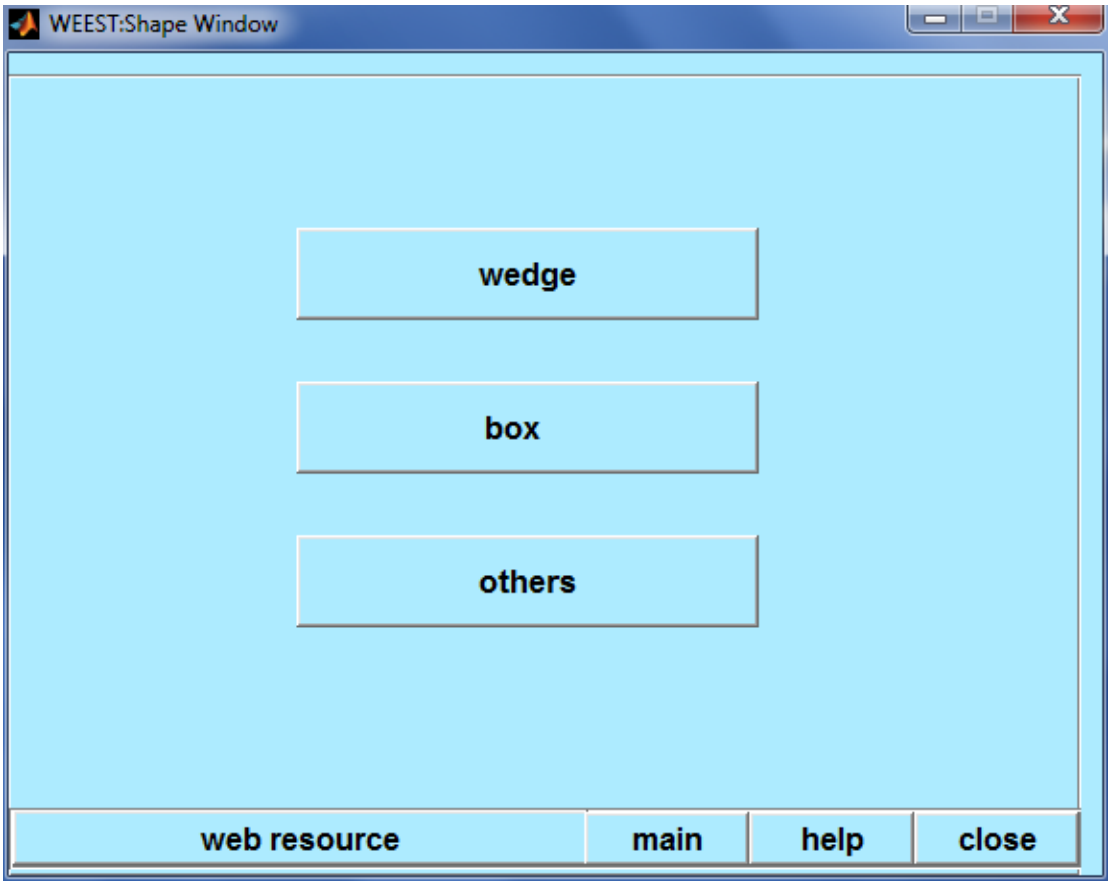

FIGURE A.2: Shape window of WEEST

By clicking on a shape, we can see another window will appear as shown in Fig. (A.3) where we can choose a button to compute the results for free-surface profile, pressure distribution or force acting on the body.

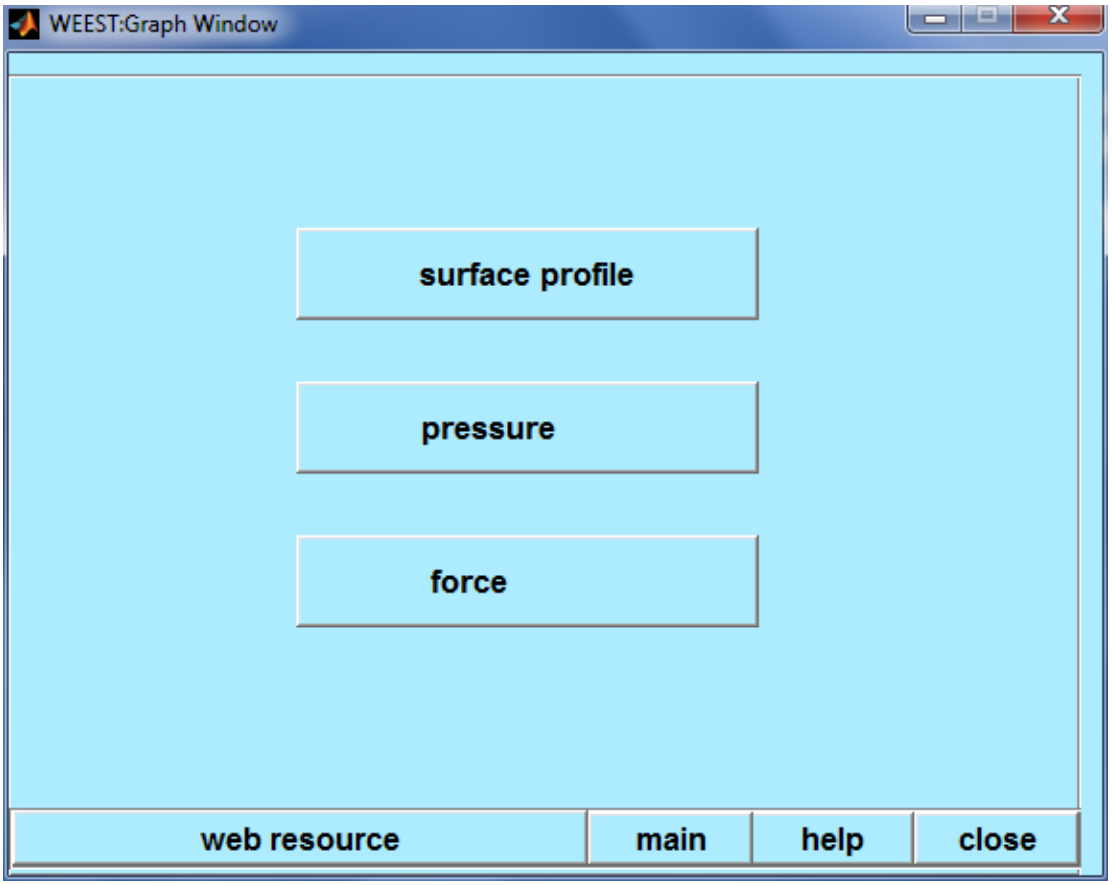

FIGURE A.3: Graph window of WEEST

Finally, another window (called WEEST input) will appear as in Fig (A.4) by clicking on a button on the window shown in Fig. (A.3). Here we can give the input values for which we want to compute results for the particular shape.

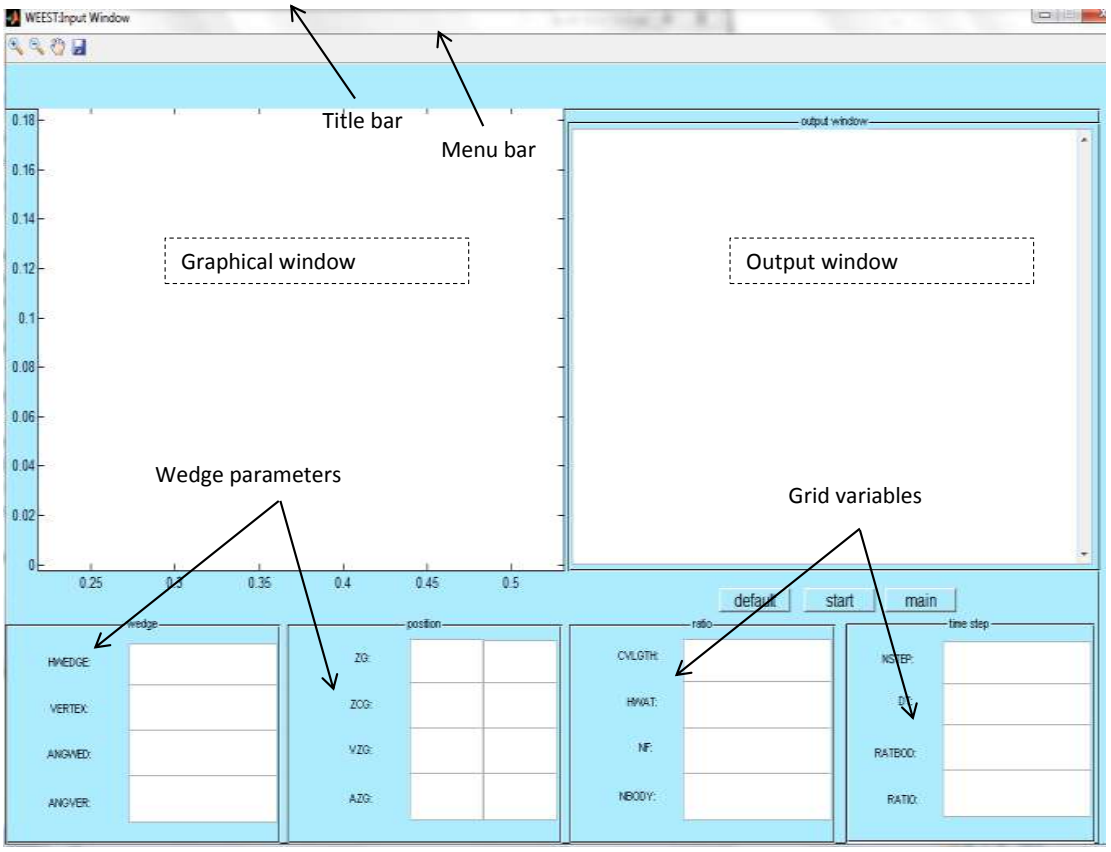

FIGURE A.4: Input window of WEEST

A.2 Example for entry of a symmetric wedge

This section presents computed results using the WEEST tool for a symmetric wedge of vertical half-wedge angle of 30^o entering water with constant velocity. Fig. (A.5) shows the free-surface profile changing with time, whereas Fig. (A.6) and (A.7) represent the pressure along the wetted part of the wedge and the force respectively.

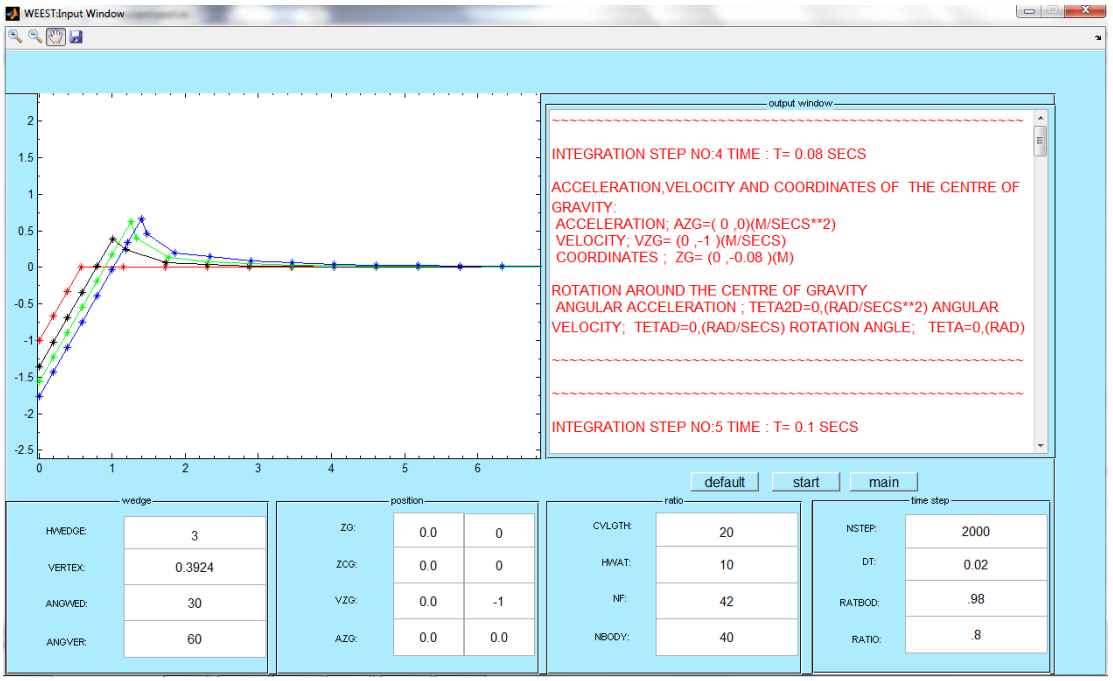

FIGURE A.5: Deformed free-surface profile of the symmetric wedge SW30 submerged at a non-dimensional initial depth $\widehat{d}_i = -1$ entering with constant velocity of Froude number $F_r = 0.5$ plotted at different non-dimensional times τ.

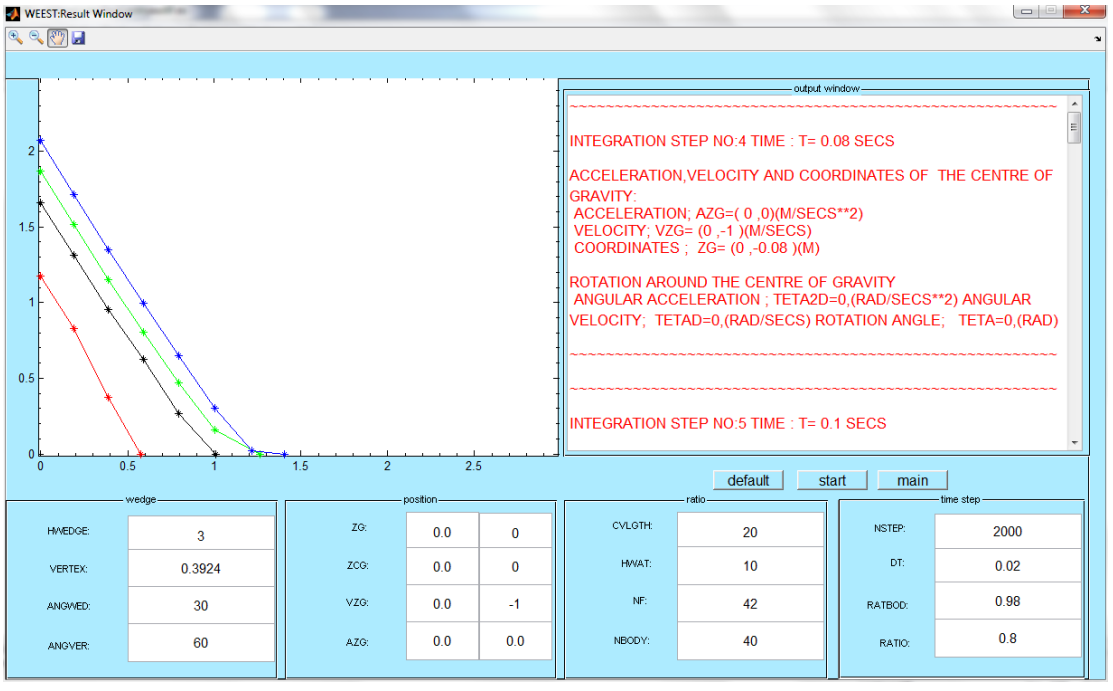

FIGURE A.6: Pressure distribution along the symmetric wedge SW30 submerged at a non-dimensional initial depth $\widehat{d}_i = -1$ entering with constant velocity of Froude number $F_r = 0.5$ plotted at different non-dimensional times τ.

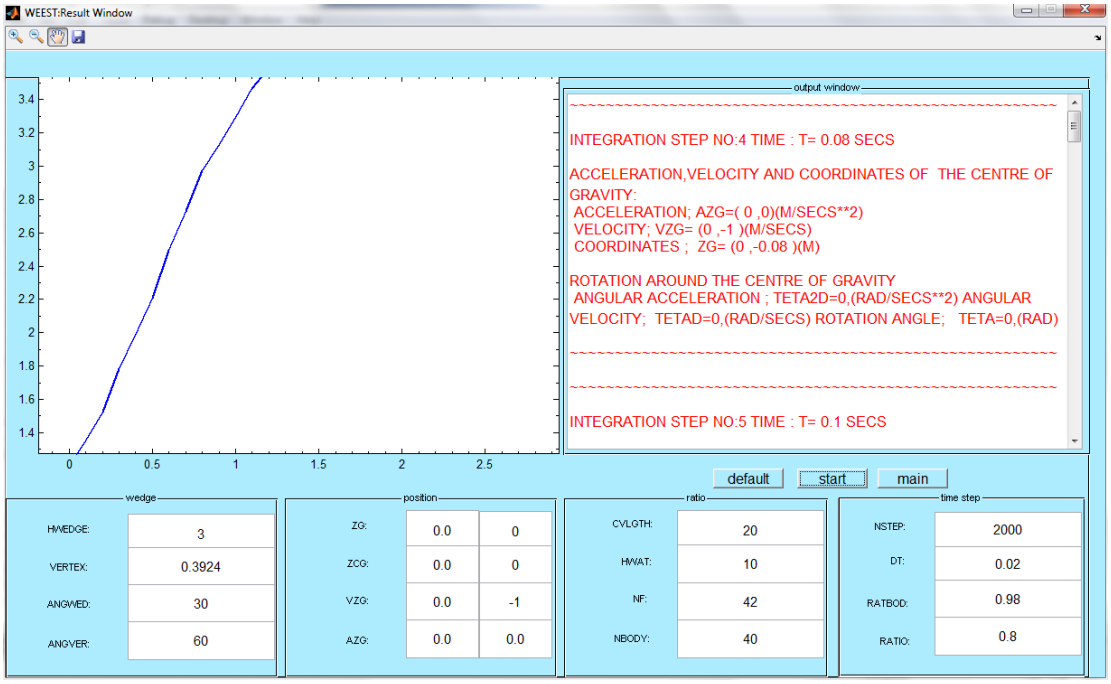

FIGURE A.7: Force experienced by the symmetric wedge SW30 submerged at a non-dimensional initial depth $\widehat{d}_i = -1$ entering with constant velocity of Froude number $F_r = 0.5$ plotted at different non-dimensional times τ.

Appendix B

Documentation of Numerical Results using Matlab

This appendix gives details about the contents of the CD which consists of all the results produced for all the test cases of each shape entering and exiting water with constant velocity and constant acceleration.

On opening the CD, we can see two main folders in the RESULTS folder, ENTRY where the results for entry cases stored, and EXIT where the results for exit cases stored. Each main folder has some subfolders such as asymmetricWedges, symmetricWedges, boxes, truncatedWedges and combinedBody (clicking on the main folder for Exit). By opening each folder, we can observe considered cases for each shape. By opening the cases, we can see the folders for constant velocity and constant acceleration entry or exit.

By double clicking on the constant velocity or constant acceleration, we can view other folders which consist of the results for the test cases such as for constant velocity (convergence check, time effect, Froude number effect, finite depth effect, speed of intersection points varying with Froude numbers and depths and comparison of Mackie's theory for symmetric wedges) or for constant acceleration (time effect, acceleration effect and added mass effect for symmetric wedges and boxes).

Take, for example, the result showing the Froude number effect of a symmetric wedge (SW20) entering water with constant velocity. By opening the CD and then double clicking on the Entry folder in the RESULTS folder to select the folder of FroudeNumberEffect of the symmetric wedge (SW20) entering with constant velocity, we can see the following window as shown in Fig. (B.1). By selecting

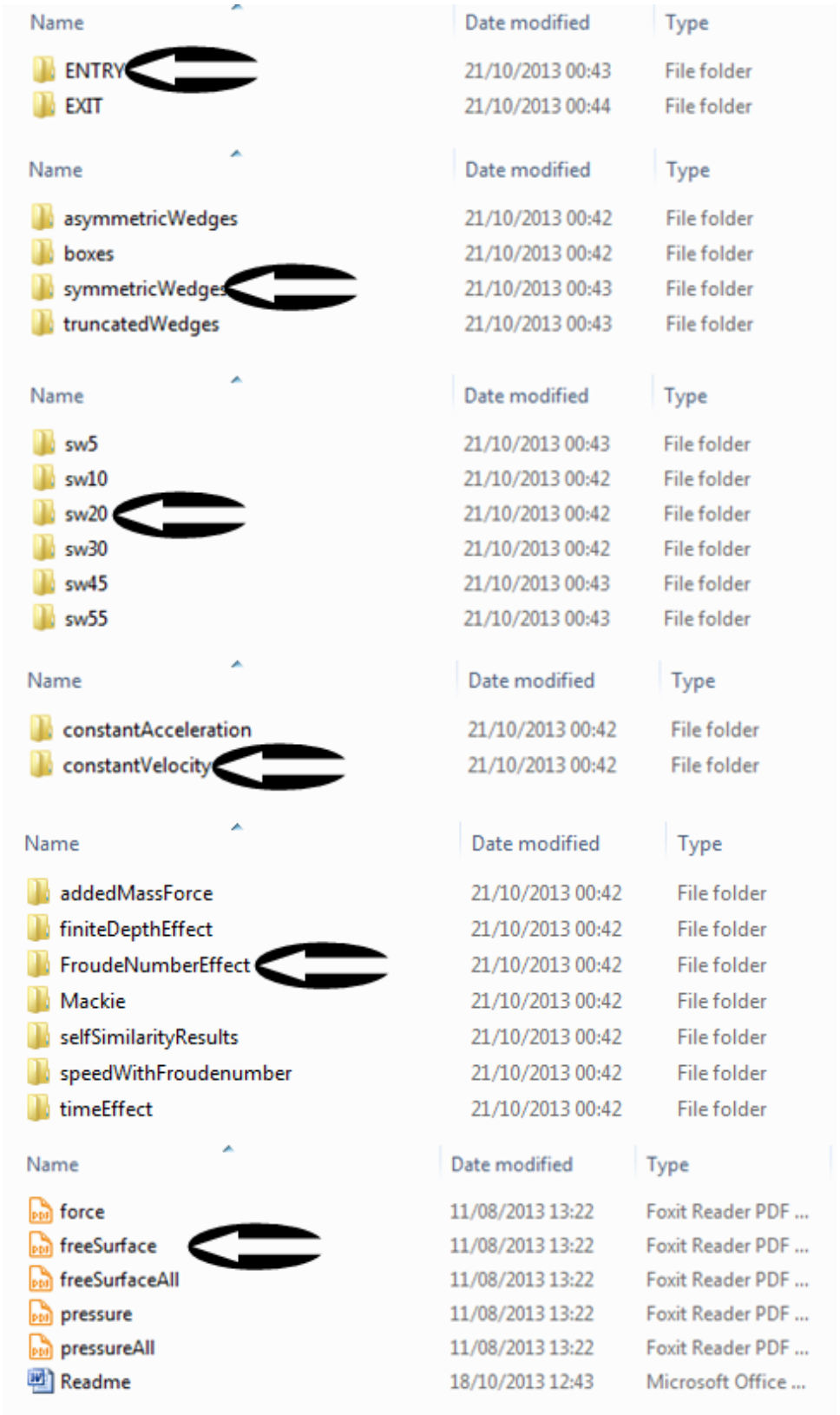

FIGURE B.1: Folders for the entry case

the folder for FroudeNumberEffect, we can view the results for free-surface profile, pressure distribution along the body and numerical force experienced by the body.

References

[1] Abramowitz, M., and Stegun, I. A., (1965). *Handbook of mathematical functions, with formulas, graphs and mathematical tables.* Dover Publication, Inc., ISBN: 0-486-61272-4.

[2] Bagnold, R., (1939). *Interim Report on Wave Pressure Research.* J. Inst. Civil Eng., Vol. 12, pp. 202-226.

[3] Barringer, I., (1996). *Water exit of two-dimensional bodies.* PhD Thesis, Brunel University, UK.

[4] Battistin, D., and Iafrati, A., (2004). *A numerical model for the jet flow generated by water impact.* Journal of Engineering Mathematics, Vol. 48(3), pp. 353-374.

[5] Cooker, M. J., (1990). *The interaction between steep water waves and coastal structures.* Ph.D Thesis, University of Bristol.

[6] Dean, R. G., and Dalrymple, R. A., (1984). *Water Wave Mechanics for Engieers and Scientist.* Prentice Hall Inc., ISBN: 981-02-0420-5.

[7] Dobrovol'skaya, Z. N., (1969). *On Some Problems of Similarity Flow of Fluid with a Free Surface.* J. Fluid Mech., Vol. 36, pp. 805-829.

[8] Dobrovol'skaya, Z. N., (1966). *Numerical solution of integral equation for a two dimensional self-similar problem on motion of fluid with a free surface.* Zh. Vychisl. Mat. Mat. Fiz. Vol. 6, pp. 934-41.

[9] Faltinsen, O. M., Landrini, M., and Greco, M., (2004). *Slamming in Marine Applications.* J. Eng. Math., Vol. 48, pp. 187-217.

[10] Garabedian, P. R., (1953). *Oblique water entry of a wedge.* Comm. Pure Appl. Math., Vol. 6, pp. 157-165.

[11] Greco, M., Colicchioa, G., and Faltinsen, O. M., (2009). *Bottom slamming for a Very Large Floating Structure: Coupled global and slamming analyses.* Journal of Fluids and Structures, Vol. 25, pp. 420-430.

[12] Greenhow, M., and Moyo, S., (1997). *Water Entry and Exit of Horizontal Circular Cylinder.* Phil. Trans. R. Soc. London. Ser. A., Vol. 355, pp. 551-563.

[13] Greenhow, M., (1993). *A complex variable method for the floating-body boundary-value problem.* J. Comput. Appl. Maths, Vol. 46, pp. 115-128.

[14] Greenhow, M., (1990). *Water Exit of Slender and Non-slender Bodies.* International Workshop on Water Waves and Floating Bodies (IWWWFB).

[15] Greenhow, M., and Lin, W. M., (1983). *Nonlinear free-surface: experiments and theory.* MIT, Dept of Ocean Engineering, Rep. 83-19.

[16] Greenhow, M., (1987). *Wedge entry into initially calm water.* Appl. Ocean Res., Vol. 9, pp. 214–223.

[17] Greenhow, M., and Li, Y., (1987). *Added masses for circular cylinders near or penetrating fluid boundaries-review, extension and application to water-entry, -exit and slamming.* Ocean Engng., Vol. 14, pp. 325-348.

[18] Greenhow, M., (1987). *Water Entry and Exit of a Horizontal Circular Cylinder.* Appl. Ocean Res., Vol. 10(4), pp. 191-198.

[19] Howison, S. D., Ockendon, J. R., and Oliver, J. M., (2004). *Oblique slamming, planing and skimming.* J. Eng. Math., Vol. 48, pp. 321–337.

[20] Howison, S.D., Ockendon, J.R., Wilson, S.K., (1991). *Incompressible water-entry problems at small deadrise angles.* Journal of Fluid Mechanics, Vol. 222, pp. 215-230.

[21] Hughes, O. F., (1973). *Some characteristics of the free surface in the wedge entry problem.* Journal of Engineering Mathematics, Vol. 7(4), pp. 367-375.

[22] Hughes, O. F. (1972). *Solution of the wedge entry problem by numerical conformal mapping.* Journal of Fluid Mechanics, Vol. 56(1), pp. 173-192.

[23] Iafrati, A., and Korobkin, A. A., (2001). *Starting flow generated by a floating wedge impact.* Proc. 16th Intern. Workshop on Water Waves and Floating Bodies, Hiroshima, Japan.

[24] Iafrati, A., and Korobkin, A. A., (2000). *Liquid flow close to intersection point.* Proc. 15th Workshop on Water Waves and Floating Bodies.

[25] John, F., (1953). *Two-dimensional potential flows with a free boundary.* Com. Pure Appl. Math., Vol. 6, pp. 497-503.

[26] Kihara, H., (2004). *Numerical modeling of flow in water entry of a wedge.* In Proc. 19th International Workshop on Water Waves and Floating Bodies, Cortona, Italy, pp. 28-31.

[27] Korobkin, A. A., (2005). *Three-dimensional nonlinear theory of water impact.* 18th International Congress of Mechanical Engineering, 6-11 Ouro Preto, MG.

[28] Korobkin, A. A., Malenica, S., (2005). *Modified Logvinovich model for hydrodynamic loads on asymmetric contours entering water.* 20th International Workshop on Water Waves and Floating Bodies, Longyearbyen, Norway.

[29] Korobkin, A. A., (2004). *Analytical models of water impact.* European Journal of Applied Mathematics, Vol. 15, pp. 821-838.

[30] Korobkin, A. A., (1992). *Blunt-Body Impact on a Compressible Liquid Surface.* J. Fluid Mech., Vol. 244, pp. 431-453.

[31] Korobkin, A. A., and Pukhnachov, V. V., (1988). *Initial Stage of Water Impact.* Ann. Rev. Fluid Mech. Vol. 20, pp. 159–85.

[32] Korobkin, A. A., (1999). *Shallow-water impact problems.* J. Eng. Math. Vol. 35, pp. 233250.

[33] Kvaalsvold, J., Faltinsen, O. M., (1995). *Hydroelastic Modeling of Wet Deck Slamming on Multihull Vessels.* J. Ship Res., Vol. 39(3), 225-239.

[34] Kvaalsvold, J., (1994). *Hydroelastic Modeling of Wetdeck Slamming.* Ph.D. Thesis, Trondheim: Dept. Marine Hydrodynamics, NTNU.

[35] Lewison, G., and Maclean, W. M., (1968). *On the Cushioning of Water Impact by Entrapped Air.* Journal of Ship Research, Vol. 12, No. 2.

[36] Lundgern, H., (1969). *Wave Shock Forces: An Analysis of Deformations and Forces in the Wave and in the Foundation.* Proc. Symp. on Wave Action, Delft Hydraulics Laboratory, Delft, The Netherlands.

[37] Mackie, A. G. (1969). *The Water Entry Problem.* Q. J. Mechanics Appl Math., Vol. 22(1), pp. 1-17.

[38] Mackie, A. G., (1965). *Gravity effects in the water entry problem.* J. Aust. Math. Soc., Vol.5, pp. 427-433.

[39] Mackie, A. G. (1962). *A linearized theory of the water entry problem.* Q. J. Mechanics Appl Math., Vol. 15(2), pp. 137-151.

[40] Milne-Thompson, L. M., (1968). *Theoretical Hydrodyamics, 5th ed.* Macmillan Education LTD, ISBN: 0-333-07876-4.

[41] Moyo, S., (1996). *Hydrodynamic interaction of horizontal circular cylinders with a free surface.* PhD thesis, Department of Mathematics and Statistics, Brunel University, UK.

[42] Needham, D. J., Billingham, J., and King, A. C., (2007). *The initial development of a jet caused by fluid, body and free-surface interaction. Part 2. An impulsively moved plate.* J. Fluid Mech., Vol. 578, pp. 67–84

[43] Newman, J. N., (1977). *Marine Hydrodynamics.* The MIT Press, ISBN: 0-262-14026-8.

[44] Ochi, M. K., (1964) *Prediction of Occurrence and Severity of Ship Slamming at Sea.* Fifth Symposium of Naval Hydrodynamics, Office of Naval Research.

[45] Oliver, J. M., (2002). *Water entry and related problems.* Doctoral dissertation, University of Oxford, UK.

[46] Polyanin, A. D., and Manzhirov, A. V., (1998). *Handbook of integral equations.* CRC Press LLC., ISBN: 0-8493-2876-4.

[47] Ralston. A., and Rabinowitz. P., (2001). *A first course in numerical analysis, 2nd ed.* Dover Publications, New York, ISBN: 0-48641-454-X.

[48] Sun, H., and Faltinsen, O. M., (2007). *The influence of gravity on the performance of planing vessels in calm water.* Journal of Engineering Mathematics, Vol. 58(1), pp. 91-107.

[49] Tassin, A., Piro, D. J., Korobkin, A. A., and Maki, K. J., Cooker, M.J., (2013). *Two-dimensional water entry and exit of a body whose shape varies in time. Journal of Fluids and Structures.* Vol. 40, pp. 317-336.

[50] Tassin, A., Jacques, N., El Malki Alaoui, A., Neme, A., and Lebl, B., (2012). *Hydrodynamic loads during water impact of three-dimensional solids: modelling and experiments.* Journal of Fluids and Structures, Vol. 28, pp. 211-231.

[51] Tassin, A., Jacques, N., El Malki Alaoui, A., Neme, A., and Leble, B., (2010). *Assessment and comparison of several analytical models of water impact.* International Journal of Multiphysics, Vol. 4, pp. 125-140.

[52] Tick, L. J., (1955). *Certain Probabilities Associated with Bow Submergence and Ship Slamming in Irregular Seas.* Journal of Ship Research, SNAME, Vol. 2, No. 1.

[53] Tsai, W. T., and Yue, D. K., (1993). *Interactions between a free surface and a vortex sheet shed in the wake of a surface-piercing plate.* Journal of Fluid Mechanics, Vol. 257, pp. 691-721.

[54] Verhagen, J. H., (1967). *The Impact of a Flat Plate on a Water Surface.* J. Ship Res., 11 , No. 4, 211-223.

[55] Vinje, T., and Brevig, P., (1981a). *Breaking waves on finite water depths, a numerical study.* Ship Research Institute of Norway.

[56] Vinje, T., and Brevig, P., (1981b). *Non-linear two-dimensional ship motions.* Ship Research Institute of Norway.

[57] von Karman, T., (1929). *The impact on seaplane floats during landing.* NACA Technical Note 321.

[58] Wagner, H., (1932). *Uber Stoss und Gleitvorgänge an der Oberfläche von Flüssigkeiten.* ZAMM. 12, 193-215. (See also *the phenomena of impact and planing on water.* National Advisory Committee for Aeronautics, Translation 1366, Washington, D. C.)

[59] Xu, L., Troesch, A. W., Petterson, R., (1998). *Asymmetric Hydrodynamic Impact and Dynamic Response of Vessels.* Proceedings of 17th Int. Conf. Offsh. Mech. Arctic Eng., 98-320.

[60] Yettou, E. M., Desrochers, A., Campoux, Y., (2006). *Experimental Study on the Water Impact of a Symmetrical Wedge.* J. Fluid Dynam. Res. 38 , No. 1, 47-66.

[61] Zhao, R., Faltinsen, O., Aarsnes, J., (1997). *Water entry of arbitrary two-dimensional sections with and without flow separation.* In. 21st Symposium on Naval Hydrodynamics., National Academy Press, Trondheim, Norway, pp. 408-423.

[62] Zhao, R., and Faltinsen, O., (1993). *Water entry of two-dimensional bodies.* Journal of Fluid Mechanics, Vol. 246, pp. 593-612.